Characterization, Modelling and State Estimation of Lithium-Sulfur Batteries

Knap, Vaclav

DOI (link to publication from Publisher):
10.5278/VBN.PHD.ENG.00020

Publication date:
2017

Document Version
Publisher's PDF, also known as Version of record

Citation for published version (APA):
Knap, V. (2017). *Characterization, Modelling and State Estimation of Lithium-Sulfur Batteries*. Aalborg Universitetsforlag. Ph.d.-serien for Det Ingeniør- og Naturvidenskabelige Fakultet, Aalborg Universitet https://doi.org/10.5278/VBN.PHD.ENG.00020

CHARACTERIZATION, MODELLING AND STATE ESTIMATION OF LITHIUM-SULFUR BATTERIES

BY
VÁCLAV KNAP

DISSERTATION SUBMITTED 2017

AALBORG UNIVERSITY
DENMARK

Characterization, Modelling and State Estimation of Lithium-Sulfur Batteries

Ph.D. Dissertation

Václav Knap

Dissertation submitted September 21, 2017

Dissertation submitted: September 21, 2017

PhD supervisor: Prof. Remus Teodorescu
Aalborg University

Assistant PhD supervisor: Assist. Prof. Daniel-Ioan Stroe
Aalborg University

PhD committee: Professor Josep M. Guerrero (Chairman)
Aalborg University

Senior Scientist Søren Højgaard Jensen
Technical University of Denmark

Associate Professor David A. Howey
University Of Oxford

PhD Series: Faculty of Engineering and Science, Aalborg University

Department: Department of Energy Technology

ISSN (online): 2446-1636
ISBN (online): 978-87-7210-070-8

Published by:
Aalborg University Press
Skjernvej 4A, 2nd floor
DK – 9220 Aalborg Ø
Phone: +45 99407140
aauf@forlag.aau.dk
forlag.aau.dk

Printed in Denmark by Rosendahls, 2017

Abstract

Lithium-Sulfur (Li-S) batteries represent an appealing battery technology, which might become an alternative for the currently wide spread Lithium-ion batteries. However, the current limitations concerning the cell performance and lifetime are the major factors, which slow down their commercialization. Vast research efforts are carried out to improve the cell design and composition; nevertheless, only a minimum of work has been focused on characterizing their behavior and developing tools for a prospective use in practical applications.

Thus, this thesis has tried to fill in the aforementioned gap and it studied several aspects for understanding the Li-S batteries behavior for prospective practical applications. Therefore, the equivalent electrical circuit model for discharging of the Li-S batteries has been developed. The proposed model is able to simulate the dynamic voltage response of the studied Li-S battery cell during the discharge and is also suitable to be used for extended Kalman filter based state-of-charge (SOC) estimation. Moreover, an equivalent electrical circuit approach was also used for the analysis of the electrochemical impedance spectroscopy performed at the Li-S cell under various temperature and state-of-charge levels.

An extensive experimental laboratory testing procedure was used to characterize the Li-S cell and to develop its models. The short-term self-discharge was experimentally investigated in detail and a simple, but effective model was proposed for it. Based on this self-discharge model, the self-balancing feature of the Li-S batteries was identified, which enhances their balancing and might even lead to avoid an additional electronic circuitry usually implemented for this purpose. Furthermore, the charge recovery effect and thermal attributes were investigated. Because of the specific behavior of Li-S batteries, a specially tailored testing methodology to evaluate the battery's performance parameters change during the ageing was proposed. The testing methodology covers the characteristic behavior such as the cumulative history, rapid self-discharge and it also includes the measurements of the unique polysulfide shuttle current.

The work was also focused on state estimation, which is an important functionality of battery management systems. Recursive Bayesian filters: an extended Kalman filter, an unscented Kalman filter and a particle filter, were used for the SOC estimation of the Li-S cell based upon the voltage response of the cell and the model. The SOC estimation approach was further improved by implementing the dual extended Kalman filter, where the first filter identified online the battery model parameters, and the second filter based on these parameters estimated the SOC. This approach was also successfully accommodated for the battery state-of-health estimation in terms of capacity fade and change of the internal resistance. Furthermore, the online identified parameters were used in the dynamic model based approach to estimate the maximum available power of the battery during the dynamic use.

Resumé

Lithium-svovl (Li-S) batterier er en lovende batteriteknologi, som kan blive et alternativ til de nuværende og ofte benyttede lithium-ion batterier. De nuværende begrænsninger vedrørende celleydelsen og levetiden er dog de vigtigste faktorer, som hindrer deres kommercialisering. Der udføres en omfattende forskningsindsats for at forbedre celledesignet og batteriets sammensætning. Ikke desto mindre er der kun udført et minimum stykke arbejde angående karakterisering af deres egenskaber samt udvikling af værktøjer til en eventuel anvendelse i forskellige applikationer.

Denne afhandling har således forsøgt at udfylde ovennævnte tomrum og undersøger derfor flere aspekter til at forstå Li-S batteriers egenskaber for potentielle praktiske anvendelser. Derfor er der udviklet en elektriske kredsløbsmodel for afladning af Li-S batterierne. Den foreslåede model er i stand til at simulere den dynamiske spændingsrespons af en Li-S battericelle under afladningen og er også velegnet til Extended Kalman filterbaseret state-of-charge (SOC) estimering. Desuden er et ækvivalent elektrisk kredsløb også blevet brugt til at analysere den elektrokemiske impedansspektroskopi, som blev udført af Li-S-cellen under forskellige temperaturer og state-of-charge niveauer.

En omfattende eksperimentel laboratorieundersøgelsesprocedure blev brugt til at karakterisere Li-S-cellen og udvikle modeller af den. Den kortsigtede selvafladning blev eksperimentelt undersøgt i detaljer og en simpel, men effektiv model, blev foreslået til dette. Baseret på denne selvafladningsmodel, blev en selvbalanceringsfunktionen af Li-S batterierne identificeret, hvilket forbedrer deres balancering og endda kan medføre, at yderligere elektroniske kredsløb, der normalt implementeres til dette formål, kan undgås. Ydermere er ladningsgendannelseseffekten og de termiske egenskaber blevet undersøgt. På grund af Li-S batteries specifikke opførsel, blev en specifik skræddersyet testmetode til evaluering af batteriets egenskabsparametre under aldringen foreslået. Afprøvningsmetoden indbefatter den karakteristiske adfærd, så som den kumulative historie, hurtig selvafladning og den inkluderer også målinger af den unikke polysulfid shuttle current.

Denne afhandling omhandler også tilstandsestimering, hvilket er en vigtig funktionalitet af batteristyringssystemer. Rekursive Bayesian filtre, et Extended Kalman filter, et Unscented Kalman filter og et partikelfilter var anvendt til SOC-estimeringen af Li-S-cellen baseret på spændingsresponsen af cellen og modellen. SOC-estimeringsmetoden blev yderligere forbedret ved at implementere et Dual Extended Kalman filter, hvor det første filter online identificer batterimodulets parametre, og det andet filter estimer SOC baseret på disse. Denne tilgang var også succesfuld med hensyn til at inddrage batteriets state-of-health i form af kapacitetsvækkelse og ændring af den interne modstand. Desuden blev de online identificerede parametre anvendt i den dynamiske model til at estimere den maksimale tilgængelige effekt af batteriet under dynamiske brug.

Acknowledgements

To pursue a PhD has been an adventurous journey for me. I have met many great and inspiring people, broadened my horizons not only about research, but also about life, and especially life in Denmark. Therefore, I would like to express my gratitude to people who accompanied me and helped me on this nutritious, and at times entangled way.

At first, I would like to thank my supervisor Remus Teodorescu, who gave me the opportunity to do this PhD. He supported my studies since the master's degree and provided me with his trust and priceless guidance all the way. My co-supervisor Daniel-Ioan Stroe, who is both my colleague and friend, has always been there for me and patiently responded without hesitation to all my questions and struggles. I am grateful that he dedicated such care and time for advising in various aspects of my PhD study. He, together with Maciej Swierczynski, introduced me to the topic of batteries and they were unreservedly sharing their experience with me. Whenever I got into some troubles with my project, it was always Erik Schaltz, as the project manager and experienced academic, who I could turn to for a helping hand. I am also very thankful to my closest colleagues Ana-Irina Stroe, Tiberiu Stanciu, Theodoros Kalogiannis and Szymon Bęczkowski for their help with practical matters and with the laboratory related work. Moreover, I would like to express my gratitude to all the other colleagues and friends from the Department of Energy Technology for their kind help and memorable time spended at Aalborg University.

For my study abroad period, I visited Cranfield University, where I met another group of lovely people. My local supervisor was Daniel J. Auger, who treated me very kindly, and he patiently introduced me to the cryptic world of state estimation. My thanks go to Abbas Fotouhi for improving my work by his advise and insight. Furthermore, I am grateful to meet and work with Karsten Propp, who has been cheerfully assisting me in matters of my research, life and ale.

My dissertation is based on work with Lithium-Sulfur cells supplied by OXIS Energy, which I would like to acknowledge them for. Bob Hawkes

opened the door for us and provided us the necessary support to start our research. During my stay in the United Kingdom, I also met other people from this company, who has had a big impact on my work. I would like to give thanks to Tom Clever for his kindness and for introducing me into the REVB project during my stay. I am grateful to know the brilliant minds as Rajlakshmi Purkayastha and Sylwia Walus, who always had a piece of good advise for me and provided me their expertise. I also want to thank Svetlana Gracheva who survived going through all my materials, often within a very short timeframe.

My work would not be as it is, if I would not have such great input from our project partners Poul Erik Seekjær from Banke Accessory Drives and particularly Lars Barkler and Andreas Christensen from Lithium Balance. Moreover, I gratefully acknowledge the Danish Council for Strategic Research (1313-00004B) and EUDP (1440-0007) for providing financial support for this work, which was a part of the ACEMU-project.

I am feeling fortunate to have had such big support from people not related to my PhD project. I was drawing on my inspiration from Martin Leginus, whose friendship made sure that the danish sky was never too dark. Whenever I felt too homesick and I got to visit my homeland, Martin Halíř always had a safe port for me. My sanity has been maintained by all my comrades from the dancing community, who reminded me to relax and have fun. At every step, there was also my dear family, who always shown their persisting support and love. I am very grateful for them all. The last, but definitely not least, I would like to thank Nevin Dolu. She has been the spice of my life and her care about me during my PhD period has been exemplary.

To all of you, great thanks!

Contents

Thesis Details

Thesis Title:	Characterization, Modelling and State Estimation of Lithium-Sulfur Batteries towards Practical Applications
Ph.D. Student:	Václav Knap
Supervisors:	Prof. Remus Teodorescu, Aalborg University Assist. Prof. Daniel-Ioan Stroe, Aalborg University

The main body of this thesis consist of the following papers.

[A1] **V. Knap**, D. Stroe, R. Teodorescu, M. Swierczynski, and T. Stanciu, "Comparison of parametrization techniques for an electrical circuit model of Lithium-Sulfur batteries," *in 2015 IEEE 13th International Conference on Industrial Informatics (INDIN)*, pp. 1278–1283, 2015.

[A2] **V. Knap**, D. Stroe, R. Teodorescu, M. Swierczynski, and T. Stanciu, "Electrical Circuit Models for Performance Modeling of Lithium-Sulfur Batteries," *IEEE Energy Convers. Congr. Expo. (ECCE)*, pp. 1375–1381, 2015.

[A3] K. Propp, M. Marinescu, D. J. Auger, L. O'Neill, A. Fotouhi, K. Somasundaram, G. J. Offer, G. Minton, S. Longo, M. Wild, and **V. Knap**, "Multi-temperature state-dependent equivalent circuit discharge model for lithium-sulfur batteries," *J. Power Sources*, vol. 328, pp. 289–299, 2016.

[A4] D. I. Stroe, **V. Knap**, M. Swierczynski, T. Stanciu, E. Schaltz, and R. Teodorescu, "An Electrochemical Impedance Spectroscopy Study on a Lithium Sulfur Pouch Cell," *ECS Trans.*, vol. 72, no. 12, pp. 13–22, Sep. 2016.

[A5] **V. Knap**, D. I. Stroe, M. Swierczynski, R. Teodorescu, and E. Schaltz, "Study on Self-Discharge Behavior of Lithium-Sulfur Batteries," *ECS Trans.*, vol. 70, no. 1, pp. 95–103, Dec. 2015.

[A6] **V. Knap**, D.-I. Stroe, M. Swierczynski, R. Teodorescu, and E. Schaltz, "Investigation of the Self-Discharge Behavior of Lithium-Sulfur Batteries," *J. Electrochem. Soc*, vol. 163, no. 6, pp. A911–A916, 2016.

[A7] **V. Knap**, D. I. Stroe, M. Swierczynski, R. Purkayastha, K. Propp, R. Teodorescu, and E. Schaltz, "A self-discharge model of Lithium-Sulfur batteries based on direct shuttle current measurement," *J. Power Sources*, vol. 336, pp. 325–331, 2016.

[A8] **V. Knap**, T. Zhang, D. I. Stroe, E. Schaltz, R. Teodorescu, and K. Propp, "Significance of the Capacity Recovery Effect in Pouch Lithium-Sulfur Battery Cells," *ECS Trans.*, vol. 74, no. 1, pp. 95–100, Dec. 2016.

[A9] **V. Knap**, D. I. Stroe, A. Christensen, K. Propp, A. Fotouhi, D. J. Auger, E. Schaltz, R. Teodorescu, "Self-Balancing Feature of Lithium-Sulfur Batteries ," *submitted in a journal*, 2017.

[A10] D. I. Stroe, **V. Knap**, M. Swierczynski, E. Schaltz, "Thermal Behavior and Heat Generation Modeling of Lithium Sulfur Batteries ," *ECS Trans.*, vol. 77, no. 11, pp. 467–476, 2017.

[A11] **V. Knap**, D.-I. Stroe, R. Purkayastha, S. Walus, D. J. Auger, A. Fotouhi, and K. Propp, "Methodology for Assessing the Lithium-Sulfur Battery Degradation for Practical Applications," *ECS Trans.*, vol. 77, no. 11, pp. 479–490, 2017.

[A12] K. Propp, D. J. Auger, A. Fotouhi, S. Longo, and **V. Knap**, "Kalman-variant estimators for state of charge in lithium-sulfur batteries," *J. Power Sources*, vol. 343, pp. 254–267, Mar. 2017.

[A13] K. Propp, D. J. Auger, A. Fotouhi, M. Marinescu, **V.Knap** and S. Longo, "Dual extended Kalman filter for online estimation of model parameters and state of charge in lithium-sulfur batteries," *submitted in a journal*, 2017.

[A14] **V. Knap**, D. J. Auger, K. Propp and A. Fotouhi, "Concurrent Real-Time Estimation of State of Health and Maximum Available Power in Lithium-Sulfur Batteries," *submitted in a journal*, 2017.

[A15] **V. Knap**, K. Theodoros, R. Purkayastha, B. Szymon, D.-I. Stroe, E. Schaltz, and R. Teodorescu, "Transferring the Incremental Capacity Analysis to Lithium-Sulfur Batteries," ECS Trans., vol. 77, no. 11, pp. 1919–1927, 2017.

In addition to the main papers, the following publications have also been made.

[B1] D. I. Stroe, **V. Knap**, M. Swierczynski, A. I. Stroe, and R. Teodorescu, "Suggested operation of grid-connected lithium-ion battery energy storage system for primary frequency regulation: Lifetime perspective," *IEEE Energy Convers. Congr. Expo. (ECCE)*, pp. 1105–1111, 2015.

[B2] D.-I. Stroe, M. Swierczynski, A.-I. Stroe, **V. Knap**, R. Teodorescu, and S. J. Andreasen, "Evaluation of different methods for measuring the impedance of Lithium-ion batteries during ageing," *in 2015 Tenth International Conference on Ecological Vehicles and Renewable Energies (EVER)*, pp. 1–8, 2015.

[B3] K. Propp, A. Fotouhi, **V. Knap**, and D. J. Auger, "Design, Build and Validation of a Low-Cost Programmable Battery Cycler," *ECS Trans.*, vol. 74, no. 1, pp. 101–111, Dec. 2016.

[B4] M. Swierczynski, D. I. Stroe, **V. Knap**, S. K. Kaer, and R. Teodorescu, "Two-Dimensional Thermal Modeling of Lithium-Ion Battery Cell Based on Electrothermal Impedance Spectroscopy," *ECS Trans.*, vol. 72, no. 11, pp. 33–38, Sep. 2016.

[B5] **V. Knap**, S. K. Chaudhary, D.-I. Stroe, M. Swierczynski, B.-I. Craciun, and R. Teodorescu, "Sizing of an Energy Storage System for Grid Inertial Response and Primary Frequency Reserve," *IEEE Trans. Power Syst.*, vol. 31, no. 5, pp. 3447–3456, Sep. 2016.

[B6] D.-I. Stroe, **V. Knap**, M. Swierczynski, A.-I. Stroe, and R. Teodorescu, "Operation of a Grid-Connected Lithium-Ion Battery Energy Storage System for Primary Frequency Regulation: A Battery Lifetime Perspective," *IEEE Trans. Ind. Appl.*, vol. 53, no. 1, pp. 430–438, Jan. 2017.

This thesis has been submitted for assessment in partial fulfillment of the PhD degree. The thesis is based on the submitted or published scientific papers which are listed above. Parts of the papers are used directly or indirectly in the extended summary of the thesis. As part of the assessment, co-author statements have been made available to the assessment committee and are also available at the Faculty.

Preface

This PhD dissertation has been part of Advanced Components for Electro Mobility Usage (ACEMU) project. The ACEMU project was supported by The Danish Council for Strategic Research and the Energy Technology Development and Demonstration Programme (EUDP). The principal investigators were Remus Teodorescu from Aalborg University, the Department of Energy Technology, and Lars Barkler from Lithium Balance. Other project partners, besides Aalborg University and Lithium Balance, were Banke Accessory Drives and Meldgaard Miljø. The main project objective was to obtain enough knowledge about Lithium Sulfur (Li-S) batteries to integrate them in a specific application with market potential and to develop new power electronics solutions for e-mobility applications[1]. The research activities of this thesis are part of the work package 1, which was focused on characterization, modelling and state estimation of the Li-S batteries.

For my study abroad I visited Cranfield University for a five months period, through which I joined the Revolutionary Electric Vehicle Battery (REVB) project. The REVB project was closely dedicated to the Li-S battery technology and it was led by OXIS Energy with other collaborators being Cranfield University, Imperial College London and Ricardo. The focus of my research at Cranfield University was mainly on state-of-charge and state-of-health estimation.

The results of research, in which I was involved, are summarized and presented in this dissertation. They are the output of our jointly effort to understand the Li-S batteries and to advance the field of their practical utilization.

Vaclav Knap
Aalborg University, September 21, 2017

---

[1] Source: official ACEMU project webpages: `http://www.acemu.et.aau.dk`.

Part I

Summary

Chapter 1

Introduction

Technological progress within the society results into spreading automation, portability and 'smartification', which often use batteries as an electrochemical energy storage devices capable to store and to provide electrical energy on demand. Different sizes of batteries can be found in various applications from small batteries in medical devices (pacemakers), wearable and portable electronics (watches, mobile phones) to large batteries in electric vehicles and grid energy storage units.

Currently, the battery technology, which dominates the market of mobile phones, laptops, electric vehicles [1,2], but also penetrates to aerospace, marine and power systems [3–5], is Lithium-ion (Li-ion). This is due to their relatively high gravimetric and volumetric energy density and long lifetime, compared to previously used Ni-MH, Ni-Cd and lead-acid batteries [1]. Today's Lithium-ion cells reach 80–240 Wh/kg gravimetric energy density, 230–670 Wh/l volumetric energy density and 1000–2000 cycle life [6].

An emerging battery technology, which provides a perspective alternative to Li-ion batteries, is the Lithium-Sulfur (Li-S). For pre-commercial cells, it has already achieved gravimetric energy density of 160–350 Wh/kg [7,8] and it has the capability to reach 500–600 Wh/kg [7,8] in near future, which is more than double of the Li-ion cells, while the volumetric energy density for the Li-S cells is approximately the same as for the Li-ion batteries (around 700 Wh/l) [8]. A comparison of various electrochemical storage systems, especially Li-ion and Li-S, is shown in Fig 1.1. Furthermore, it is expected that the price of the Li-S batteries will be lower than the one of Li-ion batteries due to the use of Sulfur, which is an abundant active material [7,8]. Moreover, the Li-S batteries can offer unique features, such as improved safety by withstanding and operating during and shortly after a nail penetration [9], and self-balancing, which allows to use the Li-S cells without any additional power electronics circuitry [A9].

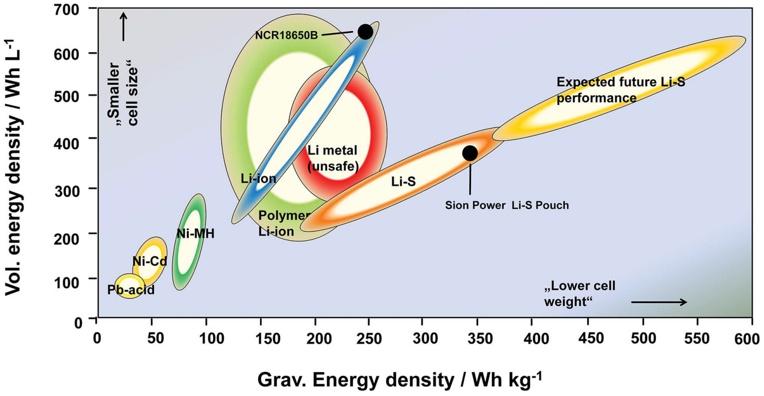

Fig. 1.1: Energy density comparison of various electrochemical storage systems. Reprinted from [8] with permission of John Wiley & Sons 2017.

1.1 Fundamentals of Lithium-Sulfur chemistry

The Li-S batteries are a solution based chemistry and in contrary to the Li-ion batteries, they are not based on the intercalation process. Generally, they consist of a lithium metal anode, an organic liquid electrolyte and a sulfur composite cathode [10], as illustrated in Fig. 1.2.

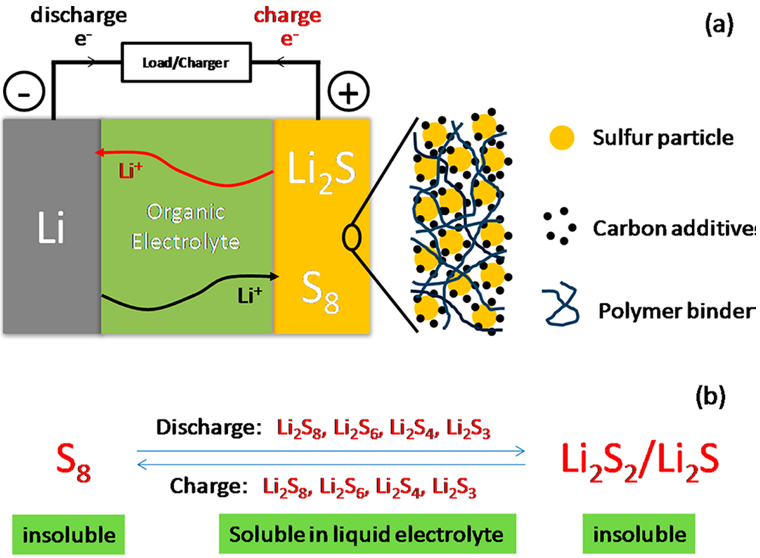

Fig. 1.2: Typical composition of the Li-S cell (a) and illustrated species together with their solubility (b). Reprinted with permission from [10]. Copyright 2017 American Chemical Society.

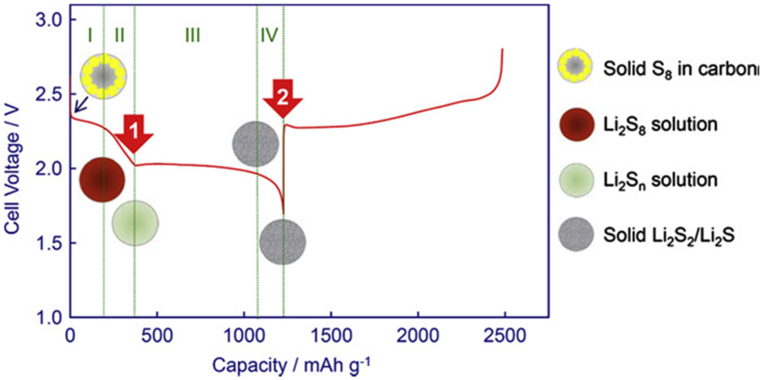

Fig. 1.3: Typical voltage profile for charging and discharging of the Li-S cell during the first cycle. Reprinted from [11] with permission from Elsevier 2017.

The typical charging and discharging voltage profile of Li-S cells the first cycle is shown in Fig. 1.3. The discharge process can be described by four reduction stages according to the sulfur species phase change with the following reactions [11]:

$$\text{Stage I: } S_8 + 2Li \rightarrow Li_2S_8 \tag{1.1}$$

$$\text{Stage II: } Li_2S_8 + 2Li \rightarrow Li_2S_{8-n} + Li_2S_n \tag{1.2}$$

$$\text{Stage IIIa: } 2Li_2S_n + (2n-4)Li \rightarrow nLi_2S_2 \tag{1.3}$$

$$\text{Stage IIIb: } Li_2S_n + (2n-2)Li \rightarrow nLi_2S \tag{1.4}$$

$$\text{Stage IV: } Li_2S_2 + 2Li \rightarrow 2Li_2S \tag{1.5}$$

During stage I, the solid sulfur is reduced and it forms Li_2S_8, which dissolves into liquid electrolyte and it takes place at the high voltage plateau. The dissolved Li_2S_8 is further reduced in stage II into shorter chain polysulfide species, while the voltage experiences a sharp decrease. Because the concentration of the polysulfide species is increasing, it also increases the viscosity of the solution. Further during discharge (stage III), the low voltage plateau is formed and short chain polysulfide species start to precipitate (transfer from liquid phase to solid phase on the cathode), resulting in the formation of insoluble Li_2S_2 or Li_2S. In the last stage IV, the solid Li_2S_2 is reduced to the solid Li_2S. Due to the non-conductive and insoluble character of these species, it causes a high polarization and this step has slow kinetics [11].

Furthermore, because of the high solubility of the long chain polysulfides (n > 4) in the electrolyte, these long polysulfides diffuse to the lithium anode, where by reacting with the lithium they are reduced to the short chain poylsulfides. This increase of the short chain polysulfide concentration at the anode leads to their flow back to the cathode, where they can form the long chain polysulfides again. This parasitic reaction is called polysulfide shuttle and it is responsible for lithium corrosion, and causes rapid self-discharge and low coulombic efficiency [12, 13].

In Fig. 1.3, there are two small voltage peaks noticeable. The peak highlighted by arrow 1 is actually a voltage dip caused by the highest viscosity of the solution due to the combination of length of the species and their concentration. Arrow 2 points to the voltage peak, which is being also referred as a voltage ″bump″ or ″kink.″ This behavior appears at the beginning of the charging due to change in polarization, caused by solid Li_2S_2 and Li_2S species being dissolved back to the electrolyte to form longer chain species [11].

The general description of the Li-S chemistry has been provided above. However, the actual Li-S mechanisms and reaction pathways are more complex and yet not completely understood or there has not been found a consensus about them [7]. Nevertheless, there is a huge effort across the scientific community to expose all the secrets of the Li-S batteries by variety of *in-situ* [7, 14–16] or *ex-situ* [7, 14–16] characterization techniques or modelling [17–19], which significantly helps in the improvement of the Li-S cell design.

1.2 Challenges of Li-S batteries

There are several challenges for Li-S batteries, which are necessary to be addressed in order to allow for a successful market penetration. One area is the cell performance. To effectively compete with the Li-ion batteries, the gravimetric energy density of the Li-S batteries has to be considerably higher and the volumetric energy density should be at least the same [6, 20]. The power capability of the cells should also not be neglected. Even though the Li-S cells are primarily energy cells, the limited useable current [6, 20] can be an obstacle for some applications. Moreover, the cell testing becomes too time demanding and thus expensive (in the case of this work typical C-rate is 0.1 for charging and 0.2 for discharging, which means 15 hours per cycle). Furthermore, one of the biggest drawbacks is the short lifetime of the Li-S cells [6, 20], which applies both to the calendar life and also to the cycle life. Moreover, last but not least is the rapid self-discharge at the higher state-of-charge (SOC) levels, caused by the polysulfide shuttle [11, 21].

Another challenge, as it was already mentioned, is to fully identify the mechanisms of the Li-S batteries. Most of the polysulfide species are in liquid form at the cathode or in the electrolyte and they are difficult to observe. After charging/discharging it lasts very long time for the cell to reach the equilibrium state and until then, the cell might significantly drift its SOC or concentration of the species might be changed. Moreover, the cell's inner state is also changed during the disassembling for *ex-situ* analysis [7].

The last group of challenges is related to the Li-S battery application design and their practical use. The characteristics and behavior of Li-S batteries at various conditions is not generally known. Li-S batteries, contrary to Li-ion batteries, have a non-monotonic voltage profile and a region with a rapid self-discharge, which makes it very difficult for accurate SOC estimation by classical methods [22,23], or also to apply classical analysis methods. Moreover, Li-S batteries suffer reversible and irreversible capacity loss [7,14], which is increasing the difficulty for state-of-health (SOH) estimation. All of this requires new tools and methods or adjustment and improvement of the current ones, in order to provide the same accuracy, safety and comfort of using Li-S batteries as it happens nowadays with Li-ion batteries.

1.3 Research objectives

The overall aim of this dissertation is to fill in the gap about the knowledge regarding Li-S batteries towards their practical use and to provide tools, such as models, estimation techniques and methodologies, which will help to introduce the Li-S batteries into practice. The outline of the dissertation follows the specific objectives of this work, which are:

1. **Electrical circuit models for Li-S batteries:** The electrical circuit models (ECM) are commonly used either for analysis of the batteries' electrochemical properties or for their simplified modelling. An investigation of the different ECM structures is done, together with the comparison of different parametrization techniques for modelling a performance model, which is able to reproduce electrical dynamic behavior of the Li-S cells. Such a model can help system engineers with integration of the Li-S battery technology. Due to its low computational effort it can be run on-board in a battery management system. Moreover, it can be used as a base for the battery state estimation. Afterwards, an ECM is proposed for the analysis of eletrochemical impedance spectroscopy (EIS) measurements and by that identify the basic processes in the used Li-S cell.

2. **Behavior, attributes and features of Li-S batteries:** A deeper knowledge about the Li-S batteries behavior, attributes and features allows for a more reliable utilization. Therefore, various characterization tests are applied to identify essential battery parameters, their behavior and

dependencies. The Li-S batteries were experimentally investigated in terms of electrical and thermal attributes. Furthermore, based on the tests some specific phenomena were identified and investigated, such as capacity charge recovery and self-discharge, as these processes highly influence the interpretation of the results. The self-discharge was also modelled and it led to the discovery of the self-balancing feature of the Li-S batteries. The experience obtained from the Li-S cell testing resulted also in proposing an optimized methodology for the reference performance test specifically adjusted for the Li-S batteries which is used for example to track changes of the battery parameters during ageing.

3. **State estimation of Li-S batteries:** The state estimation has a very important role in terms of practical use of the batteries. It provides information about useability of batteries, such as if the battery is charged enough, if it needs to be replaced, etc. However, due to the specific Li-S characteristics, many of the classical approaches are not suitable for accurate and reliable estimation. Therefore, this work was focused on tailoring the SOC and SOH estimation methods, which are going to address this challenge.

1.4 Lithium-Sulfur cells used in this work

The Li-S cells used in this work are 3.4 Ah long-life type Li-S pouch cells manufactured by OXIS Energy. They consist of a carbon/sulfur composite cathode, a lithium foil anode, organic solvent and polymeric separator. The main electrical, thermal, and mechanical parameters of the cell are summarized in Table 1.1. A single pouch cell is shown in Fig. 1.4 a). The pouch cell is attached on a test fixture for easy and quick connection of the power and voltage sensing cables. The cell mounted on the test fixture is shown in Fig. 1.4 b).

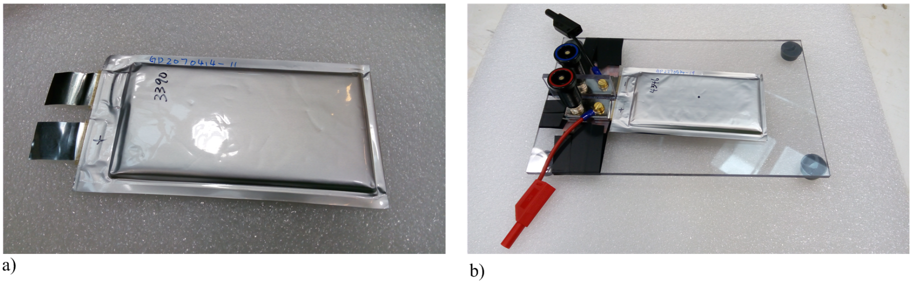

a)

b)

Fig. 1.4: a) a new 3.4 Ah Li-S pouch cell. b) the pouch cell attached on the testing fixture.

Table 1.1: Main electrical, thermal and mechanical parameters of the Li-S battery cells.

Parameter	**Value**
Nominal capacity	3.4 Ah
Nominal voltage	2.05 V
Maximum voltage	2.45 V
Minimum voltage	1.5 V
Nominal charging current	0.34 A (0.1 C-rate)
Nominal discharging current	0.68 A (0.2 C-rate)
Temperature operation range	+5°C to +80°C
Temperature storage range	–27°C to +60°C
Weight	Approx. 50.7 g
Nominal dimension (without tabs)	145x78x5.6 mm

Chapter 2

Electrical circuit models for Li-S batteries

Battery modelling can be approached from different perspectives. Ramadesigan et al. classified levels of modelling into market, system and sandwich levels [24]. Usually, the accuracy and predictability of the models correspond to their complexity and level of detail. ECMs can be fitted into the system and sandwich level categories. The ECMs are popular among the engineers, because of their intuitive use due to their electrical circuit structure and an use of electrical quantities, which make them easy to be integrated into more complex system models. They have typically lower computational requirements than more complex models, thus they are suitable to run on-board [25].

The ECMs can be found integrated in system models like electric vehicles [26–28] or electrical grids [29–31]. They contribute into better design and optimization of electronic circuits and systems [32–34]. They are used as models for emulation of the battery [35] and hardware-in-the-loop testing [29, 36]. The ECMs are also used in battery management systems (BMS) [37, 38], typically for state estimation (charge, health, available power, temperature etc.). Moreover, they are very often used in the EIS analysis, which is a non-destructive method that can provide useful insights into the physical processes taking place inside of the cell [39].

2.1 For dynamic electrical behavior and for state estimators

The ECM for dynamic electrical simulations consists most often of a voltage source, representing the open-circuit voltage (OCV), a series connected resistor and from zero up to three parallel resistor-capacitor couples connected in series [28, 40, 41]. The meaning of the circuit elements might be related to specific physical processes [25, 42], or only be abstract and be parametrized and optimized for the better model accuracy during the simulations [40, 41].

ECMs have been developed and matured for various battery types, as for example lead-acid [32, 43, 44], nickel-metal hydride (NiMH) [45–47] and Li-ion [25, 41, 48] batteries. However, until recently they have not been used for the Li-S batteries in terms of electrical performance modelling and simulations. The use of the ECM for EIS analysis has a different goal and it will be discussed in Chapter 2.2. The first mention of an operational ECM for Li-S batteries was done by Somasundaram et al. [49] in 2014, as a part of Revolutionary Electric Vehicle Battery Project (REVB).

In order to advance this topic, as the first step a parametrization techniques suitability for the Li-S ECM was compared in [A1]. Secondly, selected parametrization method was applied to the ECMs with one to four RC elements in [A2] to evaluated their accuracy. In the study presented in [A2], the model parameters' dependence on on the SOC and C-rate was considered. Further on. Abbas et al. [50] have evaluated and compared the ECMs with zero to three RC elements in terms of simulation accuracy, and complexity by the time necessary for their parametrization; and the influence of temperature was included. The ECM with 2 RC elements was considered as the best trade-off between accuracy and complexity; however, other model structures might be more suitable to use according to the purpose and specific requirements. Additionally, aspects of Li-S battery modelling and the its difference from Li-ion technology was summarized in [22].

Subsequently, the multi-temperature state-dependent equivalent circuit discharge model for Li-S batteries was proposed in [A3]. The simplicity was preferred, as the model should be used online for state estimation, thus the ECM structure contained one resistor in series with a RC element, illustrated in Fig. 2.1. The mixed pulse discharge profile, shown in Fig. 2.2, was preferred for the parametrization to the discharge profile obtain from a galvanostatic intermittent titration technique (GITT), used in [A1], [A2]. The benefit of the mixed pulse discharge profile is that it already contains pulses with three different C-rates. Therefore, it reduces the time necessary to obtain the required information (the GITT in [A2] had to be repeated three times to get parameters for 3 C-rates) and the degradation of the cell by reduced amount of performed cycles.

In order to obtain the parameter values for the circuit elements, the prediction error minimization (PEM) [51] was applied individually to each current pulse, including the relaxation period of 300 seconds before and after each pulse. The parametrization was done for the behavioral model, shown in Fig. 2.1 b). The benefits of the use of the behavioral model for the parametrization is that it has no "reciprocal" parameters. Moreover, it is more straightforward and intuitive to apply parameter constraints. Oth-

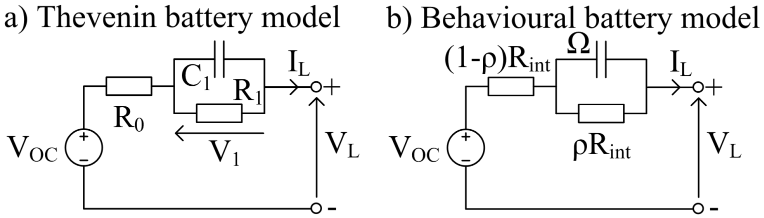

Fig. 2.1: Structure of the Thévenin battery model and the proposed Behavioral battery model, used for the parametrization.

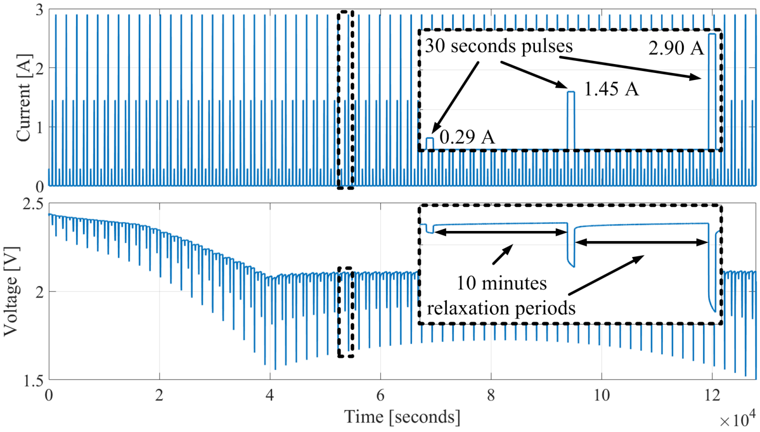

Fig. 2.2: Mixed pulse discharge test used for the parametrization of the Li-S ECM. The positive current stands for discharge.

erwise, the parametrization is numerically identical as it is for the classical Thévenin model and the parameters can be recomputed from the Thévenin to the behavioral model:

$$\Omega = \frac{1}{R_1 C_1} \tag{2.1}$$

$$R_{int} = R_0 + R_1 \tag{2.2}$$

$$\rho = \frac{R_1}{R_{int}} \tag{2.3}$$

or from the behavioral to the Thévenin model:

$$R_1 = \rho R_{int} \tag{2.4}$$

$$R_0 = R_{int} - R_1 \tag{2.5}$$

$$C_1 = \frac{1}{R_1 \Omega} \tag{2.6}$$

where, Ω has the meaning of the "dynamic bandwidth" and it is determined based on R_1 and C_1. R_{int} stands for the "total steady-state resistance". The "dynamic fraction" of the response is described by ρ.

The essential model equations (at first written for the Thévenin model), where the current I_L is considered as the input and the battery voltage V_L is the output, are written as:

$$V_L = V_{OC}(\chi) - V_1 - R_0(\chi) I_L \tag{2.7}$$

Thus, the model has two dynamic states. They are the state-of-charge (SOC), expressed symbolically as χ, and the voltage over the RC element V_1. The derivative of the states are computed as:

$$\dot{\chi} = -\frac{1}{Q_{cap}} I_L \tag{2.8}$$

$$\dot{V}_1 = -\frac{1}{R_1(\chi)C_1(\chi)} V_1 + \frac{1}{C_1} I_L \tag{2.9}$$

where Q_{cap} is the capacity of the cell expressed in Coulombs (for practical reasons $A \cdot s$ are used).

The equations rewritten for the behavioral model would take form as:

$$V_L = V_{OC}(\chi) - V_1 - (1 - \rho(\chi))\, R_{int}(\chi) I_L \tag{2.10}$$

$$\dot{\chi} = -\frac{1}{Q_{cap}} I_L \tag{2.11}$$

$$\dot{V}_1 = -\Omega(\chi) U_1 + \rho(\chi) R_{int}(\chi) \Omega(\chi) I_L \tag{2.12}$$

The identified circuit parameters for a temperature of 20 °C are shown in Fig. 2.3. The parameters for the temperature range 10–50 °C are presented in detailed in [A3]. Generally, the identified parameters are in agreement with the value presented in other studies [7]. There are clearly visible two voltage plateaus: high and low; and there is a peak in resistance R_0 between them, which is related to the increased viscosity of the electrolyte, as it was mentioned in Chapter 1.1.

The identified parameters have shown only a small dependence on the applied C-rate levels. Therefore, they were considered for modelling as independent on C-rate. The included dependencies are the SOC and the temperature. The parameters are implemented in the model as functions, instead of look-up tables, because the model is intended to be used for state estimation

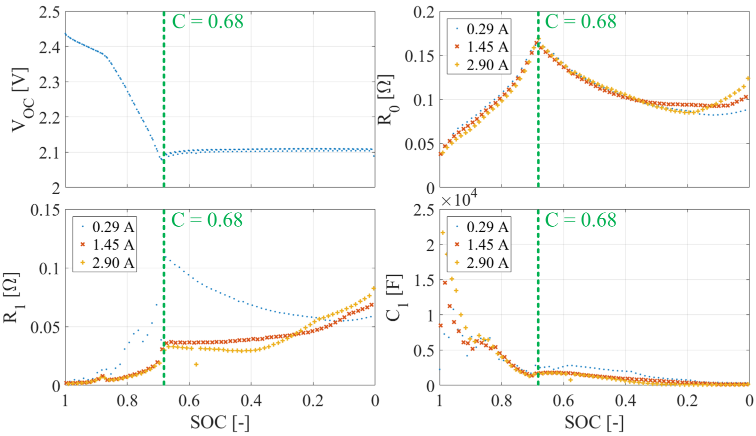

Fig. 2.3: Identification results for V_{OC}, R_0, R_1 and C_1 from the mixed pulse discharge profile at 20 °C.

and the derivative of the parameters will be needed. The general polynomial function is given in (2.13).

$$\begin{aligned} f_{parameter}(\chi) = {} & p_{10}x_1^9 + p_9x_1^8 + p_8x_1^7 + p_7x_1^6 + p_6x_1^5 \\ & + p_5x_1^4 + p_4x_1^3 + p_3x_1^2 + p_2x_1 + p_1 \end{aligned} \tag{2.13}$$

has been used for the parameter fitting. However, because of the sudden change in the parameter trend between the voltage plateaus, which is difficult to reproduce by only one polynomial, two polynomial functions were combined in order to obtain V_{OC} and R_0 more accurately. One polynomial was used for each plateau, as follows:

$$\begin{aligned} f_{\text{parameter}}(\chi) = {} & (1 - \gamma_{\text{m,c}}(\chi)) \quad f_{\text{parameter}-\text{low}}(\chi) \\ & + \gamma_{\text{m,c}}(\chi) \quad f_{\text{parameter}-\text{high}}(\chi) \end{aligned} \tag{2.14}$$

Because the parameter functions are required to be differentiable (for the later use of the Kalman filter for state estimation), the combining function γ is written as:

$$\gamma_{\text{m,c}}(\chi) := \begin{cases} 0, & \text{if a} \\ \frac{1}{2} + \frac{1}{2}\sin\left(2m(\chi - c)\right), & \text{if b} \\ 1, & \text{if c} \end{cases} \tag{2.15}$$

Where the conditions a, b and c stands for the different ranges of the function,

$$\begin{aligned} \text{a}: \ 2m(\chi - c) &< -\frac{\pi}{2}, \\ \text{b}: \ -\frac{1}{2}\pi \leq 2m(\chi - c) &< \frac{\pi}{2}, \\ \text{c}: \ 2m(\chi - c) &> \frac{\pi}{2}, \end{aligned} \tag{2.16}$$

here, c, illustrated in Fig. 2.3 for 20 °C, stands for point where both functions are equally represented and m is a scaling factor for the maximal gradient of the sinusoidal function, determining the transition range between both polynomials. The final form of the state space model takes the following form:

$$\begin{aligned} \dot{x}(t) &= A(t)x(t) + B(t)u(t) \\ y(t) &= C(t)x(t) + D(t)u(t) \end{aligned} \tag{2.17}$$

where the state space representation of A, B, C and D is:

$$\begin{aligned} A &= \begin{bmatrix} \frac{-1}{f_{R_1}(\chi)\, f_{C_1}(\chi)} & 0 \\ 0 & 0 \end{bmatrix} \quad B = \begin{bmatrix} \frac{1}{f_{C_1}(\chi)} \\ \frac{-1}{3600 Q_{\text{cap}}} \end{bmatrix} \\ C &= \begin{bmatrix} -1 & f_{\text{V}_{\text{OC}}}(\chi) \end{bmatrix} \quad D = \begin{bmatrix} f_{R_0}(\chi) \end{bmatrix}. \end{aligned} \tag{2.18}$$

with parameters $V_{OC}(\chi)$, $R_0(\chi)$, $C_1(\chi)$ and $R_1(\chi)$ being determined by the nonlinear functions described above. The specific value of the polynomial coefficients can be found in [A3].

The NEDC driving profile, illustrated in Fig. 2.4, was used for the model validation. The cell was placed at room temperature of 23 °C and it was tested using a Kepco BOP 100-10MG. The model accuracy was quantified by the root mean square error (RMSE):

$$RMSE = \sqrt{\frac{\sum(V_{t,i} - \widehat{V}_{t,i})^2}{n}} \tag{2.19}$$

where n is the number of data points, $V_{t,i}$ is the measured voltage and $\widehat{V}_{t,i}$ is the model voltage. The NEDC validation test is presented in Fig. 2.4 and it resulted in 32 mV RMSE, which is considered satisfactorily with respect to the voltage range of the test (voltage between 1.5 V to 2.45 V), and that the ECM with only one RC element was used and the dependence on C-rate was neglected.

The presented ECM for the Li-S batteries can be considered as a good starting point model for this technology. It opens possibilities for work on

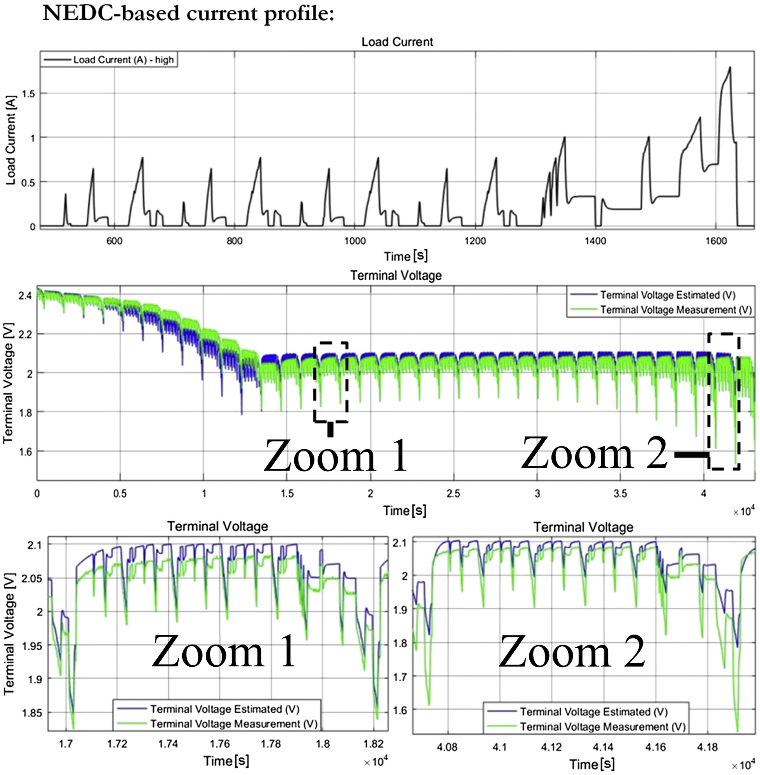

Fig. 2.4: Comparison of the measured battery terminal voltage and the battery model voltage for NEDC driving cycle at 23 °C. The Zoom 1 and Zoom 2 areas show additional detail. Reprinted from [A3], doi: 10.1016/j.jpowsour.2016.07.090, under the terms of the CC BY.

state estimation and it provides a basic electrical behavior of the Li-S batteries. However, the model is dedicated only to discharge operation and it does not include the cell self-discharge or any other complex mechanisms of this chemistry. For more accurate representation of the Li-S mechanisms it might be beneficial to move a step higher in complexity and look into zero [17] or one [52] dimensional models.

2.2 For electrochemical analysis from electrochemical impedance spectroscopy

Electrochemical impedance spectroscopy (EIS) is a non-destructive measurement technique used for investigation and analysis of the electrochemical properties, (in our context) of batteries. The measurement is based on applying a sinusoidal current or voltage to the battery and observing the output signal: voltage (galvanostatic mode) or current (potentiostatic mode), respectively. In a linear (or pseudo-linear) system, the observed signal has the same frequency as the input, but it is phase-shifted. This procedure is repeated for several frequencies, and thus the impedance spectrum is obtained. The impedance can be computed as [53]:

$$|Z| = \frac{U}{I} = \frac{U_0 sin(\omega t)}{I_0 \dot{s}in(\omega t + \varphi)} = Z_0 \frac{sin \omega t}{\sin(\omega t + \varphi)} \tag{2.20}$$

where the quantities with lower index of 0 (e.g. Z_0) represents the magnitudes of the signal, t is time, ω is radial frequency ($\omega = 2\pi f$) and φ is the phase shift. The impedance can be also described as composed from the real $Re(Z)$ and imaginary $Im(Z)$ parts:

$$|Z| = \sqrt{Re(Z)^2 + Im(Z)^2} \tag{2.21}$$

The experimentally obtained impedance spectrum can be then approximated by the impedance of an equivalent circuit, which consists of electrical circuit elements, such as resistors, capacitors, constant-phase elements and inductances; and each of these elements can be related to some physical process inside the battery.

The EIS technique has been applied to the Li-S batteries to study different aspects and mechanisms. The charging and discharging processes and their effects on the electrolyte and electrode surfaces was studied in [54] by Kolosnitsyn et al. They showed that the dissolution of lithium polysulfides has a great influence on the electrolyte conductivity and that the electrolyte properties have effects on the processes taking place at both electrodes. The same authors presented in [55], that the internal resistance at the same SOC is dependent according to how it was reached: by charging or discharging, because of the different polysulfide species being formed. Moreover, the influence of the electrode and electrolyte compositions on the cell impedance was studied at the Li-Li symmetrical cells in [56], which provides a deeper insight into the Li-S interfacial properties and separation of the processes at the specific electrodes. Alternative characterization methods as X-ray diffraction (XRD), scanning electron microscopy (SEM) and energy-dispersive X-ray spectroscopy (EDS) were applied to the Li-S battery in [57] in combination with EIS to further understand the electrochemical processes related to the specific parts of the spectra. The obtained results were implying that the reduction reaction is prevailed by interfacial charge transfer impedance at the high voltage plateau, while at the low voltage plateau, the reduction reaction is governed by the mass transport in the cathode. Additionally, at the start of the low voltage plateau, the solid Li_2S was detected and with the following discharge it increased on its density. The effect of temperature to the Li-S processes was studied by EIS in [58], where also the cell was cycled and the capacity fading mechanisms were studied. During the cycling ageing, the charge transfer resistance increase was observed, which was believed to be caused by the changes in the sulfur cathode conductivity and the properties of the cathode surface. The degradation study introduced in [39] has agreed about changes in the cathode having a big influence to the capacity fade; however, they have observed reduction of the cathodic charge transfer resistance. In general, there has also not been found a general consensus about the meaning of the specific circuit elements used to fit the impedance spectrum [39, 54–58].

An extensive characterization of the 3.4 Ah Li-S pouch cell by the EIS technique was done and presented in [A4]. The cell was investigated in terms of SOC and temperature dependence. The influence of the SOC on the impedance spectra measured at 15 °C is shown in Fig. 2.5. There are clearly two noticeable trends of the spectra curves according to the SOC. The impedance curves are moving to the right side of the Nyquist plane (higher real impedance) when SOC decreases in the interval 70–100 % SOC, as presented in Fig. 2.5 a). However, for the interval 0–65 % SOC, the trend of the impedance curves is opposite, they are moving to the left (lower real impedance) with the SOC decrease.

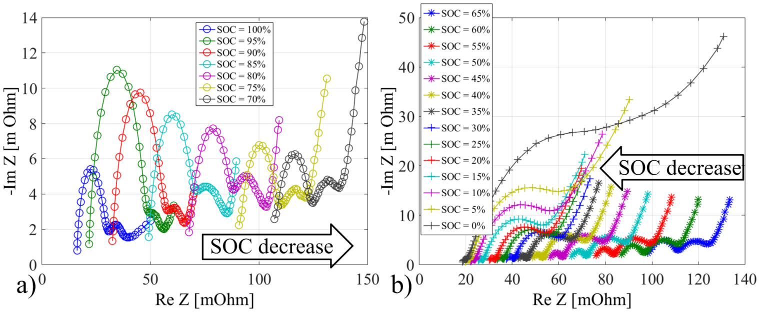

Fig. 2.5: Impedance spectra of the Li-S pouch cell measured at 15 °C. a) SOC interval 70 - 100 %, b) SOC interval 0 - 65 %. Republished with permission of Electrochemical Society, from [A4], 2017; permission conveyed through Copyright Clearance Center, Inc.

An electrical circuit for fitting the Nyquist curves has been considered based on the shape of the obtained plots, illustrated in Fig. 2.5 for 15 °C, and the circuit structure is presented in Fig 2.6. Constant-phase elements (CPEs) are used instead of the capacitors, because they provide a better fit for non-ideal behaviour of the system.

The obtained ohmic resistance *Rs*, presented in Fig. 2.7 a), is in agreement with the identified parameters in [A3], illustrated in Fig. 2.3, and with the results presented in literature [7, 39, 54]. The peak in the *Rs* is caused by the most viscose state of the electrolyte and it is also the transition point between the high and low voltage plateaus. It is observed that this inflection point

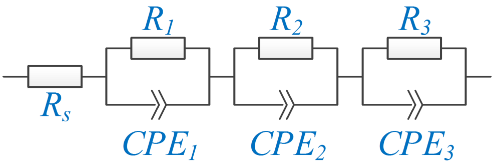

Fig. 2.6: Equivalent electrical circuit used for fitting of the EIS spectra. Republished with permission of Electrochemical Society, from [A4], 2017; permission conveyed through Copyright Clearance Center, Inc.

is at 70 % SOC for 15 °C and with increasing temperature it is moving to higher SOC, shown in Fig. 2.7 up to 85 % SOC for 45 °C. In Fig. 2.7 b), there is shown the resistance $R1$, which is exponentially growing with the SOC increase for all observed temperature levels. Cañas et al. [39] observed the same behaviour and they believed that $R1$ (in their work labeled as $R2$) is related to the charge transfer of sulfur intermediates on the cathode side. Observed $R2$ in Fig. 2.7 c) is high for the low SOC and then it rapidly decreases; and again it can increase at 100 % SOC. Cañas et al. [39] attributes this element to the formation and dissolution of Li_2S and S_8. The diffusion process should be represented by the resistance $R3$; however, the fitting returned scattered values, shown in Fig 2.7 d), and a clear conclusion about its dependence SOC and temperature could not be drawn.

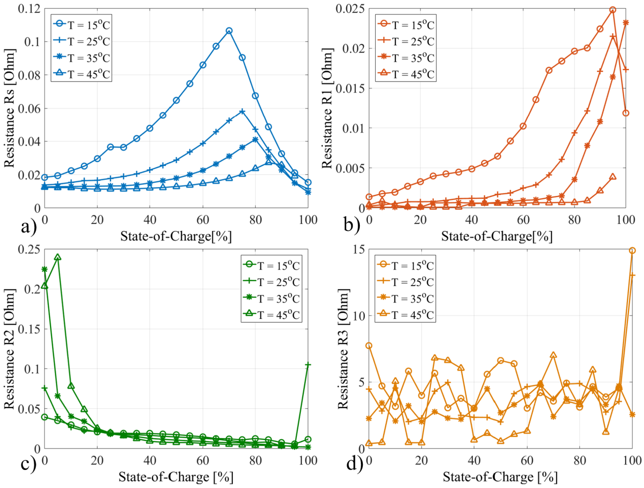

Fig. 2.7: Variations of resistance a) Rs, b) $R1$, c) $R2$, d) $R3$ with SOC and temperature. Republished with permission of Electrochemical Society, from [A4], 2017; permission conveyed through Copyright Clearance Center, Inc.

The 3.4 Ah Li-S pouch cell was studied by EIS in terms of dependence on the SOC and temperature. The obtained results were related to the studies on coin cells in literature. Thus, the meaning of the electrical circuit elements have been assigned. Furthermore, the established base-ground will be beneficial for following investigation of Li-S battery degradation by EIS.

Chapter 3

Behavior, attributes and features of Li-S batteries

In order to develop an efficient product and to get the most out of the batteries, it is necessary to have a prior knowledge about their characteristics and behavior, which gets reflected into the application design. Many studies about the Li-S batteries are dedicated in development of better cells; however, they are usually limited to the coin-cell level [59–61]. The performance of the coin cells do not always correspond 100 % to the performance of pouch cells (or any larger format cells). The high areal sulfur loading in the Li-S pouch cells causes steeper polysulfide shuttle and high areal current at the lithium anode [62]. Such high current (e.g. 160 mA instead of 0.5–5 mA at the coin cell) is not able to be equally distributed and it may cause growth of lithium dendrites [63]. Even though, the studies about the Li-S pouch cells have started to appear in the literature, they are still rather scarce. Methods to develop better performing Li-S pouch cells, were investigated in [64–66]. The electrochemical properties and mechanisms were studied in [67–69]. Specifically, the degradation was focused in [70–72]. Nail penetration and the safety of the Li-S pouch cell were presented in [9]. The Li-S pouch cell was used for parametrization and modelling in [50,73] and in the previously presented papers [A1], [A2] and [A3].

The continuous discharging and charging curve for the tested cell were obtained for various currents at 15, 25 and 35 °C and they are presented in Fig. 3.1 and 3.2. Before every characterizing cycle, there was performed a pre-conditioning cycle, which is described in detail in Chapter 3.5, and the charging and discharging curves were obtained individually. From the obtained curves it is obvious that the capacity highly depends on the temperature as well as on the applied C-rate. With increase of the discharging current, the low voltage plateau gets reduced, while the high voltage plateau seems not influenced, besides the larger voltage drop.

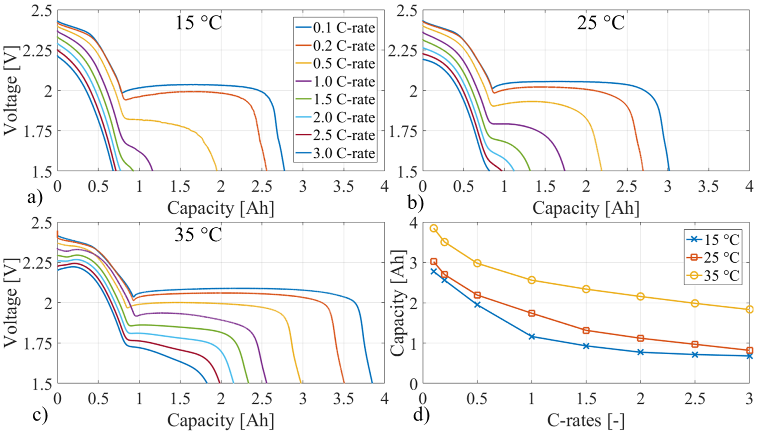

Fig. 3.1: Discharging voltage curves at various C-rates for a) 15 °C, b) 25 °C and c) 35 °C. d) Continuous discharging capacity at various C-rates for the three temperatures. Before the discharge, the cell was charged by 0.1 C-rate. The 1.0 C-rate discharge curve at 35 °C does not follow the exact trend, because it was obtained additionally.

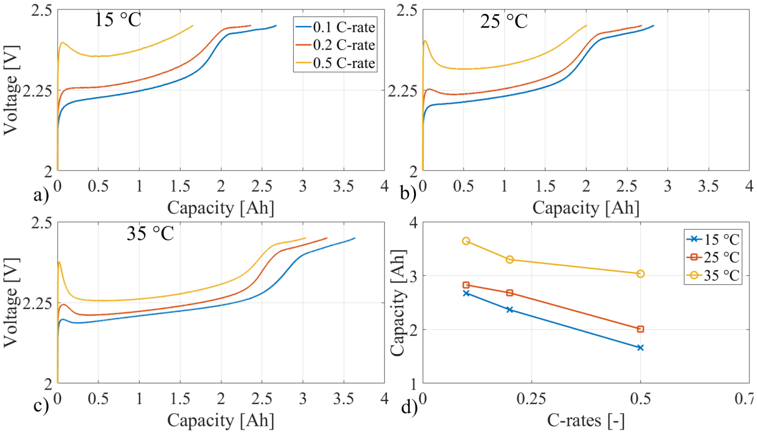

Fig. 3.2: Charging voltage curves at various C-rates for a) 15 °C, b) 25 °C and c) 35 °C. d) Continuous charging capacity at various C-rates for the three temperatures.

3.1 Self-discharge

Self-discharge is an important attribute of the batteries, which influence their capability to store the charge over a long period of time, affect their efficiency, and economy. The Li-S batteries experience a rapid self-discharge mainly due to the polysulfide shuttle mechanism [21]. This self-discharge can reach up to tens of percent in a range of hours or days, which needs to be reflected in the applications design and laboratory tests. Therefore, it is important to characterize the self-discharge and provide a tool for its prediction.

The self-discharge is often investigated in a process of developing new cells in order to compare them to the previous or well-established ones, as it was performed for example in [74–76]. However, the investigation is limited only to one or two conditions (e.g. SOC or temperature) and it is done at the coin cell level. The self-discharge process was quantified in relation to the polysulfide shuttle by Mikhaylik and Akridge in [21], where different cell idling times were considered; and they have observed that the self-discharge takes place only at the high voltage plateau, while the charge at the low voltage plateau seems stable over a period of weeks. Moreover, a prismatic cell was investigated for the self-discharge at 100 % and 40 % SOC at 20 °C for various storage time in [77].

A thorough investigation of the self-discharge behavior of the Li-S cell was performed in [A5] and [A6]. The test protocol, presented in Fig. 3.3, included the pre-conditioning cycle, a cycle to set the depth-of-discharge (DOD), idling of the cell (relaxation), discharge to obtain the remaining capacity and the nominal cycle to obtain the actual capacity after the storage. The quantification of the self-discharge follows the methodology presented in [77] and it is visualized in Fig. 3.4.

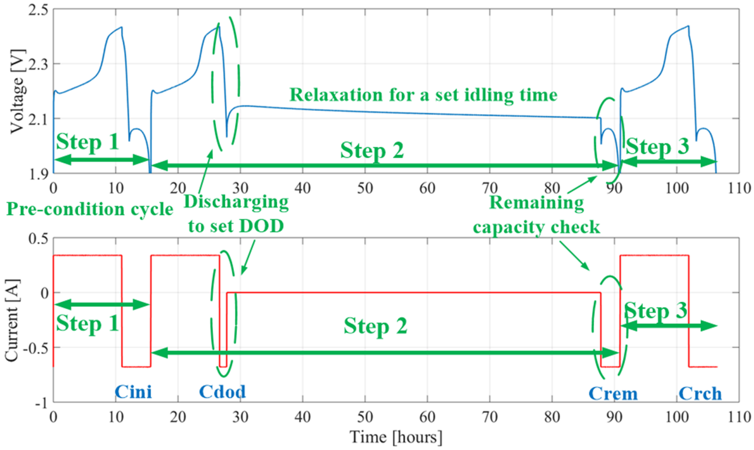

Fig. 3.3: The test protocol for systematic self-discharge measurement by idling the cell at the specific conditions. Republished with permission of Electrochemical Society, from [A6], 2017; permission conveyed through Copyright Clearance Center, Inc.

At first, the self-discharge dependence on DOD over its whole range at 35 °C for 60 hours idling time was examined. The evolution of the voltage during the idling period is shown at Fig. 3.5. During idling at the high volt-

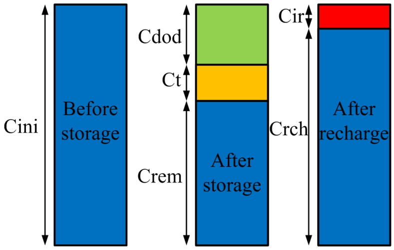

$$C_t = (C_{ini} - C_{dod} - C_{rem})/C_{ini} * 100$$

$$C_{sd} = (C_{rch} - C_{rem} - C_{dod})/C_{ini} * 100$$

$$C_{ir} = (C_{ini} - C_{rch})/C_{ini} * 100$$

Fig. 3.4: Quantification of the self-discharge and separation of the capacity values. C_t is the total capacity loss during the idling, C_{ini} is the initial discharge capacity, C_{dod} is the discharged capacity to the specific DOD point, C_{rem} is the remaining capacity after the idling time, C_{sd} is reversible capacity loss, also noted as the self-discharge rate, C_{rch} is the new actual discharge capacity during recharge after the idling and C_{ir} is the irreversible capacity loss. Republished with permission of Electrochemical Society, from [A6], 2017; permission conveyed through Copyright Clearance Center, Inc.

age plateau (Fig. 3.6 a)), the voltage decays significantly from its maximum, reached at the voltage recovery after the discharge. The voltage decay is related to the self-discharge observed at the high voltage plateau, as it is seen in Fig. 3.6. The self-discharge rate is the highest for a fully charged cell and it is decreasing with the decrease of the SOC. When the inflection point is reached and the cell appears at the low voltage plateau, the self-discharge rate becomes very low, closer to zero or negative, which is perceived as the capacity recovery effect, discussed in detail in Chapter 3.2.

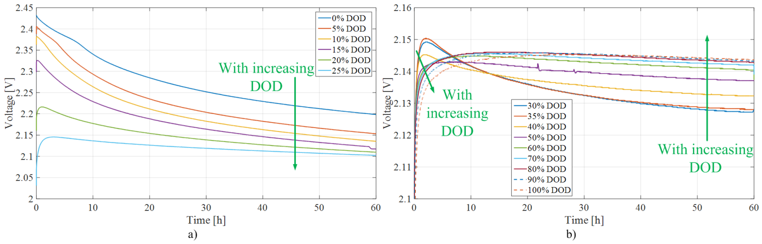

Fig. 3.5: Voltage evolution during 60 hours idling at 35 °C, a) for initial DOD between 0 and 25 %, b) for initial DOD between 30 and 100 %. Republished with permission of Electrochemical Society, from [A6], 2017; permission conveyed through Copyright Clearance Center, Inc.

Further, the influence of temperature was studied by idling the cell of various DODs in the interval 0–30 % for 4 hours at the temperature levels of 15, 25, 35 and 45 °C. From the results, presented in Fig. 3.7, it can be observed that the self-discharge rate increases with the increase of the temperature until 35 °C. For a temperature of 45 °C, the self-discharge rate seems to be lower; however that is caused by the 'shift' in the SOC. The self-discharge rate is believed to be actually considerable higher and it causes loss of the

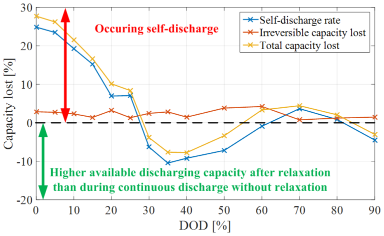

Fig. 3.6: The self-discharge results obtained from the measurement at 35 °C after 60 hours of idling for various DOD. Republished with permission of Electrochemical Society, from [A6], 2017; permission conveyed through Copyright Clearance Center, Inc.

capacity at the high voltage plateau, which leads to the high voltage plateau 'shrinkage,' as it is illustrated in Fig. 3.8.

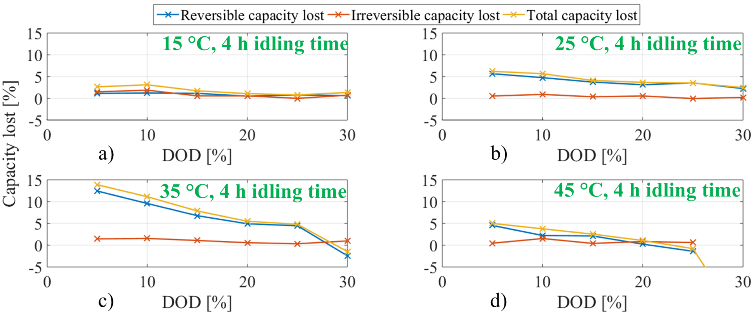

Fig. 3.7: The self-discharge results obtained from the measurement for various DOD and temperature levels with 4 hours of idling period. Republished with permission of Electrochemical Society, from [A6], 2017; permission conveyed through Copyright Clearance Center, Inc.

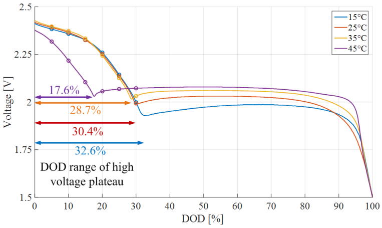

Fig. 3.8: Positions of the measured points for self-discharge at the voltage curve during continuous discharge with relation to DOD levels related separately to each temperature. Republished with permission of Electrochemical Society, from [A6], 2017; permission conveyed through Copyright Clearance Center, Inc.

The next step was to evaluate the influence of the idling time on the self-discharge rate; the results are graphically summarized in Fig. 3.9. There is an increase of the absolute self-discharged capacity with the longer idling time;

however, its steepness is decreased. This can be understood in the way that there is a higher self-discharge at a higher SOC, which over time causes a drift in the SOC, which causes subsequently a lower self-discharge. Moreover, in the range of 0–20 % DOD and 15–35 °C, it seems that the self-discharge is more sensitive to the initial SOC, rather than to the temperature.

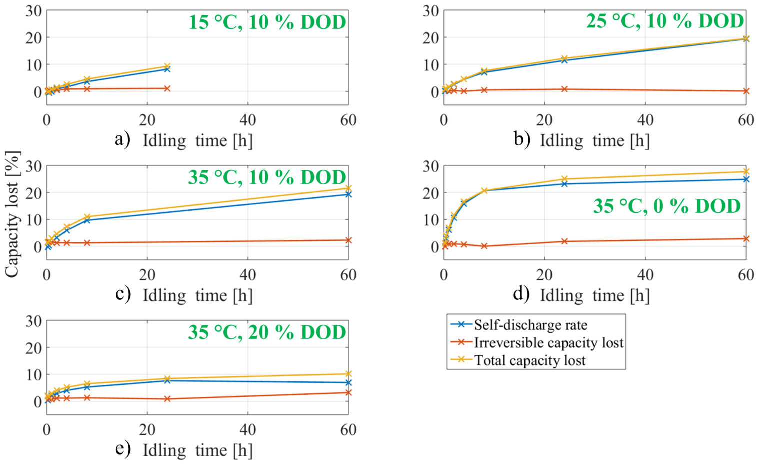

Fig. 3.9: The measured self-discharge for various temperature, DOD and idling time. Republished with permission of Electrochemical Society, from [A6], 2017; permission conveyed through Copyright Clearance Center, Inc.

The methodology presented in [21] was applied to the gathered data in order to obtain the self-discharge constant of the tested Li-S cell. It should be possible to apply the self-discharge constant in order to predict the self-discharge of the cell at different idling conditions. However, the accuracy of this prediction has been found not sufficiently accurate [A6]. Therefore, an alternative method for the self-discharge prediction needs to be developed.

Moy et al. have presented a methodology for the direct measurement of the polysulfide shuttle current in [13]. With the hypothesis that the polysulfide shuttle is the main responsible process for the self-discharge, it should be possible to use this polysulfide shuttle current as the self-discharging current and by that predict the self-discharge of the cell. The direct measurement of the polysulfide shuttle current is based on applying the constant voltage charging mode to the cell. The polysulfide shuttle causes the self-discharge and by that the voltage decay. Because the voltage is kept constant, after a settling period the internal self-discharge current gets compensated by the external current, which is measured. This methodology was utilized in [A7] to develop a model for the self-discharge. The measured values of the shuttle current are presented in Fig. 3.10 and they were used to fit the following equation:

$$I_{sh} = c \cdot exp(d \cdot Temp) \cdot exp((e \cdot Temp + f) \cdot DOD) \tag{3.1}$$

where I_{sh} is the shuttle current, $Temp$ is the temperature and DOD is the depth-of-discharge. The remaining variables c, d, e and f are the fitted parameters. By fitting these parameters, the first version of the model mathematical expression can be obtained. However, this version is burdened by the error in the DOD values in Fig. 3.10, because they do not account for the self-discharge happening during the measurement. Therefore, the first version of the model is used to 'correct' these DOD values and account for the self-discharge during the measurement. The updated DOD values were then used for another fitting process, which led to a more accurate model. The model was validated for four conditions by using the similar procedure as shown in Fig. 3.3. It proofed the model to be valid with a relative error of the final estimated capacity between 1.60–6.65 % for the specific cases, presented in Table 3.1. The relative error was computed according to (3.2), where C_{meas} is the final capacity measured and C_{est} is the final capacity estimated.

$$Err_{rel} = \frac{C_{meas} - C_{est}}{C_{meas}} \cdot 100 \tag{3.2}$$

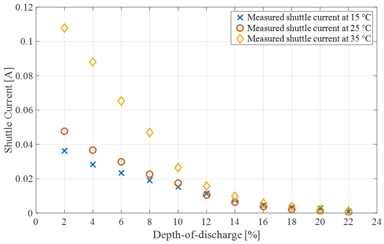

Fig. 3.10: The measured shuttle current values for pre-determined DOD points. Reprinted from [A7] with permission from Elsevier 2017.

Table 3.1: Comparison of the capacities measured and estimated by the proposed self-discharge model.

Validation cases	Final capacity measured	Final capacity estimated	Absolute error	Relative error
Validation Case 1 0 % DOD, 20 °C, 4 h idling	2.606 Ah	2.5642 Ah	0.0418 Ah	1.60 %
Validation Case 2 0 % DOD, 30 °C, 12 h idling	2.262 Ah	2.4125 Ah	-0.1505 Ah	6.65 %
Validation Case 3 10 % DOD, 25 °C, 6 h idling	2.273 Ah	2.3335 Ah	-0.0605 Ah	2.66 %
Validation Case 4 15 % DOD, 35 °C, 2 h idling	2.399 Ah	2.4937 Ah	-0.0947 Ah	3.95 %

3.2 Capacity charge recovery

During the tests oriented on self-discharge in [A5] and [A6], it has been found a negative value of the self-discharge rate for some conditions, as illustrated in Fig. 3.6. This means that the total obtained capacity before and after idling was higher than the capacity obtained from the continuous discharge. This behavior of batteries is often refereed as a capacity charge recovery [78], which is the effect, when the battery recovers partially or fully the capacity 'lost' due to the discharge with high currents. This 'lost' of capacity due to high currents is referred as the rate capacity effect. The Li-S batteries show very high dependence of the capacity on the applied current, as presented in Fig. 3.1. Consequently, the rate capacity effect is significant for the Li-S batteries. This process may be connected to the formation of insulating Li_2S species on the cathode, which as it was shown by scanning electron microscopy in [79] increases with discharge current. Due to the increased coverage of the surface by Li_2S species, the Li-S batteries show larger activation over-potential, which leads to the diminished discharge capacity at high current [80]. Therefore, with the high rate capability effect, it is assumed that the Li-S batteries have also high charge recovery effect, which can influence their testing or be significant for their practical application. Thus, the capacity charge recovery effect was systematically investigated in [A8].

Because of the high self-discharge at the high voltage plateau [A5], [A6] and [A7], this plateau was omitted from the test and the cell was charged only to 2.26 V by 0.1 C-rate. Then the cell was sequentially discharged by repeatedly applying a current pulse followed by a relaxation period until the cut-off voltage of 1.5 V was reached. The general test procedure, including the pre-conditioning cycle described in [A11], is illustrated in Fig. 3.11 and the investigated discharging conditions are presented in Table 3.2.

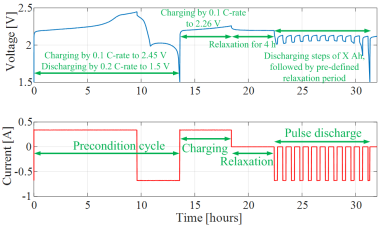

Fig. 3.11: Test procedure of the pulse discharge to capture the capacity recovery effect. Republished with permission of Electrochemical Society, from [A8], 2017; permission conveyed through Copyright Clearance Center, Inc.

Initially, the test was done for relaxation periods of 0.5, 1, 5, 10, 30, 60, 120, 240 and 480 minutes at 25 °C, by discharging with a current of 0.2 C-rate with 0.2 Ah steps. The obtained results are presented in Fig. 3.12. Because

Table 3.2: The test matrix for considered C-rates, discharging steps lengths and temperatures.

	Discharging step lengths [Ah]		
C-rate	0.05	0.1	0.2
0.2	✓	✓	✓*
0.5	-	-	✓
1.0	-	-	✓

*the measurement was performed for 15, 25, and 35 °C

the difference in measured available capacity between 240 minutes (= 4 hours) and 480 minutes (= 8 hours) was only 0.5 %, and due to the time demanding feature of the test, four hours were considered as a sufficient relaxation period for the test at other conditions. Thus the investigated relaxation periods were settled to be 1, 5, 10, 60 and 240 minutes.

The available discharge capacity at all measured conditions exhibit an exponential dependency on the relaxation time between pulses, which is in agreement with the results published in [52]. As it was expected, due to the high rate capability effect, the discharge capacity is more reduced by applying high currents and then consequently a high available capacity can be obtained by introducing relaxation periods during the discharge as results from Fig. 3.12 b). In the cases when the cell is discharged by shorter pulses, it causes only a smaller gradient of ionic concentration over the cell. Therefore, the charge recovery is faster. It is shown in Fig. 3.12 c), that the saturation point of the available capacity was reached already in one hour for 0.05 Ah pulses, instead of four hours for 0.2 Ah pulses. Temperature is influencing the available discharge capacity mainly in two ways. At low temperature, the ionic diffusion is low, which causes higher resistance and the discharge voltage cut-off limit is reached earlier. Consequently, the discharge capacity is reduced. Then, the cell has high potential to recover more capacity by introducing the relaxation periods. However, the diffusion process is slowed down at the low temperature, which results into slow re-equilibrating, as presented in Fig. 3.12 d).

3.3 Self-balancing

The self-discharge of the Li-S batteries, discussed in Chapter 3.1, has also an impact on their balancing. Cell balancing is an important part of the battery operation, which influence their safety, amount of useable capacity and lifetime. Focusing on a series-connection of the cells, their charging and discharging is limited by the highest and lowest charged cell, respectively, as it is illustrated in Fig. 3.13. Therefore, if cells with different SOC are present, the useable capacity, which is possible to obtain from the string of the cells, is reduced [81–83].

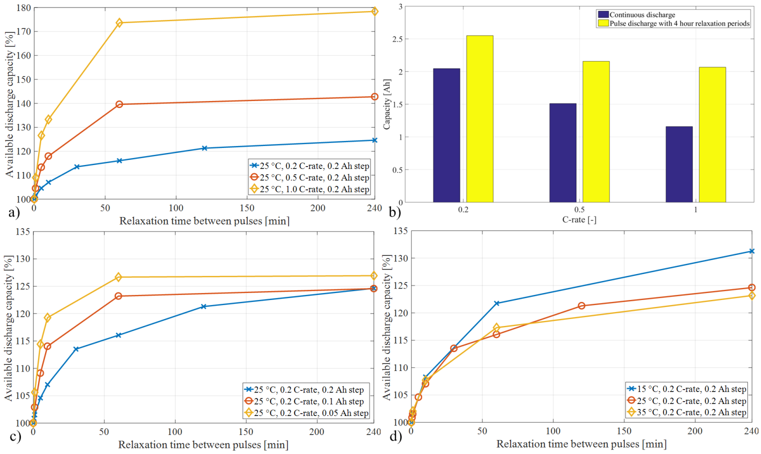

Fig. 3.12: Measured available discharge capacity during the pulse discharge experiments for a)various C-rates, c) various discharge step lengths, d) various temperatures. Comparison between continous discharge and pulse discharge at 25 °C, 0.2 C-rate and 0.2 Ah step with 4 hour relaxation periods is shown in b). Republished with permission of Electrochemical Society, from [A8], 2017; permission conveyed through Copyright Clearance Center, Inc.

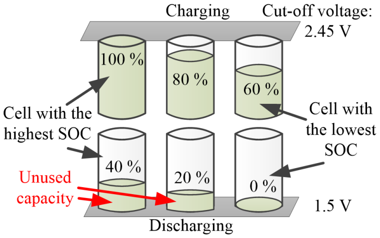

Fig. 3.13: Illustration of the cells with an unbalanced state-of-charge and consequently resulting an unused capacity. Voltage levels are typical for cycling of Li-S cells. Reprinted from [A9], 2017.

Balancing methods are typically divided into two groups: passive and active, according to how they treat the stored energy. The excess energy is dissipated at the passive methods, while it is re-routed and transferred at the active methods. The most common passive method is the energy dissipation on a shunt resistor, which is easy to implement and represents a low cost solution; however, this approach is not energy efficient and it might require relatively long time to balance the cells. The active methods are based mainly on interconnection of the cells by power electronic devices, which transfer the energy between the cells or control the flow of current. These methods are expected to have higher efficiency than the passive ones. Moreover, the balancing is much faster. The drawback is the higher cost, higher complexity and potentially lesser reliability [81–85].

Li-S batteries, due to their unique characteristics, allow a different passive balancing method. This is an 'electrochemistry based' balancing of the cells through the dissipation of the energy by the inherent self-discharge. This so-called self-balancing of the Li-S batteries have been introduced in [A9].

Firstly, the method was theoretically proposed and modelled based on previous work: the discharge model [A3] and the self discharge model [A7]. The proposed model is used for the prediction of the self-balancing and investigation of its sensitivity for various conditions. Afterwards, the proposed model was validated by experimental measurements.

A single Li-S cell was modelled, as it is illustrated in Fig. 3.14, by the integration of three parts: the discharging model, presented in [A3] to reproduce the discharging behavior; the look-up tables, obtained from the laboratory measurements to reproduce the charging behavior; and the self-discharge model, introduced in [A7].

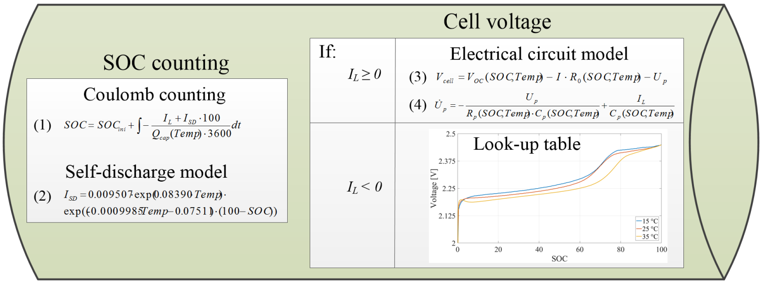

Fig. 3.14: Model of the Li-S cell, capable to reproduce charging and discharging voltage, and the self-discharge behavior. Reprinted from [A9], 2017.

To evaluate the self-balancing capability, three series-connected cells were considered for simulation and experimental studies. The cells were initially unbalanced by setting their SOC to 0, 10 and 20 % for the cell S1, S2 and S3, respectively. The cells were cycled five times (charging - discharging) according to actually set limits. The discharging cut-off limit was always 1.5 V.

Three metrics were introduced in order to quantify and evaluate the balancing capability:

1. **Maximum difference in SOC** ($max\ \Delta SOC$) The difference between the highest charged cell and the lowest charged cell is expressed by the $max\ \Delta SOC$. At the beginning of the cells' cycling, the initialization of the cells results into $max\ \Delta SOC =$ 20 %. The ideally balanced cells with respect to the SOC would have $max\ \Delta SOC =$ 0 %.

2. **Throughput discharge capacity** (TDC) The TDC stands for the capacity, which was obtained from discharging the cells connected in series.

Because of the series connection, the TDC can be limited by differences in cells' SOC, as it is illustrated in Fig. 3.13. It is expected that balancing the cells will lead into higher TDC as the cells will get more equalized.

3. **Dissimilarity of the discharging curves** (DDC) It is assumed that the ideal balanced cells should exhibit an uniform behavior, which results into similar characteristics (voltage value) and uniform exposure to various mechanisms. The DDC expresses the non-uniformity in the cells' discharging voltage profiles and it is obtained as follows:

$$V_{mean}(t) = \frac{V_{S1} + V_{S2} + \cdots + V_{Sn}}{n} \tag{3.3}$$

$$DDC = \frac{\sum_{i=1}^{n} |V_{mean}(t) - V_{Si}(t)|}{n} \tag{3.4}$$

where $V_{mean}(t)$ is the average voltage curve for the cells 1 to n and V_{Si} stands for an i-th cell voltage curve.

The simulation studies were performed for various charging voltage cut-off limits, for various relaxation periods at the charged state and for various temperature levels. The results are summarized in Fig. 3.15. The cells are getting faster balanced in term of cycles by charging them to the higher voltage limits, letting them idling for longer time at the high SOC and by exposing them to higher temperatures.

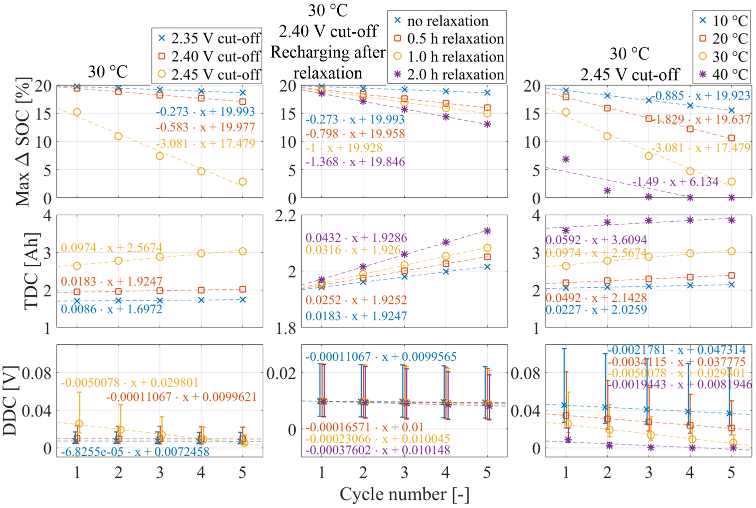

Fig. 3.15: Simulation results for five cycles of three identical Li-S cells connected in series. x stands for number of cycles. Reprinted from [A9], 2017.

The comparison of experimental and simulation results is presented in Fig. 3.16. The *max* ΔSOC in the comparison is not matching due to the fact that the proposed model is not capable to reproduce the capacity recovery effect, which is present at the real cells. However, it still remains valid for for predictive purposes of the model. The TDC obtained during simulations and experiments is in close agreement with each other. Moreover, the DDC shows very close match for charging to 2.45 V. For the charging limit of 2.40 V, the DDC has a similar trend; however, the slope of the curve is by one or nearly two orders different, which is probably the result of the fact that real cells were not completely identical, as it is the case of the simulations.

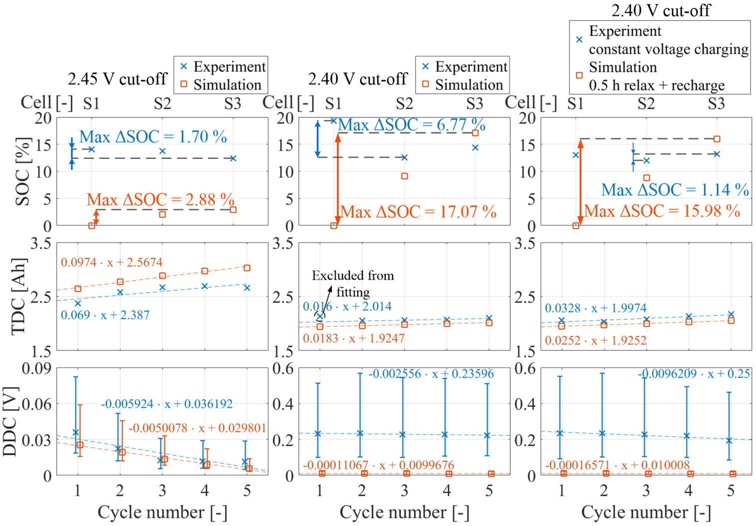

Fig. 3.16: Comparison of experimental and simulation results for five cycles of three Li-S cells connected in series. x stands for number of cycles. Reprinted from [A9], 2017.

The self-balancing feature of the Li-S batteries was introduced and experimentally verified. It opens new possibilities how to enhanced Li-S cell balancing during their operation by adjusting conditions as charging limits, idling periods and temperature. Moreover, the proposed model can be used for the prediction of the self-balancing.

3.4 Thermal properties

Another important aspect of the batteries is their thermal properties, because they have influence on their safety, operation and an impact also to the electrical or lifetime properties. Only a limited amount of studies was found dealing specifically with the thermal behavior of Li-S batteries. A Li-S coin cell was studied by isothermal micro-calorimetry in Ref. [86, 87]. Moreover, Adair et al. [88] developed a 2D transient method for Li-S thermal characteristics simulations. Therefore, the goal was to investigate the temperature behavior and to identify the internal resistance and entropic heat coefficient, which will be in future work used for the thermal modelling. The work in detail is presented in [A10].

The identified internal resistance obtained from applying current pulses at the specific SOC levels is shown in Fig. 3.17 and it is in agreement with the previously obtained results by another approaches. The internal resistance is related to the Joule heating, thus it is partially responsible for the battery heat generation.

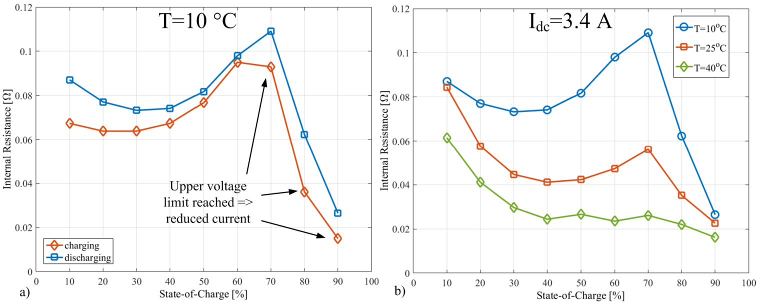

Fig. 3.17: Variation of the internal resistance with the SOC and temperature. b) republished with permission of Electrochemical Society, from [A10], 2017; permission conveyed through Copyright Clearance Center, Inc.

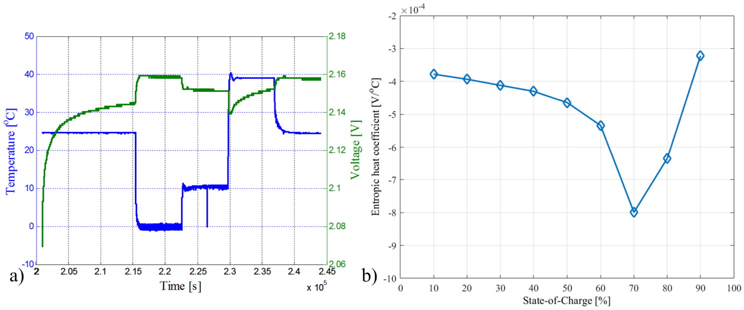

Fig. 3.18: a) Voltage behavior during the thermal cycle at 50 % SOC. b) The variation of the EHC as function of SOC. Republished with permission of Electrochemical Society, from [A10], 2017; permission conveyed through Copyright Clearance Center, Inc.

The entropic heat coefficient (EHC), sometimes referred as temperature coefficient, stands for potential derivative with respect to the temperature. It was determined from the open circuit potentiometry measurements, in which the cells is brought to a specific SOC level and while it is idling, the environment temperature is changed by steps, as illustrated in Fig. 3.18 a). The EHC is used to determine the reversible entropic heat, which participates at the battery heat generation, the found values for the EHC are presented in Fig. 3.18 b). Because the EHC has negative value, independently on the SOC, it is considered that the discharging reaction is exothermic (releasing heat) and charging process is endothermic (absorbing heat).

3.5 Degradation

One of the drawback of the Li-S batteries remains to be their relatively short lifetime. Yan et al. [89] attributes the capacity loss mainly to the three following processes:

- consumption of sulfur into the liquid electrolyte
- passivating electrodes surfaces by precipitation of non-conductive Li_2S_2 and Li_2S
- incomplete conversions (during discharging: Li_2S_2 to Li_2S, during charging: long-chain polysufide species to elemental sulfur)

Moreover, the formation of the passivation films leads also to the increase of the internal resistance [89].

For the product design, it is beneficial to know and understand how the important battery parameters change during the ageing at the different conditions. Therefore, a commonly used approach is to expose the cell to the controlled ageing conditions and to periodically perform a reference performance test (RPT), to retrieve the actual battery parameters. This approach is widely used for Li-ion batteries and it is addressed in the literature [90–92] and also in standards like ISO 12405-1/2 [93,94] and IEC 62660-1/2 [95,96]. It is useful to have similar guidelines for the Li-S batteries. However, due to their specific characteristics and behavior, it is not possible to apply to them identical procedures, which are used for the Li-ion batteries. Thus, such guidelines were developed based on the theoretical knowledge and experimental experience with the Li-S batteries and they were presented in [A11].

Pre-conditioning cycles: The actual performance of the Li-S batteries depends, beside other factors, on their 'cumulative history' [17, 97] which is believed to be related mainly to the precipitation of lithium sulfide. Therefore, it is necessary to perform pre-conditioning cycles before the targeted measurement, in order to 're-set' this history. To illustrate the history effect, the cell was cycled and each of the consecutive discharge was performed with a higher current rate. The resulting discharging voltage profiles are shown in Fig. 3.19 a), where it is illustrated that the profiles do not follow a coherent, expected trend. However, if between each of the previously performed cycle is interleaved a nominal cycle, which causes re-setting the history, the resulting discharging voltage curves have a consistent trend, as presented in Fig. 3.19 b).

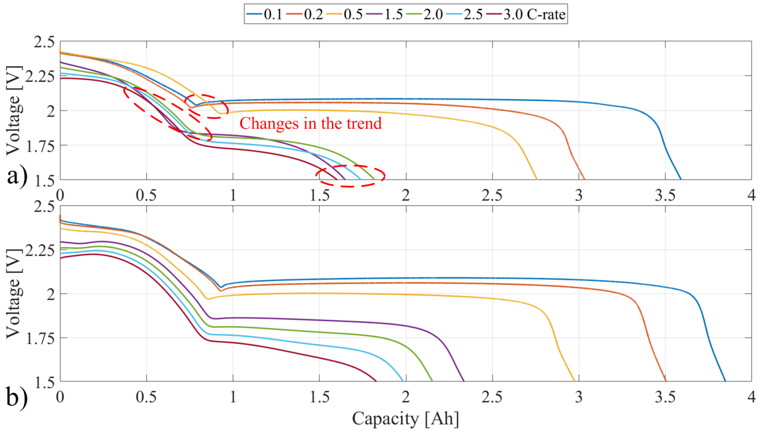

Fig. 3.19: Voltage discharge curves for different C-rates: a) without the pre-conditioning cycle, b) with the pre-conditioning cycle before every charge (0.1 C-rate) and discharge (various C-rates). Republished with permission of Electrochemical Society, from [A11], 2017; permission conveyed through Copyright Clearance Center, Inc.

In order to find out how many pre-conditioning cycles are necessary, the Li-S cell was cycled ten times at three different conditions: 1) 0.1 C-rate charging, 0.2 C-rate discharging, 50 °C; 2) 0.1 C-rate charging, 0.2 C-rate discharging, 10 °C; 3) 0.1 C-rate charging, 2.0 C-rate discharging, 30 °C. After ten cycles at the specific condition, ten nominal cycles were performed on the cell (0.1 C-rate charging, 0.2 C-rate discharging, 30 °C) and the change of the discharging capacity was observed. The capacity evolution during the nominal cycles is presented in Fig. 3.20 and it is shown that only one pre-conditioning cycle is necessary to re-set the history and bring the cell to a stable performance. It is expected that the number of pre-conditioning cycles will vary for cells of different composition or size.

Self-discharge corrections: As it was shown in [A5], [A6] and [A7], the cell suffers of rapid self-discharge at the high SOC levels. Therefore, when the resistance and power measurements are performed, which consists of discharging to a target SOC level, relaxation, applying current pulses, interleaved with another relaxation periods, the cell's SOC is drifting at the high SOC levels. This SOC drift results into assigning the obtained parameters to wrong SOC values in a range of percents. Thus, it is necessary to compensate for this significant self-discharge. This can be approached following two ways. The first way is to reduce the discharging step between the SOC levels, because an additional discharge of the cell is happening continuously

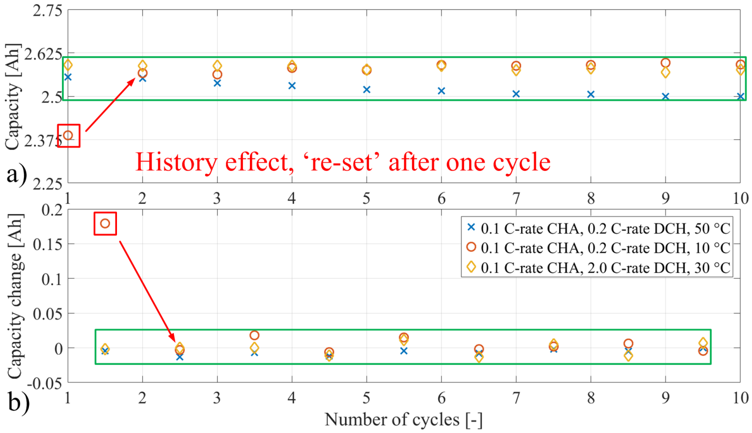

Fig. 3.20: Evaluation of the nominal cycles at 30 °C, after cycling at different conditions; a) capacity obtained from each cycle, b) change in the capacity between the cycles. Republished with permission of Electrochemical Society, from [A11], 2017; permission conveyed through Copyright Clearance Center, Inc.

anyway. The second way is to reduce the relaxation periods before and between the current pulses, because the cell does not need too long time to recover after the previously applied charge/discharge and keeping long breaks would further self-discharge the cell. For the prediction of the occurring self-discharge it is possible to use the proposed self-discharge model [A7].

Shuttle current measurement: In the ”world of the Li-ion batteries” there is no analogy to the polysulfide shuttle and its effects in such degree. For the Li-S batteries, it is a very important parameter, which implies the self-discharge rate [A7] and possibly indicates also the degradation rate [13]. Therefore, it should be included into the RPT. The methodology for the direct shuttle current measurement was proposed in [13].

The proposed RPT for the Li-S batteries takes into consideration the necessary amount of the pre-conditioning cycles, the self-discharge occurring at the high SOC levels and the ”new” battery parameter to measure. The procedure is illustrated in Fig. 3.21. Generally, for the Li-S batteries is necessary also to consider the time demand of the tests, because the Li-S batteries are so far only energy oriented cells and they do not allow high currents. Thus, only small currents can be applied, which leads to high time demand, i.e. the nominal cycle (0.1 C-rate CHA, 0.2 C-rate DCH) takes around 15 hours. Moreover, due to the short cycle life, the number of cycles performed during the RPT should be also minimized.

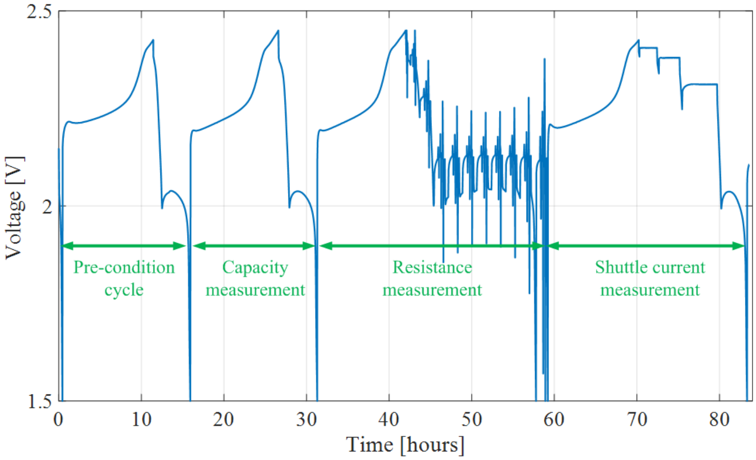

Fig. 3.21: Illustration of the proposed RPT procedure for the Li-S batteries. Republished with permission of Electrochemical Society, from [A11], 2017; permission conveyed through Copyright Clearance Center, Inc.

Chapter 4

State estimation of Li-S batteries

State estimation is an important functionality of the battery management system (BMS). It informs the user about the current state of the battery, which allows for efficient planning, i.e. charging or replacement of the batteries. It helps to avoid undesirable states of overcharge or undercharge. Moreover, it allows for smooth and safe operation [37].

Various methods for SOC estimation were investigated and developed: ampere-hour counting, open-circuit voltage based, impedance based, static battery characteristic based, fuzzy logic and machine learning based estimations [37]. The SOH estimation methods typically relies on different estimations of capacity, impedance, or correlating of these quantities to some other observable effects [37]. These methods were applied and used on commercially matured battery chemistries as are: Lead-acid [98–100], Nickel-metal Hydride (NiMH) [47,101,102] and Li-ion [100,103,104] batteries.

4.1 SOC estimation

Before the start of work at this dissertation, there have not been proposed or demonstrated any *in-situ* state estimation methods for Li-S batteries. Due to the specifics of the Li-S batteries, it is not suitable to use all the estimation techniques, which were applied to Li-ion batteries. Generally, the Li-S battery challenges were mentioned in Chapter 1.2. One group of promising state estimation approaches for the Li-S batteries is recursive Bayesian filters. Three recursive Bayesian filters: the extended Kalman filter (EKF), the unscented Kalman filter (UKF), and the particle filter (PF), were applied and investigated for the SOC estimation of Li-S batteries in [A12]. The electrical circuit model presented in Chapter 2.1, introduced in [A3], was used as the model for the estimation. The voltage over the RC elements V_1 and the SOC χ were considered as the dynamic states and they were corrected according to the measured and simulated voltage response of the cell. All three filters proven their capability to estimate the SOC for the mixed pulse discharge profile (the profile illustrated in Fig. 4.4) and the driving profile NEDC (the profile illustrated in Fig. 4.5), as it is presented in Fig. 4.1. The RMSE, computed according (2.19), is summarized for the SOC estimation in Table 4.1. The UKF was the fastest to convergence to the reference state, represented by retrospectively derived Coulomb counting, when the initial conditions were not matching the state of the cell. When the EKF and the PF were initialized at the low voltage plateau and the cell's state was at the high voltage plateau, they were not able to converge during the one full discharge. However, this can be avoided by pre-initialization of the initial state according to the OCV. Comparison of the filters according their computational requirements were done by looking at their simulation time for one mixed pulse discharge test, which lasted for 128000 seconds. The EKF resulted in the fastest simulation time of 5.25 seconds, followed by the second UKF with 7.97 seconds. The longest simulation time of 21.54 seconds took the PF.

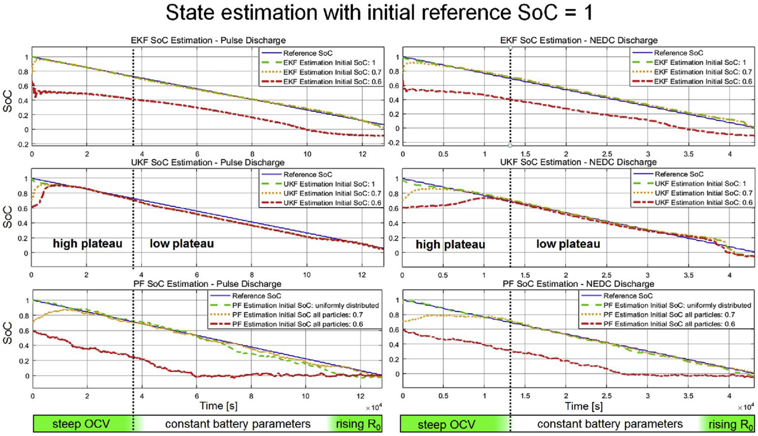

Fig. 4.1: Estimation results for EKF, UKF, PF with a mixed pulse- and a NEDC drive cycle current profile, starting with a fully charged battery, i.e. SOC = 1. Reprinted from [A12] with permission from Elsevier 2017.

Even though, the proposed filter solutions, presented in [A12], was proofed to be useful, they have some limitations, which have negative effect on the estimation accuracy. It appears especially when different current rates are applied to the cell and they cause variations in obtainable capacity at the low voltage plateau. At this region, the OCV is constant and together with the non-modelled behavior it makes the estimation less accurate. As the next

Table 4.1: RSME of SOC Estimation with EKF, UKF and PF [A12].

	Estimator	Fully charged battery		Partially charged battery (0.6 SOC)	
Algorithm	SOC$_{ini}$	Pulse RSME	NEDC RSME	Pulse RSME	NEDC RSME
EKF	1	0.0114	0.0217	0.1593	0.1696
	0.7	0.0160	0.0267	0.0860	0.0535
	0.6	0.2986	0.2732	0.1203	0.0745
UKF	1	0.0347	0.0280	0.0887	0.1743
	0.7	0.0444	0.0537	0.0240	0.0687
	0.6	0.0705	0.1199	0.0189	0.0332
PF	1	0.0576	0.0195	0.0281	0.0561
	0.7	0.0532	0.0694	0.1661	0.1176
	0.6	0.3997	0.3354	0.0383	0.0320

step to tackle with this issue, an online parameter identification technique is introduced in [A13], which estimated the battery model parameters online in agreement to the parameters obtained offline in [A3]. Consequently, the estimated parameters V_{OC} and R_0 are used for the SOC estimation, in this dual EKF setting. The previous estimation approach and the new one are illustrated in Fig. 4.2. Moreover, the online parameter estimation provides further insight into the Li-S cell operation. The use of this method also resulted in identifying ”the dynamic resistance” parameter, which was used to extend the battery model and to improve the accuracy of predicted battery voltage response at low SOC under dynamic load. The RSME for the SOC estimation, computed according to (2.19), is shown in Table 4.2 for the dual EKF approach. The comparison was done for the SOC estimation based on voltage response and for the SOC estimation based on battery parameters [A13] over several cycles including charging, and it is illustrated in Fig. 4.3. Consequently, it was concluded that the method based on the battery parameters is more accurate and robust, especially when it is applied over continuous discharging and charging profiles.

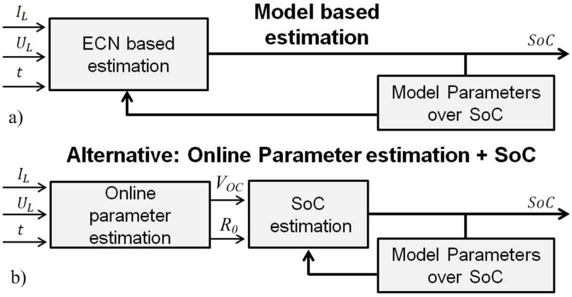

Fig. 4.2: Proposed SOC estimation methods for the Li-S batteries: a) based on voltage response, b) based on identified battery parameters (dual EKF). Reprinted from [A13], 2017.

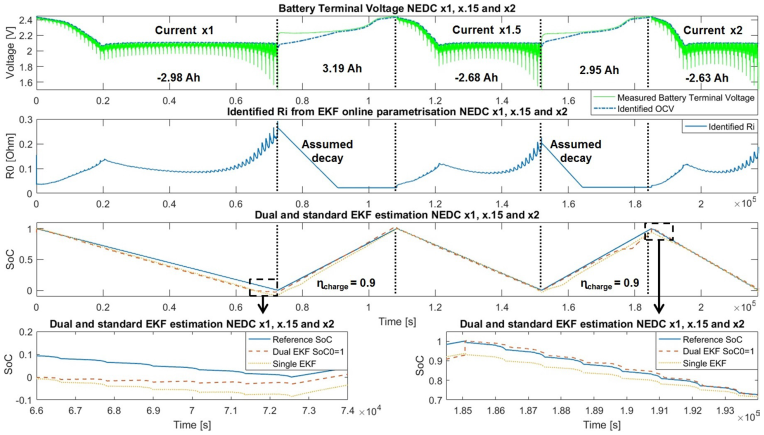

Fig. 4.3: Results of the SOC estimation with three NEDC current profiles with constant charge and comparison of two EKF based estimation methods. Reprinted from [A13], 2017.

Table 4.2: RSME of dual EKF SOC Estimation [A13].

	Estimator	Fully charged battery		Partially charged battery (0.6 SOC)	
Algorithm	SOC_{ini}	UDDS RSME	NEDC RSME	UDDS RSME	NEDC RSME
dual EKF	1	0.0346	0.0257	0.01061	0.01030
	0.7	0.0346	0.0257	-	-
	0.6	0.0455	0.0350	-	-

4.2 SOH estimation

Besides the SOC estimation, the SOH and maximum available power estimation for the Li-S batteries have been also in focus and the work is presented in [A14]. The approach is based on the previously presented online parameter identification. The parameters V_{OC} and R_0 are used to estimated not only the SOC χ, but also the SOH in terms of capacity fade (η_Q) and internal resistance change (η_R). The estimation is again based on the model and its parameters presented in [A3]. The battery model itself does not include any change of the parameters according the ageing and it does not have any prior information about it. The SOH estimation is based on the assumptions that the parameters V_{OC} and R_0 do not change with the change of the capacity fade and V_{OC} is also non-dependent on the resistance change. The states are defined as:

$$\eta_{\mathrm{Q}} = \frac{Q_{\mathrm{cap}}}{\bar{Q}_{\mathrm{cap}}} \tag{4.1}$$

$$\eta_{\mathrm{R}} = \frac{\bar{R}_0}{R_0} \tag{4.2}$$

where (η_{Q}) is the capacity fade, Q_{cap} is the maximum extractable charge from the fully charged battery at the actual age, $\bar{Q}_{\mathrm{cap}}$ is the maximum extractable charge from the fully charged battery at the beginning of life. The internal resistance change is labeled as η_{R}, the initial internal resistance is $\bar{R}_0$ and the actual internal resistance is R_0.

There is not used any process model for η_Q and η_R. Their change is assumed to be very slow in comparison to χ and they are assumed to be observed from the increasing error mean value. When the proposed SOH estimation method was applied to the mixed pulse discharge profile of the aged cell, presented in Fig. 4.4, it shown very promising results in capability of tracking all the states.

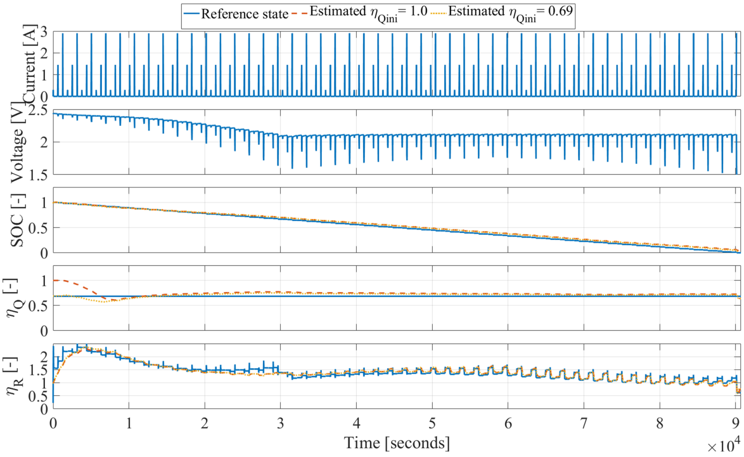

Fig. 4.4: The mixed pulse discharge test profile and the estimated results for the aged cell. The estimates converge for all states. The accuracy is higher with the initial estimate closer to the reference state. Reprinted from [A14], 2017.

To validate the estimation approach under the more realistic conditions, the driving cycles NEDC and UDDS were applied to the cell. They were scaled to a lower and to a higher current versions, with maximal current of 1.2 A and 2.9 A. The absolute maximum error was computed as follow:

$$x_{MaxErr} = \max(\left| x_{Ref} - x_{Est} \right|) \tag{4.3}$$

and the absolute mean error:

$$x_{AvgErr} = \frac{1}{n} \sum_{t=1}^{n} (\left| x_{Ref} - x_{Est} \right|) \tag{4.4}$$

where x stands for the specific state or quantity.

The estimation errors are summarized in Table 4.3. Furthermore, the results presented in Fig. 4.5 show that the η_R was accurately track for all four cases. However, the different profile dynamics result into different available capacity, which makes more difficult to estimate adequately η_Q. Moreover, η_Q is related to the SOC estimation. Thus, the less accurately is η_Q estimated, then also it leads to less accurate SOC estimation. Therefore, in order to improve the SOH estimation, the model dealing with the variable capacity under different conditions and dynamics has to be implemented. Anyway, as the first work about SOH estimation on the Li-S batteries, the proposed estimation method is a good starting point, which can still provide important information to the user.

Table 4.3: The errors of the state estimation (SOC and SOH) for the fresh cell and the aged cell [A14].

Initial conditions	Average Errors	Maximum Errors
Fresh cell, mixed pulse discharge		
$[\chi = 1\ \eta_{\mathrm{Q}} = 1\ \eta_{\mathrm{R}} = 1]$	[0.0080 0.0125 0.0140]	[0.0306 0.0559 0.2606]
$[\chi = 0.7\ \eta_{\mathrm{Q}} = 0.7\ \eta_{\mathrm{R}} = 0.7]$	[0.0112 0.0370 0.0174]	[0.1264 0.3000 0.1301]
$[\chi = 0.6\ \eta_{\mathrm{Q}} = 1\ \eta_{\mathrm{R}} = 1]$	[0.3963 0.3796 0.2440]	[0.7688 1.3897 1.2931]
Aged cell, mixed pulse discharge		
$[\chi = 1\ \eta_{\mathrm{Q}} = 1\ \eta_{\mathrm{R}} = 1]$	[0.0303 0.0633 0.0777]	[0.0550 0.3162 1.4156]
$[\chi = 1\ \eta_{\mathrm{Q}} = 0.69\ \eta_{\mathrm{R}} = 1]$	[0.0274 0.0406 0.0756]	[0.0461 0.1150 1.4155]
Aged cell, $[\chi = 1\ \eta_{\mathrm{Q}} = 1\ \eta_{\mathrm{R}} = 1]$		
NEDC12	[0.0576 0.0974 0.0828]	[0.1123 0.1565 0.5136]
NEDC29	[0.0827 0.1575 0.1796]	[0.1552 0.2412 0.6127]
UDDS12	[0.0797 0.1900 0.1163]	[0.1592 0.3258 0.6686]
UDDS29	[0.0461 0.0696 0.1301]	[0.0890 0.1632 0.6686]

4.3 Maximum available power estimation

A dynamic battery model approach was selected for the maximum available power estimation. The online identified parameters were used in terms of the behavioral model and with respect to the current and voltage limits. The maximum available power was obtained for a specific time period. This selected approach represents a computationally simple, but effective solution. The method was validated on the adjusted mixed pulse discharge profile, into which were periodically interleaved discharging pulses of 6.8 A and charging pulses 1.7 A. The validation case for the prediction of one second ahead is shown in Fig. 4.6. The errors for 1 and 10 seconds period prediction are summarized in Table 4.4, they were computed according (4.3) and (4.4).

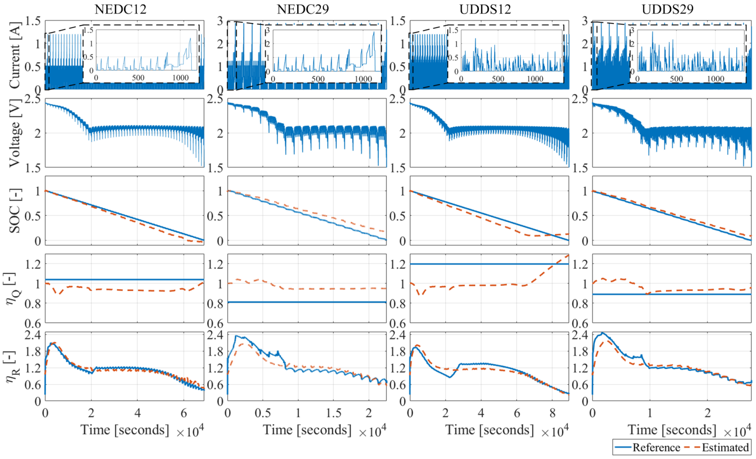

Fig. 4.5: The driving cycle mission profiles and the estimated results for the aged cell. The χ roughly follows the reference. The accuracy of the χ is dependent on the estimated η_Q, which varies with the total discharged capacity of the cell under different mission profiles, due to their different current rates and dynamics. The η_R is in general followed well and similar between the different driving cycles. Reprinted from [A14], 2017.

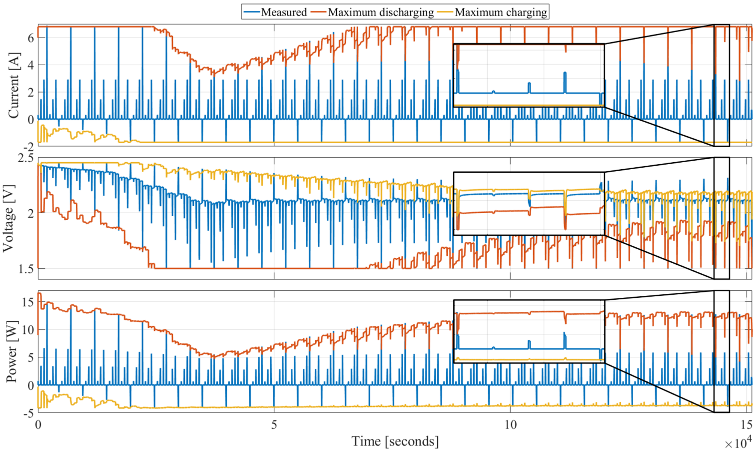

Fig. 4.6: The mixed pulse profile for maximum available power estimation and the instantaneous maximum available power at 1 second. Reprinted from [A14], 2017.

4.4 Incremental capacity analysis for SOH estimation

Next to the Kalman filter based methods, the incremental capacity analysis (ICA) was considered to use for diagnostics and further on possibly for the

SOH estimation of the Li-S batteries. ICA provides an insight into the electrochemical properties of the cell, under the constant current charging or discharging conditions [105]. The obtained cell's voltage response is translated to the dQ/dV curves, which forms peaks, typically associated with the intercalations and the phase transformations. Various Li-ion chemistries were investigated using the ICA technique under different temperature, current and ageing conditions [106–110]. Furthermore, the ICA was applied in order to estimate the SOH of the Li-ion cells [111, 112].

However, is it feasible to apply the ICA to Li-S batteries? They differ from Li-ion batteries in the charging and discharging process. Moreover, they do not often have a monotonous voltage curve as it is the case of the Li-ion batteries. These questions were targeted in [A15]. Typically, when the charging curve is monotonous, it results into two dQ/dV peaks, which were assigned to the formation of long chain and short chain lithium polysulfide species. However, when the voltage curve is not monotonous, the dQ/dV curve forms different structures, which are more difficult to analyze. Thus, it might be better to plot the curves in the inverse manner as dV/dQ, which allows for more intuitive graphical investigation. An example of the IC curves plotted as dQ/dV and dV/dQ, for charging at three different temperature levels, is shown in Fig. 4.7.

In order to see, how the ageing is reflected in the ICA, the Li-S cell was cycled at 30 °C by 0.1 C-rate charging until 2.45 V or 11 hours and by 0.2 C-rate discharging until 1.5 V. Every 20 cycles, the RPT [A11] was performed and the ICA was applied to the second charging cycle (i.e. after pre-conditioning cycle). The obtained results are presented in Fig. 4.8 and they indicate that the cell degradation is visible from the change of the ICA curves. Therefore, the method might be feasible for the SOH estimation. However, it should be considered that the method was applied under the specific and controlled conditions. Moreover, the investigated cell was exposed to only one consistent ageing setting.

Table 4.4: The errors of maximum available power estimation. Reprinted from [A14], 2017.

T	Quantity	Average Errors	Maximum Errors
1 s	$[V_{min}\ V_{max}]$ [V]	[0.0080 0.0460]	[0.1840 0.1556]
	$[I_{P_{dis.max}}\ I_{P_{ch.max}}]$ [A]	[0.3022 0.0249]	[1.7750 0.7759]
	$[P_{dis.max}\ P_{ch.max}]$ [W]	[0.5049 0.1381]	[3.0365 1.9128]
10 s	$[V_{min}\ V_{max}]$ [V]	[0.0110 0.0525]	[0.2148 0.1548]
	$[I_{P_{dis.max}}\ I_{P_{ch.max}}]$ [A]	[0.6119 0.0284]	[3.6860 0.3566]
	$[P_{dis.max}\ P_{ch.max}]$ [W]	[0.9924 0.1586]	[6.1106 0.8736]

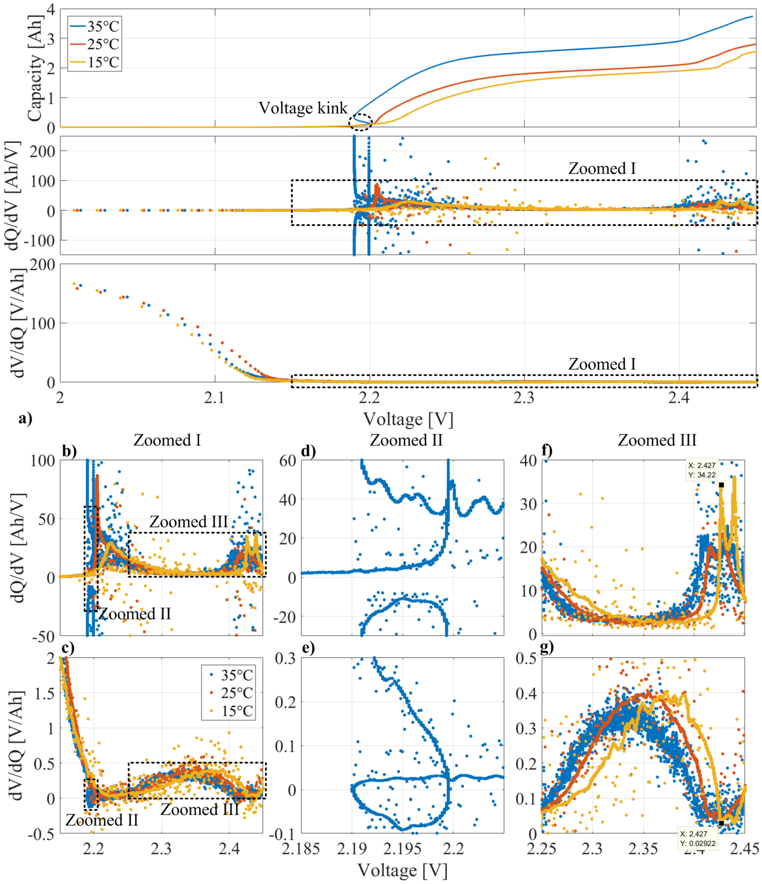

Fig. 4.7: a) The charging curves for 0.1 C-rate at various temperature levels. dQ/dV curves for zoom areas b) I, d) II and f) III. dV/dQ curves for zoom areas c) I, e) II and g) III. Republished with permission of Electrochemical Society, from [A15], 2017; permission conveyed through Copyright Clearance Center, Inc.

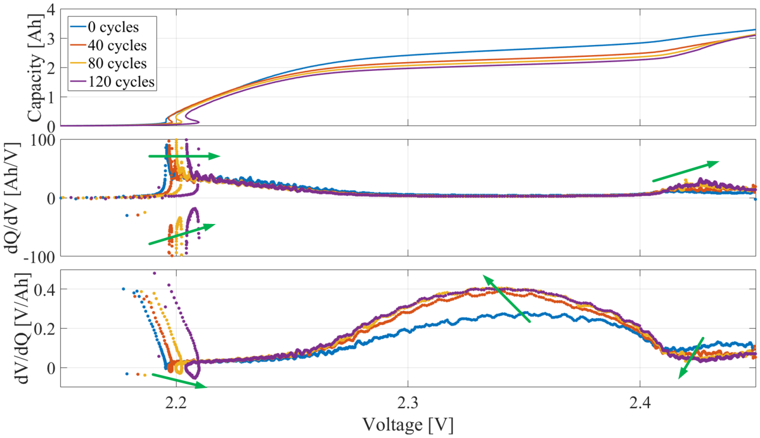

Fig. 4.8: The voltage charging and ICA curves for the cycled Li-S cell. Republished with permission of Electrochemical Society, from [A15], 2017; permission conveyed through Copyright Clearance Center, Inc.

Chapter 5

Conclusion

The topics of characterization, modelling and state estimation of Li-S batteries have been covered in this dissertation. The work was carried on the pre-commercial version of the Li-S pouch cell, with an intention to provide knowledge and tools, which will enhance its further commercialization.

The starting point for transition to full commercialization of the Li-S batteries has been set by:

- identifying battery attributes and behavior under wide operational conditions
- by providing the models, which can be further used by engineers for the battery application design
- providing basic BMS functionalities as is SOC, SOH or maximum available power estimation

In order to have a model for the state estimation and to develop a tool for developing the applications with respect to the specific Li-S battery characteristics, a discharge equivalent electrical circuit model was developed. The model is able to simulate the voltage response of the Li-S battery during both the discharge and the relaxation phases.

The equivalent electrical circuit can be also used for analysis of EIS data, which was actually done for various temperatures and SOC levels, to get a deeper insight of the Li-S battery mechanisms and their sensitivity to those conditions.

Generally, the experimental testing was widely used to characterize the cell. The short-term self-discharge was thoroughly investigated and it was identified its increase and dependence on the SOC (only at the high voltage plateau), temperature and the idling time. The collected data was further used to develop a self-discharge model, which further led to the discovery of the Li-S battery self-balancing feature. Moreover, by the experimental testing the significance of the Li-S battery charge recovery was identified and it is needed to take it in account in almost every battery operation, because it has an impact on the actual SOC. Furthermore, the basic thermal behavior was analyzed to provide the base for a thermal model.

The intrinsic characteristics of the Li-S batteries also require a specific testing approach, because just blindly transfer the methodologies from the world of Li-ion batteries is not feasible. Therefore, a testing methodology was proposed to reflect the differences in the Li-S batteries and to guide the researchers and the engineers in testing, especially in evaluation of the performance parameters change during the ageing.

In a similar manner, the state estimation has represented a challenge, because some of simple established methods are not feasible for Li-S batteries due to their specific characteristics. Thus, the recursive Bayesian filters were successfully implemented for the SOC estimation. The SOC estimation was further improved by a dual extended Kalman filter approach, when at first the battery model parameters V_{OC} and R_0 are identified online and afterward, the SOC is estimated based upon them. The same approach was used also for the SOH estimation, where besides the SOC, the SOH in terms of the capacity fade η_Q and change of the internal resistance η_R were estimated. All the identified battery parameters have been used in the case of the estimation of the maximum available power to obtain its value through the behavioral Li-S battery model. The performance and robustness of the proposed estimation techniques were validated experimentally by applying realistic driving profiles.

5.1 Main contributions

- a new equivalent electrical circuit discharge model for Li-S batteries was developed
- characteristics of the Li-S pouch cell was determined for a wide range of SOC, current and temperature conditions
- a short-term self-discharge of the Li-S battery was characterized in detail and its new, simple and effective model was developed
- capacity charge recovery of the Li-S battery was identified for various conditions
- self-balancing feature of the Li-S batteries was discovered and the model for its prediction was developed
- thermal properties of the Li-S battery in terms of the internal resistance and the entropic heat coefficient were determined

- novel methodology for assessing the degradation of the Li-S batteries for practical applications was proposed
- original methods for SOC, SOH and maximum available power estimation of the Li-S batteries were developed

5.2 Future work

Because the dissertation forms rather a starting line for the practical use of the Li-S batteries, there is a space for improvement almost in every direction. There is certainly a need for improved model of the Li-S battery, which will include the specific mechanisms and behavior, especially related to the cumulative history, reversible and irreversible degradation, and variability of the available capacity in general. While so far only discharging operation was addressed, the charging has to be considered as well. Moreover, due to the state estimation and possibility of the model to be implemented on-board, it still has to remain low computational requirements. Furthermore, the improved model will positively influence the accuracy of the state estimation and sizing of the battery systems.

Developing of the thermal model is also the next logical step, which will be reflected in the BMS, battery pack design and thermal management. Beside it, the degradation model sensitive to different ageing conditions will be valuable for the lifetime optimization and the battery application design.

Another topic is the testing methodology of the Li-S batteries. A preliminary guidelines for the Li-S performance testing were provided. However, there is a space for optimization and generalization. The goals should be a time effective testing procedure, which is easy to follow and cover all the necessary aspects of the Li-S batteries.

An effort should be also dedicated to further investigation of the charging process and optimization of the charging strategies, to reduce the necessary charging time, which is currently limiting the practical use of Li-S batteries, while the lifetime would remain the same or rather pro-longed.

References

[1] D. Deng, “Li-ion batteries: basics, progress, and challenges,” *Energy Science & Engineering*, vol. 3, no. 5, pp. 385–418, 2015.

[2] G. E. Blomgren, “The Development and Future of Lithium Ion Batteries,” *J. Electrochem. Soc.*, vol. 164, no. 1, pp. A5019–A5025, 2017.

[3] W. Walker, S. Yayathi, J. Shaw, and H. Ardebili, “Thermo-electrochemical evaluation of lithium-ion batteries for space applications,” *Journal of Power Sources*, vol. 298, pp. 217 – 227, 2015.

[4] E. Ovrum and T. Bergh, “Modelling lithium-ion battery hybrid ship crane operation,” *Applied Energy*, vol. 152, pp. 162 – 172, 2015.

[5] A. Poullikkas, “A comparative overview of large-scale battery systems for electricity storage,” *Renewable and Sustainable Energy Reviews*, vol. 27, pp. 778–788, nov 2013.

[6] E. Chemali, M. Preindl, P. Malysz, and A. Emadi, “Electrochemical and Electrostatic Energy Storage and Management Systems for Electric Drive Vehicles: State-of-the-Art Review and Future Trends,” *IEEE Journal of Emerging and Selected Topics in Power Electronics*, vol. 4, no. 3, pp. 1117–1134, sep 2016.

[7] M. Wild, L. O’Neill, T. Zhang, R. Purkayastha, G. Minton, M. Marinescu, and G. J. Offer, “Lithium sulfur batteries, a mechanistic review,” *Energy Environ. Sci.*, vol. 8, no. 12, pp. 3477–3494, 2015.

[8] M. Hagen, D. Hanselmann, K. Ahlbrecht, R. Maça, D. Gerber, and J. Tübke, “Lithium-Sulfur Cells: The Gap between the State-of-the-Art and the Requirements for High Energy Battery Cells,” *Advanced Energy Materials*, vol. 5, no. 16, aug 2015.

[9] I. a. Hunt, Y. Patel, M. Szczygielski, L. Kabacik, and G. J. Offer, “Lithium sulfur battery nail penetration test under load,” *Journal of Energy Storage*, vol. 2, pp. 25–29, 2015.

[10] A. Manthiram, Y. Fu, and Y.-s. Su, "Challenges and Prospects of Lithium-Sulfur Batteries," *Accounts of Chemical Research*, vol. 46, no. 5, pp. 1125–1134, may 2013.

[11] S. S. Zhang, "Liquid electrolyte lithium/sulfur battery: Fundamental chemistry, problems, and solutions," *Journal of Power Sources*, vol. 231, pp. 153–162, jun 2013.

[12] Y. Diao, K. Xie, S. Xiong, and X. Hong, "Shuttle phenomenon - The irreversible oxidation mechanism of sulfur active material in Li-S battery," *Journal of Power Sources*, vol. 235, pp. 181–186, aug 2013.

[13] D. Moy, A. Manivannan, and S. R. Narayanan, "Direct Measurement of Polysulfide Shuttle Current: A Window into Understanding the Performance of Lithium-Sulfur Cells," *Journal of the Electrochemical Society*, vol. 162, no. 1, pp. A1–A7, nov 2014.

[14] R. Xu, J. Lu, and K. Amine, "Progress in Mechanistic Understanding and Characterization Techniques of Li-S Batteries," *Advanced Energy Materials*, vol. 5, no. 16, pp. 1–22, 2015.

[15] R. Xu, I. Belharouak, X. Zhang, R. Chamoun, C. Yu, Y. Ren, A. Nie, R. Shahbazian-Yassar, J. Lu, J. C. Li, and K. Amine, "Insight into Sulfur Reactions in Li-S Batteries," *ACS Applied Materials & Interfaces*, vol. 6, no. 24, pp. 21 938–21 945, dec 2014.

[16] N. A. Cañas, D. N. Fronczek, N. Wagner, A. Latz, and K. A. Friedrich, "Experimental and Theoretical Analysis of Products and Reaction Intermediates of Lithium-Sulfur Batteries," *The Journal of Physical Chemistry C*, vol. 118, no. 23, pp. 12 106–12 114, jun 2014.

[17] M. Marinescu, T. Zhang, and G. J. Offer, "A zero dimensional model of lithium-sulfur batteries during charge and discharge." *Physical chemistry chemical physics : PCCP*, vol. 18, no. 1, pp. 584–93, 2016.

[18] A. F. Hofmann, D. N. Fronczek, and W. G. Bessler, "Mechanistic modeling of polysulfide shuttle and capacity loss in lithium-sulfur batteries," *Journal of Power Sources*, vol. 259, pp. 300–310, aug 2014.

[19] M. Ghaznavi and P. Chen, "Sensitivity analysis of a mathematical model of lithium-sulfur cells part I: Applied discharge current and cathode conductivity," *Journal of Power Sources*, vol. 257, pp. 394–401, jul 2014.

[20] A. Manthiram, S.-H. Chung, and C. Zu, "Lithium-Sulfur Batteries: Progress and Prospects," *Advanced Materials*, vol. 27, no. 12, pp. 1980–2006, mar 2015.

[21] Y. V. Mikhaylik and J. R. Akridge, "Polysulfide Shuttle Study in the Li/S Battery System," *Journal of The Electrochemical Society*, vol. 151, no. 11, p. A1969, 2004.

[22] A. Fotouhi, D. J. Auger, K. Propp, S. Longo, and M. Wild, "A review on electric vehicle battery modelling: From Lithium-ion toward Lithium-Sulphur," *Renewable and Sustainable Energy Reviews*, vol. 56, pp. 1008–1021, 2016.

[23] A. Fotouhi, D. Auger, K. Propp, and S. Longo, "Electric Vehicle Battery Parameter Identification and SOC Observability Analysis: NiMH and Li-S Case Studies," in *8th IET International Conference on Power Electronics, Machines and Drives (PEMD 2016)*, no. April. Institution of Engineering and Technology, 2016, pp. 1–6.

[24] V. Ramadesigan, P. W. C. Northrop, S. De, S. Santhanagopalan, R. D. Braatz, and V. R. Subramanian, "Modeling and Simulation of Lithium-Ion Batteries from a Systems Engineering Perspective," *Journal of the Electrochemical Society*, vol. 159, no. 3, pp. R31–R45, jan 2012.

[25] K. S. Hariharan and V. Senthil Kumar, "A nonlinear equivalent circuit model for lithium ion cells," *Journal of Power Sources*, vol. 222, pp. 210–217, jan 2013.

[26] M. Hannan, F. Azidin, and a. Mohamed, "Hybrid electric vehicles and their challenges: A review," *Renewable and Sustainable Energy Reviews*, vol. 29, pp. 135–150, jan 2014.

[27] J. Van Mierlo, P. Van den Bossche, and G. Maggetto, "Models of energy sources for EV and HEV: Fuel cells, batteries, ultracapacitors, flywheels and engine-generators," *Journal of Power Sources*, vol. 128, no. 1, pp. 76–89, 2004.

[28] A. Seaman, T.-S. Dao, and J. McPhee, "A survey of mathematics-based equivalent-circuit and electrochemical battery models for hybrid and electric vehicle simulation," *Journal of Power Sources*, vol. 256, pp. 410–423, jun 2014.

[29] V. Knap, R. Sinha, M. Swierczynski, D.-I. Stroe, and S. Chaudhary, "Grid inertial response with Lithium-ion battery energy storage systems," in *2014 IEEE 23rd International Symposium on Industrial Electronics (ISIE)*. IEEE, jun 2014, pp. 1817–1822.

[30] P. Mercier, R. Cherkaoui, and A. Oudalov, "Optimizing a battery energy storage system for frequency control application in an isolated power system," *IEEE Transactions on Power Systems*, vol. 24, no. 3, pp. 1469–1477, 2009.

[31] M. Swierczynski, D. I. Stroe, A. I. Stan, R. Teodorescu, and D. U. Sauer, "Selection and performance-degradation modeling of limo2/li 4ti5o12 and lifepo4/c battery cells as suitable energy storage systems for grid integration with wind power plants: An example for the primary frequency regulation service," *IEEE Transactions on Sustainable Energy*, vol. 5, no. 1, pp. 90–101, 2014.

[32] C.-J. Zhan, X. Wu, S. Kromlidis, V. Ramachandaramurthy, M. Barnes, N. Jenkins, and A. Ruddell, "Two electrical models of the lead-acid battery used in a dynamic voltage restorer," *IEE Proceedings - Generation, Transmission and Distribution*, vol. 150, no. 2, p. 175, 2003.

[33] R. Rao, S. Vrudhula, and D. N. Rakhmatov, "Battery modeling for energy aware system design," *Computer*, vol. 36, no. 12, pp. 77–87, Dec 2003.

[34] H. Chan, "A new battery model for use with battery energy storage systems and electric vehicles power systems," in *2000 IEEE Power Engineering Society Winter Meeting. Conference Proceedings (Cat. No.00CH37077)*, vol. 1, no. c. IEEE, 2000, pp. 470–475.

[35] P. Chou, C. P. C. Park, J. P. J. Park, K. P. K. Pham, and J. L. J. Liu, "B#: a battery emulator and power profiling instrument," *Proceedings of the 2003 International Symposium on Low Power Electronics and Design, 2003. ISLPED '03.*, pp. 288–293, 2003.

[36] J. V. Barreras, C. Fleischer, A. E. Christensen, M. Swierczynski, E. Schaltz, S. J. Andreasen, and D. U. Sauer, "An Advanced HIL Simulation Battery Model for Battery Management System Testing," *IEEE Transactions on Industry Applications*, vol. 52, no. 6, pp. 5086–5099, 2016.

[37] W. Waag, C. Fleischer, and D. U. Sauer, "Critical review of the methods for monitoring of lithium-ion batteries in electric and hybrid vehicles," *Journal of Power Sources*, vol. 258, pp. 321–339, jul 2014.

[38] Y. Xing, E. W. M. Ma, K. L. Tsui, and M. Pecht, "Battery Management Systems in Electric and Hybrid Vehicles," *Energies*, vol. 4, no. 12, pp. 1840–1857, oct 2011.

[39] N. a. Cañas, K. Hirose, B. Pascucci, N. Wagner, K. A. Friedrich, and R. Hiesgen, "Investigations of lithium-sulfur batteries using electrochemical impedance spectroscopy," *Electrochimica Acta*, vol. 97, pp. 42–51, may 2013.

[40] M. Einhorn, F. V. Conte, C. Kral, and J. Fleig, "Comparison, selection, and parameterization of electrical battery models for automotive ap-

plications," *IEEE Transactions on Power Electronics*, vol. 28, no. 3, pp. 1429–1437, 2013.

[41] X. Hu, S. Li, and H. Peng, "A comparative study of equivalent circuit models for Li-ion batteries," *Journal of Power Sources*, vol. 198, pp. 359–367, jan 2012.

[42] D. Andre, M. Meiler, K. Steiner, H. Walz, T. Soczka-Guth, and D. U. Sauer, "Characterization of high-power lithium-ion batteries by electrochemical impedance spectroscopy. II: Modelling," *Journal of Power Sources*, vol. 196, no. 12, pp. 5349–5356, 2011.

[43] M. Ceraolo, "New dynamical models of lead-acid batteries," *IEEE Transactions on Power Systems*, vol. 15, no. 4, pp. 1184–1190, 2000.

[44] Z. Shen and C. D. Rahn, "Physics-Based Model of a Valve-Regulated Lead-Acid Battery and an Equivalent Circuit," *Journal of Dynamic Systems, Measurement, and Control*, vol. 135, no. 4, p. 041011, may 2013.

[45] E. Kuhn, C. Forgez, and G. Friedrich, "Modeling diffusive phenomena using non integer derivatives," *The European Physical Journal Applied Physics*, vol. 25, no. 3, pp. 183–190, mar 2004.

[46] Y. Ota and Y. Hashimoto, "Modeling of voltage hysteresis and relaxation of HEV NiMH battery," *Electrical Engineering in Japan (English translation of Denki Gakkai Ronbunshi)*, vol. 175, no. 1, pp. 1–7, 2011.

[47] M. Galeotti, C. Giammanco, L. Cin??, S. Cordiner, and A. Di Carlo, "Synthetic methods for the evaluation of the State of Health (SOH) of nickel-metal hydride (NiMH) batteries," *Energy Conversion and Management*, vol. 92, pp. 1–9, 2015.

[48] M. Chen and G. A. Rincón-Mora, "Accurate electrical battery model capable of predicting runtime and I-V performance," *IEEE Transactions on Energy Conversion*, vol. 21, no. 2, pp. 504–511, 2006.

[49] K. Somasundaram, O. Neill, M. Marinescu, T. Zhang, G. Minton, M. Wild, and G. Offer, "Towards an operational model for a Li-S battery," London, sep 2014.

[50] A. Fotouhi, D. J. Auger, K. Propp, S. Longo, R. Purkayastha, L. O'Neill, and S. Walus, "Lithium-Sulfur Cell Equivalent Circuit Network Model Parameterization and Sensitivity Analysis," *IEEE Transactions on Vehicular Technology (under 1st review)*, 2016.

[51] L. LJUNG, *System identification: theory for the user*. London: Prentice-Hall, 1987.

[52] T. Zhang, M. Marinescu, S. Walus, and G. J. Offer, "Modelling transport-limited discharge capacity of lithium-sulfur cells," *Electrochimica Acta*, vol. 219, pp. 502–508, 2016.

[53] E. Barsoukov and J. R. Macdonald, *Impedance Spectroscopy Theory, Experiment, and Applications*, 2nd ed. John Wiley & Sons, Inc., 2005.

[54] V. Kolosnitsyn, E. Kuzmina, E. Karaseva, and S. Mochalov, "A study of the electrochemical processes in lithium-sulphur cells by impedance spectroscopy," *Journal of Power Sources*, vol. 196, no. 3, pp. 1478–1482, feb 2011.

[55] V. Kolosnitsyn, E. Kuzmina, and S. Mochalov, "Determination of lithium sulphur batteries internal resistance by the pulsed method during galvanostatic cycling," *Journal of Power Sources*, vol. 252, pp. 28–34, apr 2014.

[56] J. Conder, C. Villevieille, S. Trabesinger, P. Novák, L. Gubler, and R. Bouchet, "Electrochemical impedance spectroscopy of a Li-S battery: Part 1. Influence of the electrode and electrolyte compositions on the impedance of symmetric cells," *Electrochimica Acta*, vol. 244, pp. 61–68, 2017.

[57] L. Yuan, X. Qiu, L. Chen, and W. Zhu, "New insight into the discharge process of sulfur cathode by electrochemical impedance spectroscopy," *Journal of Power Sources*, vol. 189, no. 1, pp. 127–132, apr 2009.

[58] Z. Deng, Z. Zhang, Y. Lai, J. Liu, J. Li, and Y. Liu, "Electrochemical Impedance Spectroscopy Study of a Lithium/Sulfur Battery: Modeling and Analysis of Capacity Fading," *Journal of the Electrochemical Society*, vol. 160, no. 4, pp. A553–A558, jan 2013.

[59] W. Ahn, K.-B. Kim, K.-N. Jung, K.-H. Shin, and C.-S. Jin, "Synthesis and electrochemical properties of a sulfur-multi walled carbon nanotubes composite as a cathode material for lithium sulfur batteries," *Journal of Power Sources*, vol. 202, pp. 394–399, mar 2012.

[60] D. Moy and S. R. Narayanan, "Mixed Conduction Membranes Suppress the Polysulfide Shuttle in Lithium-Sulfur Batteries," *Journal of The Electrochemical Society*, vol. 164, no. 4, pp. A560–A566, 2017.

[61] Z. Hao, L. Yuan, Z. Li, J. Liu, J. Xiang, C. Wu, R. Zeng, and Y. Huang, "High performance lithium-sulfur batteries with a facile and effective dual functional separator," *Electrochimica Acta*, vol. 200, pp. 197–203, 2016.

[62] X. B. Cheng, C. Yan, J. Q. Huang, P. Li, L. Zhu, L. Zhao, Y. Zhang, W. Zhu, S. T. Yang, and Q. Zhang, "The gap between long lifespan Li-S coin and pouch cells: The importance of lithium metal anode protection," *Energy Storage Materials*, vol. 6, pp. 18–25, 2017.

[63] L. Gireaud, S. Grugeon, S. Laruelle, B. Yrieix, and J. M. Tarascon, "Lithium metal stripping/plating mechanisms studies: A metallurgical approach," *Electrochemistry Communications*, vol. 8, no. 10, pp. 1639–1649, 2006.

[64] M. Weinberger and M. Wohlfahrt-Mehrens, "Novel strategies towards the realization of larger lithium sulfur/silicon pouch cells," *Electrochimica Acta*, vol. 191, pp. 124–132, 2016.

[65] R. Song, R. Fang, L. Wen, Y. Shi, S. Wang, and F. Li, "A trilayer separator with dual function for high performance lithium-sulfur batteries," *Journal of Power Sources*, vol. 301, pp. 179–186, 2016.

[66] C. Y. Fan, S. Y. Liu, H. H. Li, H. F. Wang, H. C. Wang, X. L. Wu, H. Z. Sun, and J. P. Zhang, "Synergistic Design of Cathode Region for the High-Energy-Density Li-S Batteries," *ACS Applied Materials and Interfaces*, vol. 8, no. 42, pp. 28 689–28 699, 2016.

[67] B. Jin, J.-U. Kim, and H.-B. Gu, "Electrochemical properties of lithium-sulfur batteries," *Journal of Power Sources*, vol. 117, no. 1-2, pp. 148–152, may 2003.

[68] S. Waluś, C. Barchasz, J.-F. Colin, J.-F. Martin, E. Elkaïm, J.-C. Leprêtre, and F. Alloin, "New insight into the working mechanism of lithium-sulfur batteries: in situ and operando X-ray diffraction characterization." *Chemical communications (Cambridge, England)*, vol. 49, no. 72, pp. 7899–901, 2013.

[69] M. J. Lacey, K. Edström, and D. Brandell, "Analysis of soluble intermediates in the lithium-sulfur battery by a simple in situ electrochemical probe," *Electrochemistry Communications*, vol. 46, pp. 91–93, 2014.

[70] S.-E. Cheon, S.-S. Choi, J.-S. Han, Y.-S. Choi, B.-H. Jung, and H. S. Lim, "Capacity Fading Mechanisms on Cycling a High-Capacity Secondary Sulfur Cathode," *Journal of The Electrochemical Society*, vol. 151, no. 12, p. A2067, 2004.

[71] H. Noh, J. Song, J.-K. Park, and H.-T. Kim, "A new insight on capacity fading of lithium-sulfur batteries: The effect of Li2S phase structure," *Journal of Power Sources*, vol. 293, pp. 329–335, 2015.

[72] Y. Jung and S. Kim, "New approaches to improve cycle life characteristics of lithium-sulfur cells," *Electrochemistry Communications*, vol. 9, no. 2, pp. 249–254, feb 2007.

[73] T. Zhang, M. Marinescu, L. O'Neill, M. Wild, and G. Offer, "Modeling the voltage loss mechanisms in lithium-sulfur cells: the importance of electrolyte resistance and precipitation kinetics." *Physical Chemistry Chemical Physics*, vol. 17, no. 35, pp. 22 581–22 586, 2015.

[74] N. Azimi, Z. Xue, N. D. Rago, C. Takoudis, M. L. Gordin, J. Song, D. Wang, and Z. Zhang, "Fluorinated Electrolytes for Li-S Battery: Suppressing the Self-Discharge with an Electrolyte Containing Fluoroether Solvent," *Journal of The Electrochemical Society*, vol. 162, no. 1, pp. 64–68, 2015.

[75] M. L. Gordin, F. Dai, S. Chen, T. Xu, J. Song, D. Tang, N. Azimi, Z. Zhang, and D. Wang, "Bis(2,2,2-trifluoroethyl) ether as an electrolyte co-solvent for mitigating self-discharge in lithium - Sulfur batteries," *ACS Applied Materials and Interfaces*, vol. 6, no. 11, pp. 8006–8010, 2014.

[76] J.-Q. Huang, T.-Z. Zhuang, Q. Zhang, H.-J. Peng, C.-M. Chen, and F. Wei, "Permselective Graphene Oxide Membrane for Highly Stable and Anti-Self-Discharge Lithium-Sulfur Batteries," *ACS Nano*, vol. 9, no. 3, pp. 3002–3011, mar 2015.

[77] C. E. Parfitt, "Characterisation, Modelling and Management of Lithium Sulphur Batteries for Spacecraft Applications," Ph.D. dissertation, University of Warwick, 2012.

[78] M. R. Jongerden and B. R. Haverkort, "Battery Modeling," Centre for Telematics and Information Technology, University of Twente, Tech. Rep., 2008.

[79] F. Y. Fan, W. C. Carter, and Y.-M. Chiang, "Mechanism and Kinetics of Li2S Precipitation in Lithium-Sulfur Batteries," *Advanced Materials*, vol. 27, pp. 5203–5209, 2015.

[80] S.-E. Cheon, K.-S. Ko, J.-H. Cho, S.-W. Kim, E.-Y. Chin, and H.-T. Kim, "Rechargeable Lithium Sulfur Battery II. Rate Capability and Cycle Characteristics," *Journal of The Electrochemical Society*, vol. 150, no. 6, p. A800, 2003.

[81] P. A. Cassani and S. S. Williamson, "Significance of battery cell equalization and monitoring for practical commercialization of plug-in hybrid electric vehicles," *Conf. Proc. - IEEE Appl. Power Electron. Conf. Expo. - APEC*, pp. 465–471, 2009.

[82] S. Li, C. C. Mi, and M. Zhang, "A high-efficiency active battery-balancing circuit using multiwinding transformer," *IEEE Trans. Ind. Appl.*, vol. 49, no. 1, pp. 198–207, 2013.

[83] J. V. Barreras, C. Pinto, R. De Castro, E. Schaltz, S. J. Andreasen, and R. E. Araújo, "Multi-objective control of balancing systems for li-ion battery packs: A paradigm shift?" *2014 IEEE Veh. Power Propuls. Conf. VPPC 2014*, 2015.

[84] Y. H. Hsieh, T. J. Liang, S. M. Chen, W. Y. Horng, and Y. Y. Chung, "A Novel High-Efficiency Compact-Size Low-Cost Balancing Method for Series-Connected Battery Applications," *Power Electron. IEEE Trans.*, vol. 28, no. 12, pp. 5927–5939, 2013.

[85] C.-H. Kim, M.-Y. Kim, and G.-W. Moon, "A Modularized Charge Equalizer Using a Battery Monitoring IC for Series-Connected Li-Ion Battery Strings in Electric Vehicles," *IEEE Trans. Power Electron.*, vol. 28, no. 8, pp. 3779–3787, 2013.

[86] J. Seo, C.-S. Kim, J. Prakash, and K. Zaghib, "Thermal characterization of Li/sulfur cells using isothermal micro-calorimetry," *Electrochemistry Communications*, vol. 44, pp. 42–44, jul 2014.

[87] J. Seo, S. Sankarasubramanian, C.-S. Kim, P. Hovington, J. Prakash, and K. Zaghib, "Thermal characterization of Li/sulfur, Li/ S-LiFePO4 and Li/S-LiV3O8 cells using Isothermal Micro-Calorimetry and Accelerating Rate Calorimetry," *Journal of Power Sources*, vol. 289, pp. 1–7, 2015.

[88] D. Adair, K. Ismailov, Y. Massalin, and Z. Bakenov, "Thermal Management of Lithium/Sulphur Cells Using a Simple 2D Model," *Modern Environmental Science and Engineering*, vol. 2, no. 04, pp. 246–250, 2016.

[89] J. Yan, X. Liu, and B. Li, "Capacity Fade Analysis of Sulfur Cathodes in Lithium-Sulfur Batteries," *Advanced Science*, vol. 3, no. 12, p. 1600101, dec 2016.

[90] G. Mulder, N. Omar, S. Pauwels, F. Leemans, B. Verbrugge, W. De Nijs, P. Van Den Bossche, D. Six, and J. Van Mierlo, "Enhanced test methods to characterise automotive battery cells," *Journal of Power Sources*, vol. 196, no. 23, pp. 10 079–10 087, 2011.

[91] The Idaho National Laboratory, "Battery Test Manual For Plug-In Hybrid Electric Vehicles," The Idaho National Laboratory, Tech. Rep. INL-EXT-12-27920, 2012.

[92] D.-I. Stroe, M. Swierczynski, A.-I. Stan, R. Teodorescu, and S. J. Andreasen, "Accelerated Lifetime Testing Methodology for Lifetime Estimation of Lithium-Ion Batteries Used in Augmented Wind Power Plants," *IEEE Transactions on Industry Applications*, vol. 50, no. 6, pp. 4006–4017, nov 2014.

[93] *ISO 12405-1:2011 Electrically propelled road vehicles - Test specification for lithium-ion traction battery packs and systems - Part 1: High-power applications*, Std., 2011.

[94] *ISO 12405-2:2012 Electrically propelled road vehicles - Test specification for lithium-ion traction battery packs and systems - Part 2: High-energy applications*, Std., 2012.

[95] *IEC 62660-1: Electrically propelled road vehicles - Test specification for lithium-ion traction battery packs and systems - Part 1: High power applications*, Std., 2011.

[96] *IEC 62660-2: Secondary batteries for the propulsion of electric road vehicles - Part 2: Reliability and abuse testing for lithium-ion cells*, Std., 2011.

[97] S. Risse, S. Angioletti-Uberti, J. Dzubiella, and M. Ballauff, "Capacity fading in lithium/sulfur batteries: A linear four-state model," *Journal of Power Sources*, vol. 267, pp. 648–654, dec 2014.

[98] M. Shahriari and M. Farrokhi, "Online state-of-health estimation of vrla batteries using state of charge," *IEEE Transactions on Industrial Electronics*, vol. 60, no. 1, pp. 191–202, Jan 2013.

[99] B. S. Bhangu, P. Bentley, D. A. Stone, and C. M. Bingham, "Nonlinear observers for predicting state-of-charge and state-of-health of lead-acid batteries for hybrid-electric vehicles," *IEEE Transactions on Vehicular Technology*, vol. 54, no. 3, pp. 783–794, May 2005.

[100] M. Coleman, C. K. Lee, C. Zhu, and W. G. Hurley, "State-of-charge determination from emf voltage estimation: Using impedance, terminal voltage, and current for lead-acid and lithium-ion batteries," *IEEE Transactions on Industrial Electronics*, vol. 54, no. 5, pp. 2550–2557, Oct 2007.

[101] P. Singh, C. F. Jr., and D. Reisner, "Fuzzy logic modelling of state-of-charge and available capacity of nickel/metal hydride batteries," *Journal of Power Sources*, vol. 136, no. 2, pp. 322 – 333, 2004, selected papers presented at the International Power Sources Symposium.

[102] A. Fotouhi, K. Propp, and D. J. Auger, "Electric vehicle battery model identification and state of charge estimation in real world driving cycles," in *Computer Science and Electronic Engineering Conference (CEEC), 2015 7th*, Sept 2015, pp. 243–248.

[103] G. L. Plett, "Extended Kalman filtering for battery management systems of LiPB-based {HEV} battery packs: Part 3. State and parameter estimation ," *Journal of Power Sources*, vol. 134, no. 2, pp. 277 – 292, 2004.

[104] M. Charkhgard and M. Farrokhi, "State-of-charge estimation for lithium-ion batteries using neural networks and ekf," *IEEE Transactions on Industrial Electronics*, vol. 57, no. 12, pp. 4178–4187, Dec 2010.

[105] M. Dubarry, V. Svoboda, R. Hwu, and B. Yann Liaw, "Incremental Capacity Analysis and Close-to-Equilibrium OCV Measurements to Quantify Capacity Fade in Commercial Rechargeable Lithium Batteries," *Electrochemical and Solid-State Letters*, vol. 9, no. 10, pp. A454–A457, 2006.

[106] M. Kassem, J. Bernard, R. Revel, S. Pélissier, F. Duclaud, and C. Delacourt, "Calendar aging of a graphite/LiFePO 4 cell," *Journal of Power Sources*, vol. 208, pp. 296–305, 2012.

[107] M. Dubarry, B. Y. Liaw, M. S. Chen, S. S. Chyan, K. C. Han, W. T. Sie, and S. H. Wu, "Identifying battery aging mechanisms in large format Li ion cells," *Journal of Power Sources*, vol. 196, no. 7, pp. 3420–3425, 2011.

[108] M. Dubarry, C. Truchot, M. Cugnet, B. Y. Liaw, K. Gering, S. Sazhin, D. Jamison, and C. Michelbacher, "Evaluation of commercial lithium-ion cells based on composite positive electrode for plug-in hybrid electric vehicle applications. Part I: Initial characterizations," *Journal of Power Sources*, vol. 196, no. 23, pp. 10 328–10 335, 2011.

[109] J. V. M. M. Berecibar, M. Dubarry, N. Omar, I. Villarreal, "Degradation mechanism detection for NMC batteries based on Incremental Capacity curves," *Evs29*, pp. 1–12, 2016.

[110] X. Han, M. Ouyang, L. Lu, and J. Li, "Cycle life of commercial lithium-ion batteries with lithium titanium oxide anodes in electric vehicles," *Energies*, vol. 7, no. 8, pp. 4895–4909, 2014.

[111] C. Weng, Y. Cui, J. Sun, and H. Peng, "On-board state of health monitoring of lithium-ion batteries using incremental capacity analysis with support vector regression," *Journal of Power Sources*, vol. 235, pp. 36–44, 2013.

[112] E. Riviere, P. Venet, A. Sari, F. Meniere, Y. Bultel, U. Claude, B. Lyon, U. D. Lyon, and V. Cedex, "LiFePO 4 Battery State Of Health Online Estimation Using Electric Vehicle Embeded Incremental Capacity Analysis," *Vehicle Power and Propulsion Conference (VPPC), 2015 IEEE*, pp. 1–6, 2015.

Part II

Papers

Paper A1

Comparison of parametrization techniques for an electrical circuit model of Lithium-Sulfur batteries

Vaclav Knap, Daniel-Ioan Stroe, Remus Teodorescu,
Maciej Swierczynski, and Tiberiu Stanciu

The paper has been published in the proceedings of the *IEEE 13th International Conference on Industrial Informatics (INDIN)*, pp. 1278–1283, 2015, doi:10.1109/INDIN.2015.7281919. Reprinted, with permission of the IEEE, 2017. Accepted version of the paper.

Comparison of Parametrization Techniques for an Electrical Circuit Model of Lithium-Sulfur Batteries

Vaclav Knap, Daniel-Ioan Stroe, Remus Teodorescu, Maciej Swierczynski, and Tiberiu Stanciu
Department of Energy Technology, Aalborg University, Denmark
Email: vkn@et.aau.dk

***Abstract*—Lithium-Sulfur (Li-S) batteries are an emerging energy storage technology, which draw interest due to its high theoretical specific capacity (approx. 1675 Ah/kg) and theoretical energy density of almost 2600 Wh/kg. In order to analyse their dynamic behaviour and to determine their suitability for various commercial applications, battery performance models are needed. The development of such models represents a challenging task especially for Li-S batteries because this technology during their operation undergo several different chemical reactions, known as polysulfide shuttle. This paper focuses on the comparison of different parametrization methods of electrical circuit models (ECMs) for Li-S batteries. These methods are used to parametrize an ECM based on laboratory measurements performed on a Li-S pouch cell. Simulation results of ECMs are presented and compared against measurement values and the accuracy of parametrization methods are evaluated and compared.**

I. INTRODUCTION

Lithium-Sulfur (Li-S) batteries belong to a recently hot discussed topic among the emerging battery technologies. It is due to their high theoretical specific capacity and theoretical energy density, which would result in a decreased weight of battery cells. Furthermore, the sulfur abundance decreases the battery manufacturing cost in comparison to metals used in lithium-ion batteries and it is as well more environmentally friendly [1].

Nowadays, Li-S batteries become commercially available, even though their performance is still far from their theoretical limits. For analysing their performance at different conditions (e.g. temperature, state-of-charge (SOC) or current), there is a need for an accurate battery performance model. Moreover, this performance model may be required to run online in certain applications and in this case it needs to have a fast computation time. All these requirements can be met by an equivalent circuit model (ECM). Moreover, ECMs are based on basic electrical components (e.g. voltage sources, resistors etc.), which can be easily integrated into a complex model, e.g. an electric vehicle [2]–[4].

An important task for developing the specific ECM of a battery is to parametrize it. At first, the appropriate measurements have to be performed. The widely used measurement methods for parametrizing an ECM are electrochemical impedance spectroscopy (EIS) [5] or current pulse-based methods [6], [7]. The next step is the selection of the ECM topology, which is followed by the estimation of the parameters from the measurement data. Researchers have proposed different methods, which are dealing with this task by means of different parametrization approaches [5], [7]–[14]. In the literature, mainly the determination of ECM's parameters based on the EIS measurements have been used for the Li-S batteries [15], [16]. Identification of the parameters from current pulse-based measurements for a Li-S battery has been so far used only in [17]; however, the parametrization technique has not been specified.

This paper gives an overview of different parametrization methods for a Li-S battery ECM. These methods are applied to a Li-S pouch battery cell and in consequence, the ECM parameters are estimated. Finally, simulations for the obtained ECMs are performed and the parametrization techniques are evaluated and compared.

The paper is structured as follows: Section II describes briefly fundamentals of Li-S batteries. Afterward, in Section III, there is introduced an ECM for Li-S batteries. The measurement methods for parametrization of the proposed ECM and parametrization techniques are presented in Section IV. Thus, it is followed by the description of an experiment and results in Section V and the discussion of obtained results in Section VI. Conclusions and future work are summarized in Section VII.

II. LITHIUM-SULFUR BATTERIES

The Li-S battery is composed of a sulfur compound cathode, an electrolyte (polymer or liquid), and a lithium anode. Furthermore, different additives and binders can be added in order to improve the battery's characteristics. Sulfur is a perspective cathode material, which offers a high theoretical specific capacity of approximately 1675 mAh/g. Moreover, the theoretical energy density of a Li-S battery is approx. 2600 Wh/kg, which is five times more than the theoretical energy density of Lithium-ion (Li-ion) batteries. The basic Li-S redox reaction is written as [18]:

$$16Li + S_8 \longrightarrow 8Li_2S. \tag{1}$$

However, the internal chemical processes of the Li-S battery are more complex than in the case of commercial Li-ion batteries. The reduction of sulfur from S_8 to S is a multi-stage process during which different types of polysulfides (Li_2S_n) are formed and dissolved. In Fig. 1, there is shown the typical discharge voltage profile for a Li-S battery and four stages are illustrated, together with their corresponding dominant chemical reactions [18]. During the reverse operation (charging),

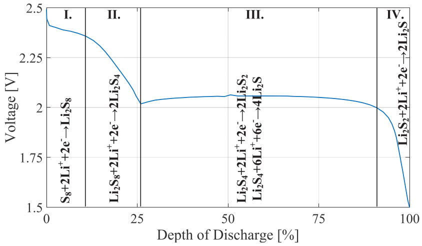

Fig. 1. Voltage profile of a Li-S cell during discharging.

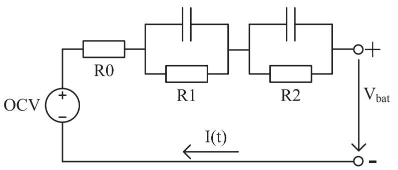

Fig. 2. An electrical circuit model for a Li-S battery cell.

the polysulfides with a shorter chain length are oxidized and recombined to polysulfides with a longer chain length. This process of polysulfide circulation is known as a polysulfide shuttle.

The polysulfides with a longer chain length are vastly soluble in frequent liquid organic electrolytes. However in the case of the polysulfides Li_2S and Li_2S_2, their insolubility in the organic electrolytes causes their sedimentation on the anode surface and in areas of the cathode, which are electronically insulated. In this way, the sedimented Li_2S/Li_2S_2 do not participate anymore in the charging and discharging of the battery. Consequences of the polysulfide shuttle are an increased internal battery resistance, fast capacity degradation, low coulombic efficiency, and high self-discharge. Therefore, one of the scientific focus is to avoid these negative effects of the polysulfide shuttle. Nevertheless, the polysulfide shuttle has also a positive effect, which is an inherent protection against cell overcharge [1].

III. A LITHIUM-SULFUR BATTERY ECM

The ECM used in this work is based on the equivalent circuit proposed in [19] for a Li-S cell in an intermediate state. For the ECMs parametrized based on EIS measurements, constant phase elements (CPEs) are usually used instead of capacitors to take into account a non-ideal behaviour of the electrode, like a roughness of the surface and porosity of a material [20]. However, if the parametrization is performed based on current pulse measurements, then, the utilized model contains only capacitors instead of CPEs. The layout of the ECM used in this work for modeling the dynamic behaviour of the Li-S cell is presented in Fig. 2. According to [19], R_0 represents the electrolyte resistance, R_1 stands for the total surface layers resistance of the sulfur and lithium electrodes, C_1 is the distributed surface layers capacitance on both electrodes, R_2 expresses the charge transfer resistance on the sulfur electrode and C_2 interprets the double layer capacitance distributed on the surface of the pores in the sulfur electrode.

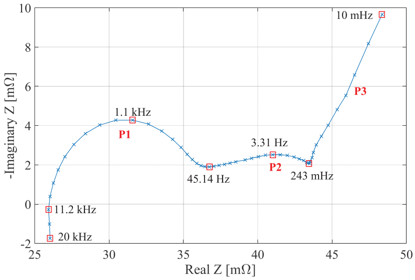

Fig. 3. Measured impedance spectra of a Li-S cell.

IV. MEASUREMENT AND PARAMETRIZATION TECHNIQUES

There are two types of widely used measuring methods, which provide input data for parametrizing of ECMs: the EIS and the current pulse-based methods.

A. *EIS Measurements*

EIS was firstly used as a method for characterizing the electrical attributes of materials. The measurement technique is based on applying a sinusoidal voltage or current and measuring the phase shift and amplitude of the non-applied signal in order to obtain the AC impedance relevant to the applied frequency. Usually, multiple frequencies are considered during the measurement and the final result is the impedance spectrum of the battery cell [5]. The spectrum is graphically presented as a Nyquist plot, as it is shown in Fig. 3 for a Li-S battery. In Fig. 3, there are marked phases of the Li-S battery, where according [16]: P1 is caused by the charge transfer of sulfur intermediates, P2 comes from the formation and dissolution of S_8 and Li_2S, and P3 represents diffusion processes.

The EIS can be applied to the battery during a relaxation period [15], [21]. The obtained data are in that case exactly for the specific level of SOC, however it does not reflect the battery parameters dependence on different C-rates. Another option is to superimpose a charging or discharging current during the EIS measurement [22]. This allows for including battery impedance dependence on the charging/discharging battery current. In this case, the battery state is not stationary and the measurement has to be sufficiently fast in order to be valid to a certain level or range of SOC. In [21], an alternative EIS measurement method is presented by applying a superimposed current pulses.

In order to obtain values of the ECM elements, the Nyquist plot is fitted commonly by using a complex nonlinear least squares fitting method [5]. Specialized softwares allow to fit the data to different topologies of ECMs, e.g. ZView software is used in [15]. Nevertheless, in this work the EIS technique was not used to parametrize the ECM.

B. *Current Pulse Measurements*

Methods based on DC current pulses are divided into two types. The first type is a hybrid pulse power characterization (HPPC) test [6]. The HPPC method consists of a procedure, when the battery is brought to a desired SOC level and is

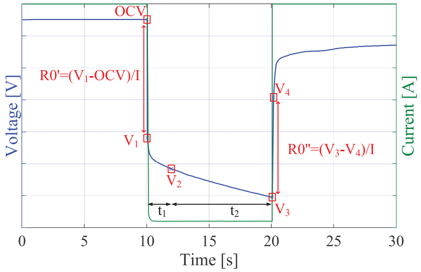

Fig. 4. The current pulse and its voltage response for the Li-S battery.

left for a certain period of time to relax and achieve thermodynamic stability. After the relaxation period, a short charging or discharging current pulse is applied and another relaxation period follows before a second current pulse of opposite orientation is applied. It is again followed by the relaxation period. Afterward, the battery is recharged to the new SOC and the steps are repeated for the whole SOC interval. The typical length of the current pulse is 10 seconds [6]; alternatively, a current pulse of 18 seconds can be used [23]. The voltage response of a LiS battery to 10 second current pulse is shown in Fig. 4. Therefore, the SOC during the pulse is usually assumed to be constant; however this assumption may introduce some model inaccuracy, especially for high current pulses.

The second pulse-based method is referred to as galvanostatic intermittent titration technique (GITT) [24]. It consists of constant current pulses in one direction, during which the SOC is shifted to a new level, and of relaxation periods between them. The current pulses do not have to be equally long. For example, battery regions with high voltage dynamics are measured with pulses shifting the SOC about 1%. For more stable voltage regions, the applied current pulses may change the SOC about 10% [7], [25].

C. *Parameterization methods based on pulse measurements*

Several procedures are proposed in literature for deriving the parameters of the ECMs from pulse measurements. They use the voltage response data during the current pulse [8]–[10] or during the relaxation period after finishing the pulse [7], [11], or they combine both approaches [12].

In references [8], [9], there is described a method that uses the Battery Parameter Estimator Spreadsheet, which is based on a multiple linear regression of measured HPPC data. The process of data fitting is performed manually by using an MS Excel spreadsheet and it is described only for an ECM with one R-C element. This methods is further improved in [9] by using Matlab/Simulink parameter estimation tool and it is referred to as Simulink Parameter Estimation Method. The improved method is supposed to be more accurate and faster; moreover it is suitable for any ECM structure.

The method presented in [10], was originally proposed for the ECM with two R-C elements and it uses the HPPC method applied to a Li-ion battery with current pulse lengths of 10 seconds. Four voltage points are identified during the voltage response under the applied current, as shown in Fig. 4; they are the open-circuit voltage (OCV), the instantaneous voltage drop after applying the current (V_1), the voltage at 2 seconds (fast dynamics) (V_2) and the voltage at 10 seconds (slow dynamics). From the considered voltage values the ECMs parameters are computed as:

$$R_0 = (OCV - V_1)/I \tag{2}$$

$$R_1 = (V_1 - V_2)/I \tag{3}$$

$$R_2 = (V_2 - V_3)/I \tag{4}$$

$$\tau_1 = R_1 C_1 \tag{5}$$

$$\tau_2 = R_2 C_2 \tag{6}$$

Afterwards, the battery voltage is simulated and compared with the measurements:

$$\begin{aligned} V_s(t) = OCV + I(t)R_0 + I(t)R_1(1 - e^{-\frac{t}{\tau_1}}) + \\ + I(t)R_2(1 - e^{-\frac{t}{\tau_2}}) \end{aligned} \tag{7}$$

$$LSE = (V_{meas}(t) - V_s(t))^2 \tag{8}$$

where $V_s(t)$ is the simulated voltage, $V_{meas}(t)$ is the measured voltage, $I(t)$ is the applied current, t is the time, LSE is the squared error, which is going to be minimized, and τ_1 and τ_2 represents time constant of fast and slow dynamics, respectively. The ECMs parameters are optimized by using the unconstrained optimisation algorithm $fminsearch$ (Nelder-Mead) in Matlab to minimize the error.

The next method, proposed in [7], identifies time constants from the relaxation voltage. The voltage during relaxation, after the initial voltage drop, is expressed as:

$$u_{relax} = OCV - \sum_{i=1}^{n} U_i e^{-\frac{t}{\tau_i}} \tag{9}$$

where u_{relax} is the voltage during relaxation period, U_i is the polarization voltage of ith R-C branch and τ_i is the time constant of the ith R-C branch. Each ith time constant is estimated according:

$$\hat{\tau_i} = \frac{t_{i2} - t_{i1}}{ln(\frac{u_\tau(t_{i1})}{u_\tau(t_{i2})})} \; for \; u_\tau \neq 0 \tag{10}$$

where a hat is used for an estimated value, i stands for the number of the R-C branch, t_{ix} are time coordinates, illustrated in Fig. 5, and u_τ is the transient circuit voltage. The algorithm starts from the longest time constant and proceeds to the shortest one. The assumption is that the time constants have different time scales. The time gap between time windows for a longer and a shorter time constant should be at least three times the value of the shorter time constant, the illustration is shown in Fig. 5. It ensures a negligible influence of the shorter constant branch voltage to the longer time constant parameter extraction, as the voltage of the shorter constant branch dropped under 5% of its initial value. At each step, the transient voltage for the specific time constant is estimated and it is subtracted from the transient voltage for the following time constant identification. The resistance R_i of the ith R-C element is extracted through:

$$R_i = \frac{\hat{U_i}}{I_{cp}(1 - e^{-\frac{t_{cp}}{\hat{\tau_i}}})}, \tag{11}$$

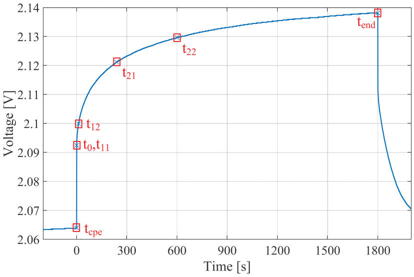

Fig. 5. The relaxation voltage period and the illustration of the point determination for two time constants.

where I_{cp} is the amplitude of the current pulse and t_{cp} is the duration of the pulse. C_i is obtained as follows:

$$C_i = \frac{\hat{\tau}_i}{R_i} \tag{12}$$

The method can be applied to an ECM with n-combinations of R-C elements.

The other methods presented in [11], [12], [26], do not preliminarily separate the fast and slow time constants from the voltage profile. In one of them, a genetic algorithm is used to find the best result of an applied regression equation; however the time constants have to be approximately known in advance in order to run the regression algorithm [26]. Alternatively, the measured data are fitted to an equation describing the voltage, with preliminary computation of a series resistor, and optimized by a least-square error method [11], [12].

V. EXPERIMENT DESCRIPTION

Laboratory measurements were performed on a Li-S pouch cell supplied by OXIS Energy with a nominal capacity of 3.4 Ah. The cell test connection is shown in Fig. 6, the temperature in the climatic chamber was set to 35° C. At first, two full cycles (0.1 C CHA, 0.2 C DCH) were performed between 2.45 V (SOC=100%) and 1.5 V (SOC=0%). From the second cycle, the reference discharge capacity of 2.918 Ah was measured and the capacity values corresponding to 2.5% and 5% SOC steps were computed accordingly. The GITT was performed with a discharging current of 0.2 C and 30 minutes relaxation time between the pulses, with exception of 1.5 minutes for 100% SOC, 8 minutes for 95%, 15 minutes for 90% and 21 minutes for 85%, as it is shown in Fig. 7. The first pulse at 100% SOC lasted only 18 seconds in order to be able obtain discharging parameters for this SOC level. The OCV was derived from the relaxation period. For high SOC levels (i.e. 100-85%), the cell reached the relaxed state, which is considered as the point where the influence of recovery phase is equal to the influence of self-discharge. Therefore, as the OCV value was considered to be maximal voltage, as illustrated in Fig. 7. For the lower SOC levels (i.e. 80% and less), 30 minutes period was not enough to reach fully relaxed stage. For these cases, the voltage at the end of relaxation period was used for the OCV value. The obtained OCV versus SOC curve is presented in Fig. 8.

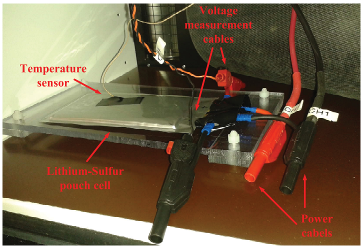

Fig. 6. Illustration of the Li-S battery cell during laboratory measurements.

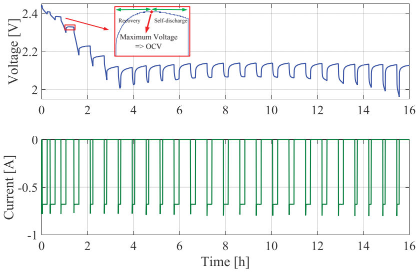

Fig. 7. GITT procedure for discharging of a Li-S cell.

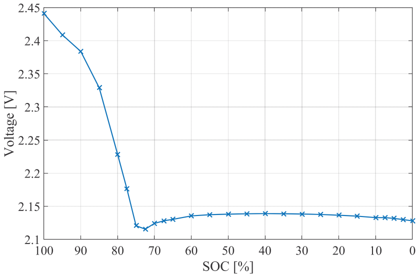

Fig. 8. Open circuit voltage of the Li-S cell derived from the relaxation voltage of GITT for discharging steps with 0.2 C-rate.

The three previously described parametrization techniques were applied to the measured data.. Afterward, the GITT current profile, shown in Fig. 7, is applied to the parametrized battery model and the resulting voltage profile is compared to the measured one and the sum-of-squared-errors (SSE) (13) is evaluated.

$$SSE = \sum((V_{meas}(t) - V_s(t))^2) \tag{13}$$

A. *Parametrization Technique 1 (PT1)*

The PT1 follows the procedure described in [10]. At first, the original time coordinates were used for 10 seconds current pulse. This case is labeled as PT1a. The time measurement points are presented in Table I. For the optimization, six iteration steps were used as a good compromise between the consistency of trend in parameters and the minimum value of the optimize function. The simulation with one second resolution of GITT profile with the parameters obtained by PT1a has a SSE of 23.35.

For PT1b, the current pulse time window was expanded to 18 seconds, according to [23]. It resulted in the GITT simulation with a SSE of 19.49. The obtained parameters of the ECM for PT1 are shown in Fig. 9.

TABLE I

THE INPUT VOLTAGE POINTS FOR THE PT1. THE CURRENT PULSE STARTS AT T = 0 S.

Voltage Point [V]	Time [s]	
	a	b
V_0	0	
V_1	0.5	
V_2	1.5	1.5
V_3	10	18

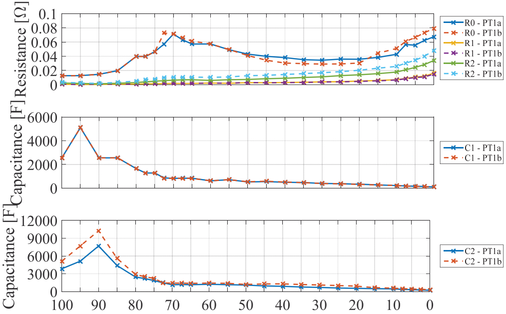

Fig. 9. PT1: Estimated values for the circuit elements.

TABLE II

THE COORDINATES FOR TIME WINDOWS SELECTION.

SOC level →	100%	95%	90%	85%	≤80%
Time point ↓	Time [s]				
t_{11}	0	0	0	0	0
t_{12}	0.5	2.5	12	12	12
t_{21}	1	7.5	60	120	240
t_{22}	1.5	20	100	300	600
t_{end}	9	58	246	630	1800

B. Parametrization Technique 2 (PT2)

The PT2 follows the methodology presented in [7]. R_0 was computed from the instantaneous voltage drop after the current interruption as shown in Fig. 4. The time windows for two time constants were selected as in the original paper [7]. However, the values for the high SOC levels (85-100%) were adjusted, as the relaxation time for them is shorter. The selected time values are presented in Table II.

Due to the too short time of relaxation period, the parameters for 100% SOC, except R_0 were not estimated. Therefore, their values were extrapolated. By comparing the GITT measurement results with the simulated results, when parametrization technique PT2 was used, returned a SSE of 0.65.

Additionally, $fminsearch$ optimization in Matlab, as in the PT1 case, was applied to these parameters (R_1, C_1, R_2, C_2, U_1 and U_2). The previously obtained values were used as initial points and 25 iteration steps were considered. The GITT simulation with these updated parameters decreased the SSE to 0.62. The extracted parameters by PT2 are shown in Fig. 10.

C. Parametrization Technique 3 (PT3)

The PT3 is based on [12]. R_0 was computed in the same way as in PT2, from the current interruption. The function for the relaxation voltage without the instantaneous drop is described as:

$$V(t) = OCV(SOC) - (U_1 exp^{-t/\tau_1} + U_2 exp^{-t/\tau_2}) \quad (14)$$

The measured relaxation voltage was fitted into (14) by Least Squares method to estimate $U_1, U_2, \tau_1$and τ_2. The specific R_i and C_i parameters were obtained by solving (11) and (12). The obtained parameters are shown in Fig. 11. In this case, a SSE equal to 1.93 was obtained.

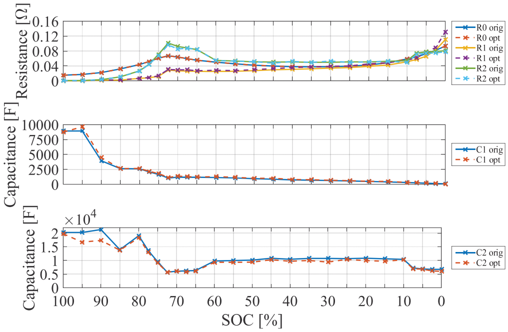

Fig. 10. PT2: Estimated values for the circuit elements.

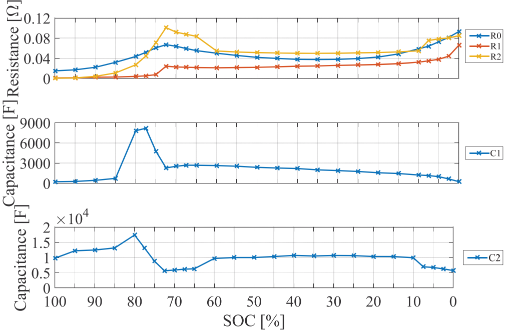

Fig. 11. PT3: Estimated values for the circuit elements.

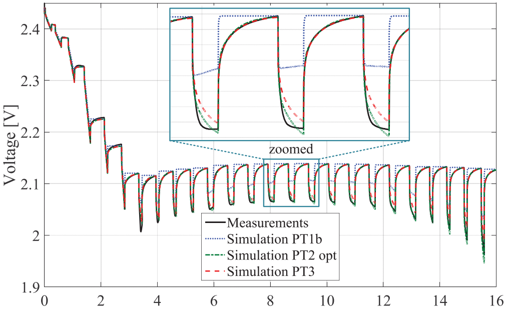

Fig. 12. Measured and simulated voltage profile.

The voltage profiles from the measurement and the ECM simulations (using different parametrization techniques) are presented in Fig. 12.

VI. DISCUSSION

From the simulations, considering an GITT profile, it is visible that PT1 was the less suitable technique for parametrization of the ECM model of a Li-S battery, as it had the significantly largest SSE of 19.49 and the parametrized model was not able to follow accurately the measured voltage curve, as it is seen from Fig. 12. This deriving of the non-representative parameters can be caused by considering too short time period of the pulse, as it might not sufficiently represent the battery dynamics.

The most accurate results were obtained for the technique PT2, especially after the optimization, as it reached only 0.62 SSE. Both PT2 and PT3 followed accurately voltage dynamics during the relaxation period. However during discharging periods, the model is not able to follow very accurately the measured battery voltage. This comes from the fact that the parametrization was performed only from the relaxation period and did not consider the battery dynamics under operation, where dynamics might be different.

The extracted parameters from the PT2 (resistances, capacitances) have a strong relationship with the character of the OCV profile (Fig. 8) and the discharging voltage profile (Fig. 1). The capacitances' curves are copying directly their shapes and the resistances' curves have an inverse character. That might be seen as a confirmation of the correctness of the derived parameters.

VII. CONCLUSIONS AND FUTURE WORK

In this work, measurement and parametrization techniques for deriving ECM parameters were presented. Afterward, the GITT was performed on the Li-S cell. The parameters for the ECM and the OCV for battery discharging were derived from the relaxation period of the voltage and from the discharging pulses.

The parametrized ECM was simulated with the same current profile as during battery laboratory measurement. The best accuracy has the model parameterized based on PT2. The simulated voltage was able to follow accurately the measured voltage with a SSE of 0.62. Therefore, the ECM for the Li-S battery was established for discharging GITT profile by 0.2 C under the temperature conditions of 35° C.

Future work will target the improvement of the parametrization technique in order to obtain a model which estimates more accurately the battery voltage during charging and discharging. The dependencies on the operating conditions, as temperature and current, can be included to the model. Such model should be also validated against different current profiles.

ACKNOWLEDGMENT

This work has been part of the ACEMU-project (1313-00004B). Authors gratefully acknowledge the Danish Council for Strategic Research and EUDP for providing financial support and thank OXIS Energy for supplying the lithium-sulfur battery cell.

REFERENCES

[1] D. Bresser, S. Passerini, and B. Scrosati, "Recent progress and remaining challenges in sulfur-based lithium secondary batteries - a review," *Chem. Commun.*, vol. 49, no. 90, pp. 10 545–10 562, Nov. 2013.

[2] X. Hu, S. Li, and H. Peng, "A comparative study of equivalent circuit models for Li-ion batteries," *J. Power Sources*, vol. 198, no. 0, pp. 359 – 367, 2012.

[3] A. Seaman, T.-S. Dao, and J. McPhee, "A survey of mathematics-based equivalent-circuit and electrochemical battery models for hybrid and electric vehicle simulation," *J. Power Sources*, vol. 256, pp. 410–423, Jun. 2014.

[4] M. Einhorn, F. V. Conte *et al.*, "Comparison, selection, and parameterization of electrical battery models for automotive applications," *IEEE Trans. Power Electron.*, vol. 28, no. 3, pp. 1429–1437, 2013.

[5] E. Barsoukov and J. R. Macdonald, *Impedance Spectroscopy Theory, Experiment, and Applications*, 2nd ed. John Wiley & Sons, Inc., 2005.

[6] "Program Battery Test Manual For Plug-In Hybrid Electric Vehicles," U. S. Department of Energy Vehicle Technologies, Tech. Rep., 2014.

[7] A. Hentunen, T. Lehmuspelto, and J. Suomela, "Time-Domain Parameter Extraction Method for Thévenin-Equivalent Circuit Battery Models," *IEEE Trans. Energy Convers.*, vol. 29, no. 3, pp. 558–566, 2014.

[8] "FreedomCAR Battery Test Manual For Power-Assist Hybrid Electric Vehicles," Idaho National Engineering & Environmental Laboratory (INEEL), Tech. Rep., October 2003.

[9] M. Daowd, N. Omar *et al.*, "Battery Models Parameter Estimation based on Matlab / Simulink ," in *The 25th World Battery, Hybrid and Fuel Cell Electric Vehicle Symposium & Exhibition Battery*, 2010.

[10] S. Thanagasundram, R. Arunachala, K. Makinejad *et al.*, "A Cell Level Model for Battery Simulation," *EEVC*, no. November, pp. 1–13, 2012.

[11] X. Lin, H. E. Perez, S. Mohan *et al.*, "A lumped-parameter electro-thermal model for cylindrical batteries," *J. Power Sources*, vol. 257, pp. 1–11, Jul. 2014.

[12] D. Liu, Z. Zhu *et al.*, "Parameter Identification of Improved Equivalent Circuits for Lithium-Ion Battery," *JCIT*, vol. 8, no. 5, pp. 1154–1162, Mar. 2013.

[13] X.-s. Hu, F.-c. Sun, and Y. Zou, "Online model identification of lithium-ion battery for electric vehicles," *J Cent South Univ T*, vol. 18, no. 5, pp. 1525–1531, 2011.

[14] X.-s. Hu, F.-c. Sun, and X.-m. Cheng, "Recursive calibration for a lithium iron phosphate battery for electric vehicles using extended Kalman filtering," *J Zhejiang Univ Sci A*, vol. 12, no. 11, pp. 818–825, 2011.

[15] Z. Deng, Z. Zhang *et al.*, "Electrochemical Impedance Spectroscopy Study of a Lithium/Sulfur Battery: Modeling and Analysis of Capacity Fading," *J. Electrochem. Soc.*, vol. 160, no. 4, pp. A553–A558, Jan. 2013.

[16] N. a. Cañas, K. Hirose, B. Pascucci *et al.*, "Investigations of lithium-sulfur batteries using electrochemical impedance spectroscopy," *Electrochim. Acta*, vol. 97, pp. 42–51, May 2013.

[17] K. Somasundaram, O. Neill, M. Marinescu *et al.*, "Towards an operational model for a Li-S battery," Poster, London, Sep. 2014.

[18] M. Barghamadi, A. Kapoor, and C. Wen, "A Review on Li-S Batteries as a High Efficiency Rechargeable Lithium Battery," *J. Electrochem. Soc.*, vol. 160, no. 8, pp. A1256–A1263, May 2013.

[19] V. Kolosnitsyn, E. Kuzmina *et al.*, "A study of the electrochemical processes in lithiumsulphur cells by impedance spectroscopy," *J. Power Sources*, vol. 196, no. 3, pp. 1478–1482, Feb. 2011.

[20] C. Barchasz, J.-C. Leprêtre *et al.*, "New insights into the limiting parameters of the Li/S rechargeable cell," *J. Power Sources*, vol. 199, pp. 322–330, Feb. 2012.

[21] V. Kolosnitsyn, E. Kuzmina, and S. Mochalov, "Determination of lithium sulphur batteries internal resistance by the pulsed method during galvanostatic cycling," *J. Power Sources*, vol. 252, pp. 28–34, Apr. 2014.

[22] E. Karden, "Using low-frequency impedance spectroscopy for characterization, monitoring, and modeling," Ph.D. dissertation, RWTH Aachen University, 2002.

[23] H. G. Schweiger, O. Obeidi, O. Komesker *et al.*, "Comparison of several methods for determining the internal resistance of lithium ion cells," *Sensors*, vol. 10, pp. 5604–5625, 2010.

[24] W. Weppner and R. A. Huggins, "Determination of the Kinetic Parameters of Mixed-Conducting Electrodes and Application to the System Li_3Sb," *J. Electrochem. Soc.*, vol. 124, no. 10, pp. 1569–1578, 1977.

[25] R. Jackey, M. Saginaw, P. Sanghvi *et al.*, "Battery Model Parameter Estimation Using a Layered Technique: An Example Using a Lithium Iron Phosphate Cell Pulse Tests to Measure Dynamic," pp. 1–14, 2013.

[26] H. He, R. Xiong, and J. Fan, "Evaluation of Lithium-Ion Battery Equivalent Circuit Models for State of Charge Estimation by an Experimental Approach," *Energies*, vol. 4, no. 12, pp. 582–598, Mar. 2011.

Paper A2

Electrical Circuit Models for Performance Modeling of Lithium-Sulfur Batteries

Vaclav Knap, Daniel-Ioan Stroe, Remus Teodorescu,
Maciej Swierczynski, and Tiberiu Stanciu

The paper has been published in the proceedings of the *IEEE Energy Conversion Congress and Exposition (ECCE)*, pp. 1375–1381, 2015, doi:10.1109/ECCE.2015.7309853.
Reprinted, with permission of the IEEE, 2017. Accepted version of the paper.

Electrical Circuit Models for Performance Modeling of Lithium-Sulfur Batteries

Vaclav Knap, Daniel-Ioan Stroe, Remus Teodorescu, Maciej Swierczynski and Tiberiu Stanciu
Department of Energy Technology, Aalborg University
Aalborg, Denmark
Email: vkn@et.aau.dk

Abstract—**Energy storage technologies such as Lithium-ion (Li-ion) batteries are widely used in the present effort to move towards more ecological solutions in sectors like transportation or renewable-energy integration. However, today's Li-ion batteries are reaching their limits and not all demands of the industry are met yet. Therefore, researchers focus on alternative battery chemistries as Lithium-Sulfur (Li-S), which have a huge potential due to their high theoretical specific capacity (approx. 1675 Ah/kg) and theoretical energy density of almost 2600 Wh/kg. To analyze the suitability of this new emerging technology for various applications, there is a need for Li-S battery performance model; however, developing such models represents a challenging task due to batteries' complex ongoing chemical reactions. Therefore, the literature review was performed to summarize electrical circuit models (ECMs) used for modeling the performance behavior of Li-S batteries. The studied Li-S pouch cell was tested in the laboratory in order to parametrize four basic ECM topologies. These topologies were compared by analyzing their voltage estimation accuracy values, which were obtained for different battery current profiles. Based on these results, the 3 R-C ECM was chosen and the Li-S battery cell discharging performance model with current dependent parameters was derived and validated.**

Keywords—Electrical circuit model, Lithium-Sulfur battery, performance modeling, validation.

I. INTRODUCTION

Because of the ongoing demand for better batteries and since today's Lithium-ion (Li-ion) batteries are close to their limits, many researches focus on new battery chemistries and compositions. Lithium-Sulfur (Li-S) batteries get a high interest as they have a high theoretical specific capacity and theoretical energy density. This, introduced to the practice, will result in lighter batteries with higher capacity. Moreover, in comparison with Li-ion batteries, the production cost and environmental impact of the Li-S batteries would be positively influenced due to the usage of sulfur instead of other (rare) metals [1].

Li-S batteries are currently entering the market, yet with their parameters far from their theoretical limits. For their suitability selection to specific applications, it is necessary to evaluate their performance under various operation conditions (e.g. temperature, state-of-charge (SOC) or current). Moreover, the development of appropriate battery management system is required. Therefore, deriving of the performance model for the Li-S battery seems as an inevitable step. This activity should be done with consideration that the model should have relatively low computational effort as it might run online in specific applications. For such purposes, it is commonly used an equivalent circuit model (ECM), which is composed of fundamental electrical components (e.g. voltage sources, resistors, capacitors etc.) and it is straightforward to integrate with other electrical system models (e.g. an electric vehicle or an energy storage in a grid) [2]–[4].

In order to achieve high accuracy of the performance model, a suitable ECM topology has to be selected. This topology might be different from the ones used for Li-ion batteries, as the Li-S battery has more complex chemical reactions [5]. So far, there were only few activities reported in literature regarding the development of ECM for performance modeling of Li-S batteries [6], [7], which used 2 R-C ECM topology. Most of the Li-S ECMs in literature are used for electrochemical analysis by electrochemical impedance spectroscopy [8]–[14] and they do not directly results to the performance model.

This paper presents a summary of various ECM topologies for Li-S batteries, together with the considered parameter dependencies and the used parametrization methods. Based on this review, four basic ECM topologies with 1 R-C to 4 R-C elements were chosen and parametrized based on laboratory measurements performed on a 3.4 Ah Li-S pouch cell. The topologies are compared according to their accuracy in fitting and their voltage estimation error.. Furthermore, one ECM topology is selected and the Li-S battery cell discharging performance model with current dependent parameters is developed and validated.

The paper is structured as follows: Li-S battery fundamentals are introduced in Section II. Section III presents the summary of ECMs for Li-S batteries. The methodology, including modeling, parametrization, comparison and validation, is described in Section IV. Section V presents and discusses the main obtained results. The conclusions are drawn in Section VI.

II. LITHIUM-SULFUR BATTERY

Typically, a Li-S battery consists of a lithium anode, a sulfur composite cathode, a polymer or liquid electrolyte and a separator. Moreover, additives and binders are used to improve the battery characteristics. Based on the electrodes' properties, a Li-S battery has a high theoretical specific capacity of around 1675 Ah/kg and a theoretical energy density close to 2600 Wh/kg. These characteristics outnumber conventional Li-ion batteries with their theoretical specific capacity of 155 Ah/kg and theoretical specific energy of up to 570 Wh/kg [1], [15].

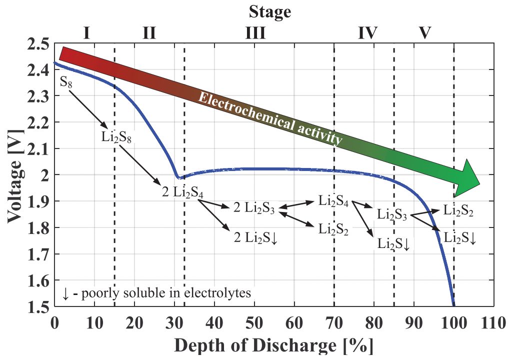

Fig. 1. Typical Li-S discharge voltage curve with illustrated stages and poly-sulfide reactions.

Li-S batteries are characterized by more complicated internal chemical reactions than today's Li-ion batteries. During usage, sulfur goes through different stages of poly-sulfides (Li_2S_n), which influences the battery electrochemical activity. The typical discharging voltage profile of a Li-S battery cell is shown in Fig. 1, together with illustrated stages and their associated prevailing reactions [5]. During discharging, lithium metal reacts with sulfur (S_8) and they form long chain poly-sulfides, which are further decomposed to short chain poly-sulfides. The final discharging product is Li_2S, which has the lowest electrochemical activity and it is insoluble in electrolytes. When Li_2S is produced, it deposits on the carbon, reducing carbon accessibility, and by that the cathode active surface area is reduced [5], [15]. Charging is the opposite process to discharging and poly-sulfide chains are formed from shorter to longer ones. However, the long chain poly-sulfides are highly soluble in electrolytes and during the high charged stages they diffuse to the lithium anode, where they react with the lithium and they are reduced to short chain poly-sulfides, which diffuse back to the cathode. This phenomenon is called ”poly-sulfide shuttle” and it causes internal resistance growth, fast capacity decrease, low coulombic efficiency, and high self-discharge. However, the poly-sulfide shuttle provides also a beneficial attribute of an inherent overcharge protection [1], [16].

III. EQUIVALENT CIRCUIT MODELS FOR LITHIUM-SULFUR BATTERIES

The structure of ECMs can differ depending on the modeled battery chemistry, targeted application and desired accuracy. A general ECM is shown in Fig. 2. It consists of a voltage source representing the open-circuit voltage (OCV) and impedance elements. The simplest ECM topology is a resistance model, which contains only one resistor in series. The clear benefit of this approach is its minimal computation requirements and simplicity, however it provides the lowest accuracy [3], [4].

In literature, the proposed ECMs for Li-S batteries are composed of resistors, capacitors, constant phase angle elements (CPEs) and Warburg impedance. Typically, CPEs are used to take into account a non-ideal behaviour of an electrode, like a roughness of the surface and porosity of a material [8]. Using CPEs and Wargburg impedance elements give better fitting accuracy. Nevertheless, they are often later on approximated with parallel R-C elements to reduce the computation effort. Thus, this paper focuses the investigation on evaluating parallel R-C elements-based ECMs, where CPEs are replaced by capacitors. The main ECM structures used to model the dynamic behaviour of Li-S batteries are shown in Fig. 3; a voltage source representing OCV is not shown, but is assumed to be part of every discussed ECM. Moreover in literature, these topologies are sometimes expanded by and additional Warburg impedance or a capacitor. These ECMs are considered as subtypes of the main structures and they are not further considered in this paper.

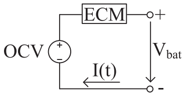

Fig. 2. A general equivalent electrical circuit.

Overall, the ECMs for a Li-S battery are composed of a series resistance and from one to four R-C parallel elements. The elements of the circuits usually represent some specific physical attributes and processes in the battery. In ECM 1, R0, R1 and C1 stands for the resistance of the electrolyte, the charge transfer resistance and the double-layer capacitance, respectively [9]. ECM 2 expands ECM 1 with R2 and C2, which express total resistance and distributed capacitance of the surface layers of both the sulfur and lithium electrodes according [13]. However, in literature, the related meaning of some ECM components varies according to used identification methods, assumptions of authors, and specific cell composition; for example in [10], R2 is connected to the nafion film resistance, as the nafion membrane coating is additionally used on the electrode surface. In a similar way related to ECM 4, authors in [17] redefine and adjust the meaning of elements that R0 is associated to the ohmic resistance caused by the

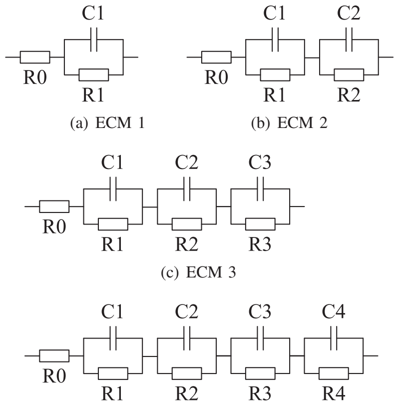

(a) ECM 1
(b) ECM 2
(c) ECM 3
(d) ECM 4

Fig. 3. Main layouts of the ECMs for Li-S batteries.

TABLE I. SUMMARY OF ECMS FOR LI-S BATTERIES.

ECM Type	Parametriz- -ation	Performance model	Reference
ECM 1	EIS	-	[8]–[12]
ECM 2	EIS, Pulse [6]	Yes [6], [7]	[6], [7], [9], [10], [13], [14]
ECM 3	EIS	-	[18]
ECM 4	EIS	-	[17]

TABLE II. DEPENDENCIES OF LI-S ECM PARAMETERS

Model type → Dependencies ↓	ECM 1	ECM 2	ECM 3	ECM 4
SOC	[8], [9], [11]	[6], [7], [13]	-	[17]
Temperature	-	[6], [7]	-	-
C-rate	-	[6]	-	-
Cycle	[11], [12]	[7]	[18]	[17]
Calendar	[12]	[14]	-	-

electrolyte resistance, current collectors and cell connections. Moreover, R1-C1 is limited here to express only the charge transfer at the anode surface and the charge transfer of sulfur intermediates is represent by R2-C2. R3-C3 is related to the formation and dissolution of S_8 and Li_2S. In low frequency region, there appear diffusion processes, which are assigned to R4-C4.

Table I summarizes the ECMs, together with their references and parametrization methods. In majority of the cases, an ECM was used for investigation of electrochemical properties of a Li-S cell, if such model was created as a performance/impedance model; it is also mentioned in Table I. As it is shown, only ECM 2 was proposed to function as a performance model and it was also validated [6].

In Table II, there are summarized the dependencies of ECM parameters, which were examined by various researches for the main structures of the ECMs. ECM 2 is the most often investigated circuit, as it includes all parameter dependencies: on state-of-charge (SOC), temperature, C-rate, and age (cycle and calendar).

Based on the literature review, ECM 2 layout appears as the most often used topology for modeling of a Li-S cell. It is followed by ECM 1, which is simplified by removing one R-C element. This reduction can decrease the computation complexity, but as a drawback the obtained model accuracy will be lower. On the other hand, by adding one or two parallel R-C elements, ECM 3 and ECM 4 configurations are obtained, which offer better accuracy at the cost of higher computation demand.

IV. METHODOLOGY

The 3.4 Ah Li-S pouch cell, supplied by OXIS Energy, was placed in a temperature chamber, where it was connected to the Digatron battery test station as shown in Fig. 4. The temperature in the chamber was maintained at 35°C.

A series of tests were applied to the battery cell in order to parametrize the ECM model and to validate it. The discharging cut-off voltage is considered as 1.5 V (SOC=0%) and charging cut-off voltage is 2.45 V (SOC=100%). A general procedure consists of a preconditioning cycle (0.1 C-rate charging (CHA), 0.2 C-rate discharging (DCH)), a capacity check (0.1 C-rate CHA, x C-rate DCH, where x=0.2, 0.35, 0.5, 0.75 and 1.0 C-rate), another nominal cycle and full charging before applying a galvanostatic intermittent titration technique (GITT) [19]. The depth-of-discharge (DOD) steps for the GITT were computed from the measured capacity with a resolution of 2.5% and 5% resolution. The relaxation time between the steps was set to 30 minutes long; exceptions were considered for 0, 5, 10, and 15% DOD where the relaxation times were set to 1.5, 8, 15, and 21 minutes, respectively. This procedure was considered in order to decrease the influence of self-discharge in these low DOD regions.

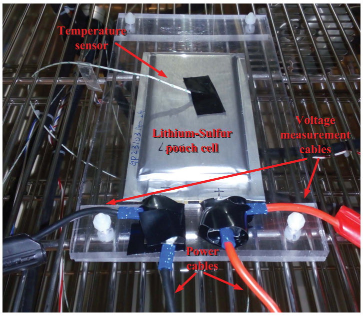

Fig. 4. Illustration of the Li-S battery cell during laboratory measurements.

A. Modeling

The model of the Li-S battery cell was implemented in Simulink according to the procedure discussed in [20]. The OCV and the circuit parameters are implemented as look-up tables, which considers their dependance on C-rate and DOD. For the C-rate dependance, the memory block is applied, which in the case of I=0 A keeps the last used value of C-rate as an input to the look-up tables. The model is considered only for the discharging case and it starts from the fully charged state (100% SOC). The SOC and DOD are calculated as follows:

$$SOC = SOC_{ini} + \int \frac{I \cdot 100}{C_{meas} \cdot 3600} dt, \qquad (1)$$

$$DOD = 100 - SOC, \qquad (2)$$

where SOC is battery state-of-charge in percentage, SOC_{ini} is the initial state-of-charge value, I is the current in Amperes, C_{meas} stands for measured capacity during the capacity check in amper-hours and DOD represents depth-of-discharge in percentage.

B. ECM parametrization and topology comparison

The ECM topology comparison is based on fitting 0.2, 0.5 and 1.0 C-rate GITT measurements separately to the 1-4 R-C ECM topologies. The voltage and current profiles for 0.2 C-rate are presented in Fig. 5. The OCV is derived from the relaxation period: a) from the maximum voltage for low DOD states, where the influence of self-discharge is very pronounced (illustrated in Fig. 5); b) from the voltage after 30 minutes relaxation period for higher DODs where voltage is increasing

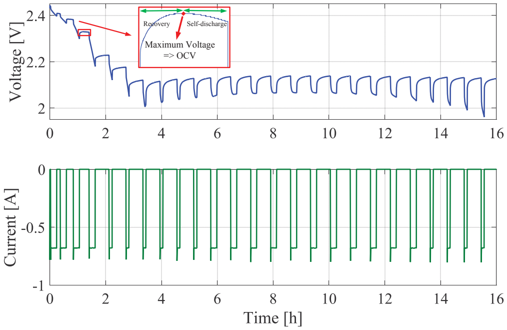

Fig. 5. GITT procedure for discharging of the Li-S cell by 0.2 C-rate [21].

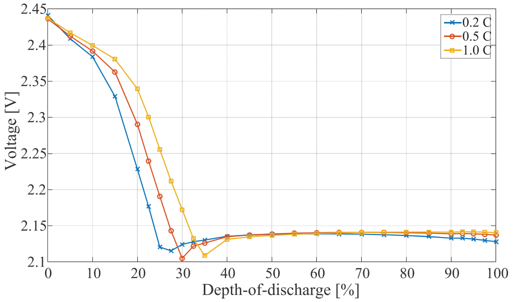

Fig. 6. Open-circuit voltage of the Li-S cell derived from the relaxation voltage of GITT for discharging steps.

during the recovery stage [21]. The obtained OCV curves in function of DOD are shown in Fig. 6.

The ECMs were parametrized following the PT3 technique, presented in [21], since it can be easily and quickly adapted to different number of R-C elements. R0 was determined from the instantaneous voltage drop, which follows after the current interruption as shown in Fig. 7. A least squares method was used to fit the measured relaxation voltage after the instantaneous voltage drop to:

$$V_{fit}(t) = OCV(DOD) - \sum_{i=1}^{n} U_i exp^{-t/\tau_i}, \tag{3}$$

where V_{fit} is the fitted voltage as a function of time t) OCV is the open-circuit voltage in function of DOD, U_i is the polarization voltage and τ_i is the time constant of i-th R-C element. The specific parameters R_i and C_i are extracted through:

$$R_i = \frac{U_i}{I_{cp}(1 - e^{-\frac{t_{cp}}{\tau_i}})}, \tag{4}$$

$$C_i = \frac{\tau_i}{R_i}, \tag{5}$$

where the current pulse amplitude is I_{cp} and duration of the current pulse is t_{cp}.

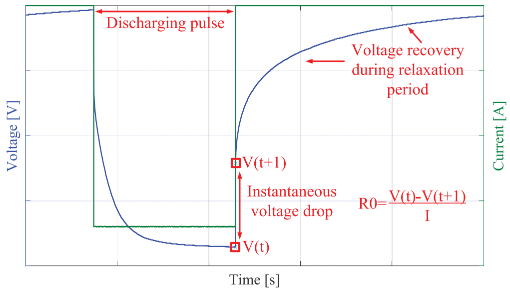

Fig. 7. The current pulse and its voltage response for the Li-S battery.

Finally, the ECM topologies with 1-4 R-C elements were compared by quantifying the sum-of-squared-errors (SSE) obtained during the fitting of relaxation voltage as well as by examining the SSE resulting from the simulation of the GITT profile.

$$SSE = \sum((V_{meas}(t) - V_s(t))^2) \tag{6}$$

where V_{meas} is the voltage profile measured in the laboratory and V_s is the voltage profile obtained from fitting or simulations.

C. The ECM validation

The most suitable ECM topology is selected and used for the model validation. The parameters dependency are integrated for 0.2, 0.5 and 1.0 C-rate. The validation was performed for 0.35 and 0.75 C-rate GITT profiles and the resulting voltage profiles are confronted with the measured ones.

V. RESULTS & DISCUSSION

A. ECM topology comparison

Four topologies with 1-4 R-C elements were parametrized by fitting the relaxation voltage. Afterward, the same current profile, which was applied for GITT procedure in the laboratory, was fed to the model, considering a one-second resolution.

The fitting accuracy of the relaxation voltage had an expected trend with more R-C elements the accuracy is increased. The example of voltage curves for 50% DOD is shown in Fig. 8. By comparing the SSE, which were obtained from fitting, and are summarized in Table III, one can observe that by moving from a 1 R-C ECM to a 2 R-C model, the SSE is reduced by an order of magnitude. By adding the third R-C element, the SSE is reduced nearly two times compared to 2 R-C. Expanding to 4 R-C elements, the model brings only a minor improvement to the fitting accuracy. However, these numbers are related only to fitting of the relaxation voltage after applied pulse.

The current GITT profile was applied to the parametrized models. The resulting voltage curves for the 0.2 C-rate case are presented in Fig. 9. The simulated voltage curves match accurately the voltage during relaxation periods for higher

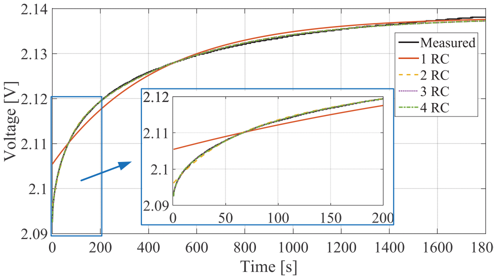

Fig. 8. The comparison of measured and fitted relaxation voltage for 0.2 C-rate at 50% DOD.

TABLE III. THE SSE COMPARISON FOR ECM TOPOLOGIES WITH 1-4 R-C ELEMENTS.

No. of R-C	SSE					
	fitting			GITT simulation		
	0.2 C	0.5 C	1.0 C	0.2 C	0.5 C	1.0 C
1 R-C	0.1736	0.2629	0.3342	7.9736	4.0169	2.9100
2 R-C	0.0181	0.0172	0.0231	1.9371	1.1589	1.5765
3 R-C	0.0095	0.0074	0.0094	0.6586	0.4544	1.2011
4 R-C	0.0093	0.0067	0.0078	3.0521	0.3842	1.2141

DOD states. In the low DOD stages, there is present a self-discharge process, as illustrated in Fig. 5, which was not implemented in the model and thus it caused a voltage estimation error. Nevertheless, the main error appearance is in the voltage response during the current pulse: 1 R-C ECM under-estimated and 4 R-C ECM over-estimated the voltage response. Moreover, the accuracy of 2 R-C element based ECM is reduced at high DOD stages.

The 3 R-C ECM, parametrized by the described method, had the best accuracy in estimating the measured voltage profile. This is reflected as well by SSEs of simulated and measured voltages in Table III, where the 3 R-C ECM has the lowest SSE. The 4 R-C ECM does not bring significant improvement to the model's accuracy and it increases the complexity of the model. The 2 R-C ECM has lower accuracy than the 3 R-C ECM, however if there is a need for low computational requirements, it might be a good trade-off solution. The 1 R-C based ECM simulation has, as expected, the highest SSE.

The 3 R-C ECM was selected for validation. All the derived parameters of the 3 R-C ECM are presented in Fig. 10-16.

B. ECM validation

Simulations with the GITT profiles of 0.35 and 0.75 C-rates, which were not used for parametrization, were performed in order to validate the developed Li-S battery model. The comparison between the measured and estimated voltage profiles is shown in Fig. 17 for the 0.35 C-rate and in Fig. 18 for the 0.75 C-rate. In both cases, the simulated voltage matches well the measured voltage at high DOD stages. However, for early discharge at low DOD there is visible a mismatch, which might be caused by not appropriately derived OCV values for the applied C-rates. This might be the result of not-accurate SOC computing due to the battery high dependance on C-rate, quick self-discharge in low DOD levels, coulombic efficiency farther from 100% or the result of ageing as the tests were done at different battery state-of-health stages. The obtained SSE values for the two validation tests are 3.9754 and 5.1440 for 0.35 and 0.75 C-rate, respectively.

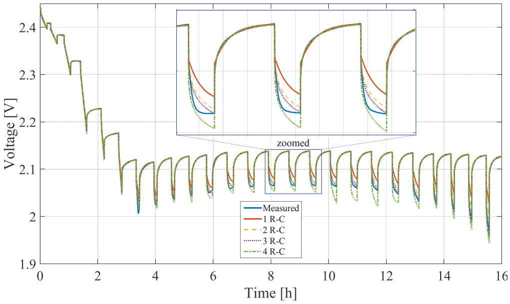

Fig. 9. The comparison of measured and simulated voltage for 0.2 C-rate GITT profile.

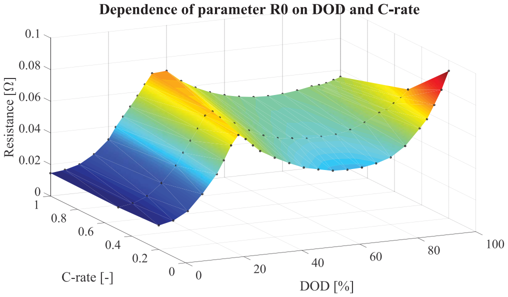

Fig. 10. Parameter R0 dependence on DOD and C-rate.

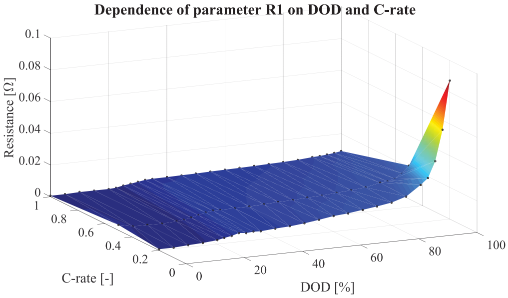

Fig. 11. Parameter R1 dependence on DOD and C-rate.

The ECM of the Li-S battery with 3 R-C elements is considered validated for pulse-discharging operation with short relaxation periods by currents between 0.2 to 1.0 C-rate. The accuracy could be further improved by more consistent test for parametrization, which reduce the effect of ageing and it will include as well available capacity dependence on the applied C-rate. Moreover, including the self-discharge effect into the model would improve the model performance in high SOC stages.

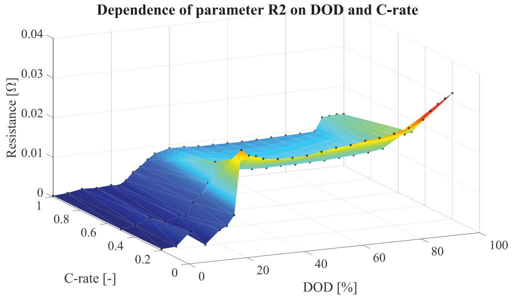

Fig. 12. Parameter R2 dependence on DOD and C-rate.

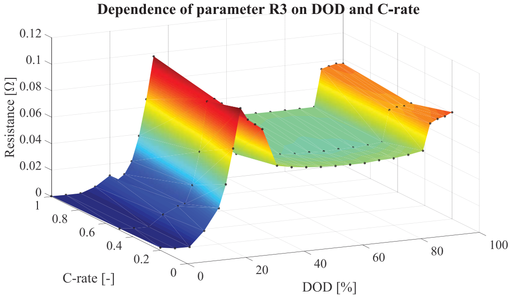

Fig. 13. Parameter R3 dependence on DOD and C-rate.

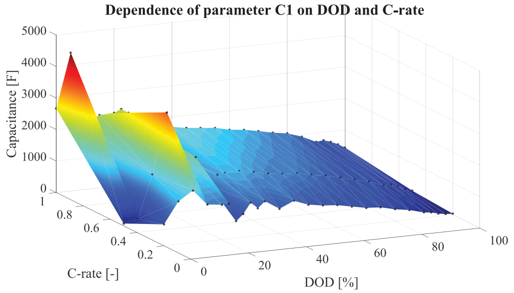

Fig. 14. Parameter C1 dependence on DOD and C-rate.

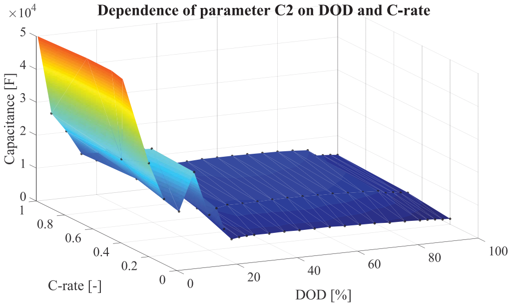

Fig. 15. Parameter C2 dependence on DOD and C-rate.

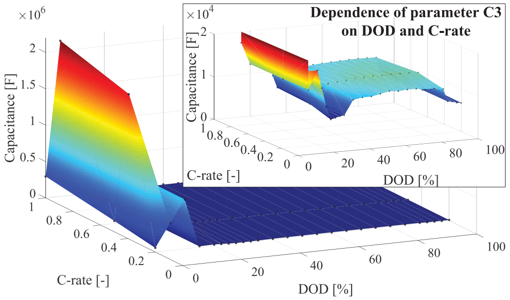

Fig. 16. Parameter C3 dependence on DOD and C-rate.

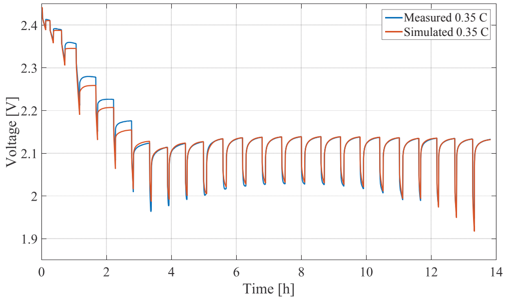

Fig. 17. The comparison of measured and simulated voltage for 0.35 C-rate.

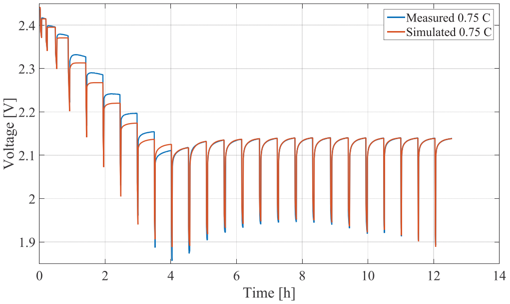

Fig. 18. The comparison of measured and simulated voltage for 0.75 C-rate.

VI. CONCLUSION

Different ECM topologies for the Li-S battery were summarized in this paper, together with their investigated dependencies on DOD and C-rate and the assigned physical meaning of the circuit elements. ECMs composed of one to four R-C elements were parametrized based on laboratory measurements performed on a 3.4 Ah Li-S pouch cell. The same GITT profile, which was used for the parametrization, was used as the input for the model simulation. The error of the fitting and the error from the simulations were evaluated and as the most suitable, the ECM with 3 R-C elements was selected for validation. For the validation process, the profiles from laboratory measurements with 0.35 and 0.75 C-rates were used. The main inaccuracies were caused by the inadequate determination of the OCV curve for the validation C-rates.

Only the discharging mode was implemented to the model. As a future work, the model should include the temperature dependence, be able to operate in charging mode and predict more accurately the response during discharging pulses.

ACKNOWLEDGMENT

This work has been part of the ACEMU-project (1313-00004B). Authors gratefully acknowledge the Danish Council for Strategic Research and EUDP for providing financial support and thank OXIS Energy for supplying the Lithium-Sulfur battery cell.

REFERENCES

[1] D. Bresser, S. Passerini, and B. Scrosati, "Recent progress and remaining challenges in sulfur-based lithium secondary batteries - a review," *Chem. Commun.*, vol. 49, no. 90, pp. 10 545–10 562, Nov. 2013.

[2] X. Hu, S. Li, and H. Peng, "A comparative study of equivalent circuit models for Li-ion batteries," *J. Power Sources*, vol. 198, no. 0, pp. 359 – 367, 2012.

[3] A. Seaman, T.-S. Dao, and J. McPhee, "A survey of mathematics-based equivalent-circuit and electrochemical battery models for hybrid and electric vehicle simulation," *J. Power Sources*, vol. 256, pp. 410–423, Jun. 2014.

[4] M. Einhorn, F. V. Conte *et al.*, "Comparison, selection, and parameterization of electrical battery models for automotive applications," *IEEE Trans. Power Electron.*, vol. 28, no. 3, pp. 1429–1437, 2013.

[5] V. Kolosnitsyn, E. Kuzmina, and E. Karaseva, "On the reasons for low sulphur utilization in the lithium-sulphur batteries," *J. Power Sources*, vol. 274, pp. 203–210, Jan. 2015.

[6] K. Somasundaram, O. Neill, M. Marinescu *et al.*, "Towards an operational model for a Li-S battery," Poster, London, Sep. 2014.

[7] Z. Deng, Z. Zhang *et al.*, "Electrochemical Impedance Spectroscopy Study of a Lithium/Sulfur Battery: Modeling and Analysis of Capacity Fading," *J. Electrochem. Soc.*, vol. 160, no. 4, pp. A553–A558, Jan. 2013.

[8] C. Barchasz, J.-C. Leprêtre *et al.*, "New insights into the limiting parameters of the Li/S rechargeable cell," *J. Power Sources*, vol. 199, pp. 322–330, Feb. 2012.

[9] L. Yuan, X. Qiu, L. Chen, and W. Zhu, "New insight into the discharge process of sulfur cathode by electrochemical impedance spectroscopy," *J. Power Sources*, vol. 189, no. 1, pp. 127–132, Apr. 2009.

[10] Q. Tang, Z. Shan, L. Wang, X. Qin, K. Zhu, J. Tian, and X. Liu, "Nafion coated sulfurcarbon electrode for high performance lithiumsulfur batteries," *J. Power Sources*, vol. 246, pp. 253–259, Jan. 2014.

[11] V. Kolosnitsyn, E. Kuzmina, and S. Mochalov, "Determination of lithium sulphur batteries internal resistance by the pulsed method during galvanostatic cycling," *J. Power Sources*, vol. 252, pp. 28–34, Apr. 2014.

[12] B. H. Jeon, J. H. Yeon, and I. J. Chung, "Preparation and electrical properties of lithium-sulfur-composite polymer batteries," *J. Mater. Process. Technol.*, vol. 143-144, pp. 93–97, Dec. 2003.

[13] V. Kolosnitsyn, E. Kuzmina *et al.*, "A study of the electrochemical processes in lithium-sulphur cells by impedance spectroscopy," *J. Power Sources*, vol. 196, no. 3, pp. 1478–1482, Feb. 2011.

[14] G. Ma, Z. Wen, Q. Wang, C. Shen, J. Jin, and X. Wu, "Enhanced cycle performance of a Li-S battery based on a protected lithium anode," *J. Mater. Chem. A*, vol. 2, no. 45, pp. 19 355–19 359, Sep. 2014.

[15] M. Barghamadi, A. Kapoor, and C. Wen, "A Review on Li-S Batteries as a High Efficiency Rechargeable Lithium Battery," *J. Electrochem. Soc.*, vol. 160, no. 8, pp. A1256–A1263, May 2013.

[16] Y. V. Mikhaylik and J. R. Akridge, "Polysulfide Shuttle Study in the Li/S Battery System," *J. Electrochem. Soc.*, vol. 151, no. 11, p. A1969, 2004.

[17] N. a. Cañas, K. Hirose, B. Pascucci *et al.*, "Investigations of lithium-sulfur batteries using electrochemical impedance spectroscopy," *Electrochim. Acta*, vol. 97, pp. 42–51, May 2013.

[18] J. Zhang, Z. Dong, X. Wang, X. Zhao, J. Tu, Q. Su, and G. Du, "Sulfur nanocrystals anchored graphene composite with highly improved electrochemical performance for lithium-sulfur batteries," *J. Power Sources*, vol. 270, pp. 1–8, Dec. 2014.

[19] Z. Shen, L. Cao, C. D. Rahn, and C.-Y. Wang, "Least Squares Galvanostatic Intermittent Titration Technique (LS-GITT) for Accurate Solid Phase Diffusivity Measurement," *J. Electrochem. Soc.*, vol. 160, no. 10, pp. A1842–A1846, 2013.

[20] L. W. Yao, J. a. Aziz, P. Y. Kong, and N. R. N. Idris, "Modeling of lithium-ion battery using MATLAB/simulink," *IECON Proceedings (Industrial Electronics Conference)*, pp. 1729–1734, 2013.

[21] V. Knap, D.-I. Stroe, R. Teodorescu, M. Swierczynski, and T. Stanciu, "Comparison of Parametrization Techniques for an Electrical Circuit Model of Lithium-Sulfur Batteries," in *Industrial Informatics (INDIN), 2015 13th IEEE International Conference on*, July 2015.

Paper A3

Multi-temperature state-dependent equivalent circuit discharge model for lithium-sulfur batteries

Karsten Propp, Monica Marinescu, Daniel J. Auger, Laura O'Neill, Abbas Fotouhi, Karthik Somasundaram, Gregory J. Offer, Geraint Minton, Stefano Longo, Mark Wild and Vaclav Knap

The paper has been published in the *Journal of Power Sources*, vol. 328, pp. 289–299, 2016, doi:10.1016/j.jpowsour.2016.07.090.

Journal of Power Sources 328 (2016) 289–299

Contents lists available at ScienceDirect

Journal of Power Sources

journal homepage: www.elsevier.com/locate/jpowsour

Multi-temperature state-dependent equivalent circuit discharge model for lithium-sulfur batteries

Karsten Propp [a], Monica Marinescu [b], Daniel J. Auger [a, *], Laura O'Neill [c], Abbas Fotouhi [a], Karthik Somasundaram [c, 1], Gregory J. Offer [b], Geraint Minton [c], Stefano Longo [a], Mark Wild [c], Vaclav Knap [a, 2]

[a] School of Aerospace, Transport and Manufacturing, Cranfield University, College Road, Bedford, MK43 0AL, UK
[b] Department of Mechanical Engineering, Imperial College London, SW7 2AZ, UK
[c] OXIS Energy LTD, E1 Culham Science Centre, Abingdon, OX14 3DB, UK

A R T I C L E I N F O

Article history:
Received 4 May 2016
Received in revised form
11 July 2016
Accepted 23 July 2016

Keywords:
Lithium-sulfur battery
Parameter estimation
System identification
Battery model

A B S T R A C T

Lithium-sulfur (Li-S) batteries are described extensively in the literature, but existing computational models aimed at scientific understanding are too complex for use in applications such as battery management. Computationally simple models are vital for exploitation. This paper proposes a non-linear state-of-charge dependent Li-S equivalent circuit network (ECN) model for a Li-S cell under discharge. Li-S batteries are fundamentally different to Li-ion batteries, and require chemistry-specific models. A new Li-S model is obtained using a 'behavioural' interpretation of the ECN model; as Li-S exhibits a 'steep' open-circuit voltage (OCV) profile at high states-of-charge, identification methods are designed to take into account OCV changes during current pulses. The prediction-error minimization technique is used. The model is parameterized from laboratory experiments using a mixed-size current pulse profile at four temperatures from 10 °C to 50 °C, giving linearized ECN parameters for a range of states-of-charge, currents and temperatures. These are used to create a nonlinear polynomial-based battery model suitable for use in a battery management system. When the model is used to predict the behaviour of a validation data set representing an automotive NEDC driving cycle, the terminal voltage predictions are judged accurate with a root mean square error of 32 mV.

1. Introduction

To increase an acceptance and a demand of electric vehicles (EV's) among the public, there is a need to overcome range anxiety [1]. Since the range of EVs is strongly connected to their energy storage, there is a request for a low cost and safe operating battery with high specific energy. Potentially fulfilling these requirements, the lithium-sulfur (Li-S) chemistry is a prospective replacement of the current lithium-ion (Li-ion) battery technology [2,3]. However, Li-S batteries still suffer from fast degradation and high self discharge [4], which leads the modelling community to be focused on elucidating the complex inner mechanisms governing the cell behaviour. Despite being essential for Li-S technology uptake, operational models and on-line diagnostic tools, capable of predicting and controlling the batteries performance in operation are lacking in the literature. Recently, commercial Li-S cells have become available (e.g. those supplied by OXIS Energy [5], Sion Power, Polyplus), offering the opportunity for application oriented research. In the framework of electric mobility this translates into investigating the cell's performance under the power and temperature demands of an EV [6]. For established battery chemistries, models have been developed, providing varying levels of insight into the cells' internal processes, at varying computational cost [7]. Since the computational power of a typical electronic control unit (ECU) or battery management system (BMS) is limited, simple low-complexity battery models are often needed for application oriented purposes. Examples of such simplified models are equivalent electrical circuit networks (ECN), which reproduce the transient behaviour of a battery with a circuit of electrical components,

---

* Corresponding author.
E-mail address: d.j.auger@cranfield.ac.uk (D.J. Auger).

[1] Permanent address: Department of Chemical and Biomolecular Engineering, National University of Singapore, Singapore.

[2] Permanent address: Department of Energy Technology, Aalborg University, Aalborg, Denmark.

http://dx.doi.org/10.1016/j.jpowsour.2016.07.090
0378-7753/

including resistors, capacitors and a voltage source [8]. The structure of these models is often independent of the cell chemistry, and as such they are not able to give insight into the cell's physical, chemical and electrochemical processes [9]. However, for Li-ion batteries, they have been successfully used for estimating the internal states, such as state of charge (SoC) and measures of battery health such as increase in resistance and decrease in effective capacity [10] (In this paper, only SoC will be considered in detail). Usually they have relatively low computational effort and use easily available measurements like current and terminal voltage. For Li-S batteries ECN models of varying accuracy and complexity have been developed in Ref. [11–14]. These models have been developed for the purpose of analyzing impedance spectroscopy data, such that they describe the cell at a fixed SoC. Because of this they are unsuited to describe performance during cycling. For an OXIS Li-S cell a first operational model including two parallel resistor-capacitor (RC) pairs, has been developed recently with good prediction of the charging process [15]. Furthermore, a comparison of ECN topologies for Li-S batteries in terms of accuracy, and a parameter identification for a three RC model for the same kind of cell were presented in Ref. [16]. In this paper, we introduce the complete framework for developing a Li-S battery model with one RC element, suitable for BMS use, and evaluate its accuracy. Thereby our approach follows the development of a standard ECN model for Li-ion batteries; parametrizing the circuit by fitting pulse discharge data. In order to investigate the temperature dependence of the various circuit parameters for the OXIS Li-S cell, here the parametrization is done for four different temperatures. Also, some of the open questions regarding the suitability of this approach to parametrize the unique properties of Li-S cells are discussed. Therefore we, after a brief introduction into the general requirements for a Li-S battery model (Section 2), (i) use a robust parameter estimation technique developed for Li-S cells, accounting for OCV differences before and after a current pulse (Section 3–4), (ii) apply a novel mixed current pulse test procedure to explore current-dependencies of the model parameters (Section 5), and (iii) identify the cell parameters at four different temperatures (Section 6). The validation of a simplified model is done in Section 7 and Section 8.

2. From Li-ion to Li-S modelling

In the literature, there are many examples of established Li-ion battery models [9,17]. The purpose of one kind, the ECN models, is to predict the output voltage, the available capacity and the degradation at relatively low computational cost [8]. These models are successful enough to be widely used in applications. The main reason for their success is that the intercalation-based chemistry of the Li-ion battery offers a relatively consistent and predictable performance when operated within its limits of charge, temperature and current rates [10]. This is not the case for the Li-S batteries, because they are based on conversion reactions rather than on intercalation. Sulfur reacts with lithium ions when reduced from elemental state S_8, via the intermediates Li_2S_8,Li_2S_4,Li_2S_2, to lithium sulfide Li_2S [18] (Fig. 1), offering theoretically a capacity of 1672 mAh g-1 [19].

However, the practical capacities currently achieved are significantly lower [9,19], mainly due to poor sulfur utilisation and fast degradation [20]. High order polysulfides are highly soluble and reactive [21] in organic electrolytes, while low order polysulfides tend to be insoluble and form an electrically insulating precipitate [4]. The details of the reduction path during discharge are still a matter of ongoing research and are probably more complex [22]. The discharge curve exhibits two regions [23] (Fig. 2): a high plateau at about 2.35 V open circuit voltage (OCV), characterized by the presence of a majority of high order polysulfides in solution (Li_2S_8, Li_2S_6), and a low plateau at around 2.1 V OCV, where lower order chains have been identified (Li_2S_4, Li_2S_3, Li_2S_2), including Li_2S which can precipitate out [24]. With the growing amount of insulating Li_2S_2 and Li_2S, the practical discharge stops at about 1256 mAh g^{-1}, indicated by the increasing cell resistance [25,26]. While charging, the oxidation of low order polysulfides forms high order chains. However, they do not all become elemental sulfur. Highly soluble, high order polysulfides diffuse to the anode and, in contact with its surface, are reduced to lower order chains. These can diffuse back to the cathode, where they are oxidised back to longer chains. This phenomenon, called the polysulfide shuttle [27], can act as overcharge protection [19], but is also responsible for self discharge and poor coulombic efficiency, and associated with capacity fade [27,28].

To identify requirements and challenges towards a fully operational low order Li-S battery model, some Li-ion approaches are listed and examined for their suitability for the Li-S chemistry.

2.1. Voltage curve

The OCV of Li-ion batteries can be measured after some rest time and is sensitive to the SoC [10] and weakly influenced by temperature [29]. Therefore it is usually represented by a variable voltage source with a function or lookup table over SoC, which simplifies the SoC estimation for those batteries [30]. Li-ion has a known predictable and reproducible temperature dependence on OCV. However, lithium sulfur due to the presence of multiple species and multiple reactions between those species has a highly variable and state dependent temperature dependence on OCV, where the state dependence can be a function of the history of the cell going back many cycles. Attempts to model the OCV [31] have been made, but are yet to include the full temperature dependence, which would be necessary to accurately reproduce this effect. Furthermore, in the low plateau, the OCV is not an indication for the SoC since it will always return to about 2.15 V, when given enough

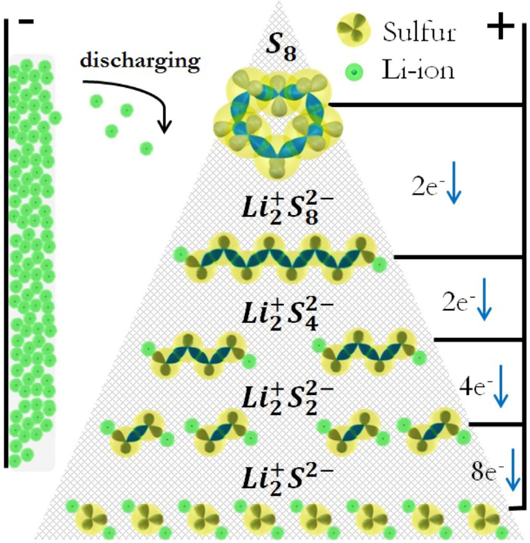

Fig. 1. Work principle of Li-S battery.

time after current is removed. (The time required will depend on the final voltage, but is typically no longer than 2 h) Additionally, the presence of self-discharge and precipitation further complicate the dependence of the rest voltage on the SoC, meaning that it is unclear how one would reliably obtain experimental data for the OCV as a function of the SoC [31]. The transient voltage behaviour of Li-ion batteries are represented by RC circuits, supplemented by parameter-functions for SoC, temperature, current and cycle number. Since the variations of the model parameters for cycle number and currents are usually small [32], they tend to be neglected or simplified [33]. For Li-S batteries the opportunities for these simplifications are unknown for practical BMS applications.

2.2. *Capacity*

To handle variations of the usable capacity in Li-ion cells, a rate factor can be applied [29]. But since the variations of the usable capacity are usually small, they are also handled with the internal resistance, causing the voltage drops to increase with higher rates and therefore cause different SoC's for the same end-of-discharge voltage [33]. For the Li-S batteries however, the amount of sulfur that can be reversibly utilised during a discharge is strongly affected by the current profile, cycling and temperature [34]. Generally high discharge capacity is only obtained at very low rates. High currents can produce a resistive layer on the cathode, hindering the utilisation of the underlying sulfur [23], leading to strong changes in the usable capacity. Cell operation for optimal utilisation of sulfur remains a challenge and is still a matter of ongoing research [11,19,35].

2.3. *Power capability*

For Li-ion batteries the power limitations are governed by the diffusion of ions into the electrodes, which is mainly defined by the battery design [36] and therefore not considered to vary rapidly with normal usage. For Li-S batteries, the specific factors limiting rate capability during operation are unknown. Slow diffusion of species through the electrolyte, bottlenecks in the electrochemical reaction pathway, and reduced availability of active surfaces are some of the possible reasons for power limitation. Generally, the polysulfide kinetics in the high plateau region are fast, leading to good rate capabilities and low cell resistance. However, the high plateau usually accounts for merely 10%–30% of a cycled cell's capacity [37]. At the boundary between the two plateaus a peak in cell resistance is observed, possibly caused by an increase in electrolyte viscosity, due to a high concentration of dissolved polysulfides. A further increase in the resistance at the end of the discharge is associated with precipitation of lower order polysulfides, leading to a decrease in the availability of both active species and active surface area. The operating temperature does impact power capability, for Li-S as well as for Li-ion cells, as lower temperatures lead to slower diffusion and lower reaction rates. However the potential for Li-S batteries to work in cold environments is seen as greater [37]

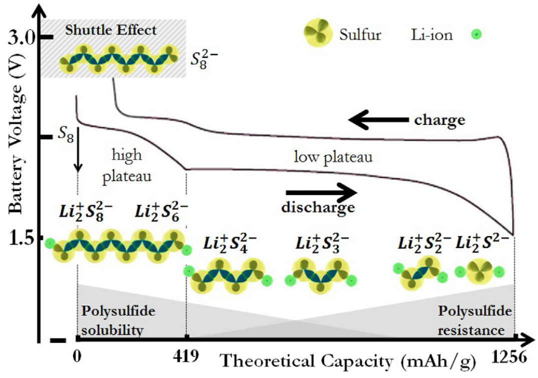

Fig. 2. Basic voltage behaviour Li-S battery.

2.4. *Degradation*

For Li-ion the major degradation modes in ECN models are the decreasing rate capability and capacity fade, caused by parasitic reactions at the anode, leading to a growth of the solid-electrolyte interphase (SEI) [38], and the consumption of active material [39]. For Li-S batteries, the degradation modes are not well known [22], and it is unclear which lead to reversible and which to irreversible degradation. Probable causes include the irreversible growth of insulating layers on the anode [40] and possibly cathode, and the associated loss in active material [41]. Much of the degradation is believed to be related to the polysulfide shuttle. In order to prevent it, overcharging is generally avoided, despite not being a safety issue in comparison to Li-ion chemistries.

The comparison shows that the Li-S chemistry is more complex in its reactions as well as the electrical behaviour than current Li-ion batteries. The unique Li-S features, (i) two regions with different properties, (ii) a flat voltage profile, (iii) self discharge mechanism during charging, (vi) high sensitivity of the usable capacity and power to cycling parameters such as current profile or temperatures, indicate a higher effort towards an application oriented model. It is not clear yet, how accurately these effects have to be represented for future Li-S BMS systems.

3. Parameter identification

There are many techniques for system identification, but a good ‘industry standard’ is prediction-error minimization (PEM), a full description of which can be found in Ljung's seminal work on system identification [42]. The key concept behind PEM is that of the ‘prediction error’, which is estimated based on recorded observations, describing the model

$$y(t) = G(q,\theta)u(t) + H(q,\theta)e(t) \tag{1}$$

as a predictor of the next output. Where G represents the transfer function, q the forward shift operator, $H(q,\theta)e(t)$ the disturbance of the system and θ is a parameter vector. The parameter vector consists of the unknown model parameters: for an ECN model, for example, it might be electrical component values. In system identification, a metric is defined, usually as a mathematical norm, such as the 'prediction error' $\varepsilon(t,\theta)$ between the measured data $y(t)$ and the model prediction $\widehat{y}(t)$ is used; an identification algorithm seeks to minimize this norm, and the minimizing parameter vector, denoted θ_N, gives the best fit.

$$\varepsilon(t,\theta) = y(t) - \widehat{y}(t|\theta) \tag{2}$$

The prediction error minimization algorithm uses numerical optimization to minimize the cost function $V_N(\theta)$, a weighted norm of the prediction error, e.g.

$$\theta_N = \arg\min V_N(\theta) = \arg\min \left|\left|\varepsilon(t,\theta)\right|\right|_2^2 \tag{3}$$

Usually the cost function includes the number of the data samples and becomes more accurate for larger values. PEM system identification is applied to each current pulse individually. To get an accurate result, the estimation window was set to 300 s before and after each pulse.

4. Battery model set

The quality of the identification strongly depends on the model set. In this section, a new linearized version of a nonlinear SoC-dependent ECN model is presented. First, a Thevenin model [43,44] (Fig. 3) is expressed in terms of its parameter dependence on SoC. The model is then reparameterized in terms of 'behaviour', rather than component values. The model is then linearized in a way that captures the dependence of the model behaviour on changing state of charge. This parameterization provides a number of benefits over a standard ECN model:

(i) The application of constraints to behaviours is possible, which makes it possible to relate constraints to observed behaviours; without a behavioural parameterization, such parameterizations are less straightforward. (Dynamic bandwidth, for example, is a function of two equivalent circuit parameters in an *RC* pair; in the new parameterization, it is a single behavioural parameter.)

(ii) The linearized form of the model explicitly captures terms relating to short-term changes in dynamic behaviour due to changes in ECN parameters caused by changing SoC. (In conventional ECN models, parameters are usually assumed constant over a short time period, but this can cause problems when the SoC has a significant short-term effect, e.g. a noticeable change in OCV during a system identification experiment.

These benefits make the model suitable for system identification tests such as those conducted in this study.

This work differs from the 'cyclic resistometry' analytical parameter technique [45] in that where cyclic resistometry attempts to measure a single physical parameter — the electrode resistance — with a series of high-frequency pulses, the techniques of this paper simultaneously identifies all ECN parameters with a 'behavioural' rather than physical interpretation.

4.1. State-of-charge—dependent 'Thevenin' model

4.1.1. Basic model equations

Consider a generic Thevenin model with ECN parameter dependence on SoC X—this is a capital 'χ' not a capital 'x'. Following common practice, the current I_L is treated as the input and the load voltage is taken as the output. Using the symbolic notation of Fig. 3, the output equation is

$$U_L = h_{U_L}(X, U_p, I_L) \tag{4}$$

where

$$h_{U_L}(X, U_p, I_L) = U_{oc}(X) - U_p - R_o(X) I_L. \tag{5}$$

The system has two dynamic states: state-of-charge, X, and 'capacitor' voltage U_p. The state derivatives are given by

$$\dot{X} = f_X(I_L) = -\frac{1}{Q_{cap}} I_L \tag{6}$$

where Q_{cap} is the capacity (in coulombs) of the battery or cell under consideration, and

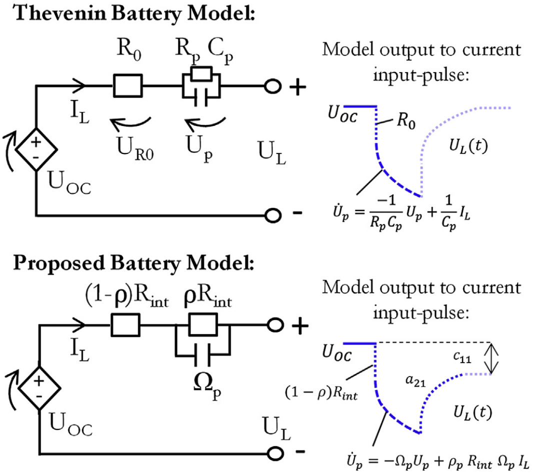

Fig. 3. Response of the Thevenin and behavioural battery model to a current pulse. (Details of the pulses used are given in Section 5).

$$\dot{U}_p = f_{\dot{U}_p}(X, U_p, I_L) \tag{7}$$

where

$$f_{\dot{U}_p}(X, U_p, I_L) = -\frac{1}{R_p(X)C_p(X)} U_p + \frac{1}{C_p(X)} I_L \tag{8}$$

4.1.2. Behavioural reparameterization

The ECN model expressed above is perhaps a little cumbersome. During system identification, it is often desirable to constrain parameter searches to sensible ranges. In battery identification, the operator will be particularly concerned to see how well steady-state model behaviour matches reality, what the bandwidth (or time constant) of the model is, and how much of the response is (as far as can be observed) instantaneous and how much lags. It is important not to lose sight of the fact that ECN models were chosen because their *behaviour* represents observed cell behaviour, not because there is a particular physical significance to the circuit elements employed.

Our circuit can be made more intuitive by working in terms of some new 'behavioural' variables:

$$\Omega_p(X) = \frac{1}{R_p(X)C_p(X)} \tag{9}$$

$$R_{int}(X) = R_o(X) + R_p(X) \tag{10}$$

$$\rho_p(X) = \frac{R_p(X)}{R_{int}(X)} \tag{11}$$

Here, Ω_p represents the dynamic bandwidth described by R_p and C_p. R_{int} is the total steady-state resistance, and effectively governs the 'settled' voltage drop due to a constant current. ρ_p represents the 'dynamic fraction' of the response: when ρ_p is zero, the voltage response is wholly instantaneous, and when ρ_p is one, the response is wholly dynamic. Using this parameterization, it is relatively easy to write down behavioural constraints, e.g.

$$\begin{aligned}\Omega_p(X) &\in [\Omega_{\min}, \Omega_{\max}]\\ R_{int}(X) &> 0\\ \rho_p(X) &\in [0, 1]\end{aligned} \tag{12}$$

The output function and state derivative functions can be rewritten in terms of the new parameterization:

$$h_{U_L} = U_{oc}(X) - U_p - \left(1 - \rho_p(X)\right) R_{int}(X) I_L \tag{13}$$

$$f_X = -\frac{1}{Q_{cap}} I_L \tag{14}$$

$$f_{\dot{U}_p} = -\Omega_p(X) U_p + \rho_p(X) R_{int}(X) \Omega_p(X) I_L \tag{15}$$

This parameterization of the model is numerically identical to the original ECN model, but there are no longer any 'reciprocal' parameters and the application of parameter constraints is straightforward and intuitive. Giving a set behavioural parameters it is of course straightforward to map these back to 'conventional' ECN parameters noting that

$$R_p(X) = \rho_p(X) R_{int}(X), \tag{16}$$

$$R_o(X) = R_{int}(X) - R_p(X) \tag{17}$$

and

$$C_p(X) = \frac{1}{R_p(X)\Omega_p(X)}. \tag{18}$$

4.2. Linearized cell model

4.2.1. Motivations for linearization

For system identification, it is common to use linearized models. In many practical approaches, it is assumed that state-dependent parameters vary sufficiently slowly to be treated as constants, and the nonlinear ECN model is effectively used as a linear model with 'frozen' SoC. Unfortunately, this does not always work. When a battery or cell is subject to a high-current discharge pulse, the change in SoC can be sufficient to cause a drop in the OCV between the start and the end of the pulse (as depicted in Figs. 3 and 4). This does not fit well with the linear model. One way to get round this in practice is subtract a voltage term representing the drop on U_{OC} caused by a change in SoC. More formally, a full linearization of the nonlinear model can be performed. When this is done, it will be seen that the nonlinear model contains all the expected 'ECN terms' but also two additional terms that we might perhaps not have expected. This is shown in the following sections.

4.2.2. Definition of operating point

The first step in the linearization process is to define an operating point. In this case, the dynamic state pair $\overline{X}, \overline{U}_L$ will be assumed. The nominal input is current, chosen such that $\dot{U}_L = 0$:

$$\overline{I}_L = \overline{U}_p / \overline{X} \tag{19}$$

and the nominal output is

$$\overline{U}_L = U_{oc}(\overline{X}) - \overline{U}_p - \left(1 - \rho_p(\overline{X})\right) R_{int}(\overline{X}) \overline{I}_L. \tag{20}$$

(Usually, operating points are chosen to represent equilibria. The operating point that has been chosen here is not strictly-speaking an equilibrium unless $\overline{I}_L = 0$ since in general $\dot{X} \neq 0$. But that does not matter: the mathematics holds regardless.)

As a next step, variables describing perturbations from nominal values are defined:

$$\begin{aligned}\widehat{u}_L &= U_L - \overline{U}_L,\\ \widehat{i}_L &= I_L - \overline{I}_L,\\ \widehat{\chi} &= X - \overline{X},\\ \widehat{u}_p &= U_p - \overline{U}_p.\end{aligned} \tag{21}$$

This allows us to express what is essentially a 'small-signal' model, though such terms are rarely used in the formal language of control theory.

4.2.3. Linear state-space representation

We can define a state vector

$$\widehat{\mathbf{x}} = [\,\widehat{\chi} \quad \widehat{u}_p\,]^T \tag{22}$$

and form a linearized model:

$$\widehat{u}_L \approx \underbrace{\begin{bmatrix} \frac{\partial h_{U_L}}{\partial X} & \frac{\partial h_{U_L}}{\partial U_p} \end{bmatrix}}_{\mathbf{c}^T} \widehat{\mathbf{x}} + \underbrace{\frac{\partial h_{U_p}}{\partial I_L}}_{D} \widehat{\imath}_L \tag{23}$$

$$\dot{\widehat{\mathbf{x}}} \approx \underbrace{\begin{bmatrix} \frac{\partial f_X}{\partial X} & \frac{\partial f_X}{\partial U_p} \\ \frac{\partial f_{U_p}}{\partial X} & \frac{\partial f_{U_p}}{\partial U_p} \end{bmatrix}}_{\mathbf{A}} \widehat{\mathbf{x}} + \underbrace{\begin{bmatrix} \frac{\partial f_X}{\partial I_L} \\ \frac{\partial f_{U_p}}{\partial I_L} \end{bmatrix}}_{\mathbf{b}} \widehat{\imath}_L \tag{24}$$

The terms of $\mathbf{c}^T$ are

$$\frac{\partial h_{U_L}}{\partial X} = \frac{\partial U_{oc}}{\partial X} + R_{int} I_L \frac{\partial \rho_p}{\partial X} - \left(1 - \rho_p\right) I_L \frac{\partial R_{int}}{\partial X} \tag{25}$$

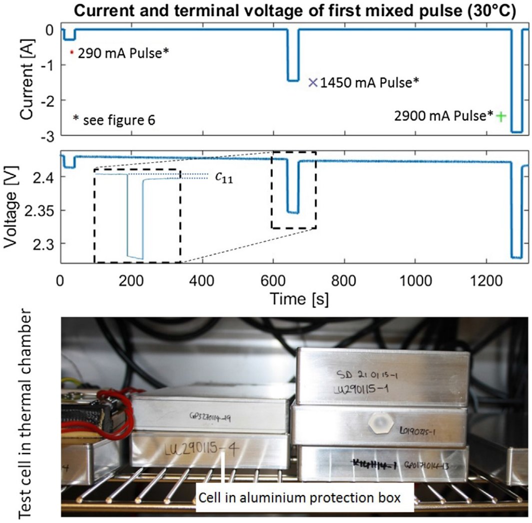

Fig. 4. Mixed pulse discharge and test installation.

$$\frac{\partial h_{U_\mathrm{L}}}{\partial U_\mathrm{p}} = -1, \tag{26}$$

the term of **D** is

$$\frac{\partial h_{U_\mathrm{L}}}{\partial I_\mathrm{L}} = -\left(1-\rho_\mathrm{p}\right)R_\mathrm{int}, \tag{27}$$

the terms of **A** are

$$\frac{\partial f_X}{\partial X} = 0, \tag{28}$$

$$\frac{\partial f_X}{\partial U_\mathrm{p}} = 0, \tag{29}$$

$$\begin{aligned}\frac{\partial f_{U_\mathrm{p}}}{\partial X} = \left(\rho_\mathrm{p}R_\mathrm{int}I_\mathrm{L} - U_\mathrm{p}\right)\frac{\partial \Omega_\mathrm{p}}{\partial X} + R_\mathrm{int}\Omega_\mathrm{p}I_\mathrm{L}\frac{\partial \rho_\mathrm{p}}{\partial X}\\ +\rho_\mathrm{p}\Omega_\mathrm{p}I_\mathrm{L}\frac{\partial R_\mathrm{int}}{\partial X},\end{aligned} \tag{30}$$

$$\frac{\partial f_{U_\mathrm{p}}}{\partial U_\mathrm{p}} = -\Omega_p, \tag{31}$$

and the terms of $\mathbf{b}^\mathrm{T}$ are

$$\frac{\partial f_X}{\partial I_\mathrm{p}} = -\frac{1}{Q_\mathrm{cap}}, \tag{32}$$

$$\frac{\partial U_\mathrm{p}}{\partial I_\mathrm{p}} = \rho_\mathrm{p}R_\mathrm{int}\Omega_\mathrm{p}. \tag{33}$$

We can therefore write:

$$\widehat{u}_\mathrm{L} \approx \underbrace{\begin{bmatrix} c_{11} & -1 \end{bmatrix}}_{\mathbf{c}^\mathrm{T}} \widehat{\mathbf{x}} + \underbrace{\left(1-\rho_\mathrm{p}\right)R_\mathrm{int}}_{D} \,\widehat{\imath}_\mathrm{L} \tag{34}$$

$$\dot{\widehat{\mathbf{x}}} \approx \underbrace{\begin{bmatrix} 0 & 0 \\ a_{21} & -\Omega_\mathrm{p} \end{bmatrix}}_{\mathbf{A}} \widehat{\mathbf{x}} + \underbrace{\begin{bmatrix} -\dfrac{1}{Q_\mathrm{cap}} \\ \rho_\mathrm{p}R_\mathrm{int}\Omega_\mathrm{p} \end{bmatrix}}_{\mathbf{b}} \widehat{\imath}_\mathrm{L}. \tag{35}$$

An important thing to note here is that there are two terms in these matrices that we might not intuitively expect if we were simply writing down the equations for an ECN circuit: c_{11} which relates changes in SoC to the open circuit voltage, and a_{21} which relates changes in SoC to the capacitor voltage.

As a final step, we can apply a state transformation:

$$\widehat{\mathbf{x}} = \underbrace{\begin{bmatrix} Q_\mathrm{cap}^{-1} & 0 \\ 0 & 1 \end{bmatrix}}_{\mathbf{T}^{-1}} \widehat{\mathbf{z}} \qquad \text{i.e.} \qquad \widehat{\mathbf{z}} = \begin{bmatrix} Q_\mathrm{cap}\widehat{\chi} \\ \widehat{u}_\mathrm{p} \end{bmatrix}$$

This yields

$$\widehat{u}_\mathrm{L} = \underbrace{\begin{bmatrix} c'_{11} & -1 \end{bmatrix}}_{\mathbf{c}_\mathbf{z}^\mathrm{T}=\mathbf{c}^\mathrm{T}\mathbf{T}^{-1}} \widehat{\mathbf{z}} + \underbrace{\left(1-\rho_\mathrm{p}\right)R_\mathrm{int}}_{D} \,\widehat{\imath}_\mathrm{L} \tag{36}$$

$$\dot{\widehat{\mathbf{z}}} \approx \underbrace{\begin{bmatrix} 0 & 0 \\ a'_{21} & -\Omega_\mathrm{p} \end{bmatrix}}_{\mathbf{A}_\mathbf{z}=\mathbf{TAT}^{-1}} \widehat{\mathbf{z}} + \underbrace{\begin{bmatrix} -1 \\ \rho_\mathrm{p}R_\mathrm{int}\Omega_\mathrm{p} \end{bmatrix}}_{\mathbf{b}_\mathbf{z}=\mathbf{Tb}} \widehat{\imath}_\mathrm{L}. \tag{37}$$

In this form, the model lends itself well to system identification. As well as the core behavioural equivalent circuit parameters U_oc, R_int, ρ_p and Ω_p—which also give R_o, R_p and C_p—there are two ‘free’ parameters c'_{11} and a'_{21} that can accommodate parameter changes within a system identification data set caused by c'_{11}. For the purposes of this study, it has been assumed that the effect of SoC on OCV is the dominant distorting effect, as it can be seen from the data that U_oc changes between the start and end of a pulse (Fig. 4). Accordingly, a'_{21} has been assumed small, but c'_{11} has been accommodated in system identification.

5. Experimental design

The battery model parameters are identified through discharge tests within temperatures from 10 °C to 50 °C. To identify the current dependencies of the model parameters without potential ageing effects, the cells were tested with current pulses of 290 mA, 1450 mA and 2900 mA with a 10 min resting time in between (Fig. 4). The measurement procedure contained pre-cycled (C/10 charge, C/5 discharge, 30 °C) 3.4 Ah long-life chemistry pouch cells from OXIS Energy, following their recommended voltage range between 2.45 V, when the battery is fully charged (SoC = 100%), and 1.5 V, when the battery is fully discharged (SoC = 0%). We have taken a practical definition of state-of-charge, essentially ‘remaining capacity’, and we have defined the end point of the test as the first instant at which the terminal voltage reaches 1.5 V, in line with the manufacturer's recommondation.

The test hardware included a Maccor 4000 battery tester with cells constantly held at temperature in sealed aluminium boxes with a Binder KB53 thermal chamber, also shown in Fig. 4.

6. Identification results

Since the tested cells are not mass produced, deviations in their discharge capacity or parameters are possible (see Table 1).

Therefore the identification has been done with two cells respectively. But since the identified parameters follow the same pattern, only the results for cell one are presented.

The identification results for the model parameters are repeated over the whole discharge range for each current pulse individually, by calculating the SoC from the integrated current, the discharge capacity of the cycle, and the assumption of an initially fully charged battery (Fig. 5). (In this work SoC is a dimensionless variable, with 0 representing fully discharged and 1 representing fully charged, following the pattern in Ref. [10].)

$$X = X_{(0)} - \frac{1}{3600Q_\mathrm{cap}}\int_0^t i(\tau)d\tau. \tag{38}$$

The average SoC is assigned for each pulse respectively by using its the start- and end-value of the SoC estimation

$$X_\mathrm{pulse} = 0.5(X_\mathrm{start} + X_\mathrm{end}). \tag{39}$$

Fig. 6 shows the identification results for each pulse over SoC, emphasising the current dependencies of the parameters. Generally the results corresponds well with previous studies. The peak of R_0 between both voltage plateaus, also reported in Ref. [22], is associated with the increased viscosity and therefore resistance of the electrolyte, due to the maximum of dissolved polysulfides in the electrolyte at this point [46]. Also due to the electrolytes conductivity, a slight increase of the internal resistance with lower temperatures is reported for a fully charged cell [12]. Additionally shown here is the less pronounced peak for the internal resistance

Table 1
Capacities of test cells.

Temperature	Test cell 1	Test cell 2
10 °C	0.67 Ah	0.68 Ah
20 °C	2.72 Ah	2.79 Ah
30 °C	2.83 Ah	2.79 Ah
50 °C	3.02 Ah	3.03 Ah

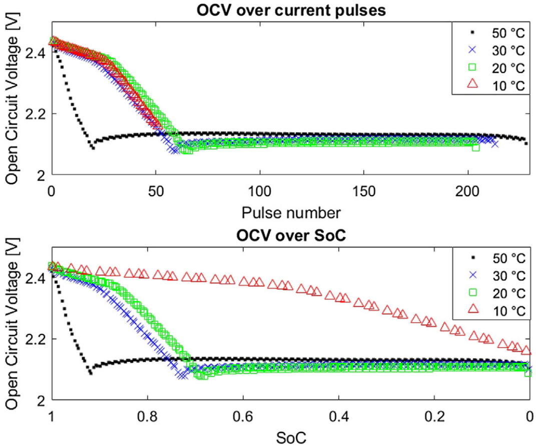

Fig. 5. Identification results for U_{OC} over Pulse and SoC.

with higher temperatures, presumable caused by the lower electrolyte viscosity. While the internal resistance and double layer capacitance vary only weakly with different rates, the charge transfer resistance R_p differs noticeably. R_p with its similar appearance than R_0 for low currents, is mostly assigned to the thickness of the Li_2S film on the anode, which depends, since high order lithium polysulfides are involved into the re-dissolution of the film, on the amount of dissolved polysulfides. Furthermore the films conductivity, depending on its surface morphology and the viscosity of electrolyte, matters [47]. The latter is likely due to the also occurring less pronounced peak with higher temperatures. With lower temperatures the usable capacity decreases (see Table 1), even when the high plateau can deliver slightly more energy due to a less pronounced shuttle effect. When the temperature gets too low, the increased internal resistance of the cell causes a deeper voltage drop. In our case, by applying discharge currents as 2900 mA, the discharging cut-off voltage of 1.5 V is reached before the beginning of the low voltage plateau. Therefore the usable capacity drops more significantly than reported in Refs. [37,48], which is mainly due to our test pattern and the higher current pulses we use.

7. Model derivation

The derived Li-S cell model excludes the identified parameters for 10 °C due to their large differences to the values of higher temperatures. Therefore, it was skipped for now and is going to be explored more in detail in the future research. It should be noted that temperature is to be used as a constant parameter in this model. Using it as a dynamic fast-varying input may produce unexpected results. (A full electrochemical model would be needed to address this.) The model from 20 °C to 50 °C uses the general state-space representation

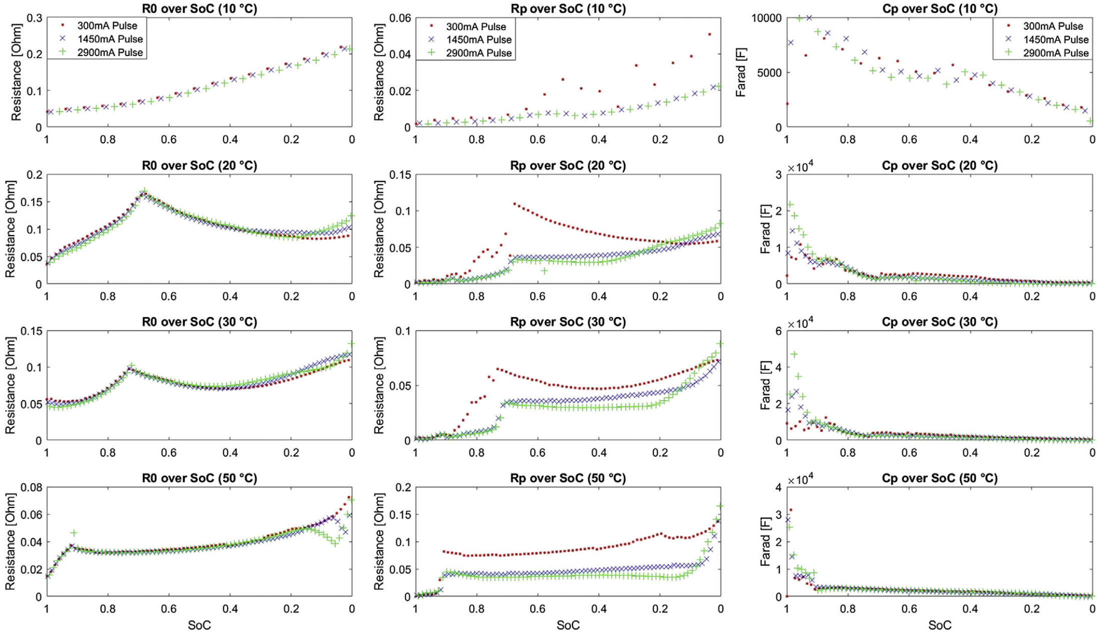

Fig. 6. Identification results for R_0, R_p and C_p for each current pulse respectively.

Table 2
Parameter functions.

Function	T	p_{10}	p_9	p_8	p_7	p_6	p_5	p_4	p_3	p_2	p_1
$f_{UOC-\text{high}}$	20					108.1	−361.13	444.73	−238.18	47.03	1.88
	30					100.81	−351.59	452.99	−254.35	52.66	1.92
	50					19.53	−47.78	43.08	−15.5	1	2.1
$f_{UOC-\text{low}}$	20		−752.62	2085.66	−2392.87	1466.98	−517.42	105.21	−11.69	0.62	2.1
	30		−705.23	1997.24	−2329.9	1445.3	−513.3	104.5	−11.55	0.614	2.1
	50		50.49	−170.36	226.3	−147.74	46.17	−3.8	−1.34	0.32	2.11
$f_{\text{R0}-\text{high}}$	20				−1300.2	6470.07	−13362.95	14656.94	−9000.23	2931.67	−395.24
	30				1408.02	−7176.99	15213.74	−17168.84	10880.87	−3673.08	516.32
	50				29.22	−98.6	122.81	−67.96	15.53	−1.06	0.07
$f_{\text{R0}-\text{low}}$	20				12.96	−28.54	25.46	−11.65	3.09	−0.42	0.11
	30				14.05	−32.34	28.45	−11.77	2.5	−0.38	0.123
	50				3.597	−9.988	10.631	−5.419	1.393	−0.216	0.063
$f_{R\text{p}}$	20	140.636	−613.186	1088.525	−1005.911	512.386	−139.174	16.887	−0.011	−0.223	0.074
	30	102.35	−489.63	968.695	−1024.135	624.963	−222.05	43.585	−3.75	−0.11	0.08
	50	270.48	−1110.38	1837.41	−1538.71	643.71	−80.4	−34.99	14.73	−2.02	0.16
$f_{C\text{p}}$	20					89414.28	−113090.73	25401.28	15392.5	−3017.3	306.23
	30					237957.9	−384453.35	193837.3	−27322.65	2574.15	216.5
	50					373976.04	−799532.2	605077.98	−193678.92	27646.74	−617.5

$$\begin{aligned}\dot{x}(t) &= \mathbf{A}(t)x(t)+\mathbf{B}(t)u(t)\\ y(t) &= \mathbf{C}(t)x(t)+\mathbf{D}(t)u(t)\end{aligned} \tag{40}$$

with added functions for the parameter-variations over the SoC. The usage of functions instead of lookup tables is due to one intended model purpose, the state estimation. The first state in $x = [x_1 x_2]^T$ represents the SoC (X), while the second state represents the transient voltage over the RC circuit (U_p).

$$\mathbf{A} = \begin{bmatrix} 0 & 0 \\ 0 & \dfrac{-1}{f_{R_\text{p}}(X) * f_{C_\text{p}}(X)} \end{bmatrix} \quad \mathbf{B} = \begin{bmatrix} \dfrac{-1}{3600Q_\text{cap}} \\ \dfrac{1}{f_{C_\text{p}}(X)} \end{bmatrix} \tag{41}$$

$$\mathbf{C} = \begin{bmatrix} f_{U_\text{OC}}(X) & -1 \end{bmatrix} \quad \mathbf{D} = \begin{bmatrix} f_{R_0}(X) \end{bmatrix}$$

The relationships between the model parameters and the SoC are handled with fitted polynomials,

$$\begin{aligned} f_\text{parameter}(X) = p_{10}x_1^9 + p_9x_1^8 + p_8x_1^7 + p_7x_1^6 + p_6x_1^5 \\ + p_5x_1^4 + p_4x_1^3 + p_3x_1^2 + p_2x_1 + p_1 \end{aligned} \tag{42}$$

shown in the matrices A to D, with parameters p_1 to p_{10}. The parameter values are identified by minimizing the squared error between function and identification results with MATLAB [49] for each temperature respectively and summarized in Table 2. As shown in Section 2 and 6, the parameters of Li-S chemistry vary in their patterns between the high and low plateau. While it is theoretically possible to represent this behaviour with a single polynomial function, the needed degree for a good quality fit would be high. To avoid this without neglecting accuracy, polynomial functions for U_OC and R_0 are determined for each plateau separately and combined smoothly and differentiable via a partial sinusoidal function γ.

$$\gamma_{\text{m,c}}(X) := \begin{cases} 0, & \text{if a} \\ \dfrac{1}{2} + \dfrac{1}{2}\sin(2m(X-c)), & \text{if b} \\ 1, & \text{if c} \end{cases} \tag{43}$$

Where the conditions a,b,c stands for the different ranges of the function,

$$\begin{aligned} &\text{a}: 2m(X-c) < -\frac{1}{2}\pi, \\ &\text{b}: -\frac{1}{2}\pi \le 2m(X-c) < \frac{1}{2}\pi, \\ &\text{c}: 2m(X-c) > \frac{1}{2}\pi, \end{aligned} \tag{44}$$

and m is a scaling factor, determining the transition range between both polynomials. The transition point between both functions is

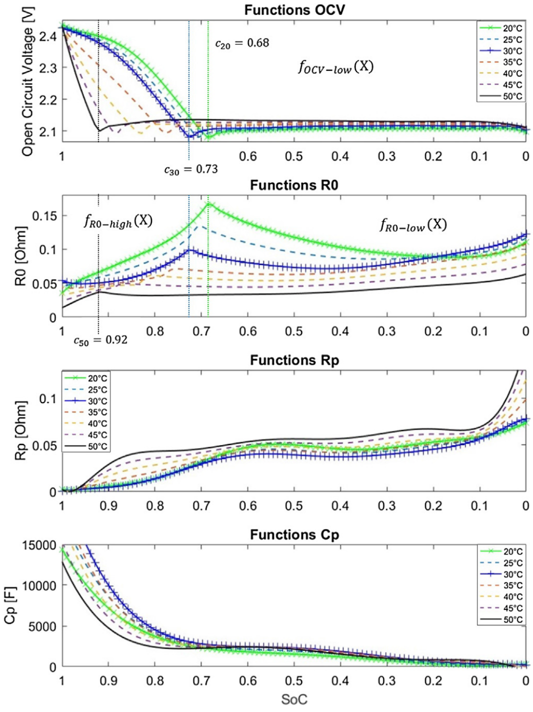

Fig. 7. Parameter functions for U_OC, R_0, R_p and C_p over SoC.

determined by c, which leads to the combined function for both polynomials:

$$f_{U_{OC}}(X) = \left(1-\gamma_{m,c}(X)\right)\ f_{U_{OC-low}}(X) \\ +\gamma_{m,c}(X) f_{U_{OC-high}}(X) \tag{45}$$

Equally the combined function for R_0 is determined, also using the same γ and c values.

$$f_{R0}(X) = \left(1-\gamma_{m,c}(X)\right) f_{R0-low}(X) \\ +\gamma_{m,c}(X)\ \ f_{R0-high}(X). \tag{46}$$

Since the variations between both plateaus are less pronounced for C_p and less consistent for R_p, the functions for these parameters are only determined with a single polynomial respectively. This decision also simplifies the estimation of the Jacobian matrix of A with foresight to a Kalman filter type state estimation. A further simplification is fitting the polynomial to all pulses, ignoring the discharge current induced fluctuations of R_p. Therefore the effects of different discharge currents have not been properly represented yet. Fig. 7 shows the resulting model parameters calculated from the polynomial functions, together with the transition points (c_{20}=0.68,c_{30}=0.73,c_{50}=0.92) for 20 °C, 30 °C and 50 °C. It is easy to spot that the variations between the temperatures changes the battery behaviour significantly. The data suggest that for an interpolation between different temperatures not only the cell capacity Q_{Cap} and the transition points c must be accounted for, but also the shape of the polynomial functions itself. Instead of using a two dimensional lookup table to cover for these variations, here the polynomial factors themselves are the subject of interpolation.

Each factor is interpolated linearly between 20 °C, 30 °C and 50 °C, leading to a 3×3 one dimensional lookup table for each factor of the polynomial. The values of the lookup tables are given in Table 2.

The intended outcome of this method is to change the shape of the parameter functions without influencing their derivability and avoiding the complexity of a two dimensional surface function. Therefore the presented model can be used for Kalman filter types of estimation [50]. The dotted lines in Fig. 7 represent these interpolated functions in 5 °C intervals, only using the linear interpolation of p_1 to p_{10} and the transition points c. For the sake of completeness however, it must be mentioned that due to the lack of experimental data for 40 °C the polynomials and transition points between 30 °C and 50 °C had been manually tweaked.

8. Model validation

To test the model for real life applications another OXIS pouch

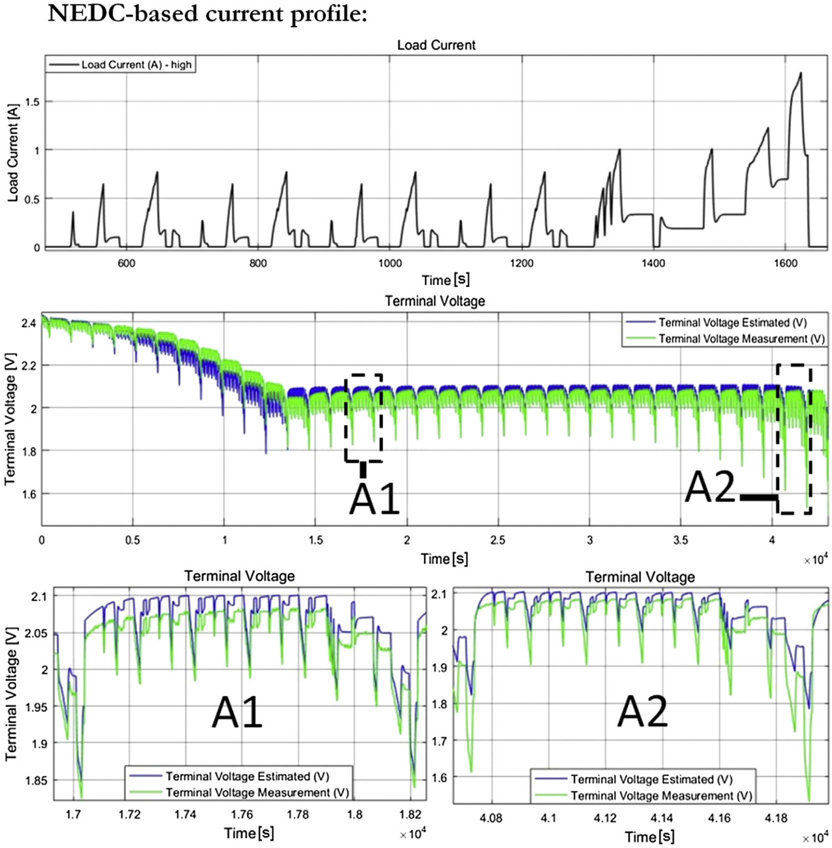

Fig. 8. Battery model and measured terminal voltage for 23 °C. Subplots A1 and A2 show 'zoomed' sections for additional detail.

cell is discharged under different conditions. As main changes to the previous measurements used for the model identification (i) a more realistic current profile is applied, based on the NEDC drive-cycle, (ii) the temperature controlled environment is neglected, allowing the cell to vary slightly around room temperature (23 °C) and (iii) different discharge hardware (a Kepco BOP 100-10 MG) is used. The NEDC drive-cycle is selected because it represents a realistic user scenario but also contains some level of abstraction [51,52]. The results of the Simulink model [53], together with the measured battery terminal voltage is shown in Fig. 8. There is no energy recovery while braking and the chosen currents are relatively small. Nevertheless the average discharge power is with 0.467 W an order of magnitude larger than the mixed pulse discharge test (0.147 W).

The model accuracy was quantified in terms of the root mean square error (RMSE):

$$\mathrm{RMSE} = \frac{1}{\sqrt{n}}\left(\sum_{i=1}^{n}\left(V_{t,i} - \widehat{V}_{t,i}\right)^2\right)^{0.5} \tag{47}$$

Where n is the number of data points, $V_{t,i}$ is the measured voltage and $\widehat{V}_{t,i}$ is the model prediction for the voltage at that point. The model was found to give an RMSE of 32 mV. This is small compared to the overall voltage range. Despite the simplifications of only one RC circuit with neglected current dependencies of R_p, the transient voltage is represented well during the entire discharge range (Fig. 8). However, some specific properties of Li-S batteries, as mentioned in Section 2, enhance the model error in certain regions. While the origins of the increasing deviation towards the end of the high plateau, likely due to the self discharge caused the polysulfide shuttle effect, are relatively well understood, the reasons the for the deviations in the low plateau are more unclear. There, mostly the decreasing voltage and the increased cell resistance are noticeable (Fig. 8, insets A1 and A2). The explanation for the first is difficult due to the difficult-to-define value of the open circuit potential. One observation, noticeable for the tested OXIS cells, is that the voltage in the low plateau, given enough time, always returns to approximately 2.1 V when left in open circuit condition. The behaviour with infinitesimally small (but non-zero) currents should be close or similar but differs towards the voltage profile of Fig. 2. Since these small discharge currents can cause the voltage to decrease towards the end of discharge, the increased error is presumably caused by the discharge current profile, leaving significantly less relaxation time, and the discharge hardware, allowing a flow of small and unmeasured leakage currents. Since these are also likely when an electric vehicle is not moving but in the switched on state, a more practical definition of the OCV, considering these small currents, might be a solution. The reason for the increased cell resistance towards the end is likely due to the different current profile as well but also can be in relation with cell variations. Nevertheless, the proposed battery model, representing the current understanding of Li-S batteries, shows good quality fit with small errors for the simplifying assumptions made and can be potentially used for a Li-S based BMS system.

9. Conclusion

After showing the differences of Li-S batteries to the current Li-ion ones, the challenges towards an operational model, capable of predicting the voltage response, capacity and power capability, but also the degradation are presented. As an initial step to address some of them, this study proposes a new robust and easy to tune battery model structure, capable of accounting for differences between the start and end of a discharge pulse. This 'behavioural' model, in combination with the PEM identification method, is used to identify the parameters of a Thevenin equivalent circuit model for different temperatures. Due to a mixed pulse discharge profile, the current dependencies of the parameters could also be revealed. Subsequently, the data is used to create a simplified battery model with polynomial functions for its parameters, which are interpolated for different temperatures. Despite the rather complex nature of the Li-S battery, the validation of the simplified model with a more realistic current profile displays a low estimation error, suggesting that some simplifications in favour for computational- or modelling-effort are possible. Nevertheless, it is also shown that for a precise estimation of the terminal voltage Li-S specific properties like self discharge in the high plateau, the OCV definition in the low plateau and the current profile dependency of the model parameters should be further investigated. Therefore, our further goals towards a usable Li-S compatible BMS system are improvements of the model itself, through implementing self discharge and current effects, and the application of the model as an observer for state of charge and state of health estimation. For a usage of these in a highly demanding environment of an electric vehicle, also the charge behaviour needs to be investigated.

Acknowledgement

This research was undertaken as part of the Revolutionary Electric Vehicle Battery (REVB) project, co-funded by Innovate UK under grant TS/L000903/1; university funding is provided by EPSRC under grants number EP/L505286/1 and EP/L505298/1. The underlying data can be accessed through the Cranfield University data repository at https://dx.doi.org/10.17862/cranfield.rd.c.3292031.

References

[1] C. Thomas, Int. J. Hydrog. Energy 34 (2009) 6005–6020.
[2] H. Budde-Meiwes, J. Drillkens, B. Lunz, J. Muennix, S. Rothgang, J. Kowal, D.U. Sauer, Proc. Institution Mech. Eng. D J. Automob. Eng. 227 (2013) 761–776.
[3] B. Scrosati, J. Hassoun, Y.-K. Sun, Energy Environ. Sci. 4 (2011) 3287–3295.
[4] Y.V. Mikhaylik, I. Kovalev, R. Schock, K. Kumaresan, J. Xu, J. Affinito, ECS Trans. 25 (2010) 23–34.
[5] OXIS Engery Ltd., (accessed 03.02.16). URL: http://www.oxisenergy.com.
[6] G.L. Plett, J. Power Sources 134 (2004) 252–261.
[7] V. Ramadesigan, P.W. Northrop, S. De, S. Santhanagopalan, R.D. Braatz, V.R. Subramanian, J. Electrochem. Soc. 159 (2012) R31–R45.
[8] X. Hu, S. Li, H. Peng, J. Power Sources 198 (2012) 359–367.
[9] A. Fotouhi, D.J. Auger, K. Propp, S. Longo, M. Wild, Renew. Sustain. Energy Rev. 56 (2016) 1008–1021.
[10] L. Lu, X. Han, J. Li, J. Hua, M. Ouyang, J. Power Sources 226 (2013) 272–288.
[11] C. Barchasz, J.-C. Leprêtre, F. Alloin, S. Patoux, J. Power Sources 199 (2012) 322–330.
[12] Z. Deng, Z. Zhang, Y. Lai, J. Liu, J. Li, Y. Liu, J. Electrochem. Soc. 160 (2013) A553–A558.
[13] J. Zhang, Z. Dong, X. Wang, X. Zhao, J. Tu, Q. Su, G. Du, J. Power Sources 270 (2014) 1–8.
[14] N.A. Cañas, K. Hirose, B. Pascucci, N. Wagner, K.A. Friedrich, R. Hiesgen, Electrochim. Acta 97 (2013) 42–51.
[15] K. Somasundaram, L. O'Neill, M. Marinescu, T. Zhang, G. Minton, M. Wild, G.J. Offer, Towards an Operational Model for a Li-s Battery, 3rd Thomas Young Centre Energy Materials Workshop, poster presentation, 2014.
[16] V. Knap, D.-I. Stroe, R. Teodorescu, M. Swierczynski, T. Stanciu, in: Energy Conversion Congress and Exposition (ECCE), IEEE, pp. 1375–1381.
[17] H. He, R. Xiong, H. Guo, S. Li, Energy Convers. Manag. 64 (2012) 113–121.
[18] X. Ji, L.F. Nazar, J. Mater. Chem. 20 (2010) 9821–9826.
[19] A. Manthiram, Y. Fu, S.-H. Chung, C. Zu, Y.-S. Su, Chem. Rev. 114 (2014) 11751–11787.
[20] V. Kolosnitsyn, E. Karaseva, Russ. J. Electrochem. 44 (2008) 506–509.
[21] H. Yamin, E. Peled, J. Power Sources 9 (1983) 281–287.
[22] M. Wild, L. ONeill, T. Zhang, R. Purkayastha, G. Minton, M. Marinescu, G. Offer, Energy Environ. Sci. 8 (2015) 3477–3494.
[23] H.S. Ryu, Z. Guo, H.J. Ahn, G.B. Cho, H. Liu, J. Power Sources 189 (2009) 1179–1183.
[24] M.U. Patel, R. Demir-Cakan, M. Morcrette, J.-M. Tarascon, M. Gaberscek, R. Dominko, ChemSusChem 6 (2013) 1177–1181.
[25] V. Kolosnitsyn, E. Kuzmina, E. Karaseva, J. Power Sources 274 (2015) 203–210.
[26] S. Xiong, K. Xie, Y. Diao, X. Hong, Ionics 18 (2012) 867–872.

[27] Y.V. Mikhaylik, J.R. Akridge, J. Electrochem. Soc. 151 (2004) A1969–A1976.
[28] Y. Diao, K. Xie, S. Xiong, X. Hong, J. Power Sources 235 (2013) 181–186.
[29] R.C. Kroeze, P.T. Krein, in: Power Electronics Specialists Conference, PESC 2008, IEEE, 2008, pp. 1336–1342.
[30] J. Xu, C.C. Mi, B. Cao, J. Deng, Z. Chen, S. Li, Veh. Technol. IEEE Trans. 63 (2014) 1614–1621.
[31] M. Marinescu, T. Zhang, G.J. Offer, Phys. Chem. Chem. Phys. 18 (2016) 584–593.
[32] L. W. Yao, J. Aziz, P. Y. Kong, N. Idris, in: Industrial Electronics Society, IECON 2013-39th Annual Conference of the IEEE, pp. 1729–1734.
[33] M. Chen, G.A. Rincon-Mora, Energy Convers. 21 (2006) 504–511.
[34] M.R. Busche, P. Adelhelm, H. Sommer, H. Schneider, K. Leitner, J. Janek, J. Power Sources 259 (2014) 289–299.
[35] D. Bresser, S. Passerini, B. Scrosati, Chem. Commun. 49 (2013) 10545–10562.
[36] T. Tran, K. Kinoshita, J. Electroanal. Chem. 386 (1995) 221–224.
[37] Y.V. Mikhaylik, J.R. Akridge, J. Electrochem. Soc. 150 (2003) A306–A311.
[38] O. Erdinc, B. Vural, M. Uzunoglu, Clean electrical power, in: International Conference on, IEEE, 2009, pp. 383–386.
[39] J. Vetter, P. Novák, M. Wagner, C. Veit, K.-C. Möller, J. Besenhard, M. Winter, M. Wohlfahrt-Mehrens, C. Vogler, A. Hammouche, J. Power Sources 147 (2005) 269–281.
[40] S. Xiong, K. Xie, Y. Diao, X. Hong, J. Power Sources 236 (2013) 181–187.
[41] P.G. Bruce, S.A. Freunberger, L.J. Hardwick, J.-M. Tarascon, Nat. Mater. 11 (2012) 19–29.
[42] L. Ljung, PTR Prentice Hall Inf. Syst. Sci. Series 198 (1987).
[43] L. Thévenin, Extension of Ohm's law to complex electromotive circuits. in: Ann. Télégr., 3^{e} series, volume 10, pp. 222–224.
[44] L. Thévenin, CR Séances l'Académie Sci. 97 (1883) 159–161.
[45] R.L. Deutscher, S. Fletcher, J.A. Hamilton, Electrochim. Acta 31 (1986) 585–589.
[46] W. Ahn, K.-B. Kim, K.-N. Jung, K.-H. Shin, C.-S. Jin, J. Power Sources 202 (2012) 394–399.
[47] V. Kolosnitsyn, E. Kuzmina, E. Karaseva, S. Mochalov, J. Power Sources 196 (2011) 1478–1482.
[48] J.R. Akridge, Y.V. Mikhaylik, N. White, Solid State Ionics 175 (2004) 243–245.
[49] MATLAB Version 8.5.0.197613 (R2015), The Mathworks, Inc., Natick, Massachusetts, 2015.
[50] M.U. Cuma, T. Koroglu, Renew. Sustain. Energy Rev. 42 (2015) 517–531.
[51] S. Samuel, L. Austin, D. Morrey, Proc. Institution Mech. Eng. D J. Automob. Eng. 216 (2002) 555–564.
[52] R. Kötz, S. Müller, M. Bärtschi, B. Schnyder, P. Dietrich, F. Büchi, A. Tsukada, G. Scherer, P. Rodatz, O. Garcia, et al., in: ECS Electro-Chemical Society, 52nd Meeting, San Francisco.
[53] Simulink Version 8.5 (R2015), The Mathworks, Inc., Natick, Massachusetts, 2015.

Paper A4

An Electrochemical Impedance Spectroscopy Study on a Lithium Sulfur Pouch Cell

Daniel-Ioan Stroe, Vaclav Knap, Maciej Swierczynski,
Tiberiu Stanciu, Erik Schaltz and Remus Teodorescu

The paper has been published in the *ECS Transactions*, vol. 72, no. 12, pp. 13–22, Sep. 2016, doi:10.1149/07212.0013ecst. Republished here with permission of Electrochemical Society, 2017; permission conveyed through Copyright Clearance Center, Inc.

ECS Transactions, 72 (12) 13-22 (2016)
10.1149/07212.0013ecst ©The Electrochemical Society

An Electrochemical Impedance Spectroscopy Study on a Lithium Sulfur Pouch Cell

D.-I. Stroe[a], V. Knap[a], M. Swierczynski[a], T. M. Stanciu[a], E. Schaltz[a], and R. Teodorescu[a]

[a] Department of Energy Technology, Aalborg University, Aalborg 9220, Denmark

The impedance behavior of a 3.4 Ah pouch Lithium-Sulfur cell was extensively characterized using the electrochemical impedance spectroscopy (EIS) technique. EIS measurements were performed at various temperatures and over the entire state-of-charge (SOC) interval without applying a superimposed DC current. The obtained results revealed a high dependency of the pouch cell's impedance spectrum on the operating conditions. An equivalent electrical circuit was proposed to further analyze the results and to quantify the contributions of different resistances to the total impedance of the Li-S pouch cell at different SOCs and temperatures.

Introduction

The demand for high energy density batteries has increased in the last decade, driven mainly by e-mobility, consumer electronics and military applications. Even though, today's Lithium-ion batteries are characterized by high performance in terms of power capability, lifetime, and safety, their volumetric and gravimetric energy density still prevents their full market penetration (1), (2). Thus, a lot research is carried out to develop rechargeable batteries chemistries with higher energy densities, which would totally fulfill the requirements of the aforementioned applications. In this respect, Lithium-air and Lithium-sulfur batteries could theoretically deliver the step-change in energy density required by applications such as e-mobility (3).

Lithium-sulfur (Li-S) batteries represent a very promising battery energy storage technology because of their high theoretical specific capacity (i.e., 1675 mAh/g) and energy density (i.e., 2600 Wh/kg) (3), (4). Furthermore, the use of sulfur, which is non-toxic, environmentally benign, and naturally abundant, as a cathode active material might reduce the battery cost and environmental concerns (5). Nevertheless, because of their inherent polysulfide shuttle mechanisms, Li-S batteries are characterized by rapid capacity fade, high self-discharge rate, and poor coulombic efficiency (5), (6).

Therefore, in order to analyze and assess the feasibility of using this new battery chemistry in various applications and for the improvement of the chemistry, a comprehensive understanding of the static and dynamic behavior is required. Electrochemical impedance spectroscopy (EIS) represents a powerful and well-established technique used for modelling purposes and/or for investigating the physical and electrochemical processes inside Li-ion batteries (7), (8); more recently, the EIS technique was applied successfully for similar purposes to Li-S batteries, as well (5), (9).

In this paper, we performed an in-depth characterization and investigation of the impedance spectra of a 3.4 Ah Li-S pouch cell. The impedance spectra was measured at various temperatures and SOC levels using the EIS technique. Furthermore, and electrical circuit was used to further process and analyze the measurements results.

State-of-the-art

The EIS technique was used to study different aspects related to Li-S batteries, as reported in the available literature. Kolosnitsyn et al. have used the EIS technique in (10) to study the changes in the properties of Li-S cell components during both charging and discharging. They shown that due to lithium polysulfides dissolution, the electrolyte conductivity changes and that the electrolyte's properties greatly influence the rate of the electrochemical process at both sulfur and lithium electrodes. In a later study (11), the same authors have obtained the impedance spectra of a Li-S coin cell for a reduced frequency range (i.e., 0.035 – 5 Hz) and illustrated that the cell's ohmic resistance reaches its maximum at the inflection point between the high voltage and low voltage plateau. Deng et al. in (5) have analyzed the changes in the Li-S cell impedance spectra by performing EIS measurements on a fully charged cell at five different temperatures and at room-temperature for different SOC levels. Furthermore, they have investigated the capacity fade mechanisms during 20 cycles by monitoring the changes in the measured impedance spectra of the Li-S cell. Similarly, Canas et al. have measured the impedance spectrum of a Li-S coin cell by means of EIS at different SOC levels over 50 cycles (9); a complex electrical circuit was used to model the EIS results and to further analyze the obtained results. The EIS technique, combined with other material dedicated techniques such as XRD and SEM, was used in (12) to investigate the electrochemical reactions of a sulfur cathode during both charging and discharging.

All the aforementioned investigation were performed on laboratory developed Li-S coin cells. To the best of our knowledge, there are no literature available EIS studies performed on pre-commercial or commercial Li-S cells. In this work, we present an extensive EIS characterization of a pre-commercial 3.4 Ah Li-S pouch cell. Furthermore, we analyzed the changes occurred in the cell's impedance spectrum due to the change in the SOC level and temperature.

Experimental Set-Up

Li-S Battery Cell under Test

For this study a pre-commercial Li-S pouch cell manufactured by Oxis Energy was used. The main parameters of this Li-S battery cell are summarized in Table I.

TABLE I. Main electrical and thermal parameters of the Li-S battery cell.

Parameter	Value
Nominal Capacity	3.4 Ah
Nominal Voltage	2.05 V
Maximum Voltage	2.45 V
Minimum Voltage	1.5 V
Nominal Charging Current	0.34 A (1C-rate)
Nominal Discharging Current	0.68 A (2C-rate)
Temperature Operation Range	+5°C to +80°C

Experiment Description

In order to fully characterize the impedance spectra of the considered 3.4 Ah Li-S pouch cell, the EIS measurements were carried out over the entire SOC interval, form 0% to 100% with a 5% SOC resolution, and considering a broad range of temperatures, from 15°C to 45°C, according to the following procedure:

1. Relaxation of the Li-S pouch cell at 15°C for two hours, in order to ensure stable thermo-dynamic conditions;
2. One nominal cycle, in order to ‘reset the history’ of the battery cell:
    a. CC charge with 0.1 C-rate (i.e., 0.34A) until the end-of-charge voltage (i.e, 2.45V) is reached;
    b. Discharge with 0.2 C-rate (i.e., 0.68A) until the end-of-discahrge voltage (i.e., 1.5V) is reached;
3. Second nominal cycle, in order to determine the cell’s capacity at the test temperature; the cell’s capacity needs to be known for the upcoming steps
4. CC charge with 0.1 C-rate (i.e., 0.34A) until the end-of-charge voltage (i.e, 2.45V) is reached;
5. EIS measurement at SOC = 100%
6. Discharge the cell with 5% SOC by a current of 0.2 C-rate.
7. Relaxation of the Li-S battery cell for a period of 30 minutes or until a decrease higher than 0.6 mV in the open circuit voltage is observed (which is caused by the pronounced self-discharge rate of the Li-S cells at high SOC levels);
8. EIS measurement at the new established SOC level;
9. Repetition of the steps 6 – 8 for the remaining SOC levels, considering a 5% SOC resolution;
10. Repetition of the steps 1 – 9 for the 25°C, 35°C, 45°C;

During all the tests, the Li-S pouch cell was placed into a temperature chamber with controlled temperature environment. Furthermore, the aforementioned temperature values refer to the temperature of the cell, which was measured by mean of a Type-K thermocouple as illustrated in Fig. 1.

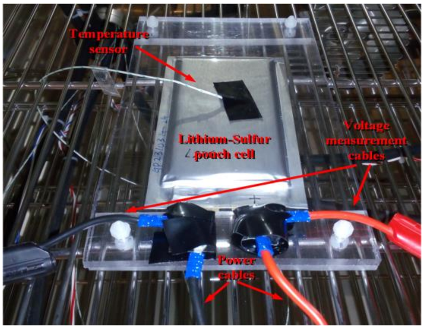

Figure 1. Li-S pouch cell placed inside the temperature chamber during the EIS characterization procedure

All the EIS measurements were performed in galvanostatic mode for a frequency sweep between 6.5 kHz and 10 mHz considering a total of 48 frequency points.

Furthermore during all the measurements no DC current was super-imposed on the small AC excitation signal.

Results

Li-S Battery Cell – Impedance Spectrum

Typical EIS Curve. A typical impedance spectrum of the considered 3.4 Ah Li-S pouch cell is presented in Fig. 2. As illustrated, the Nyquist curve is composed of a depressed semicircle in the high frequencies region (for this particular case 6.5 kHz – 27.4 Hz), a second depressed semicircle in the medium frequencies region (for this particular case 27.4 Hz – 0.11 Hz), and a straight line in the low frequencies region (for this particular case 0.11 Hz – 10 mHz). Furthermore, one can observe that the two depressed semicircles overlap each other.

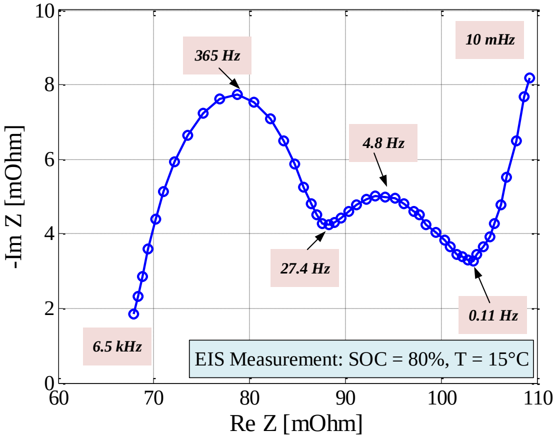

Figure 2. Typical Nyquist curve of the 3.4 Ah Li-S pouch cell.

Dependence of the Impedance Spectrum on the SOC. The impedance spectra of the Li-S pouch cell measured over the entire SOC interval at a temperature of 15°C (according to the procedure summarized in the previous section) is shown in Fig. 3. By analyzing the Nyquist curves illustrated in Fig. 3, two different trends were observed: for high SOC levels (i.e., in the interval 70% - 100% SOC), the impedance spectra shifts towards the right side of the Nyquist plane, while for low SOC levels (i.e., in the interval 0% - 65% SOC), the impedance spectra shifts towards the left side of the plane. This behavior is presented in Fig. 4 and Fig. 5. In (13) Knap et al., shown for a similar 3.4 Ah Li-S pouch cell that around 70% SOC is the inflexion point between the high voltage- and low voltage-plateau, which are characteristic for Li-S cells. Thus, the change in the shift of the impedance spectrum might be associated with the presence of the high and low voltage plateaus.

By analyzing the Nyquist curves presented in Fig. 4 and Fig. 5, one can observe that (except the case of 100% SOC), the diameter of the depressed semicircle corresponding to the high frequencies decreases with the decrease of the corresponding SOC value. On the contrary, the diameter of the second depressed semicircle, which was obtained for the medium frequencies, is increasing with the decrease of the SOC.

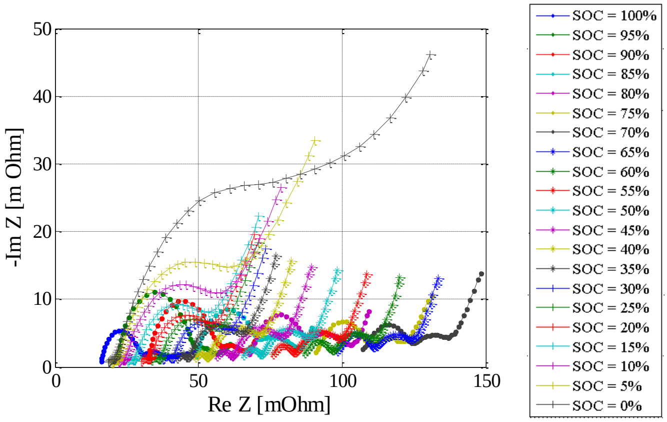

Figure 3. Impedance spectra of the Li-S pouch cell measured at 15°C

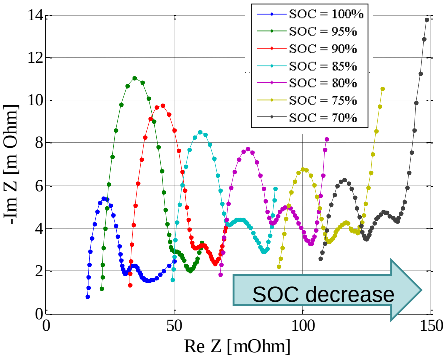

Figure 4. Impedance spectra of the Li-S pouch cell measured at 15°C and 70% - 100% SOC interval.

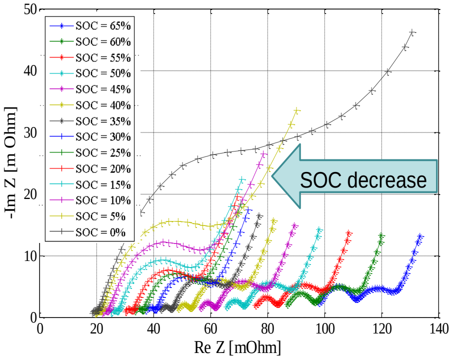

Figure 5. Impedance spectra of the Li-S pouch cell measured at 15°C and 0% - 65% SOC interval.

The impedance spectra of the Li-S pouch cell, which was measured at 25°C, 35°C, and 45°C are presented in Fig. 6 – Fig. 11. The trends that were mentioned for the impedance spectra obtained at 15°C are also valid for the other three considered temperatures. The only difference was observed for the value of the SOC where it occurs the change of the displacement of the Nyquist curves from the right side to the left side of the Nyquist plane: this behavior occurs at 75% SOC, 80% SOC and 85% SOC for 25°C, 35°C, and 45°C, respectively. Once more, this behavior might be associated with the decrease of the high voltage plateau of the Li-S pouch cell which takes place with the temperature increase; for example in (13), it is shown that for a cell temperature of 45°C, the shift between the high and low voltage plateaus occurs at approximately 82.5% SOC, while in this work, we observed the change in the EIS spectrum shift occurred for a SOC between 80% and 85% SOC.

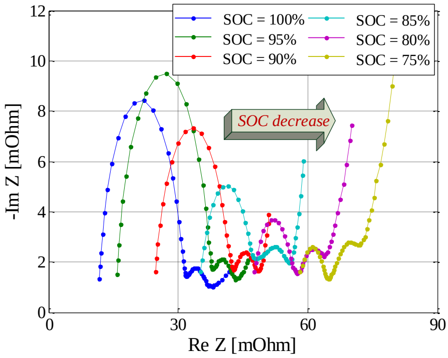

Figure 6. Impedance spectra of the Li-S pouch cell measured at 25°C and 75% - 100% SOC interval.

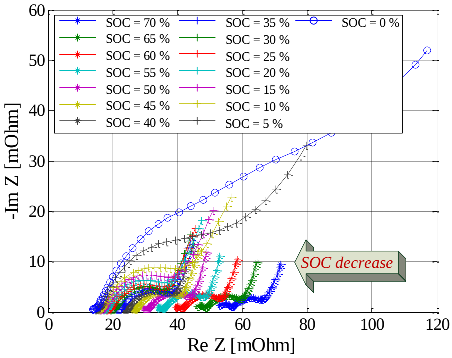

Figure 7. Impedance spectra of the Li-S pouch cell measured at 25°C and 0% - 70% SOC interval.

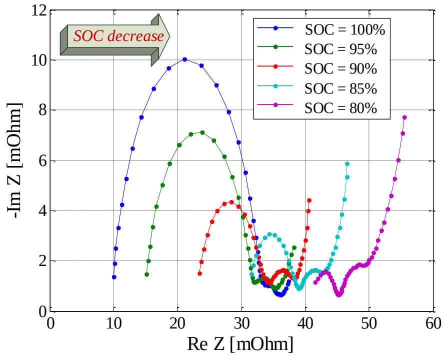

Figure 8. Impedance spectra of the Li-S pouch cell measured at 35°C and 80% - 100% SOC interval.

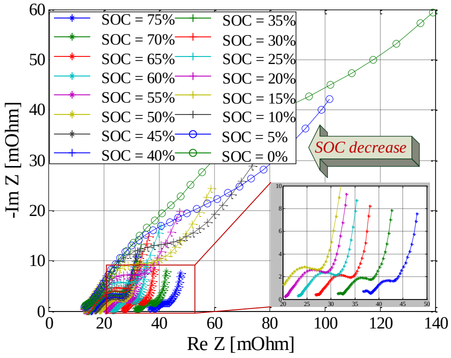

Figure 9. Impedance spectra of the Li-S pouch cell measured at 35°C and 0% - 75% SOC interval.

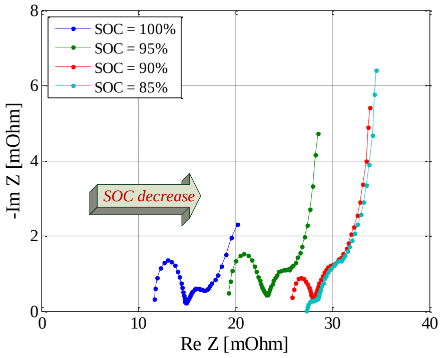

Figure 10. Impedance spectra of the Li-S pouch cell measured at 45°C and 85% - 100% SOC interval.

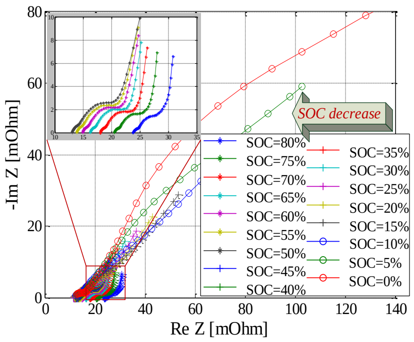

Figure 11. Impedance spectra of the Li-S pouch cell measured at 45°C and 0% - 80% SOC interval.

Dependence of the Impedance Spectrum on the Temperature. The change in the impedance spectrum of the considered Li-S pouch cell, which was caused by varying the cell temperature is presented in Fig. 12 for the case of 80% SOC. With the decrease of the temperature, it was observed a shift of the impedance spectrum towards the right hand side of the Nyquist plane; a similar behavior was presented for a laboratory-prepared Li-S coin cell by Deng et al. in (5). Furthermore, with the temperature increase, the diameter of the second depressed semicircle, corresponding to the medium frequencies, was reduced significantly, becoming almost indistinguishable for a temperature of 45°C. This decrease was as well presented in (5); however, in that case the behavior was not as pronounced as in our research. Finally, the first depressed semicircle was also influenced by the measurement temperature – with the temperature increase, a decrease of the dimeter of the semicircle was observed.

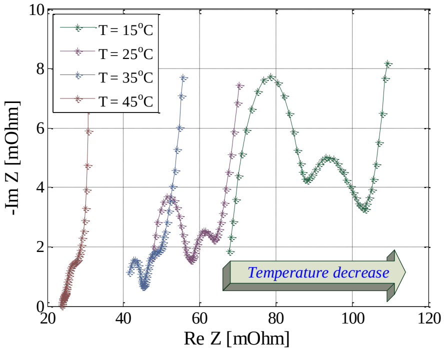

Figure 12. Impedance spectra of the Li-S pouch cell measured at 80% SOC and different temperatures.

Li-S Battery Cell – Equivalent Electrical Circuit

To better understand the dependence of the impedance spectrum on the SOC and temperature, the measured Nyquist curves were further processed by means of a curve fitting process.

Equivalent Electrical Circuit. Based on the shape of a typical Nyquist curve of the considered 3.4 Ah Li-S pouch cell (see Fig. 2), we have proposed the equivalent electrical circuit (EEC) presented in Fig. 13 to be used for the curve fitting process. The resistance Rs represents an ohmic resistance which sums the contribution from the electrolyte resistance and the resistance of the current collectors and cell connections (5), (9), (10). The first ZARC element (the parallel connection of the resistance R1 and constant phase element CPE1 (14)) models the high frequency semi-circle, while R2 and CPE2 were used to model the medium frequency semicircle. The diffusion of ions within the cathode, present at low frequencies, where modeled using a third ZARC element (composed of R3 and CPE3) (9). CPEs were used in the EEC instead of capacitors because of their better ability to approximate depressed semicircles, which were caused by the non-ideal behavior of the electrodes [2].

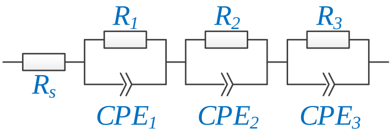

Figure 13. Equivalent electrical circuit of the 3.4 Ah Li-S pouch cell.

The suitability of the proposed EEC to fit the measured impedance spectra of the 3.4 Ah Li-S pouch cell is illustrated in Fig. 14. The accuracy of the fitting process was quantified using the normalized root mean square error (NRMSE).

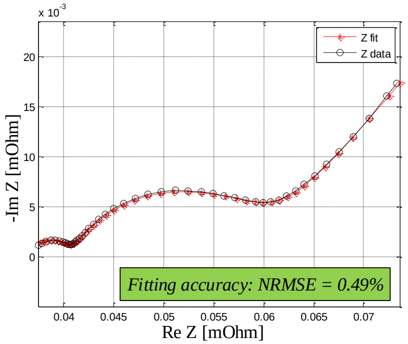

Figure 14. Curve fitting of the impedance spectrum measured at T = 15°C and SOC = 30%. Fitting accuracy: NRMSE = 0.49%. Extracted Parameters: Rs = 0.0364 Ω, R1 = 0.00425 Ω, Q1 = 0.1065 $\Omega^{-1}s^{n}$, n1 = 0.7851, R2 = 0.01933, Q2 = 7.1195 $\Omega^{-1}s^{n}$, n2 = 0.6889, R3 = 3.0691, Q3 = 218.211 $\Omega^{-1}s^{n}$, n3 = 0.5694.

Variation of the EEC Parameters with the Operation Conditions. The dependence of the resistance Rs (ohmic resistance), which was obtained from the fitting process, on the SOC and temperature is presented in Fig. 15. Independent on the Li-S cell temperature, the dependence of resistance Rs on the SOC follows two trends: the resistance increases with the SOC value until it reaches an inflection point from where it decrease steeply. A similar behavior of the resistance Rs was presented in literature (5), (9), (10). This inflection point changes monotonically with the temperature increase: for a temperature of 15°C, the inflection point was observed at 70% SOC, while for a temperature of 45°C, the inflection point was reached at 85% SOC. Furthermore, one can observe that the resistance Rs increases exponentially with the decrease of temperature. This process is caused by the decrease of the electrolyte ionic conductivity at low temperatures.

The change of the resistance R1 as function of SOC and temperature, as obtained from the curve fitting of the measured impedance spectra, are shown in Fig. 16. The resistance R1 increases exponentially with the increase in the SOC for all the four considered temperatures. Canas et al. reported in (9), a similar dependence of resistance R1 (which is defined in (9) as resistance R2) on the SOC for measurements carried out at room temperature. Furthermore, by performing dedicated tests, Canas et al, have related the resistance R1 with the charge transfer of sulfur intermediates at the cathode side (9).

Moreover, as illustrated in Fig. 16, the resistance R1 increases dramatically with the decrease of temperature; for example, at 60% SOC, the resistance R1 grows from 0.6 mOhm at 45°C to 10.2 mOhm at 15°C. The variation of resistance R2 as function of SOC for different temperatures is presented in Fig. 17. This resistive component of the EEC, decrease steeply with the increase of the SOC, independent on the considered temperature. A quasi-similar dependence was reported in (9), for a resistance denoted "R3" which was associated with the formation and dissolution of the S_8 and Li_2S compounds. For all the considered temperatures, the highest values of R2 were obtained for a discharged LiS battery cell when the accessible S_8 compound is not available; on the contrary, resistance R2 reaches its lowest values at high SOC values where sulfur dissolution occurs (9). Furthermore, for resistance R2 a reduced dependence on the temperature was observed, especially for SOC values higher than 20%. The dependence of the resistance R3 as function of SOC and temperature is shown in Fig. 18. Nevertheless, for this resistance, which is associated with the diffusion process, the fitting process has returned scattered values. Therefore, a clear conclusion regarding the variation of resistance R3 with temperature and SOC could not be drawn.

The dependence on SOC and temperature of the remaining parameters of the EEC, which are the generalized capacitances Q1, Q2, and Q3 and the depression factors N1, N2, and N3 were not analyzed.

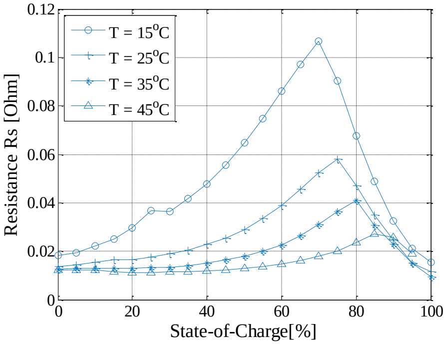

Figure 15. Variation of resistance Rs with SOC and temperature.

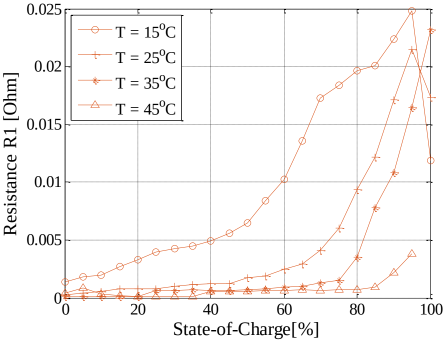

Figure 16. Variation of resistance R1 with SOC and temperature.

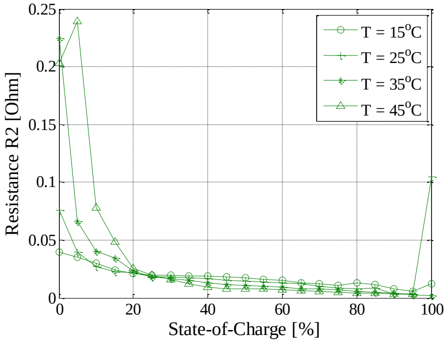

Figure 17. Variation of resistance R2 with SOC and temperature.

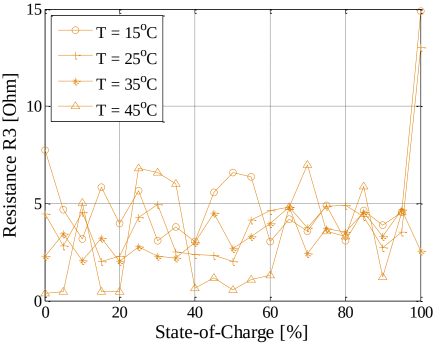

Figure 18. Variation of resistance R3 with SOC and temperature.

Conclusions

In this work, an extensive EIS characterization was performed for a 3.4 Ah Li-S pouch cell. EIS measurements were performed in galvanostatic mode, over the entire SOC interval at four different temperatures (i.e., 15°C, 25°C, 35°C, and 45°C); moreover, no superimposed DC current was applied during the EIS measurements. The obtained Nyqusit plots have shown a strong dependence on the SOC. This dependence was observed at all the temperatures. Furthermore, we have proposed an EEC – composed of a series ohmic resistance and three ZARC elements – that was used to curve fit the measured impedance spectra of the Li-S pouch cell. The results obtained from the curve fitting processes have shown different dependences of the EEC's elements on SOC and temperature. The ohmic resistance Rs has increased dramatically with the decrease in temperature and has reached its highest value at the SOC point which describes the transition between the high and low voltage profiles. Resistance R1, which in the literature is associated with the charge transfer process, shown an exponential increase with the decrease in temperature and with the increase of the considered SOC value. Furthermore, independent on the temperature, the resistance R2 decreases steeply until 20% SOC is reached; after this point, the value of resistance R2 decreases very slow and is almost not influenced by the temperature.

Acknowledgments

This work has been part of the ACEMU-project (1313-00004B). The authors gratefully acknowledge the Danish Council for Strategic Research and EUDP for providing financial support and would like to thank OXIS Energy for supplying the Lithium-Sulfur battery cells, which were used in this research.

References

1. J. B. Goodenough and K.-S. Park, *J. Am. Chem. Soc.*, **135**(4), 1167–1176 (2013).
2. B. Scrosati and J. Garche, *J. Power Sources*, **195**, 2419-2430 (2010).
3. P. G. Bruce, L. J. Hardwick, and K. M. Abraham, *MRS Bulletin*, **36**(7), 506-512 (2011).
4. X. Ji and F. Nazar, *J. Mater. Chem.*, **20**, 9821-9826 (2010).
5. Z. Deng et al., *J. Electrochem. Soc.*, **160**(4), A553 (2013).
6. D. Bresser, S. Passerini, and B. Scrosati, *Chem. Commun.*, **49**, 10545–10562 (2013).
7. D. Andre et al., *J. Power Sources*, **196**(12), 5349-5356 (2011).
8. Y.-C. Chang and H.-J. Sohn, *J. Electrochem. Soc.*, **147**(1), 50-58 (2000).
9. N. A. Canas et al., *Electrochmi. Acta*, **97**, 42-51 (2013).
10. V. S. Kolosnitsyn, E. V. Kuzimna, E. V. Karaseva, and S. E. Mochalov, *J. Power Sources* **196**(1), 1478-1482 (2011).
11. V. S. Kolosnitsyn, E. V. Kuzimna, and S. E. Mochalov, *J. Power Sources* **252**, 28-34 (2014).
12. L. Yuan, X. Qiu, L. Chen, and W. Zhu, *J. Power Sources* **189**, 127-132, (2009).
13. V. Knap et al., *J. Electrochem. Soc.*, **163**(6), A911 (2016).
14. E. Barsoukov and J. R. Macdonald, *Impedance Spectroscopy: Theory, Experiment, and Applications*, *2nd Edition*, Wiley, New York (2005).

Paper A5

Study on Self-Discharge Behavior of Lithium-Sulfur Batteries

Vaclav Knap, Daniel-Ioan Stroe, Maciej Swierczynski,
Remus Teodorescu and Erik Schaltz

The paper has been published in the *ECS Transactions*, vol. 70, no. 1, pp. 95–103, Dec. 2015, doi:10.1149/07001.0095ecst. Republished here with permission of Electrochemical Society, 2017; permission conveyed through Copyright Clearance Center, Inc.

ECS Transactions, 70 (1) 95-103 (2015)
10.1149/07001.0095ecst ©The Electrochemical Society

Study on Self-discharge Behavior of Lithium-Sulfur Batteries

V. Knap[a], D-I. Stroe[a], M. Swierczynski[a], R. Teodorescu[a] and E. Schaltz[a]

[a] Department of Energy Technology, Aalborg University, Aalborg, 9000, Denmark

Lithium-Sulfur (Li-S) batteries are a promising energy storage technology, which draws interest due to their high theoretical limits in terms of specific capacity, specific energy and energy density. However as a drawback, they suffer from a high self-discharge rate, which is mainly caused by ongoing polysulfide shuttle. In this paper, the self-discharge behavior of Li-S batteries is experimentally investigated, considering various conditions as depth-of-discharge, temperature and idling time. The self-discharge rate under different conditions is identified and quantified. Moreover, a methodology for estimating the capacity of the high voltage plateau based on a self-discharge constant was analyzed; however, the method needs further improvements in order to estimate this capacity accurately for all conditions.

Introduction

Lithium-Sulfur (Li-S) batteries have drawn a great interest in the chase for low-cost batteries with high power and energy density. Their theoretical performance, namely specific capacity of 1672 Ah/kg, specific energy of around 2600 Wh/kg and energy density of 2199 Wh/l, greatly overpass the limits of today's Lithium-ion batteries. Moreover, the usage of environmentally-friendly and abundantly-available sulfur, instead of other metals, reduces the cost and makes Li-S batteries more considerate towards environment. Nevertheless, mainly due to their characteristic polysulfide shuttle mechanism, Li-S batteries suffer of: fast capacity fade, low Coulombic efficiency, and high self-discharge (1).

Identifying the battery self-discharge characteristic is important for both practical applications (i.e. to assess appropriate energy management and to determine application economic viability) and laboratory testing (i.e. to retrieve accurate and unbiased measurement results). In Li-S batteries, the self-discharge process is related to the polysulfide shuttle and to the corrosion of the current collectors (2), (3), (4), (5). The polysulfide shuttle is caused by diffusion of high-order polysulfides (S_8^{2-}, S_6^{2-}, S_4^{2-}), which are soluble in the electrolyte, from the sulfur electrode to the lithium electrode. In there, the high order polysulfides are reduced to low-order polysulfides and the soluble ones diffuse back to the sulfur electrode (2), (6).

There is a high interest in improving the characteristics of Li-S batteries and one of these improvements targets their self-discharge behavior. Thus, several researchers have proposed different solutions for improving the Li-S batteries self-discharge characteristic. Reducing the self-discharge rate by using a gold-coated current collector instead of a bare stainless steel current collector was proposed in (3). Other improvements of Li-S batteries by advancing and utilization of cathode compositions, porous polysulfide reservoirs, porous current collectors, binders, interlayers, separators, electrode passivation layers and electrode configurations are summarized in (7).

Most of the recent studies regarding the self-discharge behavior of Li-S batteries are focused only on simple comparisons between well-established and newly developed coin cells at one or two conditions (e.g. temperature value, depth-of-discharge etc.) (8), (9), (10). In a similar manner, a study on a variety of sulfur electrode materials was conduct in (11), where the reversible and irreversible capacity loss of the materials were identified. Self-discharge characteristics of Li-S coin cells were extensively studied through open circuit voltage (OCV) measurement, electrochemical impedance spectroscopy (EIS) and discharge curve at 25 °C in (4), (5). Ryu et al., in (4), describe the self-discharge behavior for different types of current collectors. Moreover, they found a self-discharge rate of 34 % for 80 days of idling time. However, this rate has increased only to 36 % after 360 days, for a Li/TEGDME/S battery with Al current collectors. In (5), Kazazi et al. present improvements of a Li-S cell with pure sulfur cathode, by using shuttle suppressing sulfur-polypyrrole cathode materials, which reduced the self-discharge rate from 57.9 % to 29 %. Furthermore, by the use of an electrolyte 0.4 M $LiNO_3$, which prevents both the corrosion and the shuttle, they reduced the self-discharge rate to 3.1 %. Mikhaylik and Akridge quantified the self-discharge process in relation to the polysulfide shuttle in (2); they observed a high self-discharge rate at the high plateau, while at the low plateau, the charge was kept stable for several weeks. In all of their experiments presented in (2), Mikhaylik and Akridge have used prismatic cells.

Even though the aforementioned studies are providing a close insight to the self-discharge behavior of coin and prismatic Li-S battery cells, the overall characterization of this behavior has not been analyzed in literature yet, to the best of authors' knowledge. For the practical cell operation, dependencies on depth-of-discharge (DOD) and temperature are required. Moreover, a tool for self-discharge discharge estimation is needed. Therefore, an extensive systematic study of the self-discharge behavior of Li-S pouch cells is performed in this paper. The study considers the influence of idling time, (DOD) and temperatures on the self-discharge characteristics of the studied 3.4 Ah battery cells. The investigation uses open circuit voltage (OCV) measurements and discharge voltage curves for determining the self-discharged characteristic of the considered Li-S battery cells. Based on the experimental results, estimation of the remaining battery cell capacity has been done.

Experimental

The cells, which were used to perform this analysis, are 3.4 Ah Li-S pouch cells supplied by OXIS Energy. All tests were performed using Digatron BTS 600 and MACCOR Series 4000 test stations. During all the tests, the cells were placed inside temperature chambers with controlled environment temperature at 15, 25, 35, and 45 °C.

Systematic Self-Discharge Measurement

The standard test protocol, which was used for the measurement of the self-discharge of the 3.4 Ah Li-S battery cells, is illustrated in Fig. 1. The test protocol was composed of three steps as follows:

- Step 1 – pre-condition cycle on a fully discharged cell (charging: current of 0.1 C-rate (0.34 A), cut-off voltage 2.45 V or 11 hour; discharging: 0.2 C-rate (0.68 A), cut-off voltage 1.5 V) in order to have the cell in a comparable state between the tests
- Step 2 – capacity check (charging: current of 0.1 C-rate (0.34 A), cut-off voltage 2.45 V or 11 hour; discharging: 0.2 C-rate (0.68 A), cut-off voltage 1.5 V) in order to measure actual discharge capacity of the cell
- Step 3 – self-discharge measurement; the cell was fully charged and later on discharged to a pre-defined DOD value, where the cell was kept at open-circuit conditions for a certain idling time. Finally, after this idling time, the battery cell was discharged in order to measure the remaining cell capacity.

Step 1 and Step 3 were repeated for several DOD values and idling times. After several repetitions, Step 2 was inserted and the reference capacity value was updated, in order to reduce the error in the DOD level due to capacity fades.

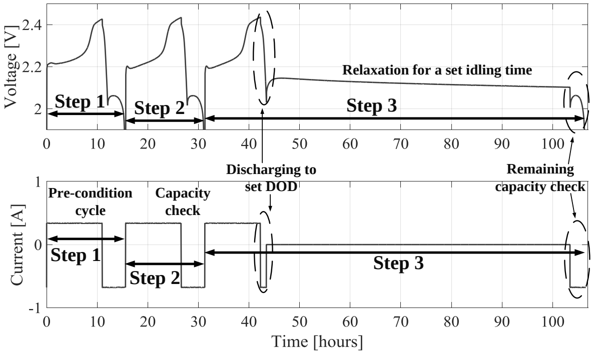

Figure 1. Standard test protocol for systematic self-discharge measurement.

Quantification of Self-Discharge Behavior

The self-discharge rate, expressed in percentage, was computed according to (4) as follows:

$$\text{Self-discharge rate (\%)} = ((C_{ini}-C_{dod})-C_{rem})/(C_{ini}-C_{dod})*100 \qquad [1]$$

Where C_{ini} is the initial discharge capacity, C_{dod} is the discharged capacity to the specific DOD point and C_{rem} is the remaining capacity after the idling time.

According to Mikhaylik and Akridge (2), the capacity of the high voltage plateau (C_H), illustrated in Fig. 2, can be expressed as in [2].

$$C_H = C_{H\_ini}*e\wedge-(k_S/t_S) \qquad [2]$$

Where C_{H_ini} is the initial high plateau discharge capacity, k_S is the self-discharge constant and t_S is the idling time. The self-discharge constant k_S is possible to be determined experimentally, as the slope of the line describing the variation of $\ln(C_H/C_{H\_ini})$ with the idling time $t_{S.}$.

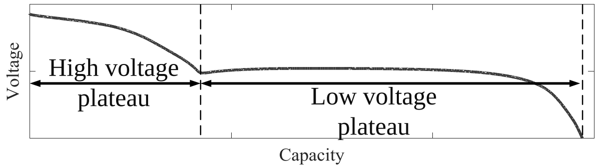

Figure 2. Typical voltage discharging profile of a Li-S battery with marked high and low voltage plateaus.

Results and Discussion

Self-Discharge Dependence on DOD Level

To identify the self-discharge dependence on the DOD level, the Li-S battery cell was kept at 35 °C for a period t_S of 60 hours. The battery cell voltage evolution during the 60 hours of relaxation is shown in Fig. 3. The voltage of the Li-S battery cell went at first through recovery phase after a discharge, where the voltage was rising. The time of the recovery phase is increasing with higher DOD levels. After the recovery phase, the voltage was decaying for all DOD levels and as one can observe, 60 hours is not enough to reach steady-state. Moreover, a relationship between a higher DOD level and a lower voltage value (after 60 hours of relaxation) corresponds only until a DOD level of 25 % DOD, which reffers to the end of discharge in the high voltage plateau and the relaxation voltages are shown in Fig. 3 (a). From 30 % DOD this trend is reversed and higher voltage values are achieved for higher considered DOD levels, which corresponds to the end of discharge in the low voltage plateau and the relaxation voltages are shown in Fig. 3 (b).

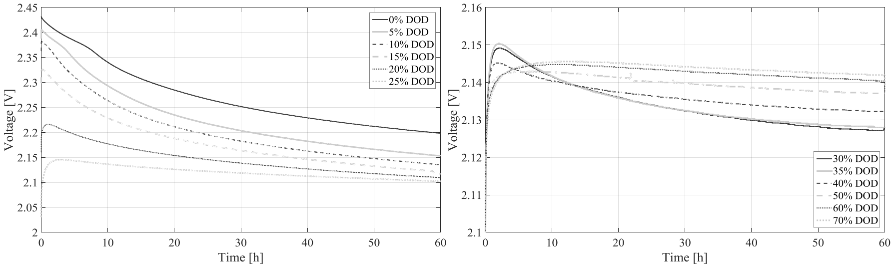

(a) (b)

Figure 3. Voltage evolution during 60 hours of relaxation at 35 °C.

The dependence of the self-discharge rate on the DOD level is shown in Fig. 4. The self-discharge rate is decreasing with increasing the DOD level and from 30 % DOD the computed value becomes negative. The negative value of the self-discharge rate is an indicator that the total discharged capacity from the cell, after 60 hours of relaxation, is higher than the discharge capacity obtained during the capacity test by continuous discharge. Thus, a higher charge in the battery cell is available to be discharged by introducing relaxation periods before discharging at the low voltage plateau. However, this behavior was observed only for DODs between 30 and 50 %. From 60 % DOD, the cell presented again self-discharge behavior.

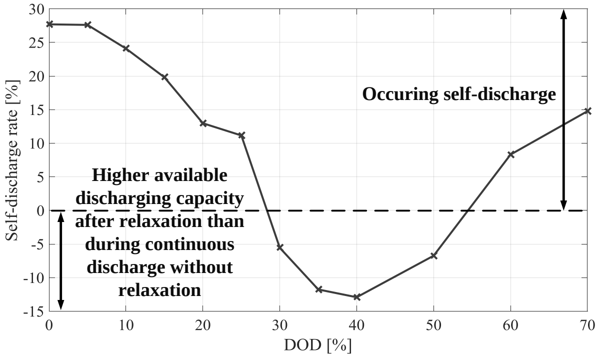

Figure 4. Self-discharge rate at 35 °C, computed after 60 hours of relaxation.

Self-Discharge Dependence on Temperature and DOD for 4 Hours Idling Time

In this test procedure, the Li-S battery cell was discharged to a specific DOD level (from 5 % to 30 % with 5 % resolution step) and t_S was set at four hours. Four measurement temperatures were considered, i.e., 15, 25, 35 and 45 °C. The self-discharge rate was computed according to [1] and its dependence on DOD and temperature is presented in Fig. 5. As expected, for the case of a four hours idling time as well, the self-discharge rate is decreasing with increasing the DOD level. By increasing the temperature from 15 °C to 35 °C, an increase of the self-discharge rate was observed; nevertheless, by further increasing the temperature to 45 °C, a decrease in the self-discharge rate was obtained. This change of trend can be explained by examinating the DOD measurement points and their position towards the high voltage plateau as illustrated in Fig. 6. The length of the high voltage plateau is decreasing with increasing the temperature; nevertheless, for temperatures of 15, 25 and 35 °C the high voltage plateau still corresponds to a DOD level around 30 %. In the case of 45 °C, the high voltage plateau reaches corresponds only to a 18 % DOD, which might be caused by the strong presence of polysulfide shuttle, which prevents the cell be fully charged and causing extremely high self-discharge in this region.

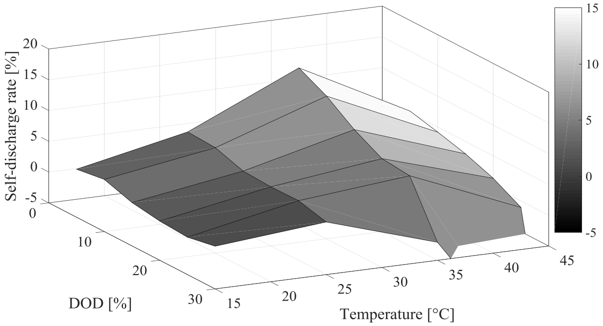

Figure 5. The self-discharge dependence on the DOD level and temperature for an idling time of 4 hours.

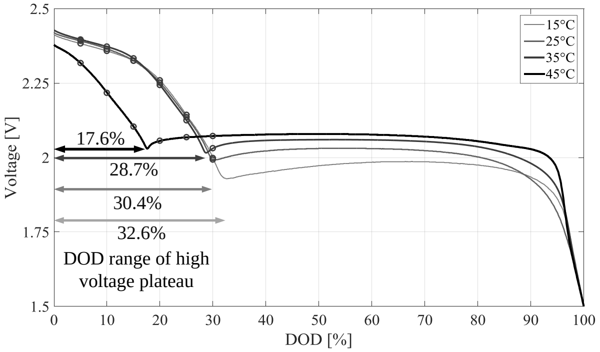

Figure 6. Positions of the measured points for self-discharge at voltage curve during continuous discharge with relation to DOD levels.

Self-Discharge Dependence on the Idling Time

During this test, the cells were stored at three conditions: 10 % DOD and 25 °C, 10 % DOD and 35 °C, and 20 % DOD and 35 °C. The self-discharge rate dependence on the idling time t_S is shown in Fig. 7. As one can see, the self-discharge rate is increasing over time, but the steepness of growth is lowered as the cell is getting more discharged. The shift in the self-discharge rate due to the increase in the temperature is shown in Fig. 7 (a); at 35 °C the self-discharge rate of the Li-S battery cell is higher than at 25 °C however the same shape of the self-discharge dependence on idling time is obtained independent on the considered temperature. The comparison between the self-discharge rate increase as function of idling time measured at 10 % and 20 % DOD is shown in Fig. 7 (b). If for short idling times (i.e., up to two hours), a similar self-discharge rate has been obtained independent on the DOD level, once the idling time has increased a steeper decrease of the self-discharge rate was observed for the higher DOD level (i.e., 10 %).

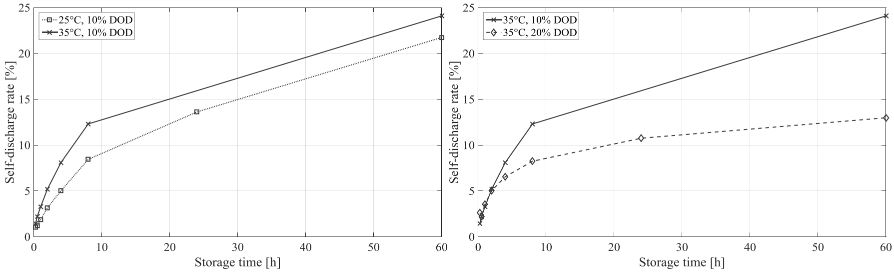

(a) (b)

Figure 7. Self-discharge rate as a function of an idling time (a) at 10 % DOD for two temperature levels and (b) at 35 °C for two DOD levels.

Self-Discharge Constant

To determine the self-discharge constant, the ratio between the measured initial and remaining capacities corresponding to the high voltage plateau was plotted against the idling time on a logarithmic scale and fitted by a linear curve as it is illustrated in Fig. 8. For this purpose, there were considered measurement data from self-discharge tests carried out for and idling time between 15 minutes and 8 hours. Based on (2), the self-discharge constants k_S were identified as the slopes of the fitting curves values, as shown in Fig. 8.

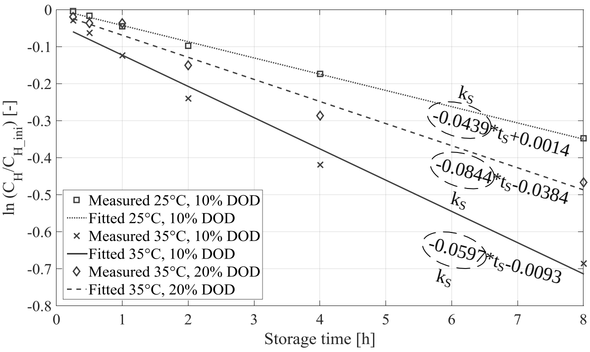

Figure 8. Logarithmic expression of remaining and initial high voltage plateau capacities from experimental results as a function of time and a fitted linear curve.

The next step was to estimate, for each considered condition (DOD and temperature), the capacity of the high voltage plateau C_H according to [2], using the previously obtained self-discharge constant k_S, and compare it with the experimental measurements. The obtained capacities corresponding to the high voltage plateau are shown in Fig. 9. The estimated and measured capacities are following the same trend; however, their values are slightly different. The relative errors corresponding to the estimation of the high voltage plateau capacity are presented in Fig. 10. By analyzing these results, one can conclude that a prediction of the self-discharge based on [2] and experimentally found self-discharge constants k_S is considered not sufficiently accurate and another approach is needed to be used.

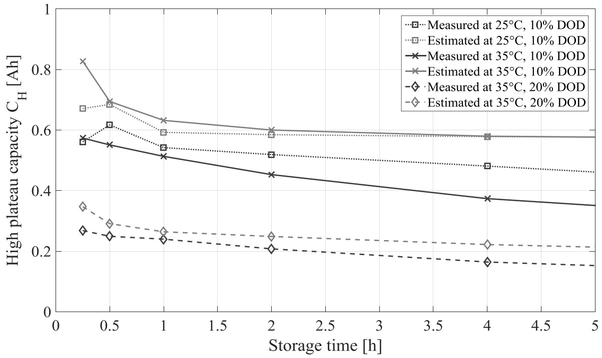

Figure 9. Estimated and measured capacities of the high voltage plateau for varying idling conditions.

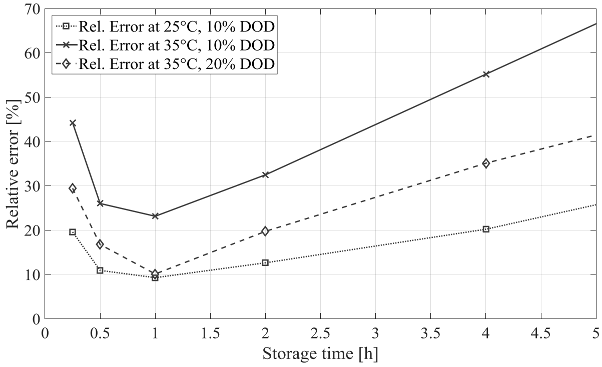

Figure 10. Relative error of the estimated C_H computed according to [2].

Conclusions

The self-discharge behavior of a 3.4 Ah Li-S battery cell was experimentally investigated in this paper. The self-discharge process is mainly caused by polysulfide shuttle and it appears especially at the high voltage plateau, where with increased DOD levels the self-discharge rate is reduced. At the low voltage plateau between 30 and 50 % DOD, for the considered idling time of up to 60 hours, the self-discharge was not observed; on the contrary, more charge was available to be discharged from the cell after idling than in the case of a continuous discharge of the Li-S battery cell.

Furthermore, the self-discharge rate was found to increase with increasing temperature, until 35 °C. At 45 °C, the self-discharge behavior is changing the trend due to a highly reduced high voltage plateau. Furthermore, an estimation of the remaining capacity was performed by identifying the self-discharge constant k_S; however, the method needs to be further improved in order to provide more accurate results for various idling conditions.

Acknowledgments

This work has been part of the ACEMU-project (1313-00004B). The authors gratefully acknowledge the Danish Council for Strategic Research and EUDP for providing financial support and would like to thank OXIS Energy for supplying the Lithium-Sulfur battery cells.

References

1. D. Bresser, S. Passerini, and B. Scrosati, *Chem. Commun.*, **49**, 10545–10562 (2013).
2. Y. V. Mikhaylik and J. R. Akridge, *J. Electrochem. Soc.*, **151**, A1969 (2004).
3. H. Ryu et al., *J. Power Sources*, **140**, 365–369 (2005).
4. H. S. Ryu et al., *Electrochim. Acta*, **52**, 1563–1566 (2006).
5. M. Kazazi, M. R. Vaezi, and a. Kazemzadeh, *Ionics (Kiel).*, 1–10 (2014).
6. D. Moy, a. Manivannan, and S. R. Narayanan, *J. Electrochem. Soc.*, **162**, A1–A7 (2014).
7. A. Manthiram, S.-H. Chung, and C. Zu, *Adv. Mater.*, **27**, 1980–2006 (2015).
8. N. Azimi et al., *J. Electrochem. Soc.*, **162**, 64–68 (2015).
9. M. L. Gordin et al., *ACS Appl. Mater. Interfaces*, **6**, 8006–8010 (2014).
10. J.-Q. Huang et al., *ACS Nano*, **9**, 3002–3011 (2015).
11. C. J. Hart et al., *Chem. Commun.*, **51**, 2308–2311 (2015).

Paper A6

Investigation of the Self-Discharge Behavior of Lithium-Sulfur Batteries

Vaclav Knap, Daniel-Ioan Stroe, Maciej Swierczynski,
Remus Teodorescu and Erik Schaltz

The paper has been published in the *Journal of The Electrochemical Society*, vol. 163, no. 6, pp. A911–A916, 2016, doi:10.1149/2.0641606jes.

Journal of The Electrochemical Society, **163** (6) A911-A916 (2016)
0013-4651/2016/163(6)/A911/6/$33.00 © The Electrochemical Society

Investigation of the Self-Discharge Behavior of Lithium-Sulfur Batteries

V. Knap,[z] D.-I. Stroe, M. Swierczynski,[*] R. Teodorescu, and E. Schaltz

Department of Energy Technology, Aalborg University, Aalborg 9000, Denmark

Lithium-Sulfur (Li-S) batteries represent a perspective energy storage technology, which reaches very high theoretical limits in terms of specific capacity, specific energy, and energy density. However, Li-S batteries are governed by the polysulfide shuttle mechanism, which causes fast capacity fade, low coulombic efficiency, and high self-discharge rate. The self-discharge is an important characteristic of Li-S batteries for both practical applications and laboratory testing, which is highly dependent on the operating conditions. Thus, to map and to understand the Li-S self-discharge behavior under various conditions, such as depth-of-discharge, temperature, and idling time, a set of experiments were performed in this work on 3.4 Ah Li-S pouch cells. The results are systematically presented in form of open-circuit voltages during idling and self-discharge separated into reversible and irreversible capacity loss. Furthermore, estimation of the actual high voltage plateau capacity based on a self-discharge constant was performed according to an earlier proposed methodology; however, the method needs further improvements in order to estimate this capacity accurately for all conditions.

Manuscript submitted January 20, 2016; revised manuscript received February 23, 2016. Published March 8, 2016.

Lithium-Sulfur (Li-S) batteries have attracted a great interest in the chase for low-cost batteries with high energy density. Their theoretical performance, namely specific capacity of 1672 Ah/kg, the specific energy of around 2600 Wh/kg and energy density of 2199 Wh/l, greatly overpass the limits of today's Lithium-ion batteries. Moreover, the usage of environmentally friendly and abundantly available sulfur, instead of other metals, reduces their cost and makes Li-S batteries more considerate toward the environment. Nevertheless, mainly due to their characteristic polysulfide shuttle mechanism, Li-S batteries suffer of: fast capacity fade, low coulombic efficiency, and high self-discharge.[1]

Identifying the battery self-discharge characteristic is important for both practical applications (i.e., to accurately estimate the SOC, to assess the appropriate energy management strategy, and to investigate the application economic viability) and laboratory testing (i.e., to retrieve accurate and unbiased measurement results). In Li-S batteries, the self-discharge process is related to the polysulfide shuttle and to the corrosion of the current collectors.[2–5] The polysulfide shuttle is caused by the diffusion of high-order polysulfides (S_8^{2-}, S_6^{2-}, S_4^{2-}), which are soluble in the electrolyte, from the sulfur electrode to the lithium electrode; there, the high-order polysulfides are reduced to low-order polysulfides and the soluble ones diffuse back to the sulfur electrode.[2,6]

There is a high interest in improving the characteristics of Li-S batteries and one of these improvements targets their self-discharge behavior. Thus, several researchers have proposed different solutions for improving the Li-S batteries self-discharge characteristic. Reducing the self-discharge rate by using a gold-coated current collector instead of a bare stainless steel current collector was proposed in Ref. 3. An alternative solution presented in Ref. 7 was the addition of an ionic liquid into the electrolyte in order to enhanced the solid electrolyte interface, which resulted in a decrease of the self-discharge. Other improvements of Li-S batteries by advancing and utilization of cathode compositions, porous polysulfide reservoirs, porous current collectors, binders, interlayers, separators, electrode passivation layers, and electrode configurations are summarized in Ref. 8.

Most of the recent studies regarding the self-discharge behavior of Li-S batteries are focused only on simple comparisons between well-established and newly developed coin cells at one or two conditions (e.g., temperature value, depth-of-discharge etc.).[9–11] In a similar manner, a study on a variety of sulfur electrode materials was conducted in Ref. 12, where the reversible and irreversible capacity loss of the materials were identified. The self-discharge characteristics of Li-S coin cells were extensively studied through open circuit voltage (OCV) measurement, electrochemical impedance spectroscopy (EIS) and discharge curve at 25°C in Refs. 4 and 5. Ryu et al., in Ref. 4, described the self-discharge behavior for different types of current collectors. Moreover, they found a self-discharge rate of 34% for 80 days of idling time. However, this rate has increased only to 36% after 360 days, for a Li/TEGDME/S battery with Al current collectors. In Ref. 5, Kazazi et al. presented improvements of a Li-S cell with a pure sulfur cathode, by using shuttle suppressing sulfur-polypyrrole cathode materials, which reduced the self-discharge rate from 57.9% to 29%. Furthermore, by the use of an electrolyte 0.4 M $LiNO_3$, which prevents both the corrosion and the shuttle, they reduced the self-discharge rate to 3.1%. Mikhaylik and Akridge quantified the self-discharge process in relation to the polysulfide shuttle in Ref. 2; they observed a high self-discharge rate at the high plateau, while, at the low plateau, the charge was kept stable for several weeks. In all of their experiments presented in Ref. 2, Mikhaylik and Akridge have used prismatic cells. Another study on the newer generation of Sion Power Li-S cells was carried out in Ref. 13; the dependence of the self-discharge on the storage time (in the range of days and months), was examined only for two depth-of-discharge (DOD) levels, i.e., 0% and 60%, at 20°C. In this study, the capacity loss during storage is separated into the irreversible and reversible capacity loss.

Even though the aforementioned studies are providing a close insight to the self-discharge behavior of coin and prismatic Li-S battery cells, the overall characterization of this behavior has not been analyzed in literature yet, to the best of authors' knowledge. For the practical cell operation, dependencies on DOD and temperature are required. Moreover, a tool for self-discharge estimation is needed. Therefore, an extensive systematic investigation of the self-discharge behavior of Li-S pouch cells is performed in this paper. The study considers the influence of the DOD, idling time, and temperature on the self-discharge characteristics of the studied 3.4 Ah Li-S pouch cells. The investigation uses open circuit voltage (OCV) measurements and discharge voltage curves for determining the self-discharge characteristic of the considered Li-S battery cells. Moreover, the reversible and irreversible capacity loss is distinguished in the study. Based on the experimental results, an estimation of the remaining battery cell capacity has been performed.

Experimental

The cells, which were used to perform this analysis, are 3.4 Ah Li-S pouch cells supplied by OXIS Energy, their electro-thermal characteristics are listed in Table I. All tests were performed using Digatron BTS 600 and MACCOR Series 4000 test stations. During all the tests, the cells were placed inside temperature chambers with controlled environment temperature at 15, 25, 35, and 45°C.

---

[*] Electrochemical Society Member.
[z] E-mail: vkn@et.aau.dk

Table I. The electro-thermal characteristics of the Li-S cell.

Nominal capacity (30°C)	3.4 Ah
Nominal voltage	2.05 V
Charge cutoff voltage	2.45 V
Discharge cutoff voltage	1.5 V
Nominal charging current	0.34 A (0.1 C-rate)
Nominal discharging current	0.68 A (0.2 C-rate)
Ambient temperature operation range	5 – 80°C

***Systematic self-discharge measurement.*—**The standard test protocol, which was used for the measurement of the self-discharge of the considered Li-S battery cells, is illustrated in Fig. 1. The test protocol was composed of three steps as follows:

- Step 1 – pre-condition cycle on a fully discharged cell (charging: current of 0.1 C-rate (0.34 A), cutoff voltage 2.45 V or 11 hours; discharging: 0.2 C-rate (0.68 A), cutoff voltage 1.5 V) in order to have the cell in a comparable state between the tests and to obtain the actual discharge cell capacity (C_{ini});
- Step 2 – the cell was fully charged and later discharged by the corresponding capacity (C_{dod}) to a pre-defined DOD value, where the cell was kept at open-circuit conditions for a certain idling time. Finally, after this idling time, the battery cell was discharged in order to measure the remaining cell capacity (C_{rem}).
- Step 3 – the cell was recharged in the similar way as in Step 1, in order to identify the new actual discharge capacity of the cell (C_{rch}), which allows to identify the irreversible capacity lost due to calendar and cycling ageing

This self-discharge test procedure was repeated for the considered DOD levels, temperature levels, and idling times.

***Quantification of self-discharge behavior.*—**The self-discharge behavior was quantified based on the methodology presented in Ref. 13 which allows to separate the reversible and irreversible capacity loss, as illustrated in Fig. 2 and computed according to 1–4:

$$C_t = (C_{ini} - C_{dod} - C_{rem})/C_{ini} * 100 \quad [1]$$

$$C_{sd} = (C_{rch} - C_{rem} - C_{dod})\,/C_{ini} * 100 \quad [2]$$

$$C_{ir} = (C_{ini} - C_{rch})\,/C_{ini} * 100 \quad [3]$$

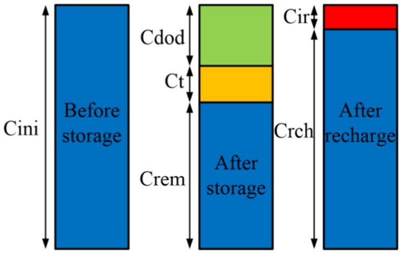

Figure 2. Illustration of self-discharge quantification and separation.

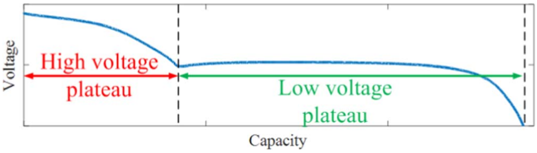

Figure 3. Typical voltage discharging profile of a Li-S battery with marked high and low voltage plateaus.

$$C_t = C_{sd} + C_{ir} \quad [4]$$

Where C_t is the total capacity loss during the idling, C_{ini} is the initial discharge capacity, C_{dod} is the discharged capacity to the specific DOD point, and C_{rem} is the remaining capacity after the idling time, C_{sd} is reversible capacity loss, which is further referred as the self-discharge rate, C_{rch} is the new actual discharge capacity during recharge after the idling and C_{ir} is the irreversible capacity loss. The irreversible capacity loss was caused by cycling and idling (storage) degradation of the LiS cells.

According to Mikhaylik and Akridge,[2] the actual capacity of the high voltage plateau (C_H), illustrated in Fig. 3, can be expressed as in 5.

$$C_H = C_{H\_ini} * e^{-(k_S/t_S)} \quad [5]$$

Where C_{H_ini} is the initial discharge capacity corresponding to the high plateau, k_S is the self-discharge constant, and t_S is the idling time. The self-discharge constant k_S is possible to be determined experimentally,

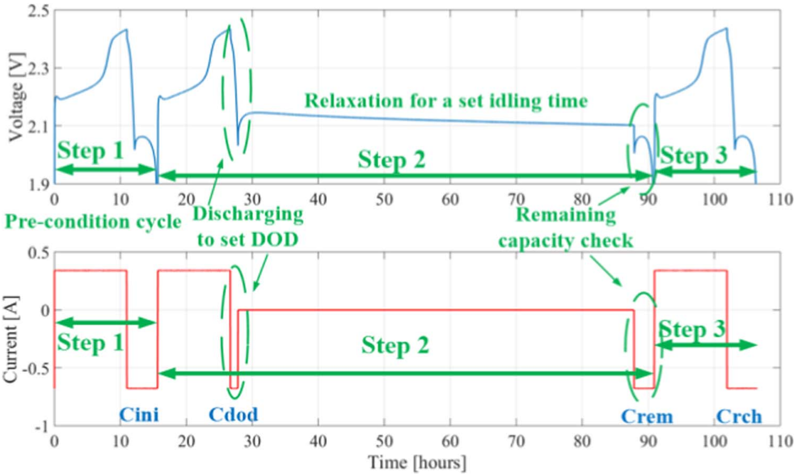

Figure 1. Standard test protocol for systematic self-discharge measurement.

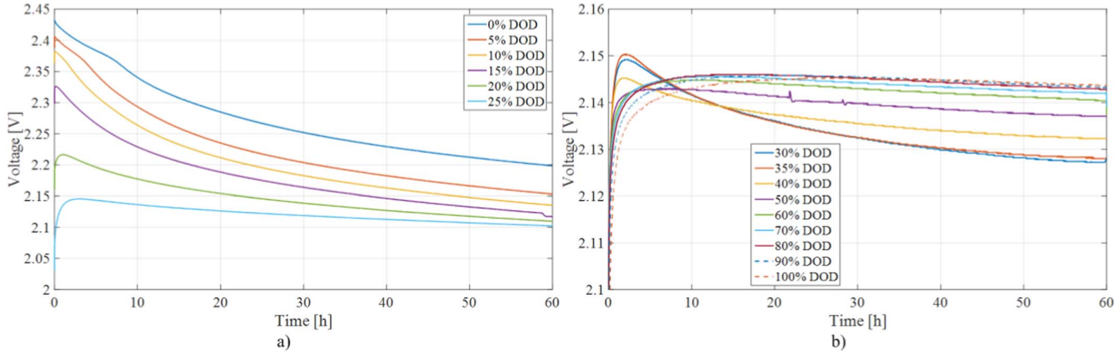

Figure 4. Voltage evolution during 60 hours of relaxation at 35°C, a) for initial DOD between 0 and 25%, b) for initial DOD between 30 and 100%.

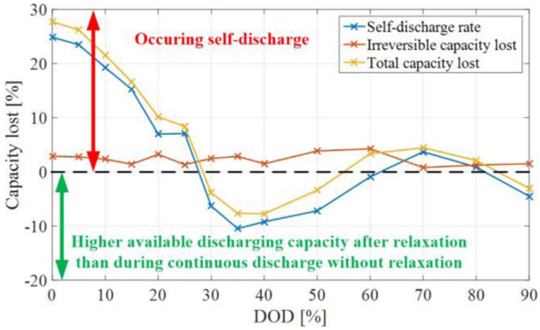

Figure 5. The self-discharge (capacity lost) at 35°C computed after 60 hours of relaxation.

as the slope of the line describing the variation of $\ln(C_H/C_{H\_ini})$ with the idling time t_S.

Results and Discussion

Self-discharge dependence on DOD level.—To identify the self-discharge dependence on the DOD level, the Li-S battery cell was kept at 35°C for a period t_S of 60 hours. The battery cell voltage evolution during the 60 hours of relaxation is shown in Fig. 4. The voltage of the Li-S battery cell went at first through a recovery phase after the discharge, where the voltage was rising. The time of the recovery phase is increasing with higher DOD levels. After the recovery phase, the voltage was decaying for all DOD levels and as one can observe, 60 hours is not enough to reach steady-state. Moreover, a relationship between a higher DOD level and a lower voltage value (at the end of the 60 hours of relaxation) corresponds only until a DOD level of 25%, which refers to the end of discharge in the high voltage plateau, as illustrated by the relaxation voltages in Fig. 4a). From 30% DOD, this trend is reversed and higher voltage values are achieved for higher considered DOD levels, which corresponds to the end of discharge in the low voltage plateau, as illustrated by the relaxation voltages in Fig. 4b).

The dependence of the self-discharge on the DOD level is shown in Fig. 5. The self-discharge rate and total capacity loss is decreasing with increasing the DOD level until 30% DOD. As this behavior occurs at the high voltage plateau, it might be related to the strong effect of the polysulfide shuttle. From 30 to 60% and for 90 to 100% DOD the computed self-discharge rate value becomes negative. The negative value of the self-discharge rate is an indicator that the actual discharged capacity from the cell, after 60 hours of relaxation, is higher than the expected discharge capacity, estimated based on the capacity test by continuous discharge without any idling. Thus, a higher charge in the battery cell is available to be discharged at these conditions by introducing relaxation periods before discharging. However, from 60 to 80% DOD, the cell presented again a positive self-discharge rate. The specific reason and proof for such a non-consistent behavior, at the low voltage plateau, has not been identified. The irreversible capacity loss takes values between 0.77 and 4.24% with an average of 2.29% of the actual total capacity.

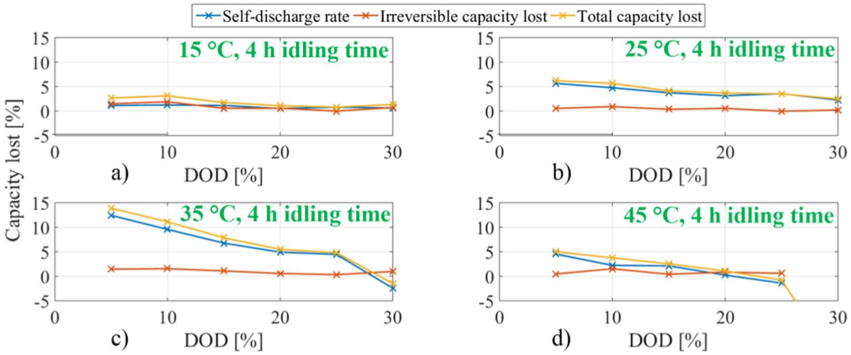

Figure 6. The self-discharge dependence break down to reversible (= self-discharge rate), irreversible and total capacity lost for 4 hours idling time at various temperatures and DOD levels.

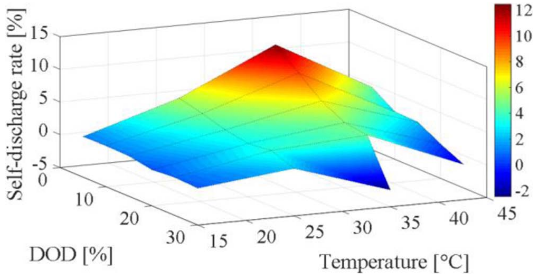

Figure 7. The self-discharge rate dependence on the DOD level and temperature for an idling time of 4 hours.

Self-discharge dependence on temperature and DOD for 4 hours idling time.—In this test procedure, the Li-S battery cell was discharged to a specific DOD level (from 5% to 30% considering a 5% resolution step) and the idling time t_S was set at four hours. Four measurement temperatures were considered, i.e., 15, 25, 35 and 45°C. The values of the capacity losses during storage were computed according to (1–4). Their dependence on DOD is presented separately for each temperature in Fig. 6. Fig. 7 shows the dependence of the self-discharge rate on DOD and temperature. As expected, for the case of four hours idling time as well, the self-discharge rate is decreasing with increasing the DOD level. By increasing the temperature from 15°C to 35°C, an increase of the self-discharge was observed; nevertheless, by further increasing the temperature to 45°C, a decrease in the self-discharge was obtained. This change of trend can be explained by examining the DOD measurement points and their position toward the high voltage plateau as illustrated in Fig. 8. As one can observe, the length of the high voltage plateau (expressed as function of DOD) is decreasing with increasing the temperature; nevertheless, for temperatures of 15, 25 and 35°C, the high voltage plateau still corresponds to a DOD level of approximately 30%. In the case of 45°C, the high voltage plateau ends at approximately 18% DOD, which might be caused by the strong presence of the polysulfide shuttle, which prevents the cell be fully charged and causing extremely high self-discharge in this region.

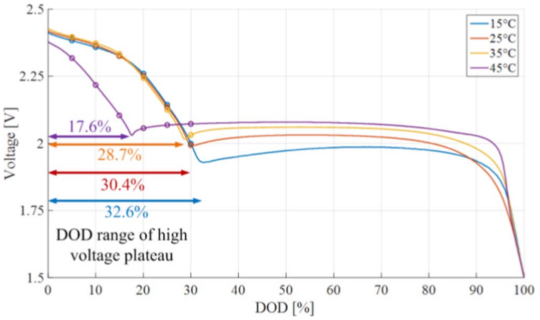

Figure 8. Positions of the measured points for self-discharge at voltage curve during continuous discharge with relation to DOD levels related separately to each temperature.

Self-discharge dependence on the idling time.—During this test, the cells were stored at five different conditions in order to identify a self-discharge trend related to temperature and DOD for various idling time values. The considered test conditions were: 10% DOD for 15, 25, and 35°C and 35°C for 0, 10, and 20% DOD. The capacity loss dependence on the idling time t_S is shown in Fig. 9. As one can see, the self-discharge is increasing over time, but the steepness of its growth reduces with increasing the DOD level. The evolution of the self-discharge rate characteristic due to the increase in the temperature is shown in Fig. 10a; the self-discharge rate of the Li-S battery cell is higher with increasing temperature within the first 24 hours. For 60 hours of idling time, the results are not conclusive. The comparison between the self-discharge rate increase as function of idling time measured at 0, 10 and 20% DOD is shown in Fig. 10b. If for short idling times (i.e., up to two hours), a similar self-discharge rate has been obtained for 10 and 20% DOD, once the idling time has increased a steeper increase of the self-discharge was observed for the lower DOD level (i.e., 10%). An overall visible trend from Fig. 10b is that the self-discharge rate is higher with a lower DOD level. Furthermore, by comparing the influence of the temperature and of the DOD influence on the

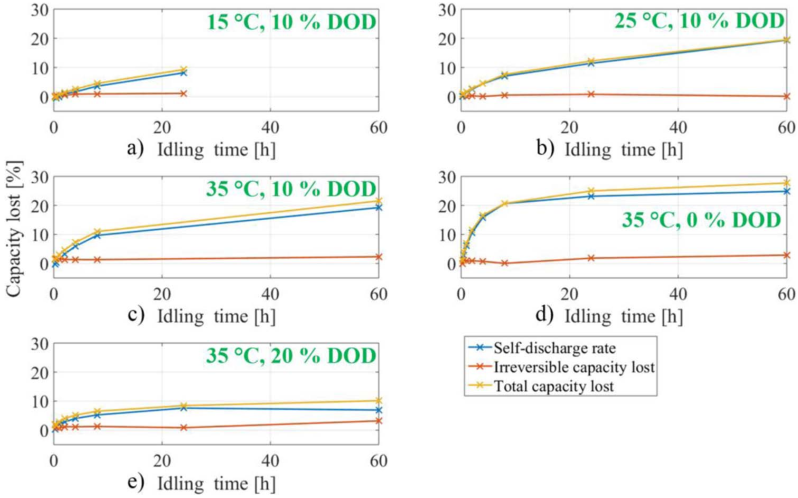

Figure 9. The self-discharge dependence break down to reversible (= self-discharge rate), irreversible and total capacity lost for various temperature, DOD and idling time.

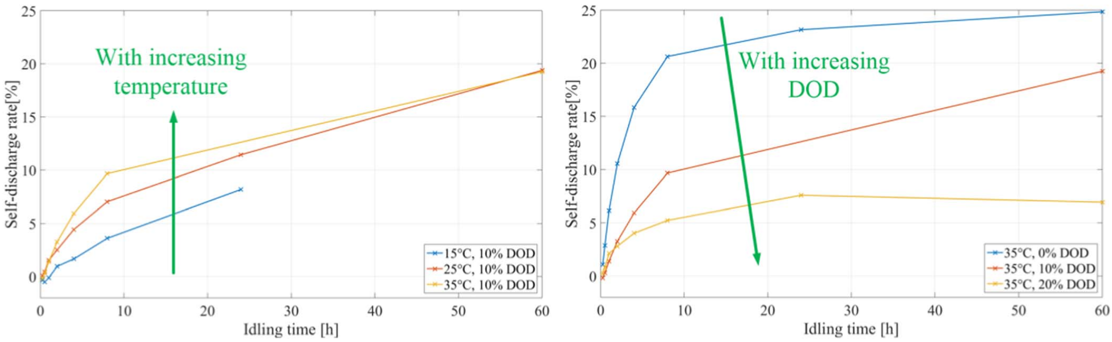

Figure 10. Self-discharge rate as a function of the idling time: a) at 10% DOD for 15, 25, and 35°C temperature levels and b) at 35°C for 0, 10, and 20% DOD levels.

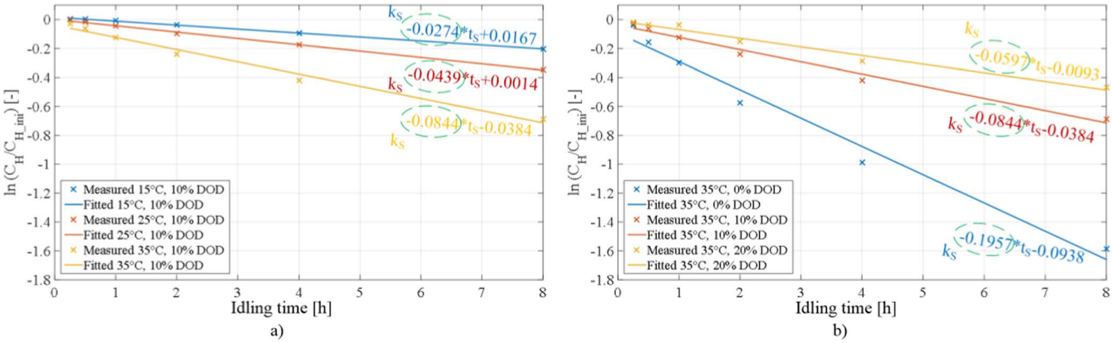

a) b)

Figure 11. Logarithmic expression of remaining and initial high voltage plateau capacities from experimental results as a function of time and a fitted linear curve: a) at 10% DOD for 15, 25 and 35°C temperature levels and b) at 35°C for 0, 10 and 20% DOD levels.

self-discharge rate, one can conclude that the DOD has a higher impact than the temperature in the range 0 – 20% DOD and 15 – 35°C.

Self-discharge constant.—To determine the self-discharge constant, the ratio between the measured initial and remaining capacities corresponding to the high voltage plateau was plotted against the idling time on a logarithmic scale and fitted by a linear curve as it is illustrated in Fig. 11. For this purpose, there were considered measurement data from self-discharge tests carried out for an idling time between 15 minutes and 8 hours. Based on Ref. 2, the self-discharge constants k_S were identified as the slopes of the fitting curves values, as shown in Fig. 11.

The next step was to estimate, for each considered condition (DOD and temperature), the capacity of the high voltage plateau C_H according to 5, using the previously obtained self-discharge constant k_S, and compare it with the experimental measurements. The obtained capacities in function of idling time, corresponding to the high voltage plateau, are shown in Fig. 12. The relative errors corresponding

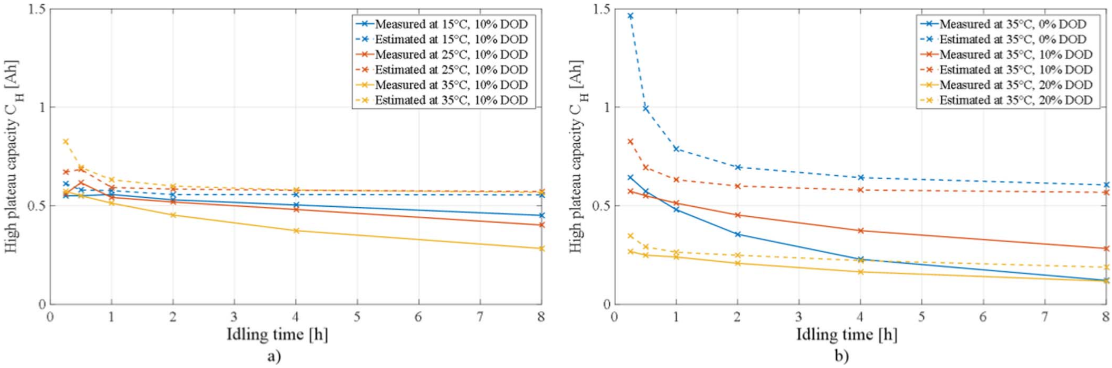

a) b)

Figure 12. Estimated and measured capacities of the high voltage plateau for various idling conditions: a) at 10% DOD for 15, 25 and 35°C temperature levels and b) at 35°C for 0, 10 and 20% DOD levels.

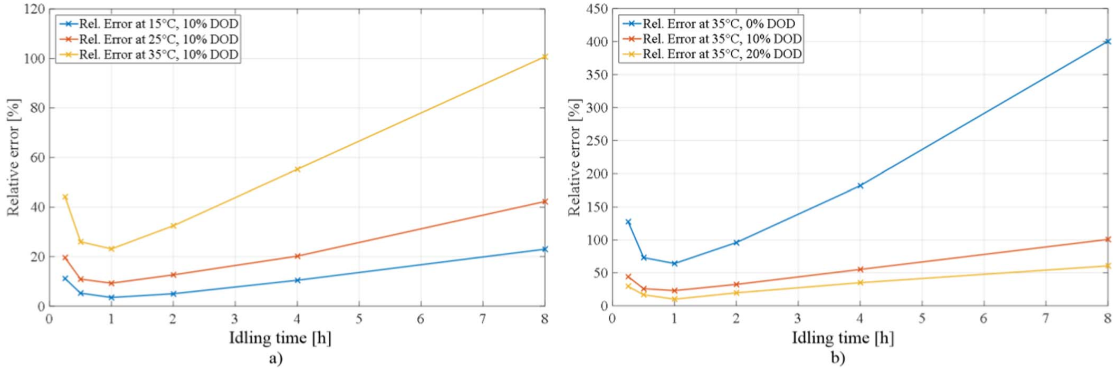

Figure 13. The relative error of the estimated C_H computed according to 5, a) at 10% DOD for 15, 25 and 35°C temperature levels and b) at 35°C for 0, 10 and 20% DOD levels.

to the estimation of the high voltage plateau capacity, which were obtained according to the methodology proposed in Ref. 2, are presented in Fig. 13. By analyzing these results, one can conclude that a prediction of the self-discharge based on 5 and experimentally found self-discharge constants k_S is considered not sufficiently accurate and another approach is needed to be used.

Conclusions

The self-discharge behavior of a 3.4 Ah Li-S battery cell was experimentally investigated and quantified in this paper. The self-discharge process is mainly caused by the polysulfide shuttle and it appears especially at the high voltage plateau, where with increased DOD levels, the self-discharge is reduced. At the low voltage plateau, between 30 and 60% DOD and between 90 and 100% DOD, for the considered idling time of up to 60 hours and temperature of 35°C, self-discharge of the Li-S battery cell was not observed; on the contrary, more charge was available to be discharged from the cell after idling than in the case of a continuous discharge of the Li-S battery cell. However, this trend is not consistent for the entire low voltage plateau at 35°C, as self-discharge was measured for the interval 60 – 80% DOD.

Furthermore, the self-discharge rate was found to increase with increasing temperature, until 35°C for four hours idling period. At 45°C, the self-discharge behavior is changing the trend due to a highly reduced high voltage plateau, which is caused by a not fully utilized charging. By comparing the temperature and DOD influence on the self-discharge rate, it was found out that the DOD has a higher influence than the temperature in the interval 0 – 20% DOD and 15 – 35°C.

By seperating the total capacity loss, occured for the investigated cases, into reversible and irreversible capacity loss, one can observe that the reversible capacity loss, referred as the self-discharge rate, which is caused by the self-discharge processes, plays a major role than the irreversible capacity loss, which comes from the degradation due to idling and cycling of the cell. The observed irreversible capacity loss appeared to be relatively constant during the experiments; in order to identify its dependence on the individual factors there is a need for further study.

Finally, an estimation of the remaining capacity corresponding to the high voltage plateau was performed by identifying the self-discharge constant k_S; however, the method needs to be further improved in order to provide more accurate results for various idling conditions.

Acknowledgments

This work has been part of the ACEMU-project. The authors gratefully acknowledge the Danish Council for Strategic Research (1313-00004B) and EUDP (1440-0007) for providing financial support and thank OXIS Energy for supplying the Lithium-Sulfur battery cells.

References

1. D. Bresser, S. Passerini, and B. Scrosati, *Chem. Commun.*, **49**, 10545 (2013).
2. Y. V. Mikhaylik and J. R. Akridge, *J. Electrochem. Soc.*, **151**, A1969 (2004).
3. H. Ryu, H. Ahn, K. Kim, J. Ahn, J. Lee, and E. Cairns, *J. Power Sources*, **140**, 365 (2005).
4. H. S. Ryu, H. J. Ahn, K. W. Kim, J. H. Ahn, K. K. Cho, and T. H. Nam, *Electrochim. Acta*, **52**, 1563 (2006).
5. M. Kazazi, M. R. Vaezi, and A. Kazemzadeh, *Ionics*, **20**, 1291 (2014).
6. D. Moy, A. Manivannan, and S. R. Narayanan, *J. Electrochem. Soc.*, **162**, A1 (2014).
7. J. Zheng, M. Gu, H. Chen, P. Meduri, M. H. Engelhard, J.-G. Zhang, J. Liu, and J. Xiao, *J. Mater. Chem. A*, **1**, 8464 (2013).
8. A. Manthiram, S.-H. Chung, and C. Zu, *Adv. Mater.*, **27**, 1980 (2015).
9. N. Azimi, Z. Xue, N. D. Rago, C. Takoudis, M. L. Gordin, J. Song, D. Wang, and Z. Zhang, *J. Electrochem. Soc.*, **162**, 64 (2015).
10. M. L. Gordin, F. Dai, S. Chen, T. Xu, J. Song, D. Tang, N. Azimi, Z. Zhang, and D. Wang, *ACS Appl. Mater. Interfaces*, **6**, 8006 (2014).
11. J.-Q. Huang, T.-Z. Zhuang, Q. Zhang, H.-J. Peng, C.-M. Chen, and F. Wei, *ACS Nano*, **9**, 3002 (2015).
12. C. J. Hart, M. Cuisinier, X. Liang, D. Kundu, A. Garsuch, and L. F. Nazar, *Chem. Commun.*, **51**, 2308 (2015).
13. C. E. Parfitt, PhD thesis, University of Warwick (2012).

Paper A7

A self-discharge model of Lithium-Sulfur batteries based on direct shuttle current measurement

Vaclav Knap, Daniel-Ioan Stroe, Maciej Swierczynski, Rajlakshmi Purkayastha, Karsten Propp, Remus Teodorescu and Erik Schaltz

The paper has been published in the *Journal of Power Sources*, vol. 336, pp. 325–331, 2016, doi:10.1016/j.jpowsour.2016.10.087. Reprinted with permission from Elsevier 2017. Accepted version of the manuscript.

A Self-discharge Model of Lithium-Sulfur Batteries Based on Direct Shuttle Current Measurement

Author Names: Vaclav Knap[a,*], Daniel-Ioan Stroe[a], Maciej Swierczynski[a], Rajlakshmi Purkayastha[b], Karsten Propp[c], Remus Teodorescu[a] and Erik Schaltz[a]

Affiliation(s): [a] Department of Energy Technology, Aalborg University, Aalborg, 9000, Denmark
[b] Oxis Energy Ltd, Culham Science Centre, Abingdon, Oxfordshire OX14 3DB, United Kingdom
[c] Centre for Automotive Engineering and Technology, Cranfield University, Bedfordshire MK43 0AL, United Kingdom
[*]Corresponding Author. Tel: +45 20294922, Fax: +45 9815 1411 E-mail Address: vkn@et.aau.dk

In the group of post Lithium-ion batteries, Lithium-Sulfur (Li-S) batteries attract a high interest due to their high theoretical limits of the specific capacity of 1672 Ah kg-1 and specific energy of around 2600 Wh kg-1. However, they suffer from polysulfide shuttle, a specific phenomenon of this chemistry, which causes fast capacity fade, low coulombic efficiency, and high self-discharge. The high self-discharge of Li-S batteries is observed in the range of minutes to hours, especially at a high state of charge levels, and makes their use in practical applications and testing a challenging process. A simple but comprehensive mathematical model of the Li-S battery cell self-discharge based on the shuttle current was developed and is presented. The shuttle current values for the model parameterization were obtained from the direct shuttle current measurements. Furthermore, the battery cell depth-of-discharge values were recomputed in order to account for the influence of the self-discharge and provide a higher accuracy of the model. Finally, the derived model was successfully validated against laboratory experiments at various conditions.

Keywords: Lithium-Sulfur battery, self-discharge, polysulfide shuttle, modelling, validation.

1. Introduction

Lithium-Sulfur (Li-S) batteries represent a promising alternative to the Lithium-ion battery chemistry, due to their high theoretical limits in terms of specific capacity (i.e. 1672 Ah kg-1) and specific energy (i.e. 2600 Wh kg-1). Furthermore, they are expected to become a cheaper and more environmentally friendly solution, mainly due to the use of sulfur, which is an abundant and benign element. However, besides other chemistry related phenomena, Li-S batteries suffer from polysulfide shuttle, which results in several commonly known drawbacks: fast capacity fade, low coulombic efficiency, and high self-discharge [1], [2].

For the practical use of the Li-S batteries, there is a need not only to characterize the self-discharge behavior as it was done in [3], but also to provide a proper simulation tool (a model), relevant for industrial applications and laboratory experiments as well; otherwise, biased results can be acquired (e.g. not corresponding depth-of-discharge (DOD) levels assigned). The main cause of self-discharge for Li-S cells was identified to be the polysulfide shuttle and afterwards the corrosion of the current collectors [4], [5],

[6], [7]. Because the polysulfide shuttle is present not only during the cell idling, but also during charging and discharging, the self-discharge appears as well during these conditions. A mechanistic model of the polysulfide shuttle causing the self-discharge of the Li-S battery cells was presented in [8]. However, the purpose of the model was to provide insights into the key battery mechanisms, rather than to be used from an end-application perspective. The mathematical model presented in [9] and a zero dimensional model for the Li-S batteries introduced in [10] are using the relations for the polysulfide shuttle derived from [4]. However, these relations are based on determining experimentally a shuttle constant k_S, which is a time-consuming procedure; moreover, it might not always provide sufficiently accurate results for the self-discharge estimation, as it was indicated in [3]. Another simple approach was used in [11], where the self-discharge current was related to the charge lost during idling at 100 % state-of-charge (SOC). The self-discharge current was identified to be proportional to the square root of the idling time. However, the model characterization tests for the 100 % SOC condition took more than nine days and it was assumed that self-discharge current is dependent on the used power profile. Furthermore, a methodology for direct shuttle current measurement was proposed in [12], where its results were analyzed and validated using the one-dimensional phenomenological model, which is based on Nernst and species concentrations equations. This methodology allows for a simple and time-effective measurement of the shuttle current at different SOC levels; it is based on the premise that the shuttle current can be observed as the steady-state current flows through the cell, while its voltage is kept constant during constant voltage operation to prevent the voltage decay.

In this paper, the direct shuttle current measurement method is used to identify the shuttle current of a 3.4 Ah Li-S pouch cell at different depth-of-discharge levels and temperatures. Furthermore, the obtained results are used to derive a simple and easy-to-use mathematical model of the self-discharge in the Li-S battery cell that is related to the polysulfide shuttle phenomenon. This model is validated against several self-discharge experiments at various conditions and it is suitable to predict the self-discharge during idling and operation of the battery.

2. Methodology

The work flow followed in this paper is summarized and presented in Fig. 1. At first, the measurements were performed and they are described in Section 2.1 for direct shuttle current measurements and in Section 2.2 for the self-discharge model validation measurements. The current shuttle measurement results are presented in Section 3 and later on in Section 3.1 it is also shown how the mathematical expression for the self-discharge model dependent on DOD and temperature is derived. Later on, there were considered three fitting cases. Fitting Case 1 (Section 3.1.1) uses the pre-determined DOD points to develop the model, Fitting Case 2 (Section 3.1.2) recomputes and ‘corrects‘ the DOD points according consideration of the self-discharge ongoing during the measurements and Fitting Case 3 (Section 3.1.3) adds up simulation of the measurement to update the DOD points. Each of these fitting cases parameterize the self-discharge model and its accuracy is later validated in Section 3.2 by an use of the validation measurements (Section 2.2) and the SOC estimation model for the validation (Section 2.3) with the consideration of the total capacity concept (Section 2.4). The discussion about SOC reference frame and cell history effect, which are related to the self-discharge model integration and use, is hold in Section 4.1. Furthermore, the alternative version of the self-discharge model considering dependence on the open-circuit voltage rather than DOD is discussed in Section 4.2.

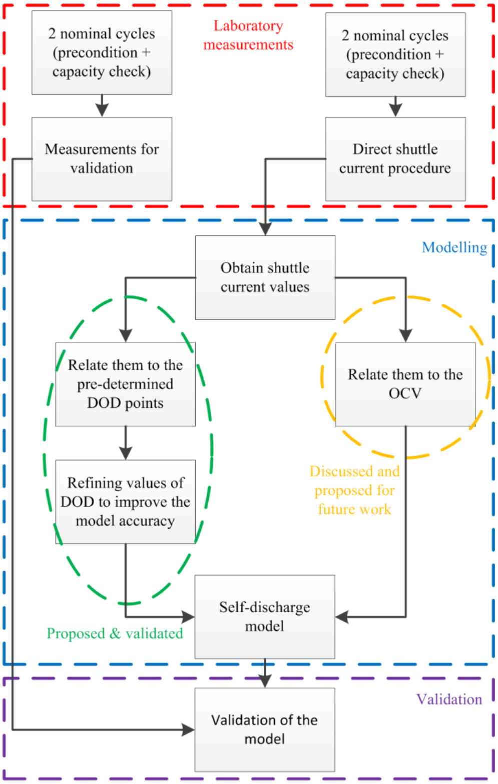

Figure 1. Work flow scheme used for the self-discharge model derivation and validation.

All the measurements were performed on a single 3.4 Ah long life chemistry Li-S pouch cell manufactured by OXIS Energy. A Digatron BTS 600 battery test station was used for the direct shuttle current measurement procedure. To avoid battery cell overcharging and in order to reduce the degradation of the cell at a high current shuttle region, for all the charging conditions, charging time limitations were applied as well (8.5 hours for 15 °C, 9 hours at 25 °C and 10.5 hours for 35 °C). The values of 0.1 and 0.2 C-rate correspond to 0.34 and 0.68 A currents, respectively.

2.1 Direct Shuttle Current Measurement

The applied test procedure for the direct shuttle current measurement is based on the methodology presented in [12] and illustrated in Fig. 2. The procedure started with two nominal cycles: 0.1 C-rate constant current charging until 2.45 V and 0.2 C-rate discharging to 1.5 V. The first cycle served as a pre-condition cycle, which is needed in order to ‘reset’ the cell’s history (as the Li-S is a soluble chemistry) and to bring the cell to the similar initial condition at the selected temperature. The second cycle was used for the cell’s capacity check and its calculation for the further procedure steps. Afterwards, the cell was charged fully (by 0.1 C-rate to 2.45 V) and discharged (by 0.2 C-rate) to a set DOD point (i.e. 2 %). Then, the cell was rested in open circuit condition in order to reach an open-circuit voltage (OCV) value. The OCV is considered as an equilibrium voltage point, which is the peak value between voltage rise during the recovery period and voltage fall during the predominant self-discharge. However, in practice, due to the noise in the voltage signal, the reliable value of the OCV was determined when the battery voltage dropped from the maximum point by 0.6 mV (three times the value of the battery test station accuracy which was equal to 0.2 mV) as it is presented in Fig. 3. In the next step, these detected OCV value was used later in two hours constant voltage charging, in order to determine the steady-state current as it is presented in Fig. 3. This steady-state current is considered as the shuttle current. All these above mentioned steps are repeated for other DOD values (2 % step resolution until 30 % DOD or until there is no detection of the voltage peak in a 12 hours relaxation period). The voltage and current signals during the direct shuttle current measurement procedure are shown in Fig. 3 for DOD equal to 10 % at 35 °C. Next, the direct shuttle current measurement procedure was repeated for other temperatures (15, 25 and 35 °C). The whole measurement procedure, (including the two full cycles performed in the beginning), lasted between 4 and 4.5 days for each of the considered temperatures.

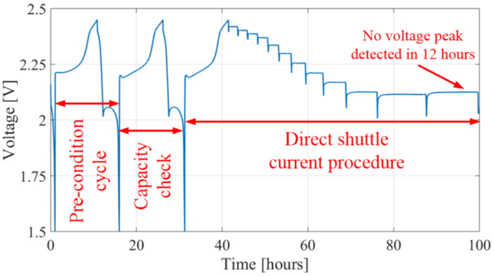

Figure 2. Overall test procedure for the direct shuttle current measurement.

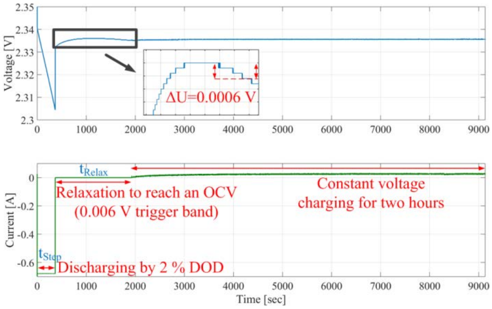

Figure 3. Illustration of current and voltage signals during the direct shuttle current measurement.

2.2 The Measurements for Validation of the Self-Discharge Model

The self-discharge measurement procedure is based on the methodology presented in [3] and it is illustrated in Fig. 4. At first, a pre-condition cycle and capacity check cycle were performed, the same as in the case of the direct shuttle current measurement. This step was followed by charging the cell (by 0.1 C-rate to 2.45 V) and discharging (by 0.2 C-rate) to a pre-determined DOD value (this discharging step was skipped for 0 % DOD). Then, the cell was kept at open circuit condition ("relaxation stage") for a specific time and afterwards fully discharged (by 0.2 C-rate to 1.5 V).

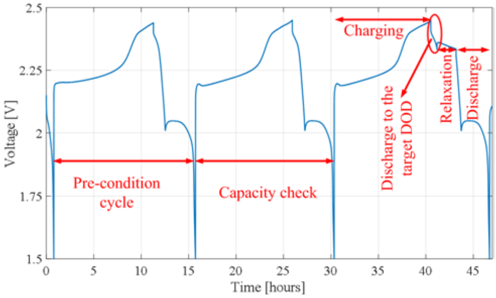

Figure 4. Test procedure for the self-discharge model validation.

2.3 Matlab/Simulink Model for Validation

The self-discharge Li-S model is going to be integrated into a Matlab/Simulink model, which allows for SOC estimation based on the coulomb counting method. The used SOC definition in this work follows the definition described in [13]. So the SOC represents the relation between the actual useable battery capacity (C_a) and the total capacity (C_t) available to be discharged after the battery being fully charged. This expressed in percentage is written as $SOC=C_a/C_t*100$. Using only coulomb counting method, without accounting for the fast self-discharge of the Li-S batteries will lead inevitably to a growing error due to not capturing the self-discharge current. The SOC estimation model is driven by following equations:

$$\mathrm{SOC} = \mathrm{SOC_{ini}} + \int(-(\mathrm{I}+\mathrm{I_{sh}})*100/(\mathrm{C_t}*3600)*\mathrm{dt}) \tag{1}$$

$$\mathrm{DOD} = 100 - \mathrm{SOC} \tag{2}$$

Where SOC is the actual state-of-charge, SOC_{ini} is the initial state-of-charge, I is the applied current (discharging current has positive sign orientation), I_{sh} is the shuttle current, C_t is the total capacity of the cell at the specific temperature, and DOD is the depth-of-discharge.

2.4 Concept of the total capacity of the Li-S batteries

The standard practice to determine the capacity of Li-S battery cells is to continuously discharge before-hand fully charged battery by a specific current at a specific temperature. The obtained discharged capacity is considered as the capacity of the cell at those conditions. However, as the polysulfide shuttle is present during the Li-S cell discharging, it causes self-discharge, which consequently reduces the measured capacity. Therefore, the term of total capacity C_t of the cell is introduced as follows:

$$C_t = C_{cdch}+C_{sd} \tag{3}$$

Where C_{cdch} is the capacity measured during the continuous discharge test for the specific current rate and temperature and C_{sd} is the capacity lost due to the self-discharge during this test. C_{sd} is obtained from the simulation of the cell's continuous discharge with C_{cdch} replacing C_t in (1). Moreover, the I_{sh} is excluded from the coulomb counting in (1) and it is integrated and recorded separately. C_{sd} is the final value of the lost capacity corresponding to the total current I_{sh} recorded during this discharge simulation. This presented concept of the total capacity allows the self-discharge model to estimate the self-discharge during dynamically changing operating conditions.

3. Measurement Results and Modelling

The current profiles obtained from the constant voltage charging steps during the direct shuttle current measurements, at 35 °C, are presented in Fig. 5. At least two hours of constant voltage charging are necessary to reach a state close to steady-state. Due to the accuracy of the test station, extra noise is appearing at the current values lower than 0.06 A. In order to get a higher accuracy of the measured shuttle current values, the measurement can be repeated using equipment dedicated for lower current ranges. However, for the demonstration purposes of the model, in this paper, it is considered sufficient to take an average of the last ten minutes of the current profile during constant voltage charging step as the value for the shuttle current. The measured shuttle current values are presented in Fig. 6, for the pre-determined DOD levels.

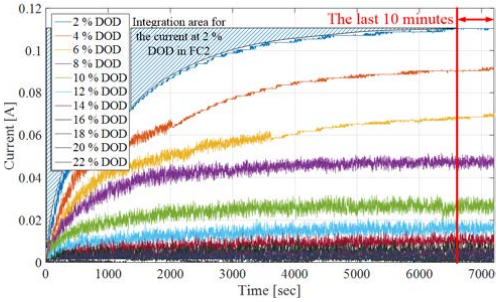

Figure 5. Battery currents during the constant voltage charging step at 35 °C. The shuttle current value is taken as the average of the last ten minutes interval. The integration area for the current at 2 % DOD used in FC2 is marked by blue stripes.

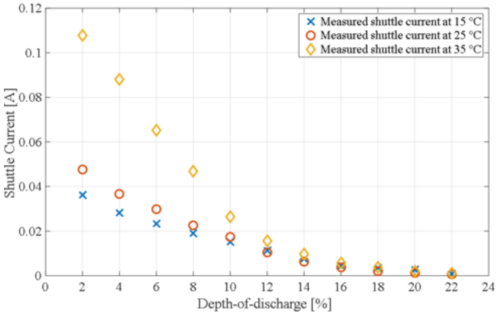

Figure 6. The measured shuttle current values for pre-determined DOD points.

3.1 Fitting procedure and deriving the model

Based on the results presented in Fig. 6, it is assumed that an exponential function can be used to describe the dependence of the shuttle current on the DOD. Therefore, all the obtained curves, one for each temperature, are fitted with the following exponential function with parameters *a* and *b*:

$$I_{sh}=a*\exp(b*DOD) \tag{4}$$

Furthermore, in a second step, the obtained parameters *a* and *b* were fitted as a function of temperature; during this step, it was found out that the dependence on temperature of parameters a and b follows an exponential and linear function, respectively. The functions for both parameters *a* and *b* are shown below:

$$a=c*\exp(d*Temp) \tag{5}$$

$$b=e*Temp+f \tag{6}$$

By substituting the functions for *a* and *b* into (4), the general mathematical model for estimating the self-discharge of Li-S batteries, considering the dependence on DOD and temperature was obtained as given in (7):

$$I_{sh}=c*\exp(d*Temp)*\exp((e*Temp+f)*DOD) \tag{7}$$

Where *Temp* is the temperature in degrees Celsius and *c*, *d*, *e* and *f* are parameters obtained by fitting the parameters *a* and *b* in function of temperature. So, the self-discharge model’s inputs are the temperature and the DOD, while the output is the self-discharge current, which should be connected to the coulomb counting, if present, or to another implemented SOC estimator.

3.1.1 Fitting Case 1

The first fitting step, referred as Fitting Case 1 (FC1), was performed by fitting the experimentally determined direct shuttle current values against the DOD points (see Fig. 6). For the last DOD level, when during the battery cell relaxation period of 12 hours a peak voltage value was not detected (as described in the methodology in the previous section), a shuttle current value equal to zero was considered for fitting purposes. The considered DOD levels are shown in Table I for FC1 and 35 °C. However, these pre-determined DOD points might not accurately correspond to the actual DOD levels of the cell as the influence of the shuttle current was not considered during the measurement procedure.

TABLE I. Considered and recomputed DOD values at 35 °C for fitting at various fitting cases.

	DOD [%]											
FC 1	2	4	6	8	10	12	14	16	18	20	22	24
FC 2	3.70	7.35	10.80	13.73	16.33	18.90	21.42	23.83	26.27	28.56	30.82	32.82
FC 3	4.17	7.15	9.93	12.60	15.74	18.81	21.86	24.89	27.91	30.99	34.27	37.24

3.1.2 Fitting Case 2

Therefore, for the Fitting Case 2 (FC2), it was assumed that the self-discharge was ongoing already during the discharging steps, during the relaxation periods before the constant voltage charging step, and during the constant voltage charging step in the characterization experiment, as it is illustrated in Fig. 3. The time values of discharging and relaxation were computed and multiplied by the measured shuttle current value for the first DOD point (i.e. 2 %), which provided an estimate of the ampere-hours lost due to self-discharge during that period. During two hours of constant voltage charging period (i.e. keeping the constant voltage at the battery terminals), the shuttle current is compensated by an external current approximately in the last ten minutes, as they are considered to be equal there. However, during the previous one hour and fifty minutes, the shuttle current is only partially compensated as the external current is lower. Therefore, the amount of the self-discharged ampere-hours can be obtained by integration of the area above the current curve in a rectangle from the beginning of the constant voltage charging up to one hour and fifty minutes time coordinates. This integration area, as an example for the current at 2 % DOD, is illustrated in Fig. 5 by the blue stripes. The same procedure was repeated for the remaining DOD points, considering also the correction from the previous DOD point. The newly obtained values are presented in Table I. Furthermore, the exact formula describing the correction procedure used for FC2 can be written as:

$$DOD_{new}(n) = \left(\sum_1^n DOD_{Step}(n) + \sum_1^n \left(t_{Step}(n) + t_{Relax}(n)\right) \cdot I_{sh}(n) + \sum_1^n \left(6600 \cdot I_{sh}(n) - \int_0^{6600} I_{meas}(n) \cdot dt\right)\right) / C_{cdch} \cdot \frac{100}{3600} \tag{8}$$

Where DOD_{new} is the new recomputed DOD point (replacing a pre-determined DOD point), n is the number of the discharging step, DOD_{Step} stands for a DOD change to reach the n-th pre-determined DOD point from the previous one, t_{Step} is time spent during the discharging step in seconds, t_{Relax} is time spent during relaxation before constant-voltage charging step in seconds, I_{sh} is the shuttle current captured for the n-th DOD point, I_{meas} is the measured external current and C_{cdch} is the capacity of the cell measured during the continuous discharge test in Ampere-hours. 6600 is the number of seconds representing one hour and fifty minutes - after this time the shuttle current is considered to be fully compensated by the external current.

3.1.3 Fitting Case 3

For the further improvement of the model, the Fitting Case 3 (FC3) was applied to obtain the total capacity. The Simulink model, including the self-discharge model obtained at the end of FC2, was fed by the current profile obtained from the direct current shuttle procedure. Thus, the DOD points, corresponding to the shuttle current values, were extracted and are presented in Table I for 35 °C.

The parameters *c*, *d*, *e* and *f* of the shuttle current model for all the fitting cases are presented in Table II.

TABLE II. Found parameters for the fitting cases.

	c	d	e	f
FC 1	0.011000	0.07765	-0.0017110	-0.07250
FC 2	0.009507	0.08390	-0.0009985	-0.07511
FC 3	0.009064	0.08709	-0.0008050	-0.08524

The presented fitting procedure with all three fitting cases and their steps are visualized in Fig. 7.

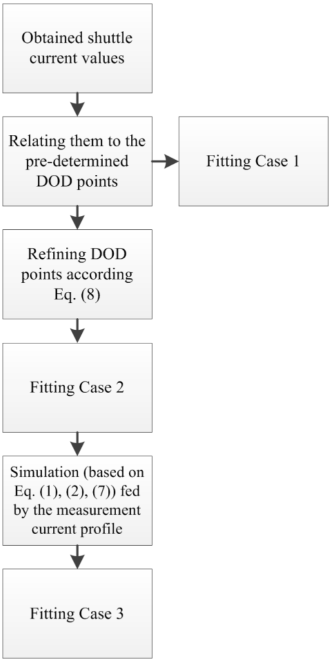

Figure 7. Illustration of the fitting procedure steps.

3.2 Validation of the self-discharge model

For the validation of the self-discharge model, four validation measurements were performed according to the procedure described in Section 2.2. The validation cases consider various temperature conditions, idling times and initial DOD levels. The specific conditions are presented in Table III. The absolute self-discharge estimation error (Err_{abs}) and relative self-discharge estimation error (Err_{rel}) were computed as follows:

$$Err_{abs}=C_{meas}-C_{est} \tag{9}$$

$$Err_{rel}=(C_{meas}-C_{est})/C_{meas}*100 \tag{10}$$

Where C_{meas} is remaining measured capacity and C_{est} is remaining estimated capacity.

A comparison of the accuracy values of the developed self-discharge model for the different used fitting cases is shown in Table III. The relative errors are noticeably reduced by moving from FC1 to FC2, except the Validation Case 1, where only a minor increase is observed. The error reduction implies the correctness of the assumptions used for FC2 and that the self-discharge due to the polysulfide shuttle is still present, no matter if the Li-S battery is in charging, relaxation or discharging stage. The further move to FC3 did not bring any improvements in terms of accuracy. However, this might be related to the fitting of the parameter *b*, which in the FC3 lost its linear character and thus the fitting error was increased. To confidently determine the new trend, it might be needed to have more temperature points available for the fitting.

TABLE III. Relative errors of validation cases for different fitting cases.

Validation cases	**Relative error**		
	Fitting Case 1	**Fitting Case 2**	**Fitting Case 3**
Validation Case 1 0 % DOD, 20 °C, 4 hours idling	1.29 %	1.60 %	1.59 %
Validation Case 2 0 % DOD, 30 °C, 12 hours idling	11.04 %	6.65 %	6.69 %
Validation Case 3 10 % DOD, 25 °C, 6 hours idling	4.62 %	2.66 %	2.82 %
Validation Case 4 15 % DOD, 35 °C, 2 hours idling	7.98 %	3.95 %	3.96 %

The detailed results for the validation of the proposed self-discharge model, which was parametrized based on FC2, are shown in Table IV. One can observe that the model is capable to predict accurately the self-discharge ongoing in Li-S batteries, for short term (e.g., less than twelve hours) with a relative error smaller than 7 %; furthermore, for most real-life applications relaxation periods longer than 12 hours are not very common. This model is applicable for the temperatures inside the characterization window between 15 and 35 °C, according to the performed experiments. It is worth to note that the self-discharge estimation error is influenced also by the irreversible degradation, appeared during the characterization and verification experiments. By accounting for this degradation, the model error can be further decreased. Moreover, because the Li-S is a solution chemistry, changes in the polysulfide species might occur, accelerated by longer time span and higher temperature, which could further negatively influence the final accuracy of the model.

TABLE IV. Measured and estimated battery cell capacities and their absolute and relative errors for four validation cases with the self-discharge model parametrized based on FC2.

Validation cases	**Final capacity measured**	**Final capacity estimated**	**Absolute error**	**Relative error**
Validation Case 1 0 % DOD, 20 °C, 4 hours idling	2.606 Ah	2.5642 Ah	0.0418 Ah	1.60 %
Validation Case 2 0 % DOD, 30 °C, 12 hours idling	2.262 Ah	2.4125 Ah	-0.1505 Ah	6.65 %

Validation Case 3 10 % DOD, 25 °C, 6 hours idling	2.273 Ah	2.3335 Ah	-0.0605 Ah	2.66 %
Validation Case 4 15 % DOD, 35 °C, 2 hours idling	2.399 Ah	2.4937 Ah	-0.0947 Ah	3.95 %

4. Discussion

4.1 SOC reference frame & cell history effect

The challenging part of the integration of the presented self-discharge model into any other model is that the battery performance model has to have the same DOD/SOC reference frame in order that the dependency states to be matched. Due to the 'rate capacity effect' [14], the available battery capacity varies according the applied current. Therefore, C_{cdch} term is also current dependent. Usually, to obtain this C_{cdch}, continuous discharge tests are used. However, alternative approaches can be followed. In [15], for practical reasons, the mixed pulse discharge was used to determine C_{cdch}. This procedure combined three different currents interleaved with the relaxation periods, which means the different charge and discharge protocols. Therefore, the DOD of the performance model has to be converted into DOD of the self-discharge model at its input. Alternatively, the self-discharge model should be parametrized by performing direct current shuttle measurement already in the target DOD reference frame, which is used in the performance model. The DOD definition of the presented self-discharge model is based on the continuous discharge capacity by a 0.2 C-rate. Moreover, this self-discharge takes place mainly in high voltage plateau; therefore if the capacity of the performance model is divided into high- and low-voltage plateau, only the high-voltage plateau capacity should be updated in the concept of the total capacity.

Another feature of the Li-S batteries is that they are a solution based chemistry, so the previous history of the cell (cycling/storage at specific conditions) influences its current performance. This feature has not been so far properly addressed at a sufficiently simplified level in order to be used for battery management systems and practical applications. Therefore our work, similar to [3], uses a pre-condition cycle as a part of the test procedure (charge and discharge protocol) in order to 'reset the memory' and to reach repeatable results.

4.2 Open-circuit voltage based self-discharge model

Alternatively, the DOD dependence of the self-discharge model can be replaced by the open-circuit voltage (OCV) dependence. By following this approach, the shuttle current values related to the OCV are presented in Fig. 8, where it is important to note that this relation is valid only for OCV values at the side of the high voltage plateau. The OCV values in the practical use can be obtained for example by online parameter identification techniques [16]. The use of the identification techniques is required because of even though the OCV is directly measurable at the cell relaxed for a sufficient long time, this condition might be difficult to reach during the operation. Thus, the control system should decide what is the actual OCV value to be used as the input for the self-discharge model.

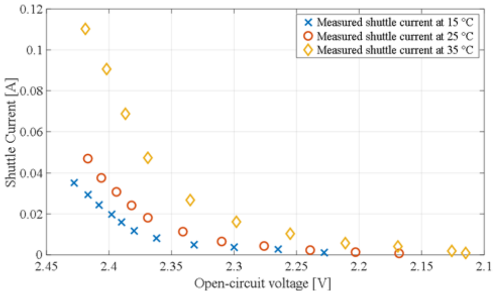

Figure 8. The measured shuttle current values related to the open-circuit voltage values (at the side of the high voltage plateau).

5. Conclusions

The direct shuttle current measurement methodology was applied to a 3.4 Ah Li-S pouch cell, which allows for the shuttle current quantification at various battery cell DODs and temperatures. In this study, the shuttle current is considered as the only source of the self-discharge and therefore, the high voltage plateau was in focus. The pre-determined DOD steps from the measurement were recomputed in order to take into account the shuttle current and thus obtain the actual corresponding DOD levels. Based on the curve fitting of the shuttle current dependency on DOD and temperature, a simple mathematical model for the self-discharge estimation of Li-S batteries was obtained. This model is dedicated to the estimation of the short-term self-discharge in the range of hours. The self-discharge of Li-S batteries is considerably higher and faster in comparison to other battery technologies and it is caused by the shuttle current and appears mainly at low DOD states. The developed model was successfully validated by the experiments considering various conditions with a relative error smaller than 7 %. Therefore, this model represents a powerful tool for the self-discharge estimation of the Li-S batteries. Due to its simplicity and low computational demand, it is suitable to be integrated into battery management systems. Moreover, it can be used also as a part of SOC estimation, which is a challenging task for this particular battery chemistry. Additionally, the concept of the total capacity for Li-S batteries is proposed in order to account for the self-discharge during the operation of the cell. Furthermore, the self-discharge model use can prevent a bias at analyzing experimental results with wrongly determined DOD values of the cell.

Acknowledgments

This work has been part of the ACEMU-project. The authors gratefully acknowledge the Danish Council for Strategic Research (1313-00004B) and EUDP (1440-0007) for providing financial support and would like to thank OXIS Energy for supplying the Lithium-Sulfur battery cells.

References

[1] D. Bresser, S. Passerini, B. Scrosati, Recent progress and remaining challenges in sulfur-based lithium secondary batteries - a review, Chem. Commun. 49 (2013) 10545–10562. doi:10.1039/c3cc46131a.

[2] M. Wild, L. O’Neill, T. Zhang, R. Purkayastha, G. Minton, M. Marinescu, G.J.

Offer, Lithium Sulfur Batteries, A Mechanistic Review, Energy Environ. Sci. (2015). doi:10.1039/C5EE01388G.

[3] V. Knap, D.-I. Stroe, M. Swierczynski, R. Teodorescu, E. Schaltz, Investigation of the Self-Discharge Behavior of Lithium-Sulfur Batteries, J. Electrochem. Soc. 163 (2016) A911–A916. doi:10.1149/2.0641606jes.

[4] Y. V. Mikhaylik, J.R. Akridge, Polysulfide Shuttle Study in the Li/S Battery System, J. Electrochem. Soc. 151 (2004) A1969. doi:10.1149/1.1806394.

[5] H. Ryu, H. Ahn, K. Kim, J. Ahn, J. Lee, E. Cairns, Self-discharge of lithium–sulfur cells using stainless-steel current-collectors, J. Power Sources. 140 (2005) 365–369. doi:10.1016/j.jpowsour.2004.08.039.

[6] H.S. Ryu, H.J. Ahn, K.W. Kim, J.H. Ahn, K.K. Cho, T.H. Nam, Self-discharge characteristics of lithium/sulfur batteries using TEGDME liquid electrolyte, Electrochim. Acta. 52 (2006) 1563–1566. doi:10.1016/j.electacta.2006.01.086.

[7] M. Kazazi, M.R. Vaezi, A. Kazemzadeh, Improving the self-discharge behavior of sulfur-polypyrrole cathode material by LiNO3 electrolyte additive, Ionics (Kiel). 20 (2014) 1291–1300. doi:10.1007/s11581-014-1095-2.

[8] A.F. Hofmann, D.N. Fronczek, W.G. Bessler, Mechanistic modeling of polysulfide shuttle and capacity loss in lithium–sulfur batteries, J. Power Sources. 259 (2014) 300–310. doi:10.1016/j.jpowsour.2014.02.082.

[9] M.R. Busche, P. Adelhelm, H. Sommer, H. Schneider, K. Leitner, J. Janek, Systematical electrochemical study on the parasitic shuttle-effect in lithium-sulfur-cells at different temperatures and different rates, J. Power Sources. 259 (2014) 289–299. doi:10.1016/j.jpowsour.2014.02.075.

[10] M. Marinescu, T. Zhang, G.J. Offer, A zero dimensional model of lithium-sulfur batteries during charge and discharge, Phys. Chem. Chem. Phys. (2015). doi:10.1039/C5CP05755H.

[11] C.E. Parfitt, Characterisation, Modelling and Management of Lithium Sulphur Batteries for Spacecraft Applications, University of Warwick, 2012.

[12] D. Moy, a. Manivannan, S.R. Narayanan, Direct Measurement of Polysulfide Shuttle Current: A Window into Understanding the Performance of Lithium-Sulfur Cells, J. Electrochem. Soc. 162 (2014) A1–A7. doi:10.1149/2.0181501jes.

[13] W. Waag, C. Fleischer, D.U. Sauer, Critical review of the methods for monitoring of lithium-ion batteries in electric and hybrid vehicles, J. Power Sources. 258 (2014) 321–339. doi:10.1016/j.jpowsour.2014.02.064.

[14] M. Doyle, J. Newman, Analysis of capacity-rate data for lithium batteries using simplified models of the discharge process, J. Appl. Electrochem. 27 (1997) 846–856. doi:10.1023/A:1018481030499.

[15] K. Propp, M. Marinescu, D.J. Auger, L. O'Neill, A. Fotouhi, K. Somasundaram, G.J. Offer, G. Minton, S. Longo, M. Wild, V. Knap, Multi-temperature state-dependent equivalent circuit discharge model for lithium-sulfur batteries, J. Power Sources. 328 (2016) 289–299. doi:10.1016/j.jpowsour.2016.07.090.

[16] A. Fotouhi, D.J. Auger, K. Propp, S. Longo, A Study on Battery Model Parametrisation Problem – Application-Oriented Trade-offs between Accuracy and Simplicity, in: 8th IFAC Symp. Adv. Automot. Control (AAC 2016), 2016: pp. 19–23.

Paper A8

Significance of the Capacity Recovery Effect in Pouch Lithium-Sulfur Battery Cells

Vaclav Knap, Teng Zhang, Daniel-Ioan Stroe, Erik Schaltz, Remus Teodorescu and Karsten Propp

The paper has been published in the *ECS Transactions*, vol. 74, no. 1, pp. 95–100, Dec. 2016, doi:10.1149/07401.0095ecst. Republished here with permission of Electrochemical Society, 2017; permission conveyed through Copyright Clearance Center, Inc.

ECS Transactions, 74 (1) 95-100 (2016)
10.1149/07401.0095ecst ©The Electrochemical Society

Significance of the Capacity Recovery Effect in Pouch Lithium-Sulfur Battery Cells

V. Knap[a], T. Zhang[b], D-I. Stroe[a], E. Schaltz[a], R. Teodorescu[a] and K. Propp[c]

[a] Department of Energy Technology, Aalborg University, Aalborg, 9000, Denmark
[b] Department of Mechanical Engineering, Imperial College London, SW7 2AZ, United Kingdom
[c] Centre for Automotive Engineering and Technology, Cranfield University, Bedfordshire MK43 0AL, United Kingdom

Lithium-Sulfur (Li-S) batteries are an emerging energy storage technology, which is technically-attractive due to its high theoretical limits; practically, it is expected that Li-S batteries will result into lighter energy storage devices with higher capacities than traditional Lithium-ion batteries. One of the actual disadvantages for this technology is the highly pronounced rate capacity effect, which reduces the available capacity to be discharged when high currents are used. This drawback might be addressed by the use of the capacity recovery effect, which by introducing relaxation periods between consecutive pulse discharges of the battery, increases the available discharge capacity of the cell. The capacity recovery effect of the Li-S cell is studied in this paper using the pulse discharge technique, considering its dependence on the applied current, discharge step length, temperature, and on the length of the relaxation period between the discharging pulses.

Introduction

Nowadays, Lithium-Sulfur (Li-S) batteries are under intensive research and development, as they are characterized by promising high theoretical limits of gravimetric (2 567 Wh/kg) and volumetric (2 199 Wh/l) energy densities. The practical reached values of gravimetric energy density at pouch cell level were reported to be around 300 Wh/kg; furthermore, it is expected to reach values of 600 Wh/kg in the near future (1), (2). However, despite their prospective advantages, Li-S batteries have not been widely commercialized due to their drawbacks, such as high self-discharge rate, short cycle lifetime, and limited rate capability. (3)

The rate capability, or the so-called rate capacity effect, is a general attribute of batteries (4). For Li-S batteries, the limited rate capability is generally believed to be associated with the formation of solid insulating species on the cathode surface. Fan et al (5) recently demonstrated by means of scanning electron microscopy that the surface coverage of the insulating Li_2S film on carbon increases with discharge current. As a result of the high Li_2S surface coverage, Li-S cells exhibit larger activation over-potential and reduced discharge capacity at high currents (6). Precipitation of Li_2S could also lead to pore blocking which impedes the ionic transport into the inner cathode. The transport limitation in Li-S batteries can be partially overcome via pulse discharge as shown in (4). Introducing relaxation periods between discharging periods allows the ionic concentrations to equalize across the cell thereby triggering a capacity recovery effect. This capacity recovery effect has been briefly reported for Li-S batteries in (7), (8).

In this paper, the results of a systematic investigation of the capacity recovery effect in a pouch Li-S battery cell are presented. The investigation was performed by applying to the Li-S battery cell various discharging current pulse profiles, in order to determine the dependence of the capacity recovery effect on the applied current, discharge step length, temperature, and on the length of the relaxation period between the discharging pulses.

Experimental

The experiment was performed on a 3.4 Ah long-life chemistry Li-S pouch cell, manufactured by OXIS Energy. Because a considerable self-discharge of the cell was observed at the high voltage plateau (8), which is caused mainly by the strong presence of the polysulfide shuttle, the experiment was focused on the low voltage plateau. Therefore, this approach allows to observe the charge recovery effect without the influence of the self-discharge, which reduces the total discharge available capacity. The experimental test procedure is illustrated in Fig. 1. At first, a precondition cycle was performed on the cell as follows: charging by 0.1 C-rate until the maximum allowed voltage of 2.45 V or 11 hours' time limit was reached and then discharging by 0.2 C-rate until the minimum allowed voltage of 1.5 V was reached. Afterwards, the cell was charged by 0.1 C-rate to 2.26 V, in order to remain inside the low voltage plateau, and relaxed for four hours to allow the same starting point for all measurements. Discharging steps of a pre-set length (in ampere-hours), followed by pre-defined relaxation periods of various lengths, were repeated until the cut-off voltage of 1.5 V was reached. The sum of the discharged capacity values measured during the pulses was computed and related to the discharge capacity obtained during the continuous discharge at the same conditions. During the test, the cell was kept in a temperature controlled environment at 25 °C, unless stated otherwise. The test matrix for the considered C-rates, discharging steps lengths and temperatures is presented in Table I.

TABLE I. The test matrix for considered C-rates, discharging steps lengths and temperatures.

	Discharging step lengths [Ah]		
C-rate	**0.05**	**0.1**	**0.2**
0.2	X	X	X *
0.5	-	-	X
1.0	-	-	X

*the measurement was performed for 15, 25, and 35 °C

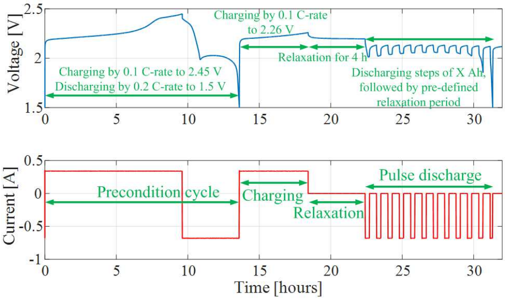

Figure 1. Test procedure of the pulse discharge to capture the capacity recovery effect.

Results and Discussion

As a base-line, the experiment, which considers the pulse discharge with 0.2 C-rate, was performed for the following relaxation period lengths: 0.5, 1, 5, 10, 30, 60, 120, 240 and 480 minutes. The available discharge capacity for the maximum relaxation time of 480 minutes (i.e., 8 hours) was 125.1 % of the capacity measured during continuous discharge at the same conditions. However, this value represents only a minimal increase over the available discharge capacity of 124.6 % measured for a relaxation period of 240 minutes (i.e., 4 hours). Therefore, the relaxation period of 4 hours was considered as a saturation threshold for the measurement of the capacity recovery effect. Thus, the other tests were performed for a reduced number of relaxation periods of 1, 5, 10, 60 and 240 minutes.

The measured available discharge capacity has an exponential dependency on the relaxation time between pulses. Similar exponential dependencies exist between discharge capacity and other test conditions such as C-rates, discharge pulse lengths and temperatures.

C-rate dependence

The potential of the Li-S cells' capacity utilization is illustrated, in Fig. 2, by the measured values of available discharge capacity of 124.6, 142.8, and 178.4 % at 0.2, 0.5 and 1 C-rate, respectively, for discharge pulses with four hours relaxation period in-between. This indicates that by a proper application design and managing of the Li-S cell, in this case relaxing between discharges (pulse discharge character), the overall discharge time is effectively increased and by that the discharge rate is reduced. Fig. 3 shows a comparison between the absolute capacity values obtained during continuous and pulse discharge with different C-rates.

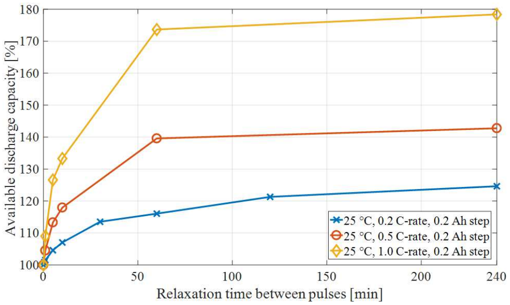

Figure 2. Measured available discharge capacity during the pulse discharge experiments for various C-rates.

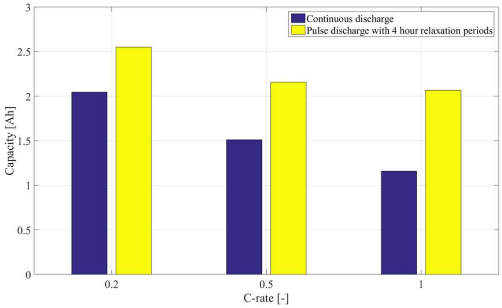

Figure 3. The measured rate capability during continuous discharge and pulse discharge at 25 °C, 0.2 C-rate and 0.2 Ah step with 4 hour relaxation periods.

Discharging step lengths dependence

The length of the discharging steps seems to have effect mainly on how fast the capacity is recovered. During a shorter discharge, smaller ionic concentration gradients are formed; consequently, the capacity is recovered faster during the following relaxation period. For the discharge step of 0.05 Ah, the cell reached the saturation point already after one hour of relaxation between pulses, while for 0.1 Ah steps, the cell's saturation point was found between one and four hours, which is considerably faster than four hours in the case of 0.2 Ah steps (see Fig. 4). The second, minor, but visible, effect of the various discharge steps is on the amount of recovered capacity. In Fig. 4, there is shown that the recovered capacity with 4 hour relaxation is similar for the cases of 0.1 and 0.2 Ah steps, but in the case of 0.05 Ah steps, the recovered capacity is by 2.3 % higher.

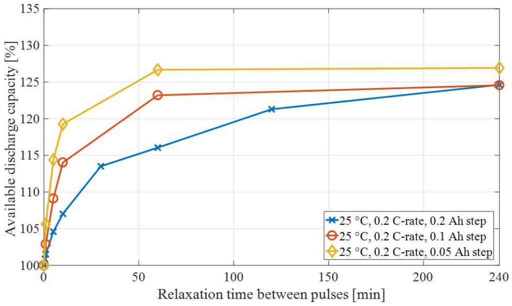

Figure 4. Measured available discharge capacity during the pulse discharge experiments for various discharge step lengths.

Temperature dependence

With the lower temperature, the cell resistance is higher (9); therefore, the cell reaches the discharge cut-off voltage limit earlier and the absolute discharge capacity is lower. The discharge capacity is further reduced at low temperatures due to the lower ionic diffusion coefficients which generally decrease exponentially with temperature. By allowing the cell for relaxation, the concentration gradients are reduced and the cell's discharge capacity is increased, as shown in Fig. 5. The amount of recoverable capacity through relaxation is larger at lower temperatures due to the more severe transport limitation at low temperatures. The rate of capacity recovery, however, is slower at low temperatures due to the slow ion re-equilibration through diffusion during relaxation.

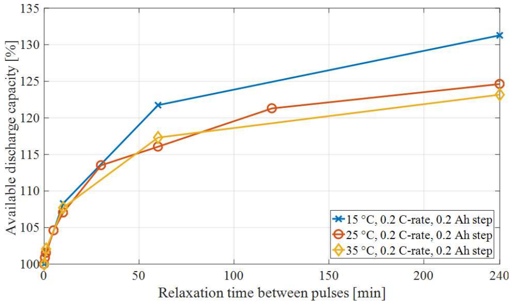

Figure 5. Measured available discharge capacity during the pulse discharge experiments for various temperatures.

Conclusions

The capacity recovery effect of the Li-S cells was studied in this paper and its significance for the possible practical applications was shown. A high recovery capacity was reached (more than 20 % above the capacity obtained during the continuous discharge) and the saturation point for this phenomenon was identified to be between one and four hours for different conditions. It is important to point out that the pulse discharge tests were done at the low voltage plateau of the Li-S cell.

Acknowledgments

This work has been part of the ACEMU-project. The authors gratefully acknowledge the Danish Council for Strategic Research (1313-00004B) and EUDP (1440-0007) for providing financial support and would like to thank OXIS Energy for supplying the Lithium-Sulfur battery cells.

References

1. OXIS Energy, *http://www.oxisenergy.com/* (2016).
2. Sion Power, *http://www.sionpower.com/* (2016).
3. P. G. Bruce, S. A. Freunberger, L. J. Hardwick, and J.-M. Tarascon, *Nat. Mater.*, **11**, 19–29 (2012).
4. V. Rao, G. Singhal, A. Kumar, and N. Navet, *VLSI Des. 2005. 18th Int. Conf.*, 105–110 (2005).
5. F. Y. Fan, W. C. Carter, and Y.-M. Chiang, *Adv. Mater.*, **27**, 5203–5209 (2015).
6. S.-E. Cheon, K.-S. Ko, J.-H. Cho, S.-W. Kim, E.-Y. Chin, and H.-T. Kim, *J. Electrochem. Soc.*, **150**, A800–A805 (2003).
7. C. E. Parfitt, thesis, University of Warwick (2012).
8. V. Knap, D.-I. Stroe, M. Swierczynski, R. Teodorescu, and E. Schaltz, *J. Electrochem. Soc.*, **163**, A911–A916 (2016).
9. Z. Deng, Z. Zhang, Y. Lai, J. Liu, J. Li, and Y. Liu, *J. Electrochem. Soc.*, **160**, A553–A558 (2013).

Paper A9

Self-Balancing Feature of Lithium-Sulfur Batteries

Vaclav Knap, Daniel-Ioan Stroe, Andreas E Christensen, Karsten Propp, Abbas Fotouhi, Daniel J Auger, Erik Schaltz and Remus Teodorescu

The paper has been submitted in 2017.

Self-Balancing Feature of Lithium-Sulfur Batteries

V. Knap[a], D.-I. Stroe[a], A. E. Christensen[b], K. Propp[c], A. Fotouhi[c], D. J. Auger[c], E. Schaltz[a], R. Teodorescu[a]

[a] Department of Energy Technology, Aalborg University, Aalborg, 9000, Denmark
[b] Lithium Balance A/S, Hassellunden 13, Smørum, 2765 Denmark
[c] Advanced Vehicle Engineering Centre , Cranfield University, Bedfordshire MK43 0AL, United Kingdom

The Li-S batteries are a prospective battery technology, which despite to its currently remaining drawbacks offers useable performance and interesting features. The polysulfide shuttle mechanism, a characteristic phenomenon for the Li-S batteries, causes a significant self-discharge at higher state-of-charge (SOC) levels, which leads to the energy dissipation of cells with higher charge. In an operation of series-connected Li-S cells, the shuttle mechanism results into a self-balancing effect which is studied here. A model for prediction of the self-balancing effect is proposed in this work and it is validated by experiments. Our results confirm the self-balancing feature of Li-S cells and illustrate their dependence on various conditions such as temperature, charging limits and idling time at high SOC.

Keywords: inherent balancing, lithium-sulfur battery, self-discharge, series-connected batteries

Introduction

Lithium-Sulfur (Li-S) battery is a prospective battery chemistry for current and future applications. Nowadays, their specific energy has reached 160–350 Wh/kg, with a prospect to accomplish 500–600 Wh/kg, which gives them an advantage above the widely used Lithium-ion (Li-ion) batteries with specific energy of 140–240 Wh/kg. Moreover, in a long-range their cost is expected to be lower than that of Li-ion batteries due to the use of less expensive active materials. However, as they are not a mature battery technology, there are several drawbacks, which have to be addressed either from the cell assembly or battery application point of view; i.e. fast capacity fade, shuttle phenomenon leading to high and quick self-discharge, solubility of active species and complex charge and discharge characteristics. (1), (2)

From the battery balancing perspective, one can see that it is an essential part of battery operation, as it has high impact on safety, amount of available capacity and battery lifetime. A proper balancing scheme primarily helps to achieve most energy per use, but also prevent states such as over-charging, over-discharging or thermal runaway, which may lead to dangerous situations. Furthermore, when cells with various state-of-charge (SOC) levels are present in a series connection, the battery pack operation is limited by the cell with the highest (charging) or the lowest (discharging) SOC, as illustrated in Fig. 1 a). Moreover, ageing phenomena are often related to cell potential, SOC level or temperature, which might vary at unbalanced cells and consequently cause non-uninform degradation, which might result in cell premature failing. (3), (4), (5)

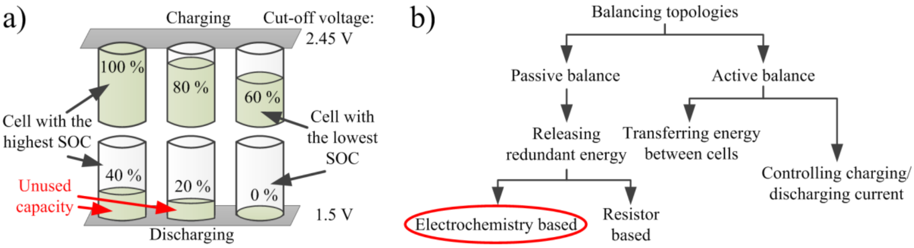

Figure 1. a) Illustration of the cells with an unbalanced state-of-charge and consequently resulting an unused capacity. Voltage levels are typical for cycling of Li-S cells. b) Classification of typical balancing methods, together with the proposed electrochemistry based method.

Balancing methods are typically classified into passive or active. The passive methods rely on dissipating the excess energy, which is usually done through a shunt resistor. This solution is simple and low cost, but may not be sufficient for applications with very strict energy use. Active methods rely on transferring energy between cells or controlling flowing current. They have usually higher efficiency and speed of balancing than the passive methods; however additional power electronic elements and controls are needed, which increase the complexity and cost of the solution. (3), (4), (5), (6), (7)

Li-S, being a complex solution based chemistry, introduces a new type of passive dissipative balancing method, which is electrochemistry-based. A classification of balancing methods is shown in Fig. 1 b), together with this new concept. Polysulfide shuttle mechanism, which is present in Li-S batteries, and explained in detail in (8) and (9), introduces high self-discharge, especially at high SOC levels. This inherent self-discharge process can be utilized for dissipating the energy of the unbalanced cells with higher charge. Therefore, by the adequate operation, the Li-S cells can be fully or at least partially self-balanced without any additional switches.

In order to demonstrate the self-balancing ability of a Li-S cell, the cell is modelled including the self-discharge behavior, which is caused by the polysulfide shuttle. The simulations are performed for three cells connected in series in order to evaluate the self-balancing capability at various conditions. Afterwards, the model and the self-discharge capability are validated by experimental tests conducted on 3.4 Ah Li-S pouch cells and the usability of the self-balancing is discussed.

The paper is structured as follows: In the second section – Methodology, the laboratory experiment is described, together with the quantification methods for evaluating the cell balancing. The third section describes the modelling of the single Li-S cell and also the general simulation platform and the fourth section presents the simulation results for various conditions. The experimental results are shown and discussed in Section 5 and the discussion related to the self-balancing capability and its practical implementation is in Section 6.

Methodology

Three Li-S cells (labelled S1, S2, S3) connected in series are tested in order to evaluate the balancing. The cells are unbalanced by setting their initial SOC to 0, 10 and 20 %, respectively. The cells are cycled five times at 0.34 A (0.1 C-rate) for charging with various cut-off limits and 0.68 A (0.2 C-rate) for discharging to the 1.5 V. These currents are considered as the nominal currents for the cell.

Laboratory experiment

The cells used for the laboratory experiment were 3.4 Ah Li-S long-life type cells from OXIS Energy. The cells were individually characterized using a Digatron BTS 600 battery test station and they were cycled in series at FuelCon Evaluator B Battery Test Station, illustrated in Fig. 2. Only the nominal currents were always applied to the cells, except during constant voltage charging mode, when the charging current was reduced. The typical 'nominal' cycle is composed from the charge and the discharge. The charge has 2.45 V or 11 hours cut-off limits, whatever is reached first, and then the cell is considered fully charged. The discharge has 1.5 V cut-off limit, when the cell is considered fully discharged.

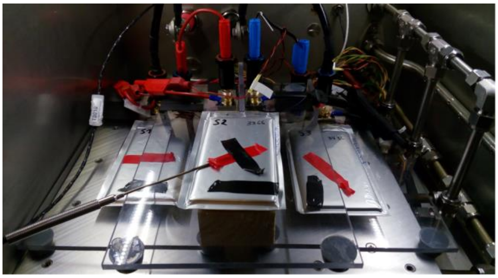

Figure 2. Three Li-S cells connected in series during cycling at FuelCon Evaluator B Battery Test Station. From left to right is cell S1, S2 and S3.

The individual characterization consisted of discharging the cell to obtain the information about the remaining charge from the previous cycling, a pre-conditioning cycle (10), a cycle to obtain the actual capacity of the cell, the direct shuttle current measurement (10) and a cycle to discharge the cell to a pre-determined SOC level. For the experimental tests, the SOC was computed according to [1],

$$\mathrm{SOC} = Q_{\mathrm{meas}} / Q_{\mathrm{cap}} \qquad [1]$$

where Q_{cap} is the capacity obtained from the capacity check cycle and Q_{meas} is:

a) the measured discharged capacity obtained during the first discharge step, when the voltage reached the discharging cut-off limit of 1.5 V,

b) the discharged amount of ampere-hours to reach the target SOC during the cycle for setting the SOC (after the cell being fully charged), computed as $Q_{\mathrm{meas}}=0.9Q_{\mathrm{cap}}$ and $Q_{\mathrm{meas}}=0.8Q_{\mathrm{cap}}$ for the remaining 10 % and 20 % of SOC, respectively.

The specific composition of the characterization for each round is shown in Table I.

TABLE I. Specific content of the characterization tests.

Characterization rounds		
1.	**2. – 4.**	**5.**
Discharge	Discharge	Discharge
Pre-condition cycle	Pre-condition cycle	Pre-condition cycle
Pre-condition cycle	Capacity check cycle	Capacity check cycle
Capacity check cycle	Cycle for setting the SOC	Shuttle current measurement
Shuttle current measurement		Cycle for setting the SOC
Cycle for setting the SOC		

During the cycling of the cells connected in series, the voltage of each cell was monitored, together with the current flowing through the cell string and temperature measured on the middle cell S2. The performed experiments together with their charging cut-off limit are illustrated in Fig. 3. The term ‘balanced cells’ means that all the cells were individually discharged to 0 % SOC at the previous characterization test. The term ‘unbalanced cells’ means that the cells were discharged at the previous characterization test to 0, 10 and 20 % SOC for cell S1, S2 and S3, respectively. A cycle for cycling the series-connected cells consisted of a charging and a discharging step. Each step (charge/discharge) was completed when the cut-off limits were reached by at least one of the cells. The discharging cut-off limit was always 1.5 V. The cells were subjected to five consecutive charging – discharging cycles.

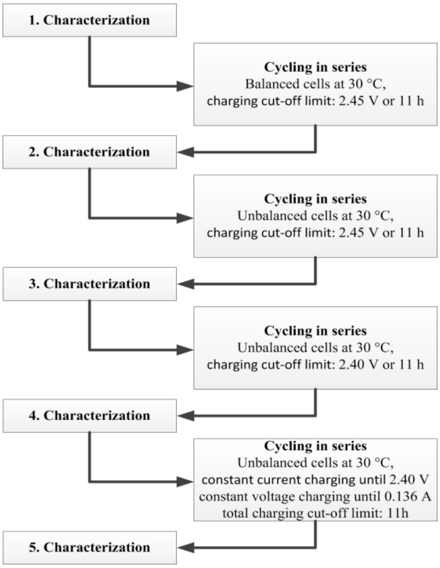

Figure 3. Test scheme.

Quantification and evaluation of balancing

In order to compare and evaluate specific balancing strategies, it is necessary to quantify their performance. For this purpose, we have selected the three following metrics. The maximum difference between the cells in SOC is represented by max ΔSOC. The performance of the series-connected cells in terms of ‘useful’ capacity is expressed by the throughput discharge capacity. Furthermore, an extent of the unified behavior of the cells is quantified as a dissimilarity of voltage discharging curves.

Maximum difference in SOC (*max ΔSOC*). The *max ΔSOC* is computed as the difference between the cell with the highest SOC and the cell with the lowest SOC. In the beginning of the balancing test, the maximum difference in SOC between the cells is *max ΔSOC* = 20 %. The ideally balanced cells in terms of SOC would have *max ΔSOC* = 0 %. In the simulations it is possible to track the SOC all the time, the value taken into account to compute *max ΔSOC* is always at the end of discharge. For the laboratory experiment, it is possible to directly evaluate the SOC only before and after cycling during the individual characterization of the cells.

Throughput discharge capacity (*TDC*). Due to the series-connection approach, the discharging capacity of the battery string is limited by the cell with the lowest SOC as it reaches the voltage cut-off limit the earliest, which results into the unused capacity in other cells (illustrated in Fig. 1 a)). Therefore, the balancing leads to the improved *TDC* of the battery string. For continuous discharge during one cycle, *TDC* is computed as integration of the load current (I_L) from the beginning of discharge (*t_bod*) until the end of discharge (*t_eod*).

$$TDC = \int_{t\_bod}^{t\_eod} |I_L / 3600| \, dt \qquad [2]$$

Dissimilarity of the discharging curves (*DDC*). The uniformity of cells behavior is another aspect, which should be considered, while dealing with balancing. The cells that do not behave similarly might lead to exposure to different mechanisms, which can further deteriorate the cells performance and lifetime. More specifically for the Li-S batteries, it can lead to different exposure of shuttling or precipitation of Li_2S. The ideal DDC has a value equal to zero, meaning the cells behave completely identical. The DDC is computed as follows:

$$V_{\mathrm{mean}}(\mathrm{t}) = (V_{\mathrm{S1}} + V_{\mathrm{S2}} + \cdots + V_{\mathrm{S}n}) / n \qquad [3]$$

$$\mathrm{DDC} = \left(\sum_1^n |V_{\mathrm{mean}}(t) - V_{\mathrm{S}i}(t)|\right) / n \qquad [4]$$

Where $V_{\mathrm{mean}}(t)$ is the average voltage curve for the cells 1 to n and $V_{\mathrm{S}i}$ stands for an *i*-th cell voltage curve.

Modelling

General model layout

The general layout of the model used for simulations is shown in Fig. 4 a). It consists of the current control unit (CCU) and three cells connected in series in a homogenous temperature environment. The CCU provides the current, which flows through all cells and it also receives the information about SOC and voltage from each cell.

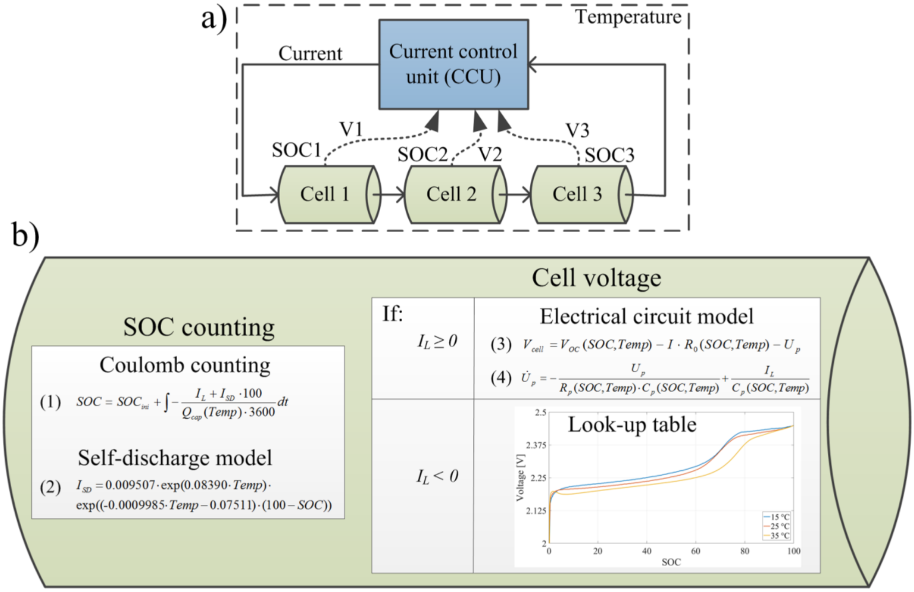

Figure 4. a) Model layout with the marked signals and inputs. b) Model structure of a single Li-S cell.

Single Li-S battery cell model

The structure of the model is illustrated in Fig. 4 b). During charging (negative I_L), the voltage provided by the model is obtained from look-up tables based on experimental measurements, dependent on SOC and temperature (*Temp*). For discharging (positive I_L) and relaxation ($I_L = 0$), the voltage is provided by the multi-temperature state-dependent equivalent circuit discharge model for Li-S batteries presented in (11). The SOC in the model is computed by coulomb counting, including the self-discharge model of Li-S batteries based on direct shuttle current measurement presented in (12). The total capacity (Q_{cap}) for coulomb counting is implemented as a look-up table dependent on temperature.

Current Control Unit

The CCU provides the current based on the user specifications. In this work, the current is limited only to its nominal values, which are 0.34 A (0.1 C-rate) for charging and 0.68 A (0.2 C-rate) for discharging The SOC, voltage and time are used for the control of the battery operation (charging/discharging/relaxation).

Determination of look-up table values

The values for Q_{cap} and charging voltage are determined from laboratory measurements. During the experiment at a single temperature, the cell was cycled two times by 0.34 A charging (to 2.45 V or 11 hours) and 0.68 discharging (to 1.5 V). This test was performed for three temperatures: 15, 25 and 35 °C. The charging and discharging capacity during the second cycle were recorded. These capacities were corrected by the self-discharged amount according to (12), by adding the DCH/CHA lost capacity due to the self-discharge to DCH/CHA measured capacity and by that obtain the DCH/CHA total capacity. The total capacity Q_{cap} was taken as an average value between the corrected charging and discharging capacity. Their values are presented in Table II. The charging voltage profiles as a function of SOC are shown in Fig. 4 b).

TABLE II. Measured and corrected capacity values due to the self-discharge.

Temp [°C]	DCH capacity measured [Ah]	Capacity lost by self-discharge [Ah]	Total DCH capacity [Ah]	CHA capacity measured [Ah]	Additional capacity due to self-discharge [Ah]	Total CHA capacity [Ah]	Average capacity [Ah]
15	2.5590	0.0140	2.5730	2.6750	0.0150	2.6600	2.6165
25	2.6970	0.0307	2.7277	2.8270	0.0342	2.7928	2.7603
35	3.5050	0.0839	3.5889	3.6400	0.1012	3.5388	3.5639

Simulation studies of ideal cells

The simulations studies were performed for three ideal (identical) cells connected in series. At first, the effect of charging voltage cut-off was studied by varying the cut-off limit to 2.35, 2.40 and 2.45 V. In the second study case, a relaxation period was introduced after the first reaching of the cut-off limit and an additional charging step was inserted. The effect of temperature on balancing was studied in the third study case. The results are graphically summarized in Fig. 5. The measured values are linearly fitted to obtain the slope of the curves. For the DDC graphs an ‘error bar’ is also plotted to present the mean, maximum and minimum values for the cell curves.

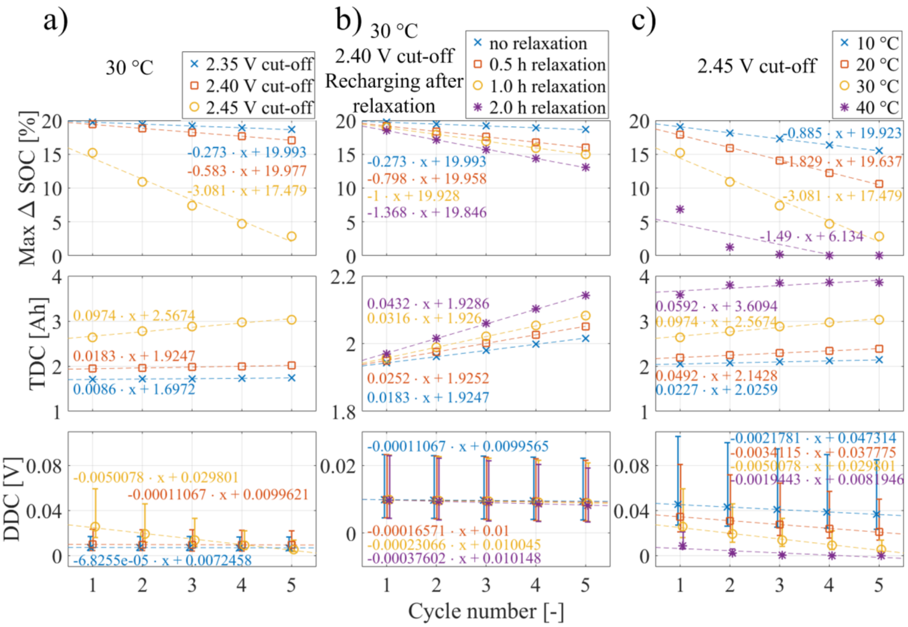

Figure 5. Simulation results from five cycles at three ideal cells connected in series, *x* stands for number of cycles. a) cycling at 30 °C to various charging cut-off limits; b) cycling at 30 °C to 2.40 V, followed by various relaxation periods and repeatedly charged to 2.40 V before the discharge; c) cycling at various temperature levels to 2.45 V charging voltage limit.

The voltage cut-off limits determines how much the cells are going to be charged. For a higher limit (2.45 V), a cell will enter and stay in the shuttling region, which helps in the balancing. From Fig. 5 a), it can be observed that allowing the cells to be charged until 2.45 V has a great impact on the balancing; already after the first cycle *max ΔSOC* is reduced by almost 5 % and after five cycles, the final *max ΔSOC* is 2.88 %. The balancing capability is reduced with lowering the voltage cut-off limits to 2.40 and 2.35 V, but it is still present. A similar trend is observable also for the *TDC* and *DDC*. For a 2.45 V cut-off limit, the *DDC* is the highest in the beginning, because there is the largest difference between the discharging voltage curves due to the character of the Li-S high voltage plateau. Nevertheless, during cycling the *DDC* is highly improved to again outperform the lower voltage cut-off limits.

The next study case was focused on the effect of the relaxation time on the self-balancing. In this case the cells were kept for a prolonged time at high SOC. When the cell was charged, it was left idling for a certain period of time and then was charged again to the charging cut-off limits before the discharge step. By doing so, the cell is left longer time at the maximum allowed SOC by charging and by that it is exposed more to the shuttling. The results presented in Fig. 5 b) were obtained for a 2.40 V charging cut-off limit and are showing that with increased relaxation time at high SOC, the cell balancing is improved.

In the next study case, different temperature levels were investigated, because the shuttle current is highly dependent on temperature (12). This behavior was expected to be reflected also into the balancing capabilities of the cell. The higher the temperature of the cells is, the faster the balancing is over the cycling, as illustrated in Fig. 5 c). There is also a noticeable change of relatively linear trend of *max ΔSOC* during the 10–30 °C interval into rather exponential for 40 °C due to rapid balancing already at the first and the second cycle.

Experimental results

The capacity values of the cells S1, S2 and S3, which were obtained during the first characterization test, are 2.933, 2.954 and 2.818 Ah, respectively. Consequently, it can be observed that the cells were already partially aged. In order to fairly evaluate the balancing capabilities, at first we needed to see how the behavior of the cells is when they are cycled as initially balanced (discharged to 1.5 V, which represents 0 % SOC). The comparison of the balanced and unbalanced cells cycled at 30 °C to 2.45 V is shown in Fig. 6. It is noticeable that for both cases, there was a remaining charge in the cells between 0.295 and 0.402 Ah, which translated to SOC represents 11–14 %; this behavior is caused by the presence of a relaxation period before every characterization test. These results are in agreement with the additional discharging capacity obtained by introducing a relaxation period after the first discharge, reported by Zhang et al. (13). Zhang et al. explain this behavior of discharging capacity by active polysulfides moving to and being trapped in the separator due to their effort of sustaining charge equilibrium throughout the cell. The charge equilibrium is being disturbed at first place by the Li+ cations being too slowly transported to the cathode during discharge. Afterward, during the relaxation period these trapped polysulfides diffuse back into the cathode. The cell model implemented in our work is not able to reproduce this behavior. Therefore, the SOC results remain only as a predictive indicator, but they are not closely matching the experimental results. From the *max ΔSOC* metric, it is seen that the initially balanced system has a *max ΔSOC* slightly, but neglectably higher than the unbalanced system. In the balanced system, the *TDC* is high and nearly constant, while the unbalanced system shows a highly reduced *TDC* in the beginning which is improved during the cycling. A similar trend is observable in the *DDC*. Even though the cells are not identical, the mean *DDC* is nearly constant for the balanced system, while it has initially a high value for the unbalanced system and over the cycling it gets closer to the balanced system. Moreover, the voltage profile during the first and the last cycle of the unbalanced system is shown in Fig. 7 to demonstrate the increased capacity and more uniform behavior of the cells after cycling. Thus, the self-balancing ability of the Li-S cells was experimentally verified.

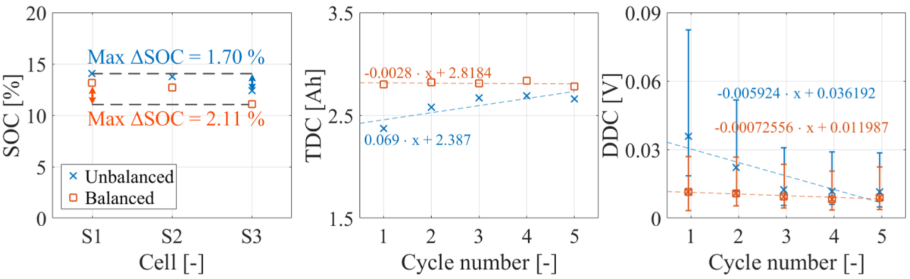

Figure 6. Comparison of experimental results for the cells initially balanced and unbalanced, cycled at 30 °C with charging cut-off of 2.45 V, *x* stands for number of cycles.

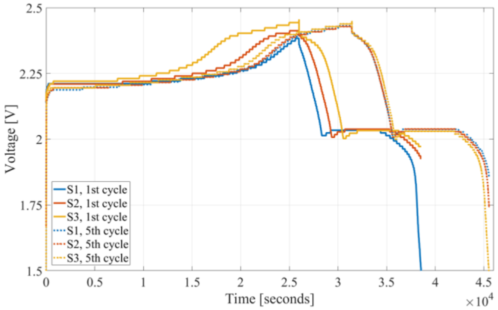

Figure 7. The first and the last cycle of the series cell cycling at 30 °C to 2.45 V.

The next step was to verify the model validity and to experimentally obtain the cell balancing capability at different conditions. The comparison of experimental and simulation results is shown in Fig. 8. For the comparison to the experimental test of charging to 2.40 V by constant current and constant voltage charging to 0.136 A was selected the simulation scenario with charging to 2.40 V, 0.5 h relaxation period, followed by recharging again to 2.40 V. This simulation scenario was selected based on the time spent for relaxation and recharging was the closest to the length of the constant voltage charging. The implemented model does not support constant voltage charging mode. It is important to note that the simulations were performed for the ‘ideal’ identical cell model. For the cycling with charging up to 2.45 V, the simulation and experimental results are closely matching. For the charging up to 2.40 V, or charging up to 2.40 V with relaxation and recharging or constant voltage charging, one can see that the predicted *max ΔSOC* do not match. The reason for it is most probably the recovery of discharging capacity due to transport limitations, as explained earlier. However, the *TDC* simulation results are very close to the experimental results and they have similar trend. The *DDC* results show very accurate match for case of charging to 2.45 V. However, for charging to 2.40 V the slope differs by one or nearly two orders between the simulation and experimental results, though the improving trend in the *DDC* is alike. Therefore, we can conclude that the implemented model can be used for predicting the balancing of Li-S cells due to the shuttle current. The *TDC* is provided with a high accuracy, while the *DDC* accuracy can vary according to the charging conditions. The SOC balancing represents more complex challenge and it is necessary to include the SOC/capacity recovered during the relaxation periods or different way of the SOC estimation.

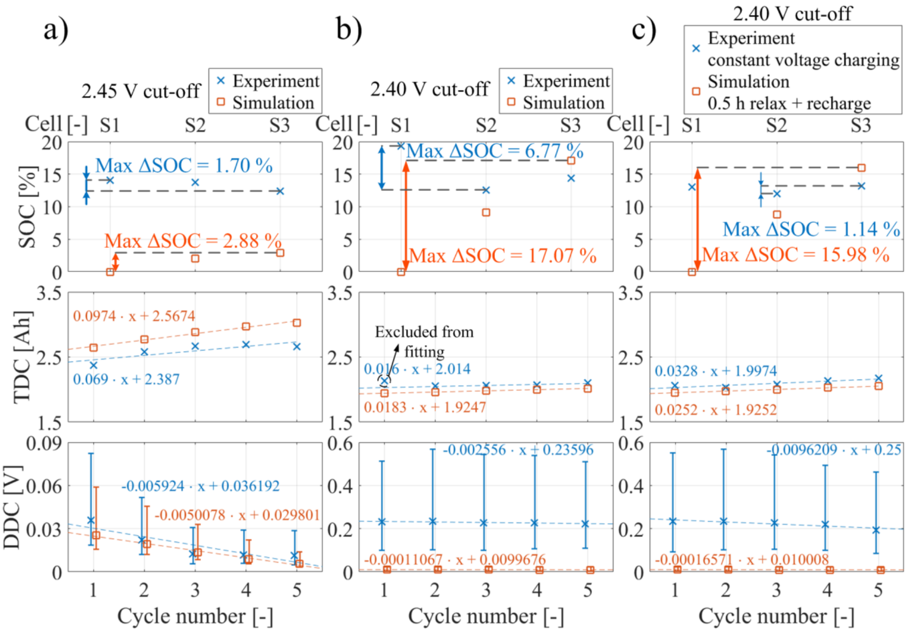

Figure 8. Comparison of experimental and simulation results, *x* stands for number of cycles. a) cycling to 2.45 V cut-off limit, b) cycling to 2.40 V cut-off limit, c) charging to 2.40 V cut-off limit and followed by constant voltage charging mode in the case of experiment or by relaxation for 0.5 hour and repeatedly charging to 2.40 V in the case of simulation.

Discussion

The self-balancing feature of the Li-S batteries opens new possibilities to reduce the amount of power electronic parts of the system and by that increase the reliability and reduce the cost, or to enhance standard balancing strategies. In a practical application, in order to extend the lifetime, the charging cut-off limit of the Li-S batteries is expected to be reduced and to be lower than 2.45 V. It was demonstrated that even with the lower charging cut-off limit of 2.35 V, the cells are able to slowly balance themselves. To take advantage of both benefits, the longer lifetime during the limited charging operation, and the rapid balancing, there can be implemented two modes of operation. The first mode would be the normal operation with reduced charging cut-off limits. The second mode would be balancing, which would try to boost the Li-S cells balancing capability. This can be obtained by changing one or several factors: increase of temperature, increase of charging cut-off limits and increase the time spent at the high voltage plateau (the higher the better). Also the constant voltage charging at the high voltage plateau can be beneficial, but it is important to consider safety in terms of cells' heating (8) and gassing (14), and also possible degradation of the cells. Generally, the degradation of the Li-S cells is a remaining question, as it is not clear how much will the cells aged at various self-balancing conditions.

Conclusions

The Li-S battery is a prospective technology, which despite to its currently remaining drawbacks offers useable performance and interesting features. In this work, the self-balancing feature of Li-S cells was investigated and modelled. At the higher SOC levels (approximately above 70 %, at the high voltage plateau), the significant self-discharge takes place, because of the polysulfide shuttle mechanism. This self-discharge during the operation of the series-connected cells results gradually in their SOC equalization due to the energy dissipation at the higher-charged cells. The self-balancing rate can be controlled and influenced by adjustment of the conditions as temperature, charging cut-off limits and time spent at the high voltage plateau. For the self-balancing prediction, a model has been proposed and verified by experiments.

Acknowledgments

This work has been part of the ACEMU-project. The authors gratefully acknowledge the Danish Council for Strategic Research (1313-00004B) and EUDP (1440-0007) for providing financial support and would like to thank OXIS Energy for supplying the Lithium-Sulfur battery cells.

References

1. M. Wild, L. O'Neill, T. Zhang, R. Purkayastha, G. Minton, M. Marinescu, and G. J. Offer, *Energy Environ. Sci.*, **8**, 3477–3494 (2015).
2. D. Bresser, S. Passerini, and B. Scrosati, *Chem. Commun.*, **49**, 10545–10562 (2013).
3. P. A. Cassani and S. S. Williamson, *Conf. Proc. - IEEE Appl. Power Electron. Conf. Expo. - APEC*, 465–471 (2009).
4. S. Li, C. C. Mi, and M. Zhang, *IEEE Trans. Ind. Appl.*, **49**, 198–207 (2013).
5. J. V. Barreras, C. Pinto, R. De Castro, E. Schaltz, S. J. Andreasen, and R. E. Araújo, *2014 IEEE Veh. Power Propuls. Conf. VPPC 2014* (2015).
6. Y. H. Hsieh, T. J. Liang, S. M. Chen, W. Y. Horng, and Y. Y. Chung, *Power Electron. IEEE Trans.*, **28**, 5927–5939 (2013).
7. C.-H. Kim, M.-Y. Kim, and G.-W. Moon, *IEEE Trans. Power Electron.*, **28**, 3779–3787 (2013).
8. Y. V. Mikhaylik and J. R. Akridge, *J. Electrochem. Soc.*, **151**, A1969 (2004).
9. D. Moy, A. Manivannan, and S. R. Narayanan, *J. Electrochem. Soc.*, **162**, A1–A7 (2014).
10. V. Knap, D.-I. Stroe, R. Purkayastha, D. J. Auger, A. Fotouhi, and K. Propp, *Methodology for Assessing the Lithium-Sulfur Battery Degradation for Practical Applications*, (2017).
11. K. Propp, M. Marinescu, D. J. Auger, L. O'Neill, A. Fotouhi, K. Somasundaram, G. J. Offer, G. Minton, S. Longo, M. Wild, and V. Knap, *J. Power Sources*, **328**, 289–299 (2016).
12. V. Knap, D. I. Stroe, M. Swierczynski, R. Purkayastha, K. Propp, R. Teodorescu, and E. Schaltz, *J. Power Sources*, **336**, 325–331 (2016).
13. T. Zhang, M. Marinescu, S. Walus, and G. J. Offer, *Electrochim. Acta*, **219**, 502–508 (2016).
14. H. Schneider, T. Weiß, C. Scordilis-Kelley, J. Maeyer, K. Leitner, H. J. Peng, R. Schmidt, and J. Tomforde, *Electrochim. Acta*, **243**, 26–32 (2017).

Paper A10

Thermal Behavior and Heat Generation Modeling of Lithium Sulfur Batteries

Daniel-Ioan Stroe, Vaclav Knap, Maciej Swierczynski
and Erik Schaltz

The paper has been published in the *ECS Transactions*, vol. 77, no. 11, pp. 467–476, Jul. 2017, doi:10.1149/07711.0467ecst. Republished here with permission of Electrochemical Society, 2017; permission conveyed through Copyright Clearance Center, Inc.

ECS Transactions, 77 (11) 467-476 (2017)
10.1149/07711.0467ecst ©The Electrochemical Society

Thermal Behavior and Heat Generation Modeling of Lithium Sulfur Batteries

D.-I. Stroe[a], V. Knap[a], M. Swierczynski[a], E. Schaltz[a]

[a] Department of Energy Technology, Aalborg University, Aalborg 9220, Denmark

Lithium Sulfur batteries are receiving a lot of research interest because of their intrinsic characteristics, such as very high energy density and increased safety, which make them a suitable solution for zero-emission vehicles and space application. This paper analyses the influence of the temperature on the performance parameters of a 3.4 Ah Lithium-Sulfur battery cell. Furthermore, the values of the internal resistance and entropic heat coefficient, which are necessary for the parametrization of a heat generation model, are determined experimentally.

Introduction

In the past years a lot of research has been carried out in order to develop batteries with very high energy density levels and improved safety, which could fulfill the requirements of next generation electrical vehicle and military applications. This is the case of Lithium-Sulfur (Li-S) batteries, which are characterized at present by very high theoretical specific capacity (i.e., 1675 mAh/g) and energy density (2600 Wh/kg) as well as improved safety levels (1). However, their market penetration at a large scale is prevented by their inherent polysulfide shuttle mechanism, which causes fast capacity fade and poor coulombic efficiency (2). Thus, research and development efforts are carried out in order to improve this chemistry (3).

Several aspects regarding the electrical and lifetime behavior of LiS batteries have been studied and are presented in literature. For example, in (4), the authors have analyzed the self-discharge behavior of Li-S batteries; high temperatures and increased state-of-charge (SOC) levels were found to enhance the self-discharge process. Stroe et al, have performed an in-depth electrochemical impedance spectroscopy characterization of a Li-S pouch battery cell (5); the influence on the SOC and temperature on the development of the Li-S battery cell's impedance spectra was thoroughly investigated. A Li-S battery cell electric model was developed and parametrized for various discharging conditions in (6). Furthermore, the degradation mechanisms responsible for Li-S battery cells' lifetime reduction were studied in (7).

Besides the electrical and lifetime characteristics, the thermal behavior of batteries is equally important. However, so far only few studies have focused on thermal aspects related to Li-S battery cells; furthermore, most of these studies were performed in laboratory assembled coin cells. For example, isothermal micro-calorimetry was used in (8) to measure the heat generation during discharging of a Li-S coin cell. A transient method for the simulation of Li-S cells characteristics is developed in (9).

In this work, we characterize the thermal behavior of a pre-commercial 3.4 Ah Li-S battery cell. The dependence of the cell's capacity on the temperature and current rate is investigated and the temperature evolution during cell discharging at different conditions is analyzed and quantified. Furthermore, the internal resistance, which is responsible for the cell's polarization heat, is determined at different temperatures (i.e., 10°C, 25°C, and 40°C) for the whole SOC interval. Lastly, by performing open circuit potentiometry measurements, the entropic heat coefficient of the tested Li-S battery cell was determined and its variation with the SOC is presented and analyzed. The results of all these measurements can be further used to parameterize a simple but comprehensive battery heat generation model.

Experimental Set-Up

This work was carried out using a long-life type Li-S pouch cell manufactured by OXIS Energy. The electrical parameters of the Li-S cell are presented in Table I.

TABLE I. Main electrical and thermal parameters of the Li-S battery cell.

Parameter	Value
Nominal Capacity	3.4 Ah
Nominal Voltage	2.05 V
Maximum Voltage	2.45 V
Minimum Voltage	1.5 V
Nominal Charging Current	0.34 A (1 C-rate)
Nominal Discharging Current	0.68 A (2 C-rate)
Temperature Operation Range	+5°C to +80°C

All the experiments were performed using a MACCOR 4000 series battery test station. During the experiments the Li-S pouch cell was placed inside a temperature-controlled climatic chamber, as illustrated in Figure 1. The temperature of the cell was monitored using a type-K thermocouple; furthermore, the temperature values referred in the following are the ones measured on the surface of the Li-S battery cell.

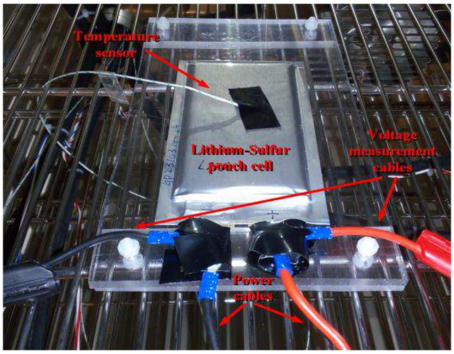

Figure 1. Li-S pouch cell placed inside the climatic chamber during the thermal characterization procedure.

Heat Generation Modeling

To build a battery thermal model, the equation for energy balance has to be considered for a given battery cooling or heating scenario. A general energy balance equation for battery systems was proposed by Bernardi et al in (10). Nevertheless, if adiabatic conditions are considered, the energy balance equation can be simplified and the accumulation of enthalpy in the battery cell will match the heat generation (11):

$$\mathrm{M} \cdot \mathrm{Cp} \cdot \mathrm{dT} / \mathrm{dt} = \mathrm{I}^2 \cdot \mathrm{Ri} + \mathrm{I} \cdot \mathrm{T} \cdot \delta \mathrm{Uavg} / \delta \mathrm{T} \quad [1]$$

Where, M represents the mass of the cell, Cp represents the mean heat capacity a constant pressure, T represents the temperature, t represents the time, I represents the battery cell current, Ri represents the internal resistance, and Uavg represents the open circuit potential.

The battery heat generation, Pgen, is expressed as in [2]. The first term in [2], known as polarization heat, is a function of the cell's internal resistance and is composed of the Joule heating within the cell and the energy dissipated in the electrode overpotentials (11). This term is always positive meaning that the polarization heat is exothermic during both charging and discharging conditions. The second term in [2] is the reversible entropic heat and is related to the entropy change; the derivative of the potential in respect to temperature is the entropic heat coefficient (EHC), which can take either positive or negative values.

$$\mathrm{Pgen} = \mathrm{I}^2 \cdot \mathrm{Ri} + \mathrm{I} \cdot \mathrm{T} \cdot \delta \mathrm{Uavg} / \delta \mathrm{T} \quad [2]$$

Thus, in order to be able to determine the heat generation of the studied Li-S battery cell, the internal resistance and the EHC have to be determined. The procedures used to determine these thermal parameters and the obtained results are presented throughout the next section.

Heat Generation Model Parametrization

In order to parameterize the heat generation model of the Li-S battery cell, the internal resistance and EHC had to be measured. Another battery performance parameter, which is temperature dependent and it was measured, is the battery capacity; furthermore, the battery capacity should be known in order to set the state-of-charge at which the internal resistance and EHC are measured. In the following, the used procedures to measure the battery capacity, internal resistance, and EHC are detailed and subsequently, the obtained laboratory results are presented.

Capacity Measurement

In order to determine the variation of the capacity of the studied Li-S battery cell with the temperature, measurements at three temperatures (i.e., 10°C, 25°C, and 40°C) were performed. Furthermore, the capacity measurements were repeated during discharge at three different C-rates, i.e., 0.2 C-rate (0.68 A), 0.5 C-rate (1.7 A), and 1 C-rate (3.4 A). Before each discharging, the Li-S battery was fully re-charged with 0.1 C-rate (0.34 A).

The procedure to measure the capacity of the Li-S battery cell was as follows:

0. Tempering of the cell for two hours at 10°C
1. Two preconditioning cycle; charging with 0.1 C-rate (0.34 A) and discharging with 0.2 C-rate (0.68 A);
2. Capacity measurement at 0.2 C-rate; charging with 0.1 C-rate (0.34 A) and discharging with 0.2 C-rate (0.68 A);
3. Capacity measurement at 0.5 C-rate; charging with 0.1 C-rate (0.34 A) and discharging with 0.5 C-rate (1.7 A);
4. One preconditioning cycle; charging with 0.1 C-rate (0.34 A) and discharging with 0.2 C-rate (0.68 A);
5. Capacity measurement at 1 C-rate; charging with 0.1 C-rate (0.34 A) and discharging with 0.5 C-rate (3.4 A);
6. Repeat steps 0. – 5. for 25°C and 40°C

The current, voltage, and temperature signals, which were logged during the capacity measurement at 10°C are presented in Fig. 2. Each of the above summarized steps of the capacity measurement test are highlighted in Fig. 2.

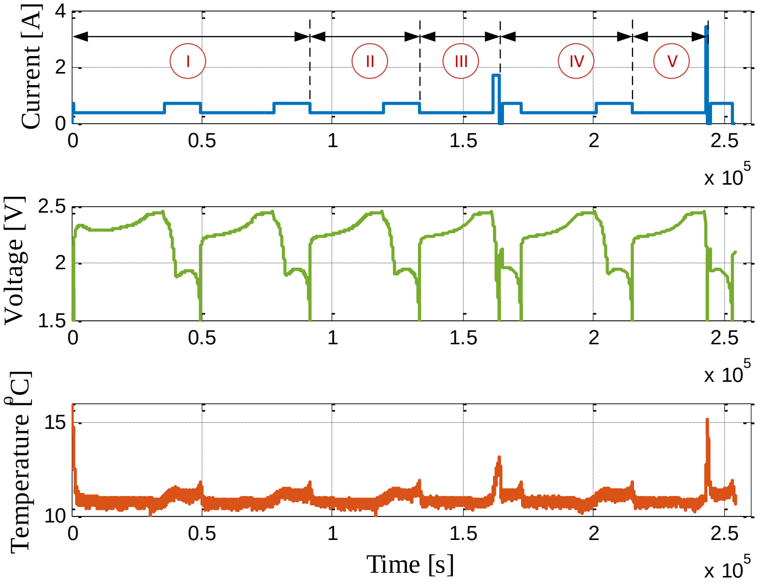

Figure 2. Li-S battery cell current (top), voltage (middle), and temperature (bottom) during the capacity measurement test performed at 10°C.

The preconditioning cycle is applied in order to reset the history of the Li-S battery cell as explained in (12) and to allow for a non-biased comparison of the capacity results at different C-rates.

The dependence of the Li-S battery's capacity on the temperature and C-rate is illustrated in Fig 4; the nine measurement points at which the capacity of the cell was measured are highlighted. As one can observe, the capacity is strongly influenced by the operating temperature. For example, for a C-rate of 1 C-rate, the battery capacity increases by 250%, from 0.968 Ah to 2.534 Ah, for a temperature increase of 30°C (from 10°C to 40°C); nevertheless, for the same temperature range, the capacity increase is less visible at lower C-rates. These results are in good agreement with the results presented in (6) for a similar temperature range and in (13) for a high temperatures range (i.e., 70°C - 90°C).

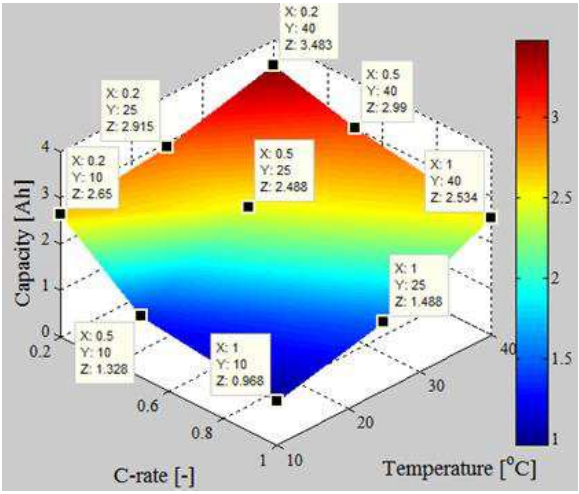

Figure 3. Dependence of the Li-S battery cell's capacity on temperature for different charging rates.

Furthermore, we have investigated the temperature evolution during all the capacity checks, and the results are presented in Fig. 4. We have observed the highest temperature increase during capacity measurement at low temperatures, with a maximum of approximately 4.5°C for the case of 1 C-rate. It is thought that these high temperature deviations at low temperature might have been caused by the increased internal resistance at low temperature which is even more accentuated at the end of the discharge process (i.e., SOC=0%). Moreover, it has to be mentioned that during the discharging process, the temperature of the cell increased monotonously, without any plateaus.

Internal Resistance Measurement

Together with the capacity, the internal resistance is a key battery parameter for battery systems optimal design in any application. This is because the battery internal resistance is closely related to the battery power, which is used for sizing purposes, and developing optimal energy management strategies. Furthermore, the internal resistance is an important parameter for battery cell heat generation modeling – the higher the resistance is, the higher the heat generation in the battery cell will be (11).

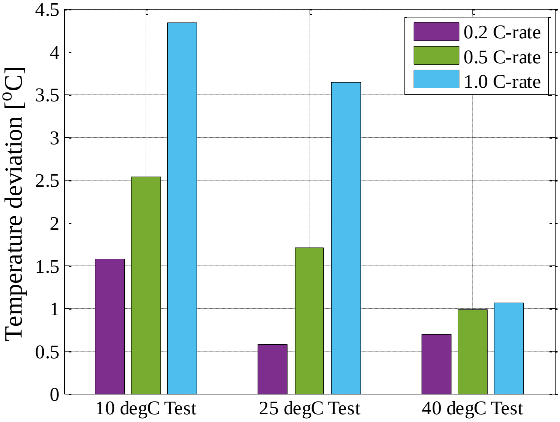

Figure 4. Measured temperature deviation during the capacity tests at different conditions.

The internal resistance of Li-S battery cells is dependent on the temperature and is strongly changing with the SOC (14). Moreover, the internal resistance of the battery cells is increasing, while the cells are ageing; however, this is out of the scope of this work.

Different procedures to measure the battery cells internal resistance can be applied (15); nevertheless, in this work, we have used the traditional DC pulse technique to determine the battery resistance for both charging and discharging conditions. Because, the battery internal resistance is dependent on the load current, we have applied charging and discharging pulses of different amplitudes (i.e., 0.1 C-rate, 0.2 C-rate, 0.5 C-rate and 1 C-rate). The measurements were performed for the 10-90% SOC interval and repeated at 10°C, 25°C, and 40°C.

The Li-S battery cell voltage response to a 20 seconds discharging pulse is presented in Fig. 5. The internal resistance was computed according to Ohm's law as given in [3].

$$Ri = \Delta V / \Delta I = (V1 - V0) / I \qquad [3]$$

Where $V0$ and $V1$ are illustrated in Figure 5 and I is the amplitude of the applied DC pulse.

The variation of the internal resistance with the battery SOC at the three considered temperatures is presented in Fig. 6; these specific values were obtained for a discharging current pulse of 3.4 A. As expected the obtained results show that the internal resistance increases with decrease of temperature. Furthermore, depending on the temperature, the variation of the resistance with the SOC changes its pattern. At 10°C and 25°C, a parabolic dependence on the SOC is observed for the 10% - 70% SOC, which is followed by a step decrease of the internal resistance at SOC higher than 70% SOC. This inflection point, at around 70% SOC, corresponds to the transition from the low voltage plateau to the high voltage plateau. For 25°C and 40°C, the highest resistance was measured at low SOCs, in this case 10% SOC. Additionally, independent on the temperature, the minimum value of the internal resistance is measured at high SOCs; furthermore, as one can observe, the value of the internal resistance at 90% SOC is quasi-independent on the temperature.

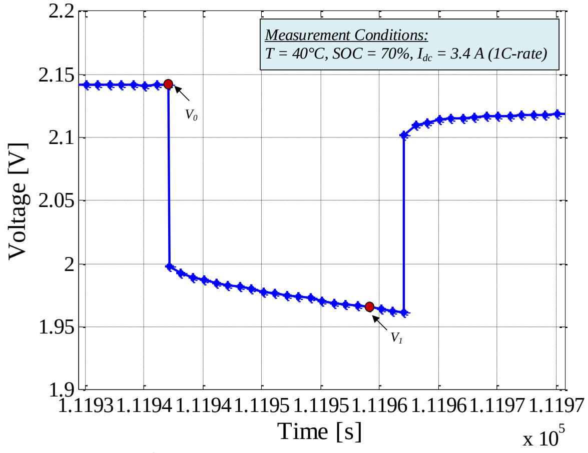

Figure 5. Voltage response of a Li-S battery cell to a discharging current pulse.

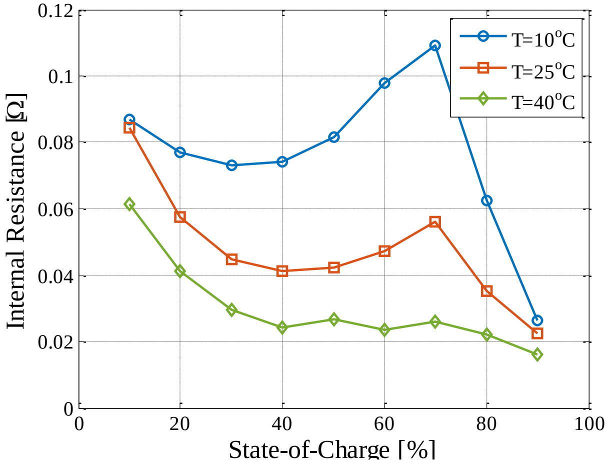

Figure 6. Variation of the internal resistance with the SOC and temperature.

Entropic Heat Coefficient Measurement

The EHC, also referred as temperature coefficient, describes the potential derivative with respect to the temperature and is determined in order to calculate the heat generation within the battery cell. In the literature there are presented several approaches for determining the EHC; however in this work, we have used the open circuit potentiometry technique to determine this coefficient (11). In order to determine the change of the EHC with the SOC, measurements were carried for the SOC interval from 90% to 10%, with a 10% resolution.

Before performing the open circuit potentiometry measurements, a preconditioning cycle was applied to the Li-S battery cell, followed by a full charging process. Then, the cell was discharged to 90% SOC, where it was left at open circuit condition, in order to reach thermo-dynamic stability. Normally, after the SOC was modified, a four hour relaxation period was considered; nevertheless, in order to reduce the influence of the high self-discharge at increased SOC levels (4), the relaxation period at 90% and 80% SOC was reduced to one hour. The relaxation was followed by the thermal cycle illustrated in Fig. 7; each temperature level was maintained for 2 hours, except for the 90% and 80% SOC, where each temperature was applied for one hour, due to the aforementioned limitations.

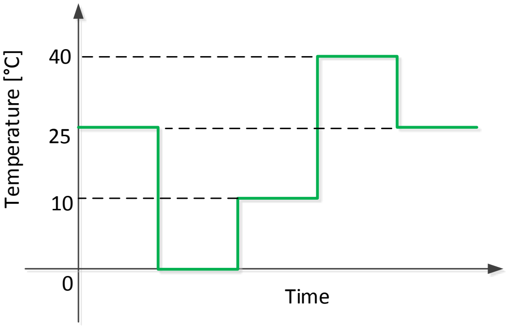

Figure 7. Thermal cycle used to determine the EHC by open circuit potentiometry.

The behavior of the Li-S battery cell voltage during the thermal cycle, at one SOC level, is presented in Fig. 8. The change in the voltage is invers proportional with the change in the temperature, except the temperature increase from 10°C to 40°C, when the battery voltage increases as well. This suggests a negative EHC (11). The same behavior was observed for all the considered SOC levels at which the EHC was measured.

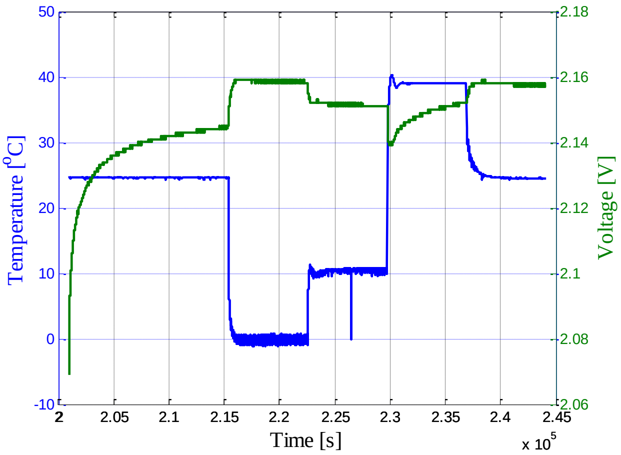

Figure 8. Voltage behavior during the thermal cycle at 50% SOC.

In order to derive the values of the EHC, the voltage profiles obtained at each SOC (as the one presented in Fig. 8), were fitted to the function given in [4] (11). The fitting was carried out using the *Curve Fitting* toolbox from MATLAB®.

$$V(t,T) = A + B \cdot T + C \cdot t \qquad [4]$$

Where, *A*, *B*, and *C* are constants and *B* corresponds to the EHC.

By following this procedure, the values of the EHC at each considered SOC were obtained and are presented in Fig. 9. The EHC has negative values for all the SOC internal, which suggests that the effect of the entropic heat is exothermic during discharging and endothermic during charging, independent on the battery current.

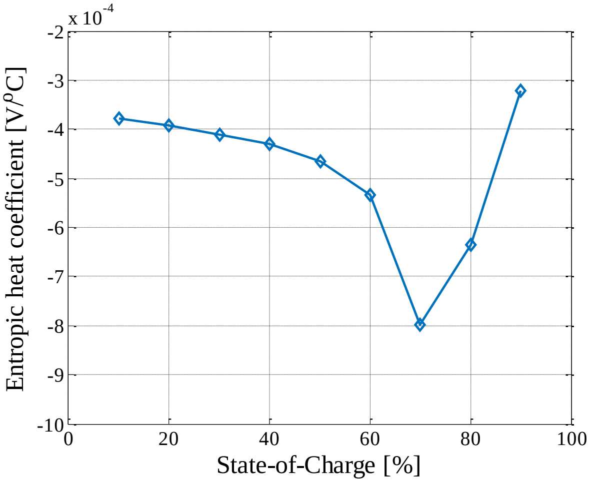

Figure 9. The variation of the EHC as function of SOC.

Conclusions

In this paper we measured the internal resistance and entropic heat coefficient of a 3.4 Ah Li-S battery cell. These are the two parameters necessary to develop a heat generation model, which represents the first step in the development of a battery thermal model. The internal resistance of the battery cell was determined at 10°C, 25°C, and 40°C and it shown a highly nonlinear variation with the SOC. Furthermore, the dependence of the internal resistance on the SOC does not follow the same pattern for all temperatures. The measured EHC has negative values independent on the considered battery SOC suggesting that the effect of the entropic heat is exothermic during discharging (i.e., heat is released) and endothermic during charging (i.e., heat is absorbed).

Acknowledgments

This work has been part of the ACEMU-project. The authors gratefully acknowledge the Danish Council for Strategic Research (1313-00004B) and EUDP (1440-0007) for providing financial support and would like to thank OXIS Energy for supplying the Lithium-Sulfur battery cells.

References

1. P. G. Bruce, L. J. Hardwick, and K. M. Abraham, *MRS Bulletin*, **36**(7), 506-512 (2011).
2. Z. Deng et al., *J. Electrochem. Soc.*, **160**(4), A553 (2013).
3. K. Xie et al., *Adv. Mater.*, **29**, 1604724 (2017).
4. V. Knap et al., *J. Electrochem. Soc.*, **163**(6), A911 (2016).
5. D.-I. Stroe et al., *ECS Trans.*, **72**(12), 13-22 (2016).
6. K. Propp et al., *J. Power Sources* **328**, 289-299 (2016).
7. X. Feng et al., *Phys. Chem. Chem. Phys.*, **16**, 16931 (2014).
8. J. Seo et al., *Electrochemistry Communications*, **44**, 42 (2014).
9. D. Adair et al., *Modern Environmental Science and Engineering*, **2**, 246 (2016).
10. D. Bernardi, E. Pawlikowski, and J. Newman, *J. Electrochem. Soc.*, **132**, 5 (1985).
11. N. Nieto et al., *J. Electrochem. Soc*, **160**(2), A212 (2013).
12. V. Knap et al., *ECS Trans.*, MA2017-01 538 (2017)
13. J, Hassoun and B. Scrosati, *Adv. Mater*., **22**, 5198 (2010).
14. V.S. Kolosnitsyn et al., *J. Power Sources*, **252,** 28 (2014).
15. H.-G. Schweiger et al., *Sensors*, **10**, 5604 (2010).

Paper A11

Methodology for Assessing the Lithium-Sulfur Battery Degradation for Practical Applications

Vaclav Knap, Daniel-Ioan Stroe, Rajlakshmi Purkayastha, Sylwia Walus, Daniel J. Auger, Abbas Fotouhi and Karsten Propp

The paper has been published in the *ECS Transactions*, vol. 77, no. 11, pp. 479–490, Jul. 2017, doi:10.1149/07711.0479ecst. Republished here with permission of Electrochemical Society, 2017; permission conveyed through Copyright Clearance Center, Inc.

ECS Transactions, 77 (11) 479-490 (2017)
10.1149/07711.0479ecst ©The Electrochemical Society

Methodology for Assessing the Lithium-Sulfur Battery Degradation for Practical Applications

V. Knap[a], D-I. Stroe[a], R. Purkayastha[b], S. Walus[b], D. J. Auger[c], A. Fotouhi[c] and K. Propp[c]

[a] Department of Energy Technology, Aalborg University, Aalborg, 9000, Denmark
[b] Oxis Energy Ltd, Culham Science Centre, Abingdon, Oxfordshire OX14 3DB, United Kingdom
[c] Advanced Vehicle Engineering Centre, Cranfield University, Bedfordshire MK43 0AL, United Kingdom

Lithium-Sulfur (Li-S) battery is an emerging battery technology receiving growing amount of attention due to its potential high contributions of gravimetric energy density, safety and low production cost. However, there are still some obstacles preventing their swift commercialization. Li-S batteries are driven by different electrochemical processes than commonly used Lithium-ion batteries, which often results in their very different behavior. Therefore, the modelling and testing have to be adjusted to reflect this unique behavior to prevent possible biases. A methodology for a reference performance test for the Li-S batteries is proposed in this study to point out the Li-S battery features and provide guidance to users how to deal with them and possible results into standardization.

Introduction

Lithium-Sulfur (Li-S) batteries are an emerging battery technology, which is gaining interest because of its high gravimetric energy density, increased safety, and expected low production cost (1), (2), (3). Because of these features, they might become an alternative to Lithium-ion (Li-ion) batteries and replace them in various areas, such as automotive, aerospace or personal equipment. However, the swift commercialization of the Li-S batteries is still hindered by their shortcomings of low coulombic efficiency, high self-discharge, and relatively rapid capacity fade (1), (2). Nevertheless, Li-S batteries have already found areas of usefulness such as in high-altitude, long endurance unmanned aerial vehicles (4).

For product design, it is important to have a tool for comparison for the performance and the lifetime of various battery solutions. Moreover, it is required to have knowledge about the degradation of the battery in order to design safe and effective operational limits and control algorithms for the battery. Typically, the batteries accelerated degradation or lifetime tests are composed of ageing process (cycling or shelf idling) and periodical evaluation through a reference performance test (RPT). In the case of Li-ion batteries, there are several established test standards like ISO 12405-1/2 (5), (6), IEC 62660-1/2 (7), (8), which are summarized in the literature (9), (10), (11), advising how the Li-ion batteries should be tested and evaluated. Similar guidelines are required for

Li-S batteries. Unfortunately, the Li-S chemistry with its specific mechanisms prevents the direct transfer of the methodologies from the Li-ion battery world. Not respecting these specific needs would lead to biased and incomplete results about the performance-degradation of the Li-S batteries.

The primary difference between Li-ion and the Li-S batteries are their charge and discharge mechanisms. Li-ion batteries undergo an intercalation process, wherein the Li ions travel from an anode to a cathode during charging and the opposite direction during discharging. The charge and discharge processes are very symmetrical and reversible, which gives them a consistent performance (12). Contrary to the Li-ion batteries, Li-S batteries are solution-based chemistry. When the Li-S battery is fully charged the sulfur at the cathode is in the dissolved form S_8^0 or in the solid S_8^0 and dissolved form S_8^{2-} (13). During the discharge, the reduction of S_8 undergoes a set of intermediate stages. At first the long polysulfide chains of Li_2S_8 and Li_2S_6 are formed, and consequently they are reduced into the short polysulfide chains of Li_2S_4, Li_2S_2 and Li_2S. During the charge, the direction of the reactions is opposite: the long chain polysulfides are formed from the short chains. However, according to the experimental observations (14), the reaction pathways seems to be different for charge and discharge. Moreover, chemical precipitation takes place at the end of discharge for lithium sulfide and at the end of charge for sulfur. Both lithium sulfide and sulfur are insulating and insoluble. Therefore, their precipitation causes both reversible and irreversible loss of the active material depending on the cycling (2). Another inherent mechanism of Li-S batteries is the polysulfide shuttle. Due to the high solubility of the long chain polysulfides, they diffuse toward the lithium anode, where they are reduced to short chain polysulfides. Then, the reverse flux is created by the high concentration of the reduced species at the anode and the reduced short chain polysulfides diffuse back to the cathode to be oxidized again. This shuttle parasitic reaction contributes to low Coloumbic efficiency, self-discharge and irreversible capacity loss (15).

Degradation studies on Li-S batteries

Various types of studies on Li-S batteries can be found in the literature, which includes some form of degradation tests and their evaluation. They can be sorted according to their objective into three main categories:

- cell development,
- mechanism investigations,
- modelling.

Cell development

Studies focused on the cell development have usually limited scope about exploring the cells degradation. They target mainly on the comparison of cycle life of the newly developed cell to the reference cell. Sometimes, the investigations go more in depth in order to explain the source of the pro-longed life. The cells are usually cycled at only one, rarely multiple, conditions (16), (17), (18).

Mechanism investigations

The goal of studies in this category is the investigation and understanding of the degradation mechanisms and influence of various factors and conditions. As an example, the effect of binders on battery performance and degradation was investigated in (19). Brückner et al studied the influence of C-rate, amount of electrolyte and sulfur loading in (20). Furthermore, the capacity fading mechanism of the cathode was analysed in (21).

Modelling

The proposed models for the degradation of the Li-S batteries have typically one of the following roles: (i) a tool for investigation of the degradation mechanisms (22), (ii) being a part of a mechanistic model to reproduce the complex Li-S battery behavior (23) or (iii) a separate component for prediction and simulation of the capacity fade (24).

Analytical techniques

Various analytical techniques have been applied to Li-S batteries which are summarized in (2), together with their benefits and limitations. However, the scope of battery degradation testing for the practical applications in this work is limited to applicable and measureable quantities of voltage, current and temperature, which can be obtained by the use of similar test equipment as needed for the degradation tests specified for Li-ion batteries in the literature (5) ,(6), (7), (8), (10), (11).

Galvanostatic techniques. These are techniques where constant current cycling conditions are implemented i.e. full cell charge and discharge operations. These can be served as pre-conditioning cycles and can provide information about cell's charging and discharging energy, capacity and efficiencies. Furthermore, the obtained voltage profiles can be analysed for their change in the shape, or expressed as $\Delta Q/\Delta V$ vs V for an incremental capacity analysis (25), (26) or as $\Delta T/\Delta V$ vs V for thermal voltammetry analysis (27). Short current pulses applied to the battery are used to obtain the voltage response and subsequently determine the internal resistance of the battery. However, if the voltage limit is reached during the current pulse, the constant current (dis)charging mode has to switch to constant voltage mode. The user should be always careful when applying a constant charging voltage mode to the Li-S batteries due to the shuttle currents, which could result into an infinite charging of the cell and by that damaging it. The same applies for the constant current charging under specific conditions (low currents, high temperatures) where the charging time constraint should be included.

Potentiostatic techniques. Cyclic voltammetry (CV) is an often used technique for the electrochemical characterization of the Li-S cells. During the CV, the cell goes through a range of constant voltage steps and the responding current is observed. Typically, the CV for Li-S batteries shows two pairs of redox peaks, which corresponds to the voltage plateaus, obtained from the charging/discharging profiles (28). Another potentiostatic method is the direct shuttle current measurement, introduced in (15) and used for characterization and modelling in (29), in which the cell is kept at a constant voltage charging mode at the high voltage plateau until the current reaches the steady state and is matched by that the internal self-discharging shuttle current.

Electrochemical Impedance Spectroscopy (EIS). For the EIS measurements, the battery is excited by a sinusoidal current or voltage and its response on the other quantity is observed. The obtained impedance spectra are usually analysed by fitting them to an electrical circuit model, in which particular elements are assigned to the specific electrochemical processes. However, for the Li-S batteries, there is no consensus regarding the representation of the specific components (22).

Experimental tests

The 3.4 Ah Li-S long-life type cells provided by OXIS Energy were used for experiments. The measurements were performed on Digatron BTS 600 battery test station. During the experiments, cells were kept in a temperature controlled environment. Temperature of 30 °C is considered as the nominal value for comparison of the cells' performance. The nominal charging current was 0.34 A (= 0.1 C-rate) and the nominal discharging current was 0.68 A (= 0.2 C-rate). The charging cut-off limits were 2.45 V or 11 hours. The discharging cut-off limit was 1.5 V. The cycle, following these charging and discharging currents and limits, is referred as the nominal cycle.

Pre-conditioning cycles

Due to the character of the Li-S chemistry, the actual performance of the cell is highly dependent on its previous history (13), (24), which is the so-called 'cumulative history' effect. This can be illustrated on the discharge capacity test for different C-rates shown in Fig. 1. For the first cell, the discharge procedure was: (i) charging to 2.45 V/11 hours by 0.1 C-rate, (ii) discharging to 1.5 V by a specific C-rate, (iii) relaxation 15 minutes and (iv) discharge to 1.5 V by 0.2 C-rate. This procedure was repeated for various C-rates from 0.1 C-rate to 3 C-rate. As it is visible in Fig. 1(a), the discharge curves do not have a homogenous trend between each other. The discharged capacity is not always in the order of the applied current, as the cell discharged by 1.5 C-rate has lower capacity than cells discharged by 2 or 2.5 C-rates. The procedure for the second cell was modified by inserting one nominal cycle (0.1 C-rate charging, 0.2 C-rate discharging) before every charging step of the discharge capacity test procedure. The resulting discharge curves for the second cell are presented in Fig. 1(b) that shows a relatively homogenous trend for the different discharging C-rates. Therefore, a pre-conditioning cycle is required in order to obtain repeatable results at common reference state of the cells. The reason for this behavior is believed to be the precipitation of lithium sulfide. Lithium sulfide can precipitate at different rates when different discharge rates are applied. More importantly, all the lithium sulfide may not re-dissolve back on charge, leading to a temporary 'loss' of capacity. By adding an additional nominal cycle, we allow complete redissolution to occur, and essentially the cell 'resets' correctly to allow for accurate measurements.

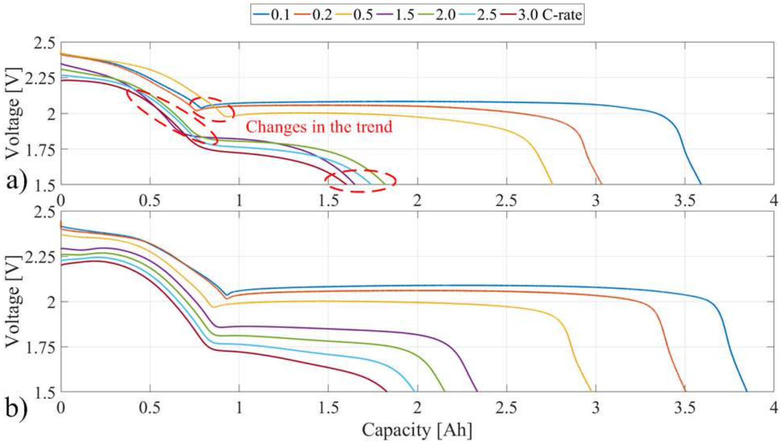

Figure 1. Voltage discharge curves for different C-rates: (a) without the pre-conditioning cycle, (b) with the pre-conditioning cycle before every charge (0.1 C-rate) and discharge (various C-rates).

The required number of pre-conditioning cycles might vary with the specific cell composition, its size and the conditions the cell is exposed to, both environmental and operational. In order to determine this number of cycles, the considered 3.4 Ah cell was exposed to 10 cycles at different specific conditions (various current and temperature), followed by 4 hours of temperature stabilization at 30 °C and subsequent 10 nominal cycles. The specific cycling conditions were selected to match the limiting conditions of the future considered degradation tests. In our case it was chosen: nominal currents at 50 °C; nominal currents at 10 °C; and 0.1 C-rate charging, 2.0 C-rate discharging currents at 30 °C. The obtained capacities from the nominal cycles at 30 °C are shown in Fig. 2, together with the capacity change between following two cycles. The capacity can be significantly different at the first cycle, but since the second cycle the changes in the capacity between the cycles are only minor. Therefore, it is concluded that only one pre-conditioning cycle is needed and the second cycle can be already used for the capacity evaluation.

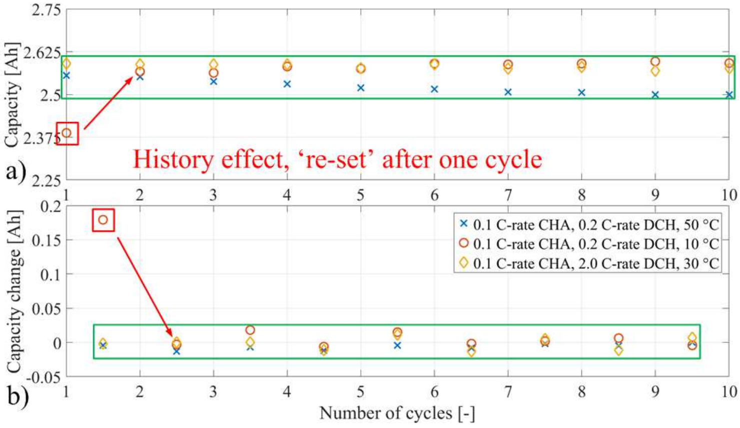

Figure 2. Evaluation of the nominal cycles at 30 °C, after cycling at different conditions; a) capacity obtained from each cycle, b) change in the capacity between the cycles.

Capacity measurement

The capacity measurement is done by using specific currents to obtain the cell capacity, energy and efficiency at the specific C-rates. For our procedure, we considered only nominal currents due to time constraints. The advantage of this consideration is that the capacity measurement and the pre-conditioning cycle are done in the same cycle. Therefore, the next step of the RPT can follow directly. The capacity obtained during the discharge is used further on for computing the SOC of the cell. The capacity measurements can be expanded by using additional C-rates; however, then adding pre-conditioning cycles before or after (due to following measurements) should be considered, together with the total time requirement for the RPT and also additional degradation of the cell during the RPT. For example, if the discharge capacity test of 1 C-rate is added, it will demand 10+1=11 hours for only the additional discharge test and also 10+5=15 hours for another pre-conditioning cycle, which will prolong the RPT by 26 hours.

Power and resistance measurement

The resistance, together with the pulse power capability, is recommended to be measured through either the hybrid pulse power characterization (HPPC) test (5), (6), (10) or through the pulse train (7), (9), (11). The HPPC test was designed for the automotive industry to evaluate the battery dynamic power capability during high pulse discharge (10 seconds, maximum discharge current), followed by a short relaxation (40 seconds) and the regenerative charge pulse (10 seconds, 0.75 of the maximum discharge current) (5). The pulse train consists of a set of charging and discharging current pulses following each other from the smallest or largest current values. The pulse is followed by another pulse with the opposite polarity in order to maintain the SOC constant. The advantage of the pulse train is that it retrieves information including the current dependence, which is especially useful when the parameter identification procedure is applied to the pulses to obtain parameter values of an electrical circuit model of the battery.

Three different values of current for charging and discharging were considered to be sufficient in order to obtain the current dependence of the battery parameters. The Li-S battery is more a high energy than a high power cell due to its relatively high resistance. Thus, even though the cell under investigation was capable of 3 C-rate continuous discharge, the total obtained capacity is significantly reduced (Fig. 1 b)) at this C-rate. Then, the discharging mode would very often be limited by voltage rather than current. Moreover, it is not a current level expected to be experienced by a single cell at the considered battery application of electric vehicles. Therefore, the current of 1 C-rate was selected as a compromise to be closer to the realistic operation scenarios. As mentioned before, the charging process of the Li-S battery is not symmetric to the discharging process, the charging pulse currents were selected to be smaller (half in our case) according to the charging capability of the cell. Finally the applied currents were 0.1, 0.2 and 0.5 C-rate for charge pulses and 0.2, 0.5 and 1 C-rate for discharge pulses.

The relaxation period between the pulses for the Li-ion batteries is recommended to be 10 minutes (7), unless the cell temperature is still higher than 2 °C of target test temperature, then the cell can be cooled down or the relaxation period can be prolonged. For the Li-S battery, we have first extended the relaxation period to 15 minutes and performed the preliminary pulse train test from 90 % SOC to 10 % SOC at 25 °C. For obtaining the necessary relaxation time between the pulses, the following assumption was taken in order to compute the settling time: the system is sufficiently relaxed when the voltage reaches 95 % of a quasi-steady state voltage value (at 15 minutes of the relaxation after the pulse) from the initial voltage drop value. Only the worst case of the current was considered, i.e. 0.5 C-rate for charging and 1.0 C-rate for discharging. The obtained settling time values are summarized in Table I. At very high SOC, the polysulfide shuttle changes the character of the recovery voltage and therefore, the settling time at 90 % of SOC varies significantly from the other SOC levels. The average values for the interval from 80 to 10 % SOC were computed to be 470 seconds = 7.83 minutes for 1.0 C-rate discharge pulses and 248 seconds = 4.13 minutes for 0.5 C-rate charge pulses. Rounding the numbers up to 10 and 5 minutes for discharging and charging consequently provides a margin to ensure that the cell should be sufficiently relaxed and the values should be valid also for the SOC levels at the neighboring temperature levels (such as 20 or 30 °C) with a lower rate of the polysulfide shuttle.

TABLE I. **Settling time after pulses at various SOC levels.**

SOC [%]	**90**	**80**	**70**	**60**	**50**	**40**	**30**	**20**	**10**	**Avg**
Pulse current	**Settling time [seconds]**									
1 C-rate DCH	108	480	586	562	569	500	452	311	297	470
0.5 C-rate CHA	622	430	89	200	353	179	316	244	173	248

When 10 and 5 minutes relaxation periods between pulses were applied, there has been observed a steep voltage drop at 100 and 90 % SOC due to the prevalence of the polysulfide shuttle. Moreover, the ‘equilibrium point’ (=the peak point between voltage recovery after discharge and voltage decay due to the self-discharge) was present relatively early. Therefore, the relaxation periods can be much shorter, which is also preferable due to smaller shift of the SOC caused by the self-discharge. It has been assumed that only half of the relaxation periods used for other SOC levels (5 minutes for discharging and 2.5 minutes for charging pulses) is sufficient for 90 % SOC and quarter of it (2.5 minutes for discharging and 1.25 minutes for charging pulses) is enough for 100 % SOC.

After the discharging steps between different SOC levels and before the first pulse, there is a requirement for an additional relaxation time to allow the cell to reach an equilibrium state. However, for some SOC levels that would mean a relaxation in range of hours, which would considerably pro-long the overall test procedure. Therefore, a 30 minutes long relaxation period is considered sufficient to reach a quasi-equilibrium state for the cell before the pulse train procedure. The applied pulse train for 0 to 80 % SOC is illustrated in Fig. 3. Again, due to the self-discharge at higher SOC levels, the relaxation is shortened to 15 minutes at 90 % SOC and it is only 1.5 minutes at 100 % SOC.

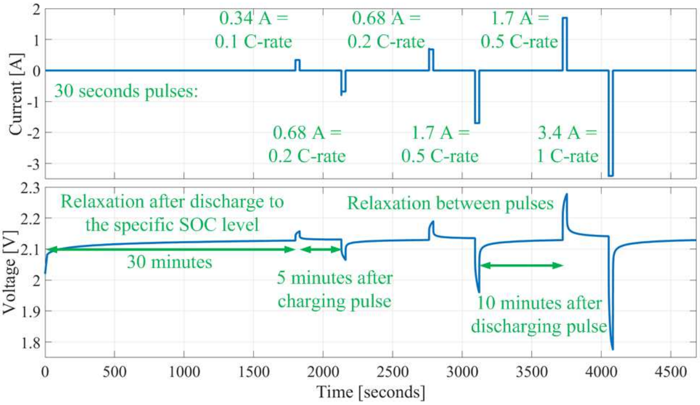

Figure 3. Illustration of the applied pulse train procedure for SOC levels between 0 and 80 % SOC.

The last step is to correctly determine the discharging step between the SOC levels. Due to inequality between the charging and discharging pulses, the SOC shifts down by 0.75 % per pulse train, except at 100 % SOC, where 0.5 C-rate charging pulse is omitted, as the limiting voltage is already reached by 0.2 C-rate charging pulse; and therefore the SOC shift down is by 1.2 %. The discharging steps should be adjusted to account for this SOC shift. Moreover, the approximate self-discharge can be estimated by the Li-S self-discharge model (29) with a consideration of a fresh cell with 3.4 Ah capacity. The pulse train procedure at 100 % lasts 14 minutes (1.5 minutes relaxation period before the first pulse, 2*0.5 minutes charging pulses, 3*0.5 minutes discharging pulses, 2*1.25 minutes relaxation after charging pulses and 3*2.5 minutes relaxation after discharging pulses), which results into loss of 0.78 % SOC. Therefore, immediately after the pulse train at 100 % SOC level, the actual SOC would be rather 98 %. So the discharge to 90 % SOC level can be reduced down to step of 7.5 % SOC, to account for the previously described occurrences and for the self-discharge during this discharging step. A similar procedure can be applied to compensate for the self-discharge during the pulse train at 90 % SOC; however, its effect is under 1 % SOC and it is considered insignificant to be dealt with. The last effect, which can be considered for adjustment of the discharging steps between SOC levels, is the charge recovery effect (30). As the cell is relaxed between the discharging steps, its effective capacity is higher than during the continuous discharge.

Therefore, the discharging step between 10 % and 0 % SOC should be controlled rather by discharging to cut-off voltage limit of 1.5 V than controlled by the amount of discharged SOC, in order to bring the cell to the state when is actually no charge available. The summary of different settings according to SOC levels are presented in Table II.

TABLE II. **Specifications for pulse train procedure at various SOC levels.**

SOC level [%]	**100**	**90**	**80 - 10**	**0**
Discharging step to the SOC level	-	7.5 %	9.25 %	to 1.5 V
Relaxation before the pulse train [min]	1.5	15	30	30
Relaxation after charging pulse [min]	1.25	2.5	5	5
Relaxation after discharging pulse [min]	2.5	5	10	10

Shuttle current measurement

The polysulfide shuttle is a unique mechanism, which has no equivalent within classical Li-ion batteries; nevertheless, for Li-S batteries it is very important, as it is related to the self-discharge, degradation, columbic efficiency and possibly also to the safety. Moy et al (15) introduced the methodology for the measurement of the polysulfide shuttle current, which is based on constant voltage charging until the external current reaches a steady-state and which indicates that it has equalized with the internal shuttle current.

The procedure follows downward SOC direction, so at first the cell has to be charged. Then the cell is discharged to the target SOC level and it is relaxed until the voltage equilibrium is reached. The voltage equilibrium is understood to be the peak voltage value, which occurs between increasing voltage in the recovery period immediately after the interruption of discharging current; and decreasing voltage due to self-discharge in pro-longed relaxation. In practice, the voltage equilibrium can be detected by the voltage falling under the threshold from the maximum voltage value, where the threshold is set with respect to the measurement accuracy and noise. When the threshold is crossed, this voltage value is used as the limit for constant voltage charging, which lasts until the current reaches steady-state value, typically limited by time. Afterwards, it is followed by the discharging to the next investigated SOC level.

The shuttle current measurement to 3.4 Ah Li-S cells was already applied in (29). From where it is known that two hours period of constant voltage charging is enough for these cells to reach steady-state. Moreover, the voltage threshold applied in Digatron BTS 600 battery test station is 0.6 mV. It is considered that three different SOC levels for the shuttle current measurement should be enough, together with the fourth level with known zero current, to use the results for the fitting and deriving a relation of the shuttle current against SOC or open circuit voltage. As the target SOC levels, 98%, 94%, and 88% of SOC were considered.

Summary

The content of the RPT for the Li-S batteries is shown in Fig. 4. The specific steps were adjusted according to needs of the specific cell type, in our case 3.4 Ah Li-S pouch cell from OXIS Energy. It has been found that 4 hours temperature stabilization and one pre-conditioning cycle (0.1 C-rate charging, 0.2 C-rate discharging) are sufficient to 'reset' the cells history and obtain comparable results from the following RPT procedure after exposing the cell to cycling at three extreme conditions. The capacity measurement is performed only for the nominal currents of 0.1 C-rate for charging and 0.2 C-rate for discharging, which allows to move to the next step of power and resistance measurement without additional pre-conditioning cycle inbetween. The power and resistance measurement is done by the pulse train starting from 100 % SOC and continue down to 0 % by the steps of 10 %. The pulses are assymetric for charging and discharging. The additional step of the RPT for the Li-S batteries is the shuttle current measurement, which allows to quantify the shuttle in a straightforward way and by that provide information about the self-discharge and the degradation rate. The voltage profile of the proposed RPT procedure is shown in Fig. 5.

Typical RPT procedure at Li-ion batteries:

- Pre-conditioning cycles
- Capacity measurement
- Power and resistance measurement

Proposed RPT procedure for Li-S batteries:

- Pre-conditioning cycles
- Capacity test
- Power and resistance measurement
- Shuttle current measurement

Figure 4. Content of the RPT for Li-ion and Li-S batteries.

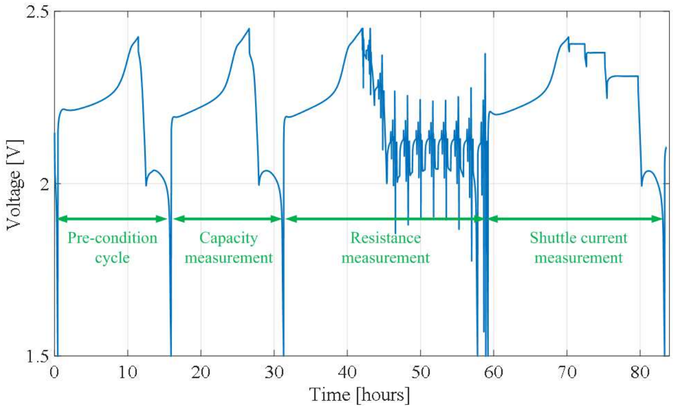

Figure 5. Illustration of the complete RPT procedure for the Li-S batteries.

Conclusions

The Li-S batteries with their unique behavior require specific approaches, where every method applied for Li-ion batteries should be reconsidered, if it is suitable or not. Often, it is not possible to directly take proven approaches from the world of Li-ion batteries, such as modelling and testing, and apply them to the Li-S batteries without introducing a bias or significant loss of accuracy. Therefore, a RPT procedure for the Li-S batteries is proposed in this manuscript, to bring attention to the specific issues and differences of this type of batteries and to provide guidance to other users. The RPT is typically used to evaluate the performance of the batteries related to the practical applications and often it is applied to identify influence of ageing at different conditions.

Acknowledgments

This work has been part of the ACEMU-project. The authors gratefully acknowledge the Danish Council for Strategic Research (1313-00004B) and EUDP (1440-0007) for providing financial support and would like to thank OXIS Energy for supplying the Lithium-Sulfur battery cells.

References

1. D. Bresser, S. Passerini, and B. Scrosati, *Chem. Commun.*, **49**, 10545–10562 (2013).
2. M. Wild, L. O'Neill, T. Zhang, R. Purkayastha, G. Minton, M. Marinescu, and G. J. Offer, *Energy Environ. Sci.* (2015).
3. I. a. Hunt, Y. Patel, M. Szczygielski, L. Kabacik, and G. J. Offer, *J. Energy Storage*, **2**, 25–29 (2015).
4. G. Xian-Zhong, H. Zhong-Xi, G. Zheng, Z. Xiong-Feng, L. Jian-Xia, and C. Xiao-Qian, *Aircr. Eng. Aerosp. Technol.*, **85**, 293–303 (2013).
5. *ISO 12405-1:2011 Electrically propelled road vehicles – Test specification for lithium-ion traction battery packs and systems – Part 1: High-power applications*, (2011).
6. *ISO 12405-2:2012 Electrically propelled road vehicles – Test specification for lithium-ion traction battery packs and systems – Part 2: High-energy applications*, (2012).
7. *IEC 62660-1: Electrically propelled road vehicles - Test specification for lithium-ion traction battery packs and systems - Part 1: High power applications*, (2011).
8. *IEC 62660-2: Secondary batteries for the propulsion of electric road vehicles - Part 2: Reliability and abuse testing for lithium-ion cells*, (2011).
9. G. Mulder, N. Omar, S. Pauwels, F. Leemans, B. Verbrugge, W. De Nijs, P. Van Den Bossche, D. Six, and J. Van Mierlo, *J. Power Sources*, **196**, 10079–10087 (2011).
10. The Idaho National Laboratory, *Battery Test Manual For Plug-In Hybrid Electric Vehicles*, (2012).
11. D.-I. Stroe, M. Swierczynski, A.-I. Stan, R. Teodorescu, and S. J. Andreasen, *IEEE Trans. Ind. Appl.*, **50**, 4006–4017 (2014).
12. H. He, B. Liu, A. Abouimrane, Y. Ren, Y. Liu, Q. Liu, and Z.-S. Chao, *J. Electrochem. Soc.*, **162**, A2195–A2200 (2015).
13. M. Marinescu, T. Zhang, and G. J. Offer, *Phys. Chem. Chem. Phys.* (2015).

14. Q. Wang, J. Zheng, E. Walter, H. Pan, D. Lv, P. Zuo, H. Chen, Z. D. Deng, B. Y. Liaw, X. Yu, X. Yang, J.-G. Zhang, J. Liu, and J. Xiao, *J. Electrochem. Soc.*, **162**, A474–A478 (2015).
15. D. Moy, a. Manivannan, and S. R. Narayanan, *J. Electrochem. Soc.*, **162**, A1–A7 (2014).
16. M. R. Kaiser, J. Wang, X. Liang, H.-K. Liu, and S.-X. Dou, *J. Power Sources*, **279**, 231–237 (2015).
17. H. Yao, G. Zheng, P.-C. Hsu, D. Kong, J. J. Cha, W. Li, Z. W. Seh, M. T. McDowell, K. Yan, Z. Liang, V. K. Narasimhan, and Y. Cui, *Nat. Commun.*, **5**, 3943 (2014).
18. X. Li, M. Rao, D. Chen, H. Lin, Y. Liu, Y. Liao, L. Xing, and W. Li, *Electrochim. Acta*, **166**, 93–99 (2015).
19. E. Peled, M. Goor, I. Schektman, T. Mukra, Y. Shoval, and D. Golodnitsky, *J. Electrochem. Soc.*, **164**, A5001–A5007 (2017).
20. J. Brückner, S. Thieme, H. T. Grossmann, S. Dörfler, H. Althues, and S. Kaskel, *J. Power Sources*, **268**, 82–87 (2014).
21. Y. Diao, K. Xie, S. Xiong, and X. Hong, *J. Electrochem. Soc.*, **159**, A1816–A1821 (2012).
22. Z. Deng, Z. Zhang, Y. Lai, J. Liu, J. Li, and Y. Liu, *J. Electrochem. Soc.*, **160**, A553–A558 (2013).
23. A. F. Hofmann, D. N. Fronczek, and W. G. Bessler, *J. Power Sources*, **259**, 300–310 (2014).
24. S. Risse, S. Angioletti-Uberti, J. Dzubiella, and M. Ballauff, *J. Power Sources*, **267**, 648–654 (2014).
25. M. Dubarry, V. Svoboda, R. Hwu, and B. Yann Liaw, *Electrochem. Solid-State Lett.*, **9**, A454–A457 (2006).
26. V. Knap, K. Theodoros, R. Purkayastha, B. Szymon, D.-I. Stroe, E. Schaltz, and R. Teodorescu, *Transferring the Incremental Capacity Analysis to Lithium-Sulfur Batteries*, (2017).
27. B. Wu, V. Yufit, Y. Merla, R. F. Martinez-Botas, N. P. Brandon, and G. J. Offer, *J. Power Sources*, **273**, 495–501 (2015).
28. Y.-X. Yin, S. Xin, Y.-G. Guo, and L.-J. Wan, *Angew. Chemie Int. Ed.*, **52**, 13186–13200 (2013).
29. V. Knap, D. I. Stroe, M. Swierczynski, R. Purkayastha, K. Propp, R. Teodorescu, and E. Schaltz, *J. Power Sources*, **336**, 325–331 (2016).
30. V. Knap, T. Zhang, D. I. Stroe, E. Schaltz, R. Teodorescu, and K. Propp, *ECS Trans.*, **74**, 95–100 (2016).

Paper A12

Kalman-variant estimators for state of charge in lithium-sulfur batteries

Karsten Propp, Daniel J. Auger, Abbas Fotouhi,
Stefano Longo and Vaclav Knap

The paper has been published in the *Journal of Power Sources*,
vol. 343, pp. 254–267, Mar. 2017,
10.1016/j.jpowsour.2016.12.087. Under a Creative Commons
license.

Journal of Power Sources 343 (2017) 254–267

Contents lists available at ScienceDirect

Journal of Power Sources

journal homepage: www.elsevier.com/locate/jpowsour

Kalman-variant estimators for state of charge in lithium-sulfur batteries

Karsten Propp, Daniel J. Auger*, Abbas Fotouhi, Stefano Longo, Vaclav Knap [1]

School of Aerospace, Transport and Manufacturing, Cranfield University College Road, Bedford, MK43 0AL, UK

HIGHLIGHTS

- Li-S batteries differ to Li-ion batteries, and require specific state of charge estimation.
- We discuss the limitations of standard SoC estimation methods with Li-S.
- A set of applicable state-of-charge estimators for Li-S batteries is developed.
- The extended Kalman Filter (KF), unscented KF and Particle filter are applied.
- The performance of the applied recursive Bayesian filters is evaluated.

ARTICLE INFO

Article history:
Received 21 September 2016
Received in revised form
21 December 2016
Accepted 22 December 2016

Keywords:
Lithium sulfur battery
State of charge
Extended Kalman filter
Unscented Kalman filter
Particle filter

ABSTRACT

Lithium-sulfur batteries are now commercially available, offering high specific energy density, low production costs and high safety. However, there is no commercially-available battery management system for them, and there are no published methods for determining state of charge *in situ*. This paper describes a study to address this gap. The properties and behaviours of lithium-sulfur are briefly introduced, and the applicability of 'standard' lithium-ion state-of-charge estimation methods is explored. Open-circuit voltage methods and 'Coulomb counting' are found to have a poor fit for lithium-sulfur, and model-based methods, particularly recursive Bayesian filters, are identified as showing strong promise. Three recursive Bayesian filters are implemented: an extended Kalman filter (EKF), an unscented Kalman filter (UKF) and a particle filter (PF). These estimators are tested through practical experimentation, considering both a pulse-discharge test and a test based on the New European Driving Cycle (NEDC). Experimentation is carried out at a constant temperature, mirroring the environment expected in the authors' target automotive application. It is shown that the estimators, which are based on a relatively simple equivalent-circuit–network model, can deliver useful results. If the three estimators implemented, the unscented Kalman filter gives the most robust and accurate performance, with an acceptable computational effort.

1. Introduction

Compared to today's widespread lithium-ion (Li-ion) battery technologies, lithium-sulfur (Li-S) offers increased specific energy storage capability [1]. A greater battery capacity is often advantageous, particularly in applications such as electric vehicles, where it can mitigate consumer concerns about driving range. Li-S batteries also have significant benefits in terms of their wide operational temperature window and safety [2]. The fact that sulfur is abundant and environmentally friendly is also attractive for large-scale cost-driven consumer applications. Commercialization has been hindered by the limitations of early-stage Li-S technologies such as quick degradation and limited sulfur utilization [3]. In recent years, considerable effort has been put into the exploration of Li-S's inner cell mechanisms, resulting in enhanced understanding [4]. Commercial cells are now available from suppliers such as OXIS Energy [5] and Sion Power [6]. Although today's cells may not fulfil every aspect of high automotive demands, they do open the opportunity for practical application oriented research.

In order to use a battery in a practical application, it is necessary

---

* Corresponding author.
E-mail address: d.j.auger@cranfield.ac.uk (D.J. Auger).

[1] Permanent address: Department of Energy Technology, Aalborg University, Aalborg, Denmark.

http://dx.doi.org/10.1016/j.jpowsour.2016.12.087

to have an appropriate battery management system (BMS). A key function of the BMS is determining the remaining usable capacity of the battery, i.e. estimation of the state of charge (SoC). This is important for many reasons: the more accurately SoC is known, the greater the proportion of a battery that can be potentially utilized without fear of overcharging and over-discharging; for consumers, it is often helpful to know how much battery life remains.

In the automotive sector in particular, there has been much research on accurate and robust SoC estimation techniques for Li-ion batteries, aimed at meeting the demanding requirements of the automotive traction battery. Here, the batteries operate in an environment with varying power loads, different operation temperatures, noisy and crude measurements, and high safety requirements [7]. For systems with limited computational power, the SoC of a Li-ion battery can be estimated through the use of equivalent–circuit-networks (ECNs) [8,9], which simulate the voltage response of the battery. Due to their simplicity they are not able to give any insight into the inner cell reactions. However, in practice this does not matter: when operated within their specified limits—in terms of state-of-charge, temperature and current rates—performance of intercalation-based lithium-ion batteries is consistent and predictable [10–13]. This behaviour and the fact that the nonlinear relationship between open-circuit voltage (OCV) and SoC is monotonic means that it is relatively straightforward to determine a Li-ion battery's SoC [14].

For Li-ion batteries, there are many viable techniques for estimating SoC *in situ*. The simplest is to measure the open-circuit voltage and relate it through a nonlinear function or lookup table to the SoC. However, this method needs the battery to be in resting condition which limits the applicability for electric vehicles while driving. For improved robustness, OCV-based estimation is combined with other methods [15]. For a given value of SoC, ECN models can be used to predict terminal voltage output from a known dynamically-changing input current. This can be used to estimate SoC with a good compromise between accuracy, robustness and simplicity. A powerful approach is the use of 'observers' or 'state estimators' which combine model-based estimation with actual measurements using principles derived from control theory, particularly the Kalman filter and its derivatives. Estimators of this kind are popular (particularly within the automotive environment) due to their ability to handle measurement noise and model inaccuracies [7]. With these estimation methods, a high battery utilization is possible, without compromising battery safety or lifetime [16].

To date, estimation techniques of this kind have not been applied to Li-S batteries. There are big differences between Li-S and the classic Li-ion chemistry. Li-ion has an intercalation based process that has a single well-known dominant reaction pathway. Li-S batteries however are more complex with multiple pathways [17], which leads to some unusual and challenging behaviour for the SoC estimation: (i) the OCV-SoC curve has two voltage 'plateaus' with different properties; (ii) the OCV-SoC curve has a large flat region, where the OCV does not change with SoC; (iii) the batteries exhibit relatively high self discharge; and (iv) the usable capacity and power exhibit sensitivity to the applied current profile. Until recently, there have been no models of a Li-S cell suitable for use in a battery management algorithm. Recent developments have been made, and there are now published ECN models of Li-S batteries during discharge that are valid for a range of temperatures [18]. However, the use of these models for the estimation of SoC, remains unexplored. As initial step towards a full BMS system for Li-S batteries, this study examines SoC estimation techniques for their applicability to Li-S batteries.

In this paper, Sec. 2 introduces Li-S batteries and their properties. Sec. 3 explores the applicability of state-estimation techniques used for lithium-ion, noting the limitations with OCV measurement and 'Coulomb counting' and concluding that a more sophisticated approach is required. Sec. 4 describes the filtering techniques that will be used for estimation: Sec. 4.1 describes an equivalent circuit model that will be used to implement such filters, and Sec. 4.2–4.4 introduces three such filters: the extended (nonlinear) Kalman filter (EKF), the 'unscented' Kalman filter (UKF) and the particle filter (PF). Sec. 5 describes the experimental evaluation of these. The results are presented in Sec. 6 where their performance and applicability are discussed.

This work has been conducted as part of an automotive battery project, and the batteries used in this study are kept at a well-maintained constant temperature environment. Accordingly, the work in this paper has been restricted to a constant temperature. (In future work, this could be extended to a varying temperature environment.)

The key contribution of this paper is the development and analysis of these three recursive Bayesian SoC estimators for Li-S. To the best of the authors' knowledge, no similar work has appeared elsewhere in the literature.

2. Lithium-sulfur batteries

A Li-S battery consists of a lithium metal anode and a sulfur-based cathode in electrolyte. Sulfur reversibly reacts with lithium ions when reduced from elemental state S_8, via the intermediates $Li_2S_8, Li_2S_4, Li_2S_2$, to lithium sulfide Li_2S, which is the key of the high theoretical capacity of sulfur (1672 mAh g-1) [19]. The large number of different species however, lead to complex inner reactions that are still a matter of ongoing research [17]. As shown in Fig. 1, the discharge curve consists of two sections [20]: a high plateau at about 2.35 V OCV, characterized by the presence of a majority of high order polysulfides in solution (Li_2S_8, Li_2S_6), and a low plateau at around 2.15 V OCV, where lower order chains have been identified (Li_2S_4, Li_2S_3) [21].

In Li-S batteries the availability of these species in the electrolyte determine the battery's behaviour. In simple words, the cathode is dissolving and participating in electrolyte [22], which causes two voltage plateaus with different behaviour (usable capacity, internal resistance, self-discharge, transient behaviour) [23,24]. As an initial step to model these effects, an equivalent circuit model was presented recently, employing the Thevenin model structure with a pulse discharge current profile and an off-line prediction error minimisation method for parameter identification [18]. The model does not explicitly consider self-discharge, but is valid for transient behaviour of the kind seen in this study. In practice, lithium-sulfur batteries do experience significant self-discharge during long

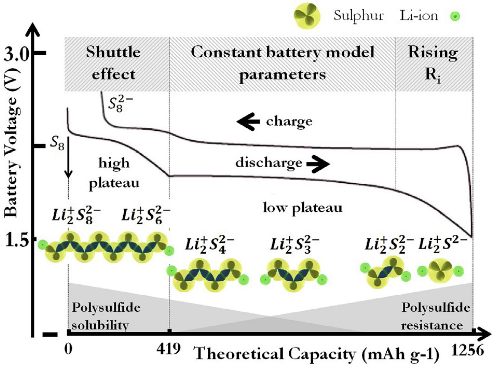

Fig. 1. Discharge/charge behaviour of a Li-S battery.

resting periods. For a shorter-term transient state estimation problem, this can be treated as uncertainty regarding the initial state. For details regarding the model derivation the reader is guided there.

Due to these unique properties of Li-S batteries, a precisely known SoC is helpful to predict the power capabilities of the battery, especially towards the end of discharge where the internal resistance raises quickly. It is not just near depletion that SoC estimation is important. Li-S batteries also need careful monitoring when they are close to fully charged to avoid the problem of 'shuttle'. While charging, the high solubility of the formed high-order polysulfide chains enables them to diffuse to the anode, where they can be reduced to lower order chains directly when in contact. The reaction circle is closed by the movement of the lower order chains back to the cathode. Here, they form high-order polysulfides again when the charging is continued. This redox reaction occurs without electrons passing through the external circuit of the battery and is called polysulfide shuttle [25], which leads, next to self-discharge in the high plateau, to poor coulombic efficiency and is associated with capacity fade [26]. Therefore overcharging should be avoided despite the fact that the shuttle effect can also protect the battery from being overcharged [19].

3. Applicability of conventional SoC estimation techniques

The behaviour of Li-S batteries discussed above leads to difficulties for SoC estimation. Each method faces different challenges: in the following section, these are explained in more detail for the most common SoC estimation techniques. (Impedance spectroscopy is not mentioned further, since it is seldom implemented for practical SoC estimation [15].)

Coulomb counting: Determining the charge flow in and out of the battery is the most common technique for SOC estimation since it is easy to implement. With a given starting point SoC_0 and the rated capacity, it is fairly simple to calculate the SoC from

$$SoC = SoC_0 + \frac{1}{C_N}\int_{t0}^{t}(I_{\mathrm{batt}} - I_{\mathrm{loss}})d\tau. \tag{1}$$

where C_N is the rated capacity, I_{batt} the battery current and I_{loss} the current consumed by loss reactions [15]. While this method is seen generally as reliable, it demands high precision current sensors (to reduce the accumulation of measurement errors over time), known values for the charge/discharge efficiency, and a precisely known initial condition [27,28]. These drawbacks lead to issues with the unique properties of Li-S batteries. Firstly, the polysulfide shuttle effect [25], mainly present in the high plateau, enhances self-discharge, poor coulombic efficiency and capacity fade [25,26]. This leads to hard to determine values for the I_{loss} or efficiency factors in the calculation and changing initial conditions for an estimator [29]. Secondly, the amount of sulfur that can be reversibly utilized during a discharge is strongly affected by the current profile, age and temperature [30]. Generally high discharge capacity is only obtained at low currents. High currents can produce a resistive layer on the cathode, hindering the utilization of the underlying sulfur [20]. This effect hampers the determination of the rated capacity, reducing the practicability of the Coulomb counting method itself significantly.

Open circuit voltage: Another common method of SoC estimation is to assign the OCV to the SoC. This is usually used in applications with low and constant currents or long resting periods. This method works well with Li-ion batteries, since they provide generally a monotonic rising relationships between OCV and SoC [14]. For Li-S however, this method is not feasible due to the non-monotonic curve, changing the gradient between the high and low plateau, and the stable OCV within the low plateau (Fig. 1). Furthermore, the whole concept of OCV for Li-S batteries is not clear due to self-discharge and precipitation [22].

Soft computing techniques: Avoiding the need for building a mathematical battery model and linearisation, soft computing techniques have the ability to model a highly non-linear system by establishing a relationship between the input and output of a system (a 'black-box' model) from training data. This makes these techniques suitable for consideration for battery applications. Particularly for SoC estimation, soft computing techniques have been used in previous studies for NiMH and Li-ion batteries [31,32]. However, there is no record in the literature where these techniques are used for Li-S batteries. (In Ref. [33], the idea is briefly proposed. However, estimation results are not presented.)

Model-based approaches: For the SoC estimation in highly dynamic environments, model-based solutions with a combination of adaptive algorithms are used. Their principle is based on an offline established model, predicting the terminal voltage of the cell during operation and an adaptive algorithm, using the error between prediction and measurement to adjust the states. As the computational power of common BMSs are limited, simplified equivalent electrical circuits are often used to reproduce the transient behaviour of a battery [34,35]. In combination with algorithms such as the extended Kalman filter [36–38], unscented Kalman filter [39–41] and particle filter [42–44] ECN models can help to estimate the batteries internal states with relatively low computational effort and simple measurements of current and terminal voltage. The main advantage of model based methods is that they combine the benefits of direct voltage measurements and 'Coulomb counting' through the use of equivalent-circuit-network models, providing a formal framework for integrating model-based predictions with real-world voltage measurements. This may make them suitable for the properties of the Li-S chemistry. The principle behind these estimation algorithms is described in the following section.

4. Implementation of state estimators

As outlined in Sec. 2 and Sec. 3, Li-S batteries have poorly understood internal dynamics, and state-of-the-art ECN models that cannot represent every aspect of the cell in detail. Methods that have been found to be robust against unmodeled dynamics in the environment are recursive filters [45], that treat the model states x and the observations y as stochastic variables with associated probability density functions [46]. For Gaussian distributions the Kalman filter (KF), minimizing the error variance between true and estimated state, is heavily applied in battery state estimation. In such estimates, the process state is first estimated from a mathematical representation of the system dynamics; this is then corrected with feedback from measurements. The continuous model, described in Sec. 4.1, is used in its discrete form for propagation of prediction- and update-step.

$$\begin{aligned} x_k &= Ax_{k-1} + Bu_{k-1} + w_{k-1} \\ y_k &= Cx_k + v_k \end{aligned} \tag{2}$$

The additional terms w_k and v_k are random variables —white, zero mean, with normal distributions—representing process and measurement noise respectively. These describe the uncertainty in each equation. Their values are determined with the process noise covariance matrix Q and measurement noise covariance matrix R, which are usually assumed to be constant and chosen by the user. Simply speaking, the determined values affect whether the Kalman filter emphasises its 'trust' on feedback from measurements or the *a priori* estimates from the system model. Larger values indicate higher uncertainty or less trust in general. Referring to [47], the

Kalman filter equations are:
Time update equations:

$$\hat{x}_{\mathrm{k}}^{-} = A\hat{x}_{\mathrm{k-1}}^{+} + Bu_{\mathrm{k-1}} \tag{3}$$

$$P_{\mathrm{k}}^{-} = AP_{\mathrm{k-1}}^{+}A^{T} + Q \tag{4}$$

Measurement update equations:

$$L_{\mathrm{k}} = P_{\mathrm{k}}^{-}C^{T}\left(CP_{\mathrm{k}}^{-}C^{T} + R\right)^{-1} \tag{5}$$

$$\hat{x}_{\mathrm{k}}^{+} = \hat{x}_{\mathrm{k}}^{-} + L_{\mathrm{k}}\left(y_{\mathrm{k}} - C\hat{x}_{\mathrm{k}}^{-}\right) \tag{6}$$

$$P_{\mathrm{k}}^{+} = (I - L_{\mathrm{k}}C)P_{\mathrm{k}}^{-} \tag{7}$$

The beauty of the filter is that it provides an efficient recursive mean, minimizing the mean of the squared error, by supporting past, present and future states, even when the precise nature of the modelled system is unknown [47]. For the state estimation of Li-S batteries the nonlinear derivatives of the KF [48] (EKF, UKF) and the particle filter (PF) are employed.

The following describes the mathematics of the three recursive filter algorithms that were implemented. All three algorithms used the same nonlinear equivalent-circuit–network model (Sec. 4.1); the three algorithms are the extended Kalman filter (Sec. 4.2), the unscented Kalman filter (Sec. 4.3) and the particle filter (Sec. 4.4).

4.1. Equivalent-circuit–network model

The Li-S battery model, used in this work, is developed and described in detail in Ref. [18] for temperatures from 20 °C to 50 °C. Here however, the temperature is assumed to be constant, assuming a controlled BMS environment at 20 °C. The identification for a Thevenin equivalent circuit model (Fig. 2) is done with a similar mixed current pulse discharge as shown in Fig. 3-A. The mixed pulse pattern in combination with identification for each pulse individually is used to unveil current-dependent parameter changes in the model. There is self-discharge in the battery, but it is only significant during long resting periods, so I_{self} can be neglected for transient applications. Fig. 2 shows the identification results, as well as the chosen simplified parameter functions over the SoC (X) for the modelled parameters. For the observer the identified parameters of all pulses are used to fit polynomial functions over SoC for the open circuit voltage U_{OCV}, the internal resistance R_0 and one parallel RC circuit C_{p} and R_{p} with MATLAB [49]. Then the derived functions are included in the general state-space form

$$\begin{aligned} \dot{x}(t) &= A(t)x(t) + B(t)u(t) \\ y(t) &= C(t)x(t) + D(t)u(t). \end{aligned} \tag{8}$$

The dynamic states $x = [x_1\ x_2]^T$ of the system are the voltage over the RC circuit U_{p} and the SoC (X), calculated through Coulomb counting. The corresponding state space representation gives

$$A = \begin{bmatrix} \dfrac{-1}{f_{R_{\mathrm{p}}}(X)\,f_{C_{\mathrm{p}}}(X)} & 0 \\ 0 & 0 \end{bmatrix} B = \begin{bmatrix} \dfrac{1}{f_{C_{\mathrm{p}}}(X)} \\ \dfrac{-1}{3600Q_{\mathrm{cap}}} \end{bmatrix} \tag{9}$$
$$C = [-1 \quad f_{\mathrm{OCV}}(X)]D = [f_{R_0}(X)].$$

In Ref. [18] it was shown that the current dependencies of the model parameters mostly influence the transient voltage behaviour, represented by C_{p} and R_{p}, and that they can be neglected without compromising the accuracy of the model significantly. But because of the parameter patterns of U_{OCV} and R_0 vary strongly between the high- and low plateau (Fig. 2), two separate polynomials were fitted over the SoC for each plateau respectively. (A single polynomial would be impractical, since behaviour changes significantly between the plateaus.)

The transition between the polynomials is realized smoothly and differentiably via a partial sinusoidal function $\gamma_{m,c}$.

$$\gamma_{\mathrm{m,c}}(X) := \begin{cases} 0, & \text{if a} \\ \dfrac{1}{2} + \dfrac{1}{2}\sin(2m(X - c)), & \text{if b} \\ 1, & \text{if c} \end{cases} \tag{10}$$

where the conditions a, b, c stands for the different ranges of the function,

$$\begin{aligned} \mathrm{a}:&\ 2m(X - c) < -\frac{1}{2}\pi, \\ \mathrm{b}:&\ -\frac{1}{2}\pi \le 2m(X - c) < \frac{1}{2}\pi, \\ \mathrm{c}:&\ 2m(X - c) > \frac{1}{2}\pi, \end{aligned} \tag{11}$$

where m is a scaling factor for the maximal gradient of the sinusoidal function, determining the transition range between both polynomials and c represents the point where both functions are equally represented. The combined equations of both polynomials and factor γ are

$$f_{\mathrm{OCV}}(X) = \left(1 - \gamma_{\mathrm{m,c}}(X)\right)\ f_{\mathrm{OCV-low}}(X) + \gamma_{\mathrm{m,c}}(X)f_{\mathrm{OCV-high}}(X) \tag{12}$$

for the open circuit voltage U_{OCV} and

$$f_{R0}(X) = \left(1 - \gamma_{\mathrm{m,c}}(X)\right)\ f_{\mathrm{R0-low}}(X) + \gamma_{\mathrm{m,c}}(X)\,f_{\mathrm{R0-high}}(X), \tag{13}$$

for the internal resistance R_0 over SoC. Since the variations between both plateaus are less pronounced for C_{p} and R_{p}, the functions for these parameters are only determined with a single polynomial respectively. This decision also simplifies the estimation of the Jacobian matrix of A for the extended Kalman filter.

For a fuller discussion of this ECN model, the reader is referred to the original source [18].

4.2. Extended Kalman filter

The basic Kalman filter algorithm, described in Sec. 4, applies to linear systems, not nonlinear systems. The Li-S equivalent-circuit–network is *nonlinear*. This means that the basic algorithm needs adaptation before it can be applied. There are several ways of doing this, which will be explored in the following sections. The simplest is the 'extended Kalman filter' (EKF).

The basic idea of the EKF is to linearise the system around the current mean of the state $\hat{x}_{k-1}^{+}$ with a first order Taylor series for the propagation of the probability densities [50]. Hence, the EKF predicts the states and measurements with a nonlinear system model f and the covariances and Kalman gain with the Jacobians of A and C, $\hat{A}$ and $\hat{C}$. Generally this linearisation works well with models containing slight non-linearities as it is the case for most classic Li-ion batteries.

Determining the Jacobians analytically increases the effort for

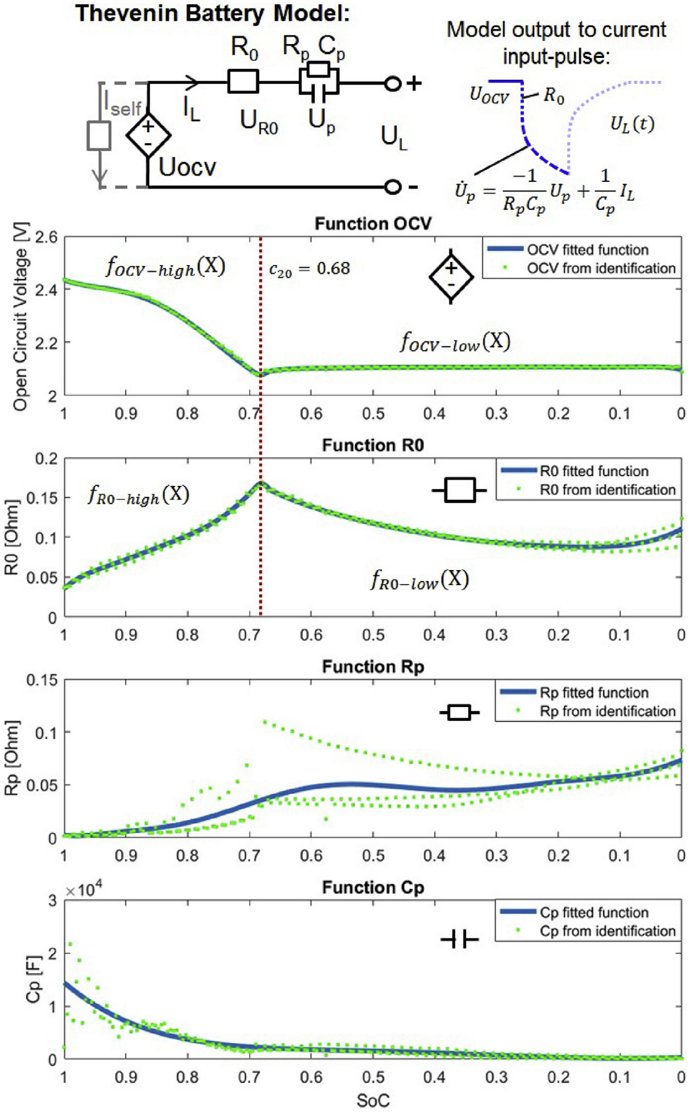

Fig. 2. Model structure and parameter functions for U_{OCV}, R_0, R_p and C_p over SoC for 20 °C.

setting up the filter with the benefit of the lowest computational effort of the proposed methods.

4.2.1. Summary of EKF algorithm

In the following, the algorithm is summarized from Ref. [16]. (Details are omitted here for brevity, but can be found in the reference.)

Nonlinear state space model

$x_k = f(x_{k-1}, u_{k-1}, w_{k-1}, k-1)$

$y_k = h(x_k, u_k, v_k, k)$

Definitions

$$\hat{A}_k = \left.\frac{\partial f(x_k,u_k,w_k,k)}{\partial x_k}\right|_{x_k=\hat{x}_k^+}, \hat{B}_k = \left.\frac{\partial f(x_k,u_k,w_k,k)}{\partial w_k}\right|_{w_k=\overline{w}_k},$$

$$\hat{C}_k = \left.\frac{\partial h(x_k,u_k,w_k,k)}{\partial x_k}\right|_{x_k=\hat{x}_k^-}, \hat{D}_k = \left.\frac{\partial h(x_k,u_k,w_k,k)}{\partial v_k}\right|_{v_k=\overline{v}_k}$$

Initialisation for k = 0

$$\hat{x}_0^+ = \mathbb{E}[x_0],\ P_0^+ = \mathbb{E}\left[\left(x_0-\hat{x}_0^+\right)\left(x_0-\hat{x}_0^+\right)^T\right]$$

Computation EKF for k = 1, 2, …

State estimate update:

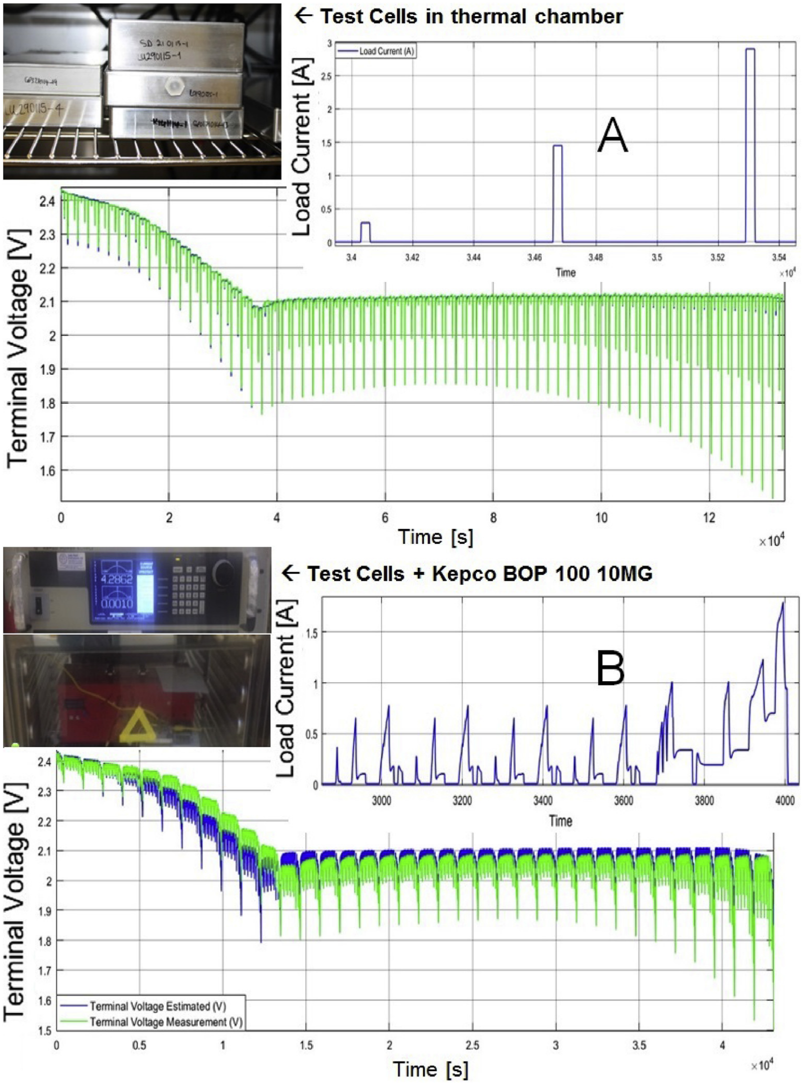

Fig. 3. Mixed pulse and NEDC current profile with test installation.

$$\hat{x}_k^- = f\left(\hat{x}_{k-1}^+, u_{k-1}, \overline{w}_{k-1}, k-1\right)$$

Error covariance update:

$$P_k^- = \hat{A}_{k-1}P_{k-1}^+\hat{A}_{k-1}^T + \hat{B}_{k-1}Q\,\hat{B}_{k-1}^T$$

Output estimate:

$$\hat{y}_k = h\left(\hat{x}_k^-,\ u_k\ ,\ v_k, k\right)$$

Kalman Gainmatrix:

$$L_k = P_k^-\hat{C}_k^T\left[\hat{C}_kP_k^-\hat{C}_k^T + \hat{D}_kR_k\hat{D}_k^T\right]^{-1}$$

State estimate measurement update:

$$\hat{x}_k^+ = \hat{x}_k^- + L_k[y_k - \hat{y}_k]$$

Error covariance measurement update:

$$P_k^+ = (I - L_k\hat{C}_k)P_k^-$$

4.3. *Unscented Kalman filter*

To improve the estimation for nonlinear systems, the covariance propagation in the UKF follows the nonlinearities with a set of sigma points, propagated through the main steps of the algorithm. The number of necessary points depends on the state vector's dimension L and leads to $2L+1$ columns for the resulting vector χ. With the principle of estimating covariances with data rather than a Taylor series, the unscented Kalman filter has the advantage that no derivatives are needed, with only slightly more computational effort. Furthermore, the covariance approximations are usually better than these of the EKF [16]. The differences between both are largely dependent on the nonlinearity of the system. For standard Li-ion batteries for example, the improvements are modest due to their small nonlinearities [16].

4.3.1. *Summary of UKF algorithm*

In the following the algorithm is summarized from Ref. [51]. (Again, details are omitted here for brevity, but can be found in the reference.)

Nonlinear state space model

$$x_k = f(x_{k-1}, u_{k-1}) + w_{k-1} \;\; y_k = h(x_k, u_k) + v_k$$

Definitions

$$Q_k = \mathbb{E}\left[w_k w_k^T\right] \;\; R_k = \mathbb{E}\left[v_k v_k^T\right]$$

Initialisation

$$\hat{x}_0^+ = \mathrm{E}[x_0]$$

$$P_0^+ = \mathrm{E}\left[\left(x_0 - \hat{x}_0^+\right)\left(x_0 - \hat{x}_0^+\right)^T\right]$$

Computation UKF for k = 1, 2, …

State estimate time update

Errorcovariance matrix squareroot :

$$\sqrt{P_{k-1}} = \mathrm{chol}(P_{k-1})$$

Create sigma points:

$$\chi_{k-1}^+ = \left[\hat{x}_{k-1}^+,\; \hat{x}_{k-1}^+ + \gamma\sqrt{P_{k-1}^+},\; \hat{x}_{k-1}^+ - \gamma\sqrt{P_{k-1}^+}\right]$$

Update sigma points:

$$\chi_k^{i,-} = f\left(\chi_{k-1}^{i,+}, u_{k-1}\right) \text{ for i } = 0, 1, 2 \ldots 2\mathrm{L}$$

Mean of updated sigma points:

$$\hat{x}_k^- = \sum_{i=0}^{2L} \alpha_i^{(m)} \chi_k^{i,-}$$

Error Covariance time update

Covariance prediction:

$$P_k^- = Q_{k-1} + \sum_{i=0}^{2L} \alpha_i^{(c)} \left(\chi_k^{i,-} - \hat{x}_k^-\right)\left(\chi_k^{i,-} - \hat{x}_k^-\right)^T$$

Output estimate

Measurement prediction for each sigma point:

$$\psi_k^i = h\left(\chi_k^{i,-}, u_k\right) \text{ for i } = 0, 1, 2 \ldots 2\mathrm{L}$$

Mean of the measurement prediction:

$$\hat{y}_k = \sum_{i=0}^{2L} \alpha_i^{(m)} \psi_k^i$$

Estimator gain matrix

Estimate the covariance of measurement:

$$P_k^{yy} = R_k + \sum_{i=0}^{2L} \alpha_i^{(c)} \left(\psi_k^i - \hat{y}_k\right)\left(\psi_k^i - \hat{y}_k\right)^T$$

Estimate cross covariance state/measurement:

$$P_k^{xy} = \sum_{i=0}^{2L} \alpha_i^{(c)} \left(\chi_k^{i,-} - \hat{x}_k^-\right)\left(\psi_k^i - \hat{y}_k\right)^T$$

Kalman gain:

$$L_k = P_k^{yy}\left(P_k^{xy}\right)^{-1}$$

State estimate update:

$$\hat{x}_k^+ = \hat{x}_k^- + L_k(y_k - \hat{y}_k)$$

Error covariance update:

$$P_k^+ = P_k^- - L_k P_k^{yy} L_k^T$$

4.4. *Particle filter*

To solve the recursive estimation problem for arbitrary probability distributions, the PF applies Monte Carlo methods to represent the probability density functions. Unlike the UKF, where just the means and covariances of the sigma points are transferred to the next step, the PF recursively estimates the whole particle set χ_t from the last step χ_{t-1}. Generally three steps are executed [52]. (i) The state transition, where each particle transition is calculated with the input u_{k-1}, after measurement noise is added to the particles of the previous step. Similar to the Kalman filter, the addition of the noise leads to an increasing variance over time. (ii) In the weighting step the observations y_k and a probability density function are used to allocate a weight to each particle, representing the probability state prediction x_k given a certain observation y_k. (iii) During resampling, the variance of the particle set is decreased by sampling a new set of particles according to their weights and allocating new, equal weights. The main advantage of the PF is the independence of the Gaussian noise assumption of the Kalman filter. However, since each particle has to be computed separately, the computational effort exceeds the Kalman filter type algorithms significantly [53].

4.4.1. *Summary of PF algorithm*

The derivation of the equations orients on chapter 4.2 of the textbook [54]. (Again, details are omitted here for brevity, but can be found in the reference.)

```
$\bar{\chi}_k = \chi_k = \varnothing$
for $m = 1$ to $M$ do
    sample $x_k^m \approx p(x_k | u_k, x_{k-1}^m)$
    $w_k^m = p(y_k | x_k^m)$
    $\bar{\chi}_k = \bar{\chi}_k + \langle x_k^m, w_k^m \rangle$
endfor
for $m = 1$ to $M$ do
    draw $i$ with probability $\propto w_k^i$
    add $x_k^i$ to $\chi_k$
endfor
return $\chi_k$
```

5. Experimental evaluation

To investigate the performance of the state estimation algorithms, batteries were discharged with two current profiles and different test rigs. The first, a mixed-current pulse test, is based on the parameter estimation in Ref. [18] and represents an abstract test in a controlled environment. Here, a pre-cycled (C/10 charge, C/5 discharge, 30 °C) 3.4 Ah long life chemistry pouch cell from OXIS Energy was tested with current pulses of 290 mA, 1450 mA and 2900 mA at 20 °C (Fig. 3-A). The test hardware included a Maccor 4000 battery tester with cells constantly held at temperature in sealed aluminium boxes inside a Binder KB53 thermal chamber, also shown in Fig. 3-A.

To represent a more practical scenario, the same kind of OXIS Energy cell was discharged with a current profile based on the New European Driving Cycle (NEDC) [55]. The related power profile, shown in Ref. [56], was chosen due to its compromise of a realistic user scenario, also containing some level of abstraction. The test hardware used in this case is a Kepco BOP100-10MG programmable power source/sink (Fig. 3-B) discharging a battery at room temperature (23 °C). The details of the experiments are summarized in Table 1.

5.1. Reference SoC estimation

The reference SoC for both test benches was calculated from the cumulated current, operating in the cells' recommended voltage range, i.e. between 2.45 V (fully charged, SoC = 1), and 1.5 V (fully discharged, SoC = 0).

$$SoC = SoC_{(0)} - \frac{1}{3600Q_{\text{cap}}}\int_0^t i(\tau)d\tau. \tag{14}$$

While Coulomb counting is a poor predictor during tests, the discharge capacity for a specified voltage window can be calculated retrospectively, giving a reference SoC that can be used for post-experimental interpretation.

5.1.1. EKF SoC estimation

For the application of the EKF algorithm with the presented Li-S battery model, the Jacobians of the matrices A and C are needed, which are presented here for convenience. With one polynomial function respectively for C_p and R_p dependent on the SoC (here presented as second state of the model x_2), the Jacobian matrix of A is populated as:

$$\widehat{A}(1,1) = \frac{-1}{f_{C_\text{p}}(x_2)\,f_{R_\text{p}}(x_2)} \quad \widehat{A}(2,1) = 0 \quad \widehat{A}(2,2) = 0 \tag{15}$$

$$\widehat{A}(1,2) = \left[\frac{\dot{f}_{C_\text{p}}(x_2)}{f_{C_\text{p}}(x_2)^2\,f_{R_\text{p}}(x_2)} + \frac{\dot{f}_{R_\text{p}}(x_2)}{f_{C_\text{p}}(x_2)\,f_{R_\text{p}}(x_2)^2}\right]x_1 - \left[\frac{\dot{f}_{C_\text{p}}(x_2)}{f_{C_\text{p}}(x_2)^2}\right]I_{Bat}, \tag{16}$$

with the same principle for C

Table 1
Discharge experiments.

Discharge	Measured Cap.	Av. Power	Av. Temp.
Pulse	9778 As	0.147 W	20 °C
NEDC	9678 As	0.467 W	23 °C

$$\widehat{C}(1,1) = -1 \quad \widehat{C}(1,2) = \dot{f}_{OCV}(x_2) - \dot{f}_{\text{R}_0}(x_2)I_{\text{Bat}}. \tag{17}$$

The derivatives of the combined functions $\dot{f}_{\text{OCV}}$ and $\dot{f}_{\text{R}_0}$ with respect to x_2 are influenced by the introduced factor γ, here substituted by $f_\gamma(x_2)$.

$$f_{\text{OCV}}(x_2) = \Big(1 - f_\gamma(x_2)\Big)f_{\text{OCV-low}}(x_2) + f_\gamma(x_2)f_{\text{OCV-high}}(x_2) \tag{18}$$

Derivation with respect to x_2 leads to

$$\begin{aligned}\dot{f}_{\text{OCV}}(x_2) = \dot{f}_{\text{OCV-low}}(x_2) - \Big(&\dot{f}_\gamma(x_2)f_{\text{OCV-low}}(x_2)\\ &+ f_\gamma(x_2)\dot{f}_{\text{OCV-low}}(x_2)\Big) + \dot{f}_\gamma(x_2)f_{\text{OCV-high}}(x_2)\\ &+ f_\gamma(x_2)\dot{f}_{\text{OCV-high}}(x_2).\end{aligned} \tag{19}$$

where $\dot{f}_\gamma$ is defined by

$$\dot{\gamma}_{m,c}(x_2) := \begin{cases} 0, & \text{if a} \\ m\cos(2m(x_2 - c)), & \text{if b} \\ 0, & \text{if c} \end{cases} \tag{20}$$

with the same conditions for a, b, c as in equation (11). The derivation of $\dot{f}_{\text{R}_0}$ follows the same pattern. As mentioned before, the unique behaviour of the Li-S battery can vary in a complex manner. Therefore it is reasonable to assume that the voltage prediction of the observer is, firstly, not necessarily accurate and, secondly, that the predicted voltage is not everywhere an indicator of the SoC. To account for this, the measurement noise value R is with 0.15 relatively high compared to the chosen model noise Q, which assumes uncorrelated states with a low uncertainty for the Coulomb counting state.

$$P_{0\ \text{EKF}} = \begin{bmatrix} 10 & 0 \\ 0 & 10 \end{bmatrix} \quad Q_{\text{EKF}} = \begin{bmatrix} 0.1 & 0 \\ 0 & 0.0000003 \end{bmatrix} \tag{21}$$

The value of the measurement noise R implies a standard deviation for the measurements of 387 mV. This is greater than the values of actual Gaussian noise observed from the measurements. However, since the battery model is not able to predict the terminal voltage for every user case precisely, deviations in this order of magnitude are possible. The values of Q, representing the system noise, were determined iteratively to give good results.

5.1.2. UKF SoC estimation

Within the UKF framework, the weights $\alpha_i^{(m)}$ and $\alpha_i^{(c)}$ are vectors containing real constant scalars with the conditions that $\sum_{i=0}^{p}\alpha_i^{(m)}$ and $\sum_{i=0}^{p}\alpha_i^{(c)}$ are equal to 1 [16]. With the scaling value

$$\lambda = \alpha^2(L + \kappa) - L$$

the weights can be calculated from

$$\gamma = \sqrt{L + \lambda}, \quad \alpha_i^{(m)} = \alpha_i^{(c)} = \frac{1}{2(L + \lambda)}$$

$$\alpha_0^{(m)} = \frac{\lambda}{L + \lambda}, \quad \alpha_0^{(c)} = \frac{\lambda}{L + \lambda} + \Big(1 - \alpha^2 + \beta\Big).$$

Here, we chose similar weights as presented in Ref. [51], defining the values 1 for α, 2 for β, $L = \dim\{x\} = 2$, and 0 for κ. Since the parameters are constant, they can be defined once prior executing the filter. The values of the measurement and system noise R and Q follow the same pattern of the EKF. However, the values for P_0 are considerably smaller since widely spread, unrestricted sigma points lead to estimation errors when they exceed the defined SoC range of 0–1 in the beginning of the estimation. Furthermore, the UKF was found to be more sensitive to the model prediction errors compared to the EKF, so larger values were used in the measurement noise matrix $R = 0.3$.

$$P_{0\ \mathrm{UKF}} = \begin{bmatrix} 1 & 0 \\ 0 & 0.014 \end{bmatrix} \quad Q_{\mathrm{UKF}} = \begin{bmatrix} 0.0005 & 0 \\ 0 & 0.0000007 \end{bmatrix} \tag{22}$$

5.1.3. PF SoC estimation

The chosen probability density function should, on the one hand, accurately determine the most likely observations, but on the other hand hinder the impoverishment of the samples over time. Examples for non Gaussian probability density functions for SoC estimation are given in Refs. [43,44]. Here however, the Gaussian distribution

$$f(x) = \frac{1}{\sigma\sqrt{2\pi}} e^{-\frac{(x-\mu)^2}{2\sigma^2}} \tag{23}$$

is used due to its simplicity and comparably to the EKF and UKF. To account for the uncertainties of the model and Coulomb counting, the standard deviations to sample the states in the prediction step are chosen in the same pattern as the EKF and UKF, allocating larger values to the transient voltage term U_p, to account for the model inaccuracies, and smaller values to the SoC state, to limit the random fluctuations when the battery behaviour does not change.

$$\mathrm{std}_{x_1} = 0.004 \quad \mathrm{std}_{x_2} = 0.0003 \tag{24}$$

The number of particles was chosen iteratively. Tests indicated a decent compromise between computational effort and estimation precision with a constant number of 30 particles.

6. Results and discussion

The results of the proposed SoC estimation algorithms are evaluated qualitatively for their convergence time, with imprecise initial states, and quantitatively by their estimation accuracy. As measure for the latter the root mean squared error (RMSE) over the hole discharge range is used.

$$\mathrm{RMSE} = \frac{1}{\sqrt{n}} \left(\sum_{i=1}^{n} \left(SoC_{t,i} - S\hat{o}C_{t,i}\right)^2 \right)^{0.5} \tag{25}$$

where n is the number of data points, $SoC_{t,i}$ is the reference SoC from the measurement and $S\hat{o}C_{t,i}$ is the estimated SoC by the filters. The accuracy and convergence depend on the quality of the model, the observability of the system itself, the quality of the measurements, their noise pattern and the users choices for the system and measurement uncertainties. In the context of the model accuracy also the discharge profile plays a role. For the pulse test, with its long resting periods, the errors in the OCV are more sensitive to the prediction error, whereas the more realistic NEDC cycle emphasises the internal resistance or transient behaviour. Since Li-S batteries suffer from self-discharge, which can lead to an imprecise initial condition for the SoC estimation, each test is performed with three different initial SoC values. While two of them are located in the high plateau ($SoC_0 = 1,\ 0.7$), one is chosen after the transition point (0.68) at ($SoC_0 = 0.6$), to test the algorithms ability to converge in between both plateaus. To test their robustness against current profile induced changes, all filters use the predetermined capacity from the mixed pulse discharge profile tests during the model identification (9778 As). The results of the SoC estimation tests are shown in Fig. 4 and Table 2. The following discussion orients on the specific properties of Li-S batteries.

High self-discharge: Self discharge, caused by the shuttle effect, occurs mainly in the high plateau. This can be difficult to handle for

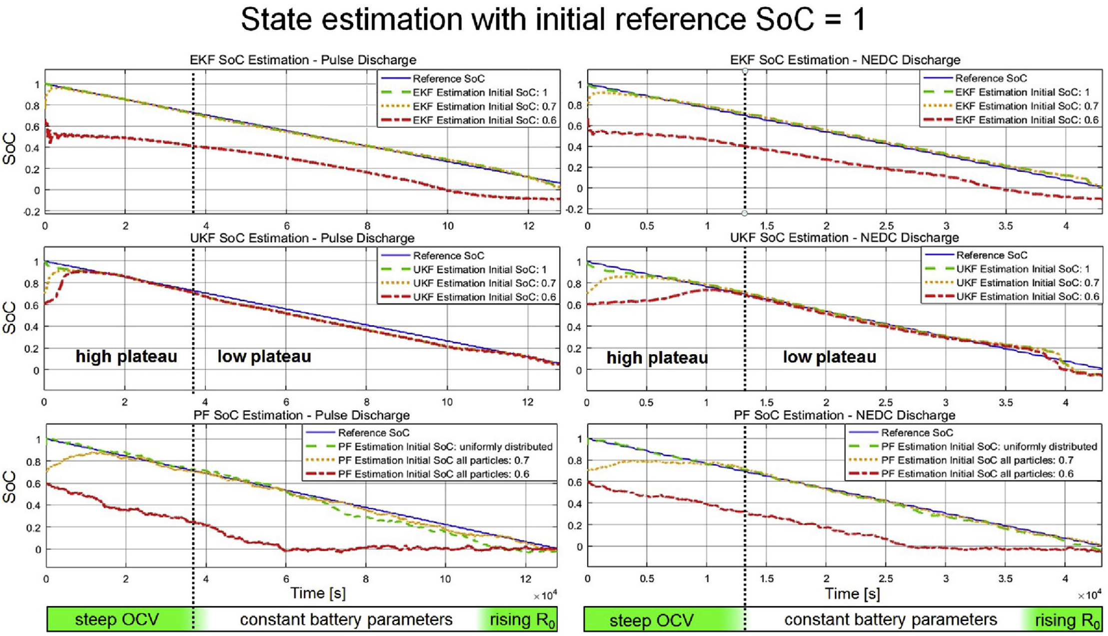

Fig. 4. Estimation results for EKF, UKF, PF with a mixed pulse- and a NEDC drive cycle current profile, starting with a fully charged battery, i.e. SoC = 1.

Table 2
RSME SoC Estimation with EKF, UKF and PF with initially fully charged battery.

Algorithm	SoC_0	Pulse RSME	NEDC RSME
EKF	1	0.0114	0.0217
	0.7	0.0160	0.0267
	0.6	0.2986	0.2732
UKF	1	0.0347	0.0280
	0.7	0.0444	0.0537
	0.6	0.0705	0.1199
PF	uni	0.0576	0.0195
	0.7	0.0532	0.0694
	0.6	0.3997	0.3354

the SoC estimators since the state changes when the monitoring system is switched off. However, the high plateau has also a steep OCV gradient which allows the estimator to converge quickly when the state changed. Therefore the estimation result does not change significantly with an imprecise initial condition as long as both states, the real one and the estimated one, are within the same plateau. Otherwise, the local minimum in the OCV can hinder the convergence. Especially the EKF, with its first order linearisation, and the PF with its particle set far away from the real SoC suffer from this effect (Fig. 4 EKF: Pulse Test, NEDC PF: Pulse Test, NEDC). Here, the UKF has the best performance. For applications demanding a quick conversion without a precise initial condition a self-discharge model is recommended.

Constant OCV: The uncertain region does not contain sufficient information in the battery behaviour to distinguish different SoCs in the low plateau, which leads to a state prediction heavily based on the Coulomb counting. The result of this is a slightly drifting SoC in that region and a slow convergence (Fig. 4 all filters: Pulse test, NEDC initial $SoC_{0\ \mathrm{ref}} = 1$). However, due to the area with increased internal resistance towards the end of discharge, the estimators are able to correct that error mostly before the depletion point. Here, the fact that the constant region is enclosed by the high plateau and an area of increased cell resistance favours the model based estimation. Furthermore, the lower self-discharge within the low plateau allows the Coulomb counting to be accurate and limits the drift.

Table 3
RSME SoC Estimation with EKF, UKF and PF with partly discharged battery.

Algorithm	SoC_0	Pulse RSME	NEDC RSME
EKF	1	0.1593	0.1696
	0.7	0.0860	0.0535
	0.6	0.1203	0.0745
UKF	1	0.0887	0.1743
	0.7	0.0240	0.0687
	0.6	0.0189	0.0332
PF	uni	0.0281	0.0561
	0.7	0.1661	0.1176
	0.6	0.0383	0.0320

Conversion with discharged battery: When starting from a partially-discharged state, e.g. where the self-discharge of the battery causes the estimated SoC to be higher than the real one (Fig. 5), the differences between the EKF and UKF are more pronounced. Here, the simulation was started at the initial reference SoC of 0.6, with the same initial conditions used in the fully-charged tests for the estimators ($SoC_{0EKF,UKF,PF} = 1, 0.7, 0.6$). In these tests, it can be seen that the estimators performance is also depending on the starting point. In general, the UKFs work best, though they can fail (Fig. 5 UKF NEDC initial $SoC_{0\ \mathrm{ref}} = 0.6$). The EKF tends to converge slowly, requiring more than a full discharge cycle. The particle filter can fail if the particles are poorly distributed at the start, but when the particles are uniformly distributed, it converges to the true state of charge very quickly. The results are summarized in Table 3.

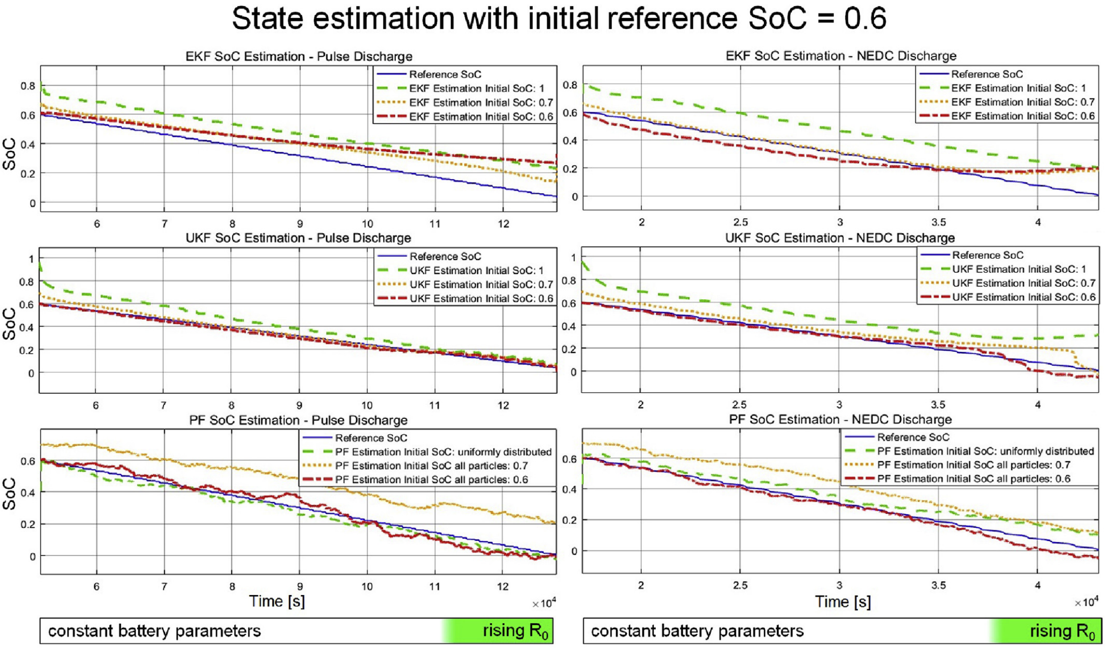

Fig. 5. Estimation results for EKF, UKF, PF with a mixed pulse- and a NEDC drive cycle current profile with an initially partly discharged battery, i.e. from SoC = 0.6.

Table 4
Discharge experiments with NEDC-low and NEDC-high profile.

Discharge	Measured Cap.	Av. Power	Av. Temp.
NEDC-low	10561 As	0.317 W	23 °C
NEDC-high	9072 As	0.610 W	23 °C

Changes of the model parameters: As mentioned before, the smaller parameter variation within the low plateau favours the SoC estimation. However, the dependence of the battery behaviour on the load profile remains a challenge. Different current rates and profiles cause different utilisations of sulfur and therefore variations in the usable capacity. While these effects are less pronounced in the high plateau, the low plateaus variations are significant. To show their effect to the model accuracy and SoC estimation, further tests were done with a decreased (added gain of 0.66 to current profile) and increased (added gain of 1.33 to current profile) NEDC profile (Table 4).

Both, Fig. 6 and Fig. 7, show the effects of the current density variations to the model accuracy and SoC estimation. For most of the discharge range the cell behaviour could still be represented well. But the increased capacity, mainly in the low plateau, leads to deviations of model prediction and measured voltage towards the end of discharge (Fig. 6), since the model uses the fixed capacity value from the pulse identification process (9778 As).

The rough capacity prediction combined with the constant OCV within the low plateau cause a negative drift of the SoC estimation in this area. Due to the strong divergence between model and measurements towards the end of discharge however, there is some correction towards the reference SoC in the end of the discharge process as well.

With higher rates the ratio of the high plateau of the whole discharge capacity increases which should enable the algorithms to correct the states longer. Nevertheless, the estimated SoC drifts towards higher values in this case. Here the differences in between the model and measurements are not significant enough to correct the states sufficiently. The results of the estimation accuracy with different current profile gains are summarized in Table 5.

To cover for the uncertainties, an improved observer model, accounting for model changes with current profiles, could be the key for improvement. However, since the inner cell mechanisms are still a matter of ongoing research, on-line parameter estimation could lead to improvements for the SoC estimation easier to obtain.

To achieve optimal results with handling the proposed model and estimation, we suggest the following steps: (i) define a simplified current profile for the intended application; (ii) measure the delivered capacities for this use-case and (iii) apply our presented battery model and estimation method with the derived capacity value.

Two plateaus with transition region: A likely consequence of the local minimum in the identified OCV curve in between the voltage plateaus, the EKF and the PF converge slowly when the initial condition is not located in the high plateau ($SoC_0 = 0.6$). To investigate filter-based solutions to improve the convergence, a simplified OCV curve, neglecting the voltage drop in between the plateaus (Fig. 8), was fitted to the OCV identification data and substituted with the previously used function.

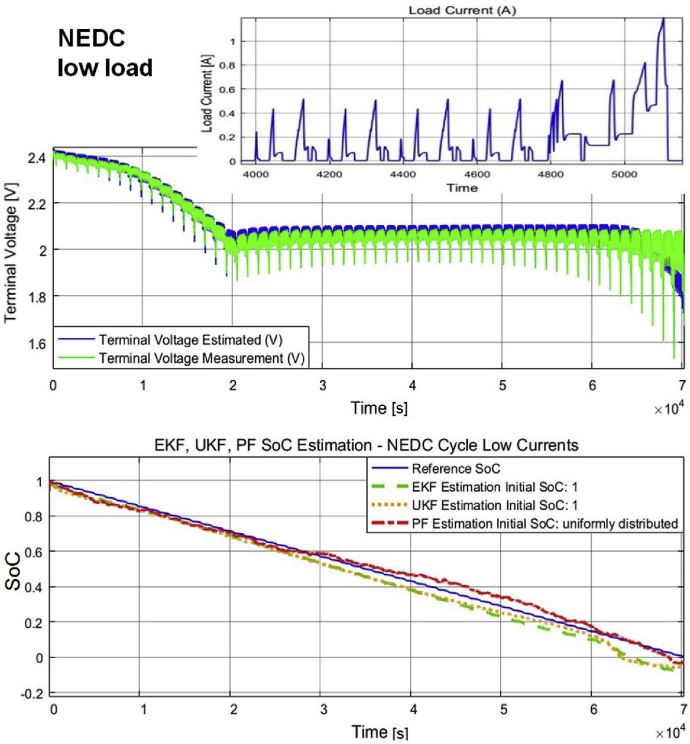

Fig. 6. Estimation results EKF, UKF, PF for a lower current NEDC drive cycle (Added gain of 0.66 to the reference NEDC drive cycle, described in Sec. 5).

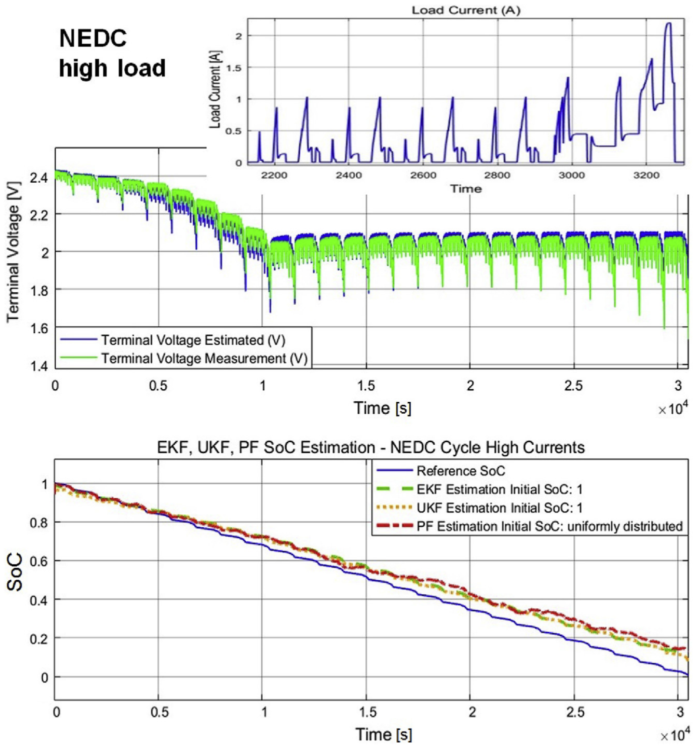

Fig. 7. Estimation results EKF, UKF, PF for a higher current NEDC drive cycle (Added gain of 1.33 to the reference NEDC drive cycle, described in Sec. 5).

Table 5
RSME SoC estimation with NEDC-low and NEDC-high profile.

Algorithm	SoC_0	NEDC-low	NEDC-high
EKF	1	0.0489	0.0580
UKF	1	0.0625	0.0546
PF	uni	0.0310	0.0694

$$
\begin{aligned}
f_{OCV-simple}(x_2) = {} & 339.78x_2^9 - 1372.71x_2^8 + 2291.23x_2^7 \\
& - 2066.02x_2^6 + 1107.76x_2^5 - 364.76x_2^4 \\
& + 72.94x_2^3 - 8.36x_2^2 + 0.48x_2 + 2.1
\end{aligned}
\tag{26}
$$

The advantage of this single polynomial is an almost monotonic behaviour ignoring highly nonlinear parts in the OCV curve, also simplifying the derivation of the Jacobian matrix. While the estimation results of the PF do not change significantly, the first order linearisation of the EKF leads to the anticipated results. As shown in Fig. 8, the convergence time for the imprecise initial SoC of 0.6 has improved significantly with only minor losses in the estimation accuracy for the rest of the discharge (Table 6).(For the simplified OCV curve, it was found necessary to set the initial covariance of the SoC to 21.)

However, all in all we can conclude that the UKF can cope best with the properties of the Li-S battery combined with a reasonable computational effort. Table 7 presents the simulation times for the reference battery model and three parallel running estimation algorithms (SoC_0: 1, 0.7, 0.6) on the same system (Intel(R) Core(TM) i5-5300 CPU @ 2.30 Ghz, 8GB RAM, 64 bit operating system).

It is shown that the additional computational effort of the particle filter does not lead to significant improvements in this case.

7. Conclusion

This paper has introduced the problem of SoC estimation for Li-S batteries, and explored the applicability of ‘standard’ techniques used for lithium-ion batteries. It was noted that Li-S batteries exhibit complex behaviours, some of which prevent the exploitation of ‘standard’ techniques in electric vehicles. Lithium-sulfur's open-circuit–voltage versus state-of-charge curve has a large flat region, meaning that open-circuit voltage is a poor indicator of SoC. Because there are multiple reaction pathways, the useful capacity of Li-S cells depends on the applied duty cycle. Furthermore, it suffers from high self-discharge, so ‘Coulomb counting’ is unlikely to be effective. As an alternative, this paper has explored three model-based methods of state estimation, all of which were variants of the recursive Bayesian filter: the extended Kalman filter, the unscented Kalman filter and the particle filter. Despite the complexities of Li-S cells, it was demonstrated in experimental tests that the model-based estimators based on an equivalent-circuit–network model were able to perform robustly.

The discussion of the results noted several ways where the complex behaviours of Li-S help to aid the estimation problem. While the high self-discharge within the high plateau hinders the determination of a precise initial SoC, the steep OCV gradient in this

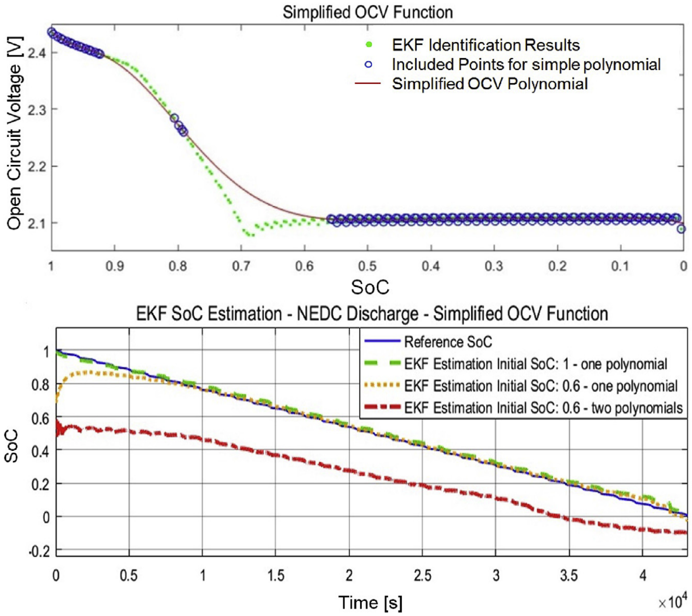

Fig. 8. Simplified OCV curve and related estimation results for the EKF.

Table 6
RSME SoC estimation with simplified OCV curve.

Algorithm	SoC_0	OCV Function	NEDC RSME
EKF	1	one poly	0.0205
	0.6	one poly	0.0272
	0.6	two poly	0.3923

Table 7
Simulation time for the pulse discharge test (128000 s).

	EKF	UKF	PF
Simulation time	5.25 [s]	7.97 [s]	21.54 [s]

region allows a quick convergence. Here, problematic and useful properties for the state estimation cancel each other out. In the low plateau, the flat OCV curve and relative constant battery parameters hinder a precise estimation. In this area also current-related changes in the usable capacity occur mostly, which is the reason why the proposed estimation methods works best within a certain discharge current range. However, due to the enclosure of the constant region by the high plateau and an area with increased internal resistance, the estimation is mostly able to converge to the correct SoC within one discharge cycle. Therefore a standard model-based estimator, with its multiple sources/states of information, is capable of predicting the SoC of a Li-S cell well enough. Hereby the unscented Kalman filter gives the most robust and accurate performance in combination with a reasonable computational effort.

It was conjectured that improvements to the model to represent self-discharge are likely to benefit the robustness of the estimators. Furthermore, a facility to deal with the current-related parameter changes, is very likely to improve the accuracy. It would also be interesting to consider whether adaptive noise covariance values could be used to improve the model fit whilst accommodating regions of greater uncertainty. The authors also are currently exploring the application of recursive parameter estimation for state estimation. A limitation of the performed tests is the constant-temperature scenario. This mirrors the highly regulated environment of the authors' intended end application, an electric vehicle test environment with a tightly-regulated temperature. However, future work should also explore any challenges associated with state estimation in an environment with significant temperature variations.

Acknowledgement

This research was undertaken as part of the project ‘Revolutionary Electric Vehicle Battery’ (REVB), co-funded by Innovate UK under grant TS/L000903/1; university funding is provided by EPSRC under grant number EP/L505286/1. Enquiries for access to the data referred to in this article should be directed to researchdata@cranfield.ac.uk. (The data used in this article is described at https://dx.doi.org/10.17862/cranfield.rd.3834057; it is subject to an embargo, and will be available from May 2022.)

References

[1] P.G. Bruce, S.A. Freunberger, L.J. Hardwick, J.-M. Tarascon, Li-o2 and li-s batteries with high energy storage, Nat. Mater. 11 (2012) 19–29.
[2] D. Bresser, S. Passerini, B. Scrosati, Recent progress and remaining challenges in sulfur-based lithium secondary batteries—a review, Chem. Commun. 49 (2013) 10545–10562.
[3] V. Kolosnitsyn, E. Karaseva, Lithium-sulfur batteries: problems and solutions, Russ. J. Electrochem. 44 (2008) 506–509.
[4] X. Ji, L.F. Nazar, Advances in li–s batteries, J. Mater. Chem. 20 (2010) 9821–9826.
[5] OXIS Engery Ltd, Lithium Sulfur Battery Technology, (accessed February 3, 2016). URL: http://www.oxisenergy.com.
[6] Sion Power Corporation, Sion Power Licerion Li-s Battery Li-Sulfur high-energy density lithium-sulfur rechargeable battery, (accessed April 18, 2016).

URL: http://www.sionpower.com.
[7] M.U. Cuma, T. Koroglu, A comprehensive review on estimation strategies used in hybrid and battery electric vehicles, Renew. Sustain. Energy Rev. 42 (2015) 517–531.
[8] A. Fotouhi, D.J. Auger, K. Propp, S. Longo, M. Wild, A review on electric vehicle battery modelling: from lithium-ion toward lithium–sulphur, Renew. Sustain. Energy Rev. 56 (2016) 1008–1021.
[9] V. Ramadesigan, P.W. Northrop, S. De, S. Santhanagopalan, R.D. Braatz, V.R. Subramanian, Modeling and simulation of lithium-ion batteries from a systems engineering perspective, J. Electrochem. Soc. 159 (2012) R31–R45.
[10] L. Lu, X. Han, J. Li, J. Hua, M. Ouyang, A review on the key issues for lithium-ion battery management in electric vehicles, J. Power Sources 226 (2013) 272–288.
[11] L.W. Yao, J. Aziz, P.Y. Kong, N. Idris, Modeling of lithium-ion battery using matlab/simulink, in: Industrial Electronics Society, IECON 2013-39th Annual Conference of the IEEE, IEEE, 2013, pp. 1729–1734.
[12] M. Chen, G.A. Rincon-Mora, Accurate electrical battery model capable of predicting runtime and iv performance, Energy Convers. IEEE Trans. 21 (2006) 504–511.
[13] O. Erdinc, B. Vural, M. Uzunoglu, A dynamic lithium-ion battery model considering the effects of temperature and capacity fading, in: Clean Electrical Power, 2009 International Conference on, IEEE, 2009, pp. 383–386.
[14] J. Xu, C.C. Mi, B. Cao, J. Deng, Z. Chen, S. Li, The state of charge estimation of lithium-ion batteries based on a proportional-integral observer, Veh. Technol. IEEE Trans. 63 (2014) 1614–1621.
[15] S. Piller, M. Perrin, A. Jossen, Methods for state-of-charge determination and their applications, J. Power Sources 96 (2001) 113–120.
[16] G.L. Plett, Sigma-point kalman filtering for battery management systems of lipb-based hev battery packs, J. Power Sources 161 (2006) 1356–1368.
[17] M. Wild, L. ONeill, T. Zhang, R. Purkayastha, G. Minton, M. Marinescu, O. GJ, Lithium sulfur batteries, a mechanistic review, Energy Environ. Sci. 8 (2015) 3477–3494.
[18] K. Propp, M. Marinescu, D.J. Auger, L. O'Neill, A. Fotouhi, K. Somasundaram, G.J. Offer, G. Minton, S. Longo, M. Wild, et al., Multi-temperature state-dependent equivalent circuit discharge model for lithium-sulfur batteries, J. Power Sources 328 (2016) 289–299.
[19] A. Manthiram, Y. Fu, S.-H. Chung, C. Zu, Y.-S. Su, Rechargeable lithium–sulfur batteries, Chem. Rev. 114 (2014) 11751–11787.
[20] H.S. Ryu, Z. Guo, H.J. Ahn, G.B. Cho, H. Liu, Investigation of discharge reaction mechanism of lithium— liquid electrolyte— sulfur battery, J. Power Sources 189 (2009) 1179–1183.
[21] M.U. Patel, R. Demir-Cakan, M. Morcrette, J.-M. Tarascon, M. Gaberscek, R. Dominko, Li-s battery analyzed by uv/vis in operando mode, ChemSusChem 6 (2013) 1177–1181.
[22] M. Marinescu, T. Zhang, G.J. Offer, A zero dimensional model of lithium–sulfur batteries during charge and discharge, Phys. Chem. Chem. Phys. 18 (2016) 584–593.
[23] H. Yamin, E. Peled, Electrochemistry of a nonaqueous lithium/sulfur cell, J. Power Sources 9 (1983) 281–287.
[24] Y.V. Mikhaylik, I. Kovalev, R. Schock, K. Kumaresan, J. Xu, J. Affinito, High energy rechargeable li-s cells for ev application: status, remaining problems and solutions, Ecs Trans. 25 (2010) 23–34.
[25] Y.V. Mikhaylik, J.R. Akridge, Polysulfide shuttle study in the li/s battery system, J. Electrochem. Soc. 151 (2004) A1969–A1976.
[26] Y. Diao, K. Xie, S. Xiong, X. Hong, Shuttle phenomenon—the irreversible oxidation mechanism of sulfur active material in li—s battery, J. Power Sources 235 (2013) 181–186.
[27] B. Pattipati, C. Sankavaram, K.R. Pattipati, System identification and estimation framework for pivotal automotive battery management system characteristics, Syst. Man Cybern. Part C Appl. Rev. IEEE Trans. 41 (2011) 869–884.
[28] K. Kutluay, Y. Cadirci, Y.S. Özkazanç, I. Cadirci, A new online state-of-charge estimation and monitoring system for sealed lead-acid batteries in telecommunication power supplies, Ind. Electron. IEEE Trans. 52 (2005) 1315–1327.
[29] V. Knap, D.-I. Stroe, M. Swierczynski, R. Teodorescu, E. Schaltz, Investigation of the self-discharge behavior of lithium-sulfur batteries, J. Electrochem. Soc. 163 (2016) A911–A916.
[30] M.R. Busche, P. Adelhelm, H. Sommer, H. Schneider, K. Leitner, J. Janek, Systematical electrochemical study on the parasitic shuttle-effect in lithium-sulfur-cells at different temperatures and different rates, J. Power Sources 259 (2014) 289–299.
[31] P. Singh, C. Fennie, D. Reisner, Fuzzy logic modelling of state-of-charge and available capacity of nickel/metal hydride batteries, J. Power Sources 136 (2004) 322–333.
[32] P. Singh, R. Vinjamuri, X. Wang, D. Reisner, Design and implementation of a fuzzy logic-based state-of-charge meter for li-ion batteries used in portable defibrillators, J. Power Sources 162 (2006) 829–836.
[33] A. Fotouhi, D.J. Auger, K. Propp, S. Longo, Electric vehicle battery parameter identification and soc observability analysis: Nimh and li-s case studies, in: 8th IET International Conference on Power Electronics, Machines and Drives (PEMD), 2016.
[34] A. Jossen, Fundamentals of battery dynamics, J. Power Sources 154 (2006) 530–538.
[35] H. He, R. Xiong, H. Guo, S. Li, Comparison study on the battery models used for the energy management of batteries in electric vehicles, Energy Convers. Manag. 64 (2012) 113–121.
[36] J. Li, J.K. Barillas, C. Guenther, M.A. Danzer, A comparative study of state of charge estimation algorithms for lifepo 4 batteries used in electric vehicles, J. Power Sources 230 (2013) 244–250.
[37] Z. Chen, Y. Fu, C.C. Mi, State of charge estimation of lithium-ion batteries in electric drive vehicles using extended kalman filtering, Veh. Technol. IEEE Trans. 62 (2013) 1020–1030.
[38] D. Yang, G. Qi, X. Li, State-of-charge estimation of lifepo 4/c battery based on extended kalman filter, in: Power and Energy Engineering Conference (APPEEC), 2013 IEEE PES Asia-Pacific, IEEE, 2013, pp. 1–5.
[39] Y. Tian, B. Xia, W. Sun, Z. Xu, W. Zheng, A modified model based state of charge estimation of power lithium-ion batteries using unscented kalman filter, J. Power Sources 270 (2014) 619–626.
[40] F. Sun, X. Hu, Y. Zou, S. Li, Adaptive unscented kalman filtering for state of charge estimation of a lithium-ion battery for electric vehicles, Energy 36 (2011) 3531–3540.
[41] W. He, N. Williard, C. Chen, M. Pecht, State of charge estimation for electric vehicle batteries using unscented kalman filtering, Microelectron. Reliab. 53 (2013) 840–847.
[42] L. Zhong, C. Zhang, Y. He, Z. Chen, A method for the estimation of the battery pack state of charge based on in-pack cells uniformity analysis, Appl. Energy 113 (2014) 558–564.
[43] X. Liu, Z. Chen, C. Zhang, J. Wu, A novel temperature-compensated model for power li-ion batteries with dual-particle-filter state of charge estimation, Appl. Energy 123 (2014) 263–272.
[44] S. Schwunk, N. Armbruster, S. Straub, J. Kehl, M. Vetter, Particle filter for state of charge and state of health estimation for lithium–iron phosphate batteries, J. Power Sources 239 (2013) 705–710.
[45] S. Thrun, W. Burgard, D. Fox, Probabilistic Robotics, MIT Press, 2005.
[46] R. Karlsson, Particle Filtering for Positioning and Tracking Applications, Linköping University Electronic Press, 2005.
[47] G. Welch, G. Bishop, An Introduction to the Kalman Filter, Department of Computer Science, University of North Carolina, 2006.
[48] D. Simon, Kalman filtering, Embed. Syst. Program. 14 (2001) 72–79.
[49] MATLAB Version 8.5.0.197613 (R2015a), The Mathworks, Inc., Natick, Massachusetts, 2015.
[50] G.L. Plett, Extended kalman filtering for battery management systems of lipb-based hev battery packs, J. Power Sources 134 (2004) 252–261.
[51] M. Rhudy, Y. Gu, Understanding nonlinear kalman filters, part ii: an implementation guide, Interact. Robot. Lett. (2013).
[52] M.S. Arulampalam, S. Maskell, N. Gordon, T. Clapp, A tutorial on particle filters for online nonlinear/non-gaussian bayesian tracking, Signal Process. IEEE Trans. 50 (2002) 174–188.
[53] A. Papazoglou, S. Longo, D. Auger, F. Assadian, Computational aspects of estimation algorithms for battery-management systems, in: 8th Conference on Sustainable Development of Energy, Water and Enviroment Systems, 2013.
[54] S. Thrun, W. Burgard, D. Fox, Probabilistic Robotics, Intelligent Robotics and Autonomous Agents, MIT Press, Cambridge and Mass, 2005.
[55] S. Samuel, L. Austin, D. Morrey, Automotive test drive cycles for emission measurement and real-world emission levels-a review, in: Proceedings of the Institution of Mechanical Engineers, Part D: Journal of Automobile Engineering vol. 216, 2002, pp. 555–564.
[56] R. Kötz, S. Müller, M. Bärtschi, B. Schnyder, P. Dietrich, F. Büchi, A. Tsukada, G. Scherer, P. Rodatz, O. Garcia, et al., Supercapacitors for peak-power demand in fuel-cell-driven cars, in: ECS Electro-chemical Society, 52nd Meeting, San Francisco, 2001.

Paper A13

Dual extended Kalman filter for online estimation of model parameters and state of charge in lithium-sulfur batteries

Karsten Propp, Daniel J. Auger, Abbas Fotouhi,
Monica Marinescu, Vaclav Knap and Stefano Longo

The paper has been submitted in 2017.

Dual extended Kalman filter for improved state of charge estimation in lithium-sulfur batteries

Karsten Propp[a], Daniel J. Auger[a,*], Abbas Fotouhi[a], Monica Marinescu[b], Vaclav Knap[c], Stefano Longo[a]

[a] *School of Aerospace, Transport and Manufacturing, Cranfield University, College Road, Bedford, MK43 0AL, UK*
[b] *Department of Mechanical Engineering, Imperial College London, SW7 2AZ, UK*
[c] *Department of Energy Technology, Aalborg University, Aalborg, 9000, Denmark*

Abstract

Lithium-sulfur (Li-S) is a promising next-generation battery chemistry which is beginning to be used in practical applications. The electrochemical behaviours of Li-S are more complex than those of lithium-ion batteries. For lithium-ion batteries, many state-of-charge estimation techniques exist, but for Li-S, only methods have been published, using single Kalman-derived estimators for a nonlinear model describing both 'slow' parameter changes and 'fast' equivalent-circuit-network behaviour. This paper explores an alternative method where the problems of parameter estimation and state estimation are handled separately, using dual extended Kalman filters. The new estimator is demonstrated experimentally with pulse-discharge tests and driving-cycle loads. The underlying equivalent circuit model is then enhanced with a new model of the relationship between current-density and internal resistance terms; estimators based on this are also demonstrated for different load profiles. With appropriate choice of estimator covariance parameters, the proposed dual estimator method gives precise and robust state estimates for a range of current densities and initial conditions. Compared to the previously published estimation technique, accuracy and robustness are improved.

Keywords: Lithium Sulfur Battery, State of Charge estimation, Extended Kalman filter, Online parameterisation, Equivalent circuit model

---

1. Introduction

For applications requiring a lightweight, cheap and safe battery, the Lithium-Sulfur (Li-S) chemistry is a promising candidate to replace the current Lithium-ion (Li-ion) technology. However, the large scale adoption of this chemistry still depends on solving performance limitations, such as relatively short cycle life, low charging efficiency and power capabilities [1, 2]. Another reason for the hesitant introduction for practical applications is their complex conversion reaction of elemental sulfur S_8, via the intermediates Li_2S_8, Li_2S_4, Li_2S_2, to lithium sulfide Li_2S [3] during discharge. Within the high plateau (see Fig. 1 top) soluble high order polysulfides (Li_2S_8, Li_2S_6) are predominant in electrolyte solution [4], which leads to a small internal resistance but also to self discharge due to the shuttle effect [5]. The low plateau is governed by insoluble species (Li_2S_4, Li_2S_3) [6] that are likely to precipitate (Li_2S_2, Li_2S) [7, 8], which cause a constant battery open circuit voltage (OCV) and a dependence of the sulfur utilisation on the applied current profile [9, 10, 11]. The resulting differences between both discharge patterns of classic Li-ion and Li-S batteries makes it difficult to

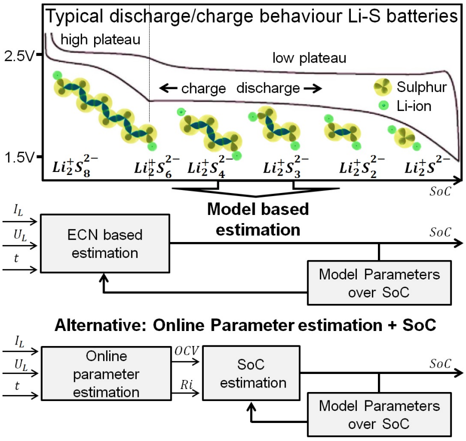

Figure 1: Behaviour and SoC estimation principles of Li-S batteries

---

[*] Corresponding author
Email address: `d.j.auger@cranfield.ac.uk` (Daniel J. Auger)

Preprint submitted to Elsevier *September 13, 2017*

design a battery management system (BMS) because, on the one hand, it still a matter of ongoing research how to operate Li-S cells optimally and, on the other hand, methods for controlling Li-ion batteries cannot be applied directly.

This is also the case for the state of charge (SoC) estimation. Due to the constant OCV, the self discharge and current related utilisation, leading to variations in the usable capacity, simple techniques like Coulomb-counting and the open-circuit-voltage-method [12] are difficult to apply. Therefore it was concluded that advanced methods are required for Li-S batteries [13]. One example for that are model based techniques, that are able to match the behaviour of the battery over the discharge range with equivalent circuit network (ECN) models (Fig. 1 middle). Although these models are usually not able to give insight into the inner cells reactions, they are relatively simple and accurate [14, 15, 16]. In [17, 18] ECN models for Li-S batteries were presented where the latter was used for Kalman filter based SoC estimation in [13]. And indeed, it could be shown that model based methods can estimate the SoC of Li-S batteries accurately. However, also limitations were found of which mostly the capacity variations in the low plateau with different current rates influenced the estimation accuracy negatively. Here the constant OCV, together with an uncertain battery behaviour lead to inaccuracies in the estimation. To address these and also to test the applicability of another estimation pattern, this study investigates an online identification technique to parametrise an ECN model and use the results for the SoC estimation (Fig. 1 bottom). The increased identification speed and the used diverse loads also aim to gain insight into the cell dynamics under more realistic conditions than the commonly used pulse current tests.

A framework for online battery parameter estimation for operational conditions relevant to automotive applications (high current rates, temperature variations and dynamic rate profiles [19]) was proposed by Chiang et al. in [20]. There, an adaptive control method in combination with a Thevenin battery model [21] is used to identify the OCV and internal resistance of lithium-iron-phosphate and lithium polymer cells. The mathematical assumptions made by Chiang (more details in Sec. 2) were incorporated by He et al. to apply an adaptive Kalman filter-based online identification for realistic load profiles in electric vehicles [22, 23]. As an adaptation of this approach we implement a behavioural interpretation of the Thevenin model, presented in [18], to simplify the parametrization of the extended Kalman filter (EKF). Furthermore the unique properties of Li-S batteries are considered for the SoC estimation since, oppositely to classic Li-ion batteries [24], the OCV itself is not sufficient for Li-S SoC estimation [25]. Therefore a dual Kalman filter is proposed, employing the identified values for both, the OCV and the internal resistance. The presented study is to the authors' knowledge the first one to adapt and apply the previously developed online identification technique to Li-S batteries.

The paper is structured in three main parts. The first one, Sec. 2, is focused on the Kalman filter based online parameter identification and its validation. The behavioural version of the Thevenin model is introduced briefly and employed for the identification. The applicability of this method for Li-S batteries is proven for two scenarios.

In the second main part, the online parameter estimation is applied to different current profiles with varying amplitudes, described in Sec. 3, and the found relationship between the current and the internal resistance is discussed in Sec. 4.

As third main part, a reduced order model of the dynamical resistance is then presented in Sec. 5, which is used for SoC estimation in Sec. 6.

2. On-line parameter estimation with EKF

The model framework for the identification is based on the Thevenin model [21], which has been proven to be a good trade off between computational effort and accuracy for intercalation based Li-ion batteries [26, 27]. For their SoC estimation the identified OCV is of interest [20]. Due to the flat OCV of Li-S batteries however, we must also use the internal resistance. Therefore both values must be identified and related to the SoC reliably. Here the behavioural interpretation of the Thevenin model, introduced in [18], helps the user to choose the right parameter boundaries, which can simplify the parameterisation of the EKF. For the sake of completeness, this integration is introduced here briefly.

2.1. Mathematical cell model

The Thevenin model describes the voltage at the battery terminal as

$$U_{\mathrm{L}}\left(t\right) = U_{\mathrm{OC}} - U_{\mathrm{P}}\left(t\right) - R_0\, I_L\left(t\right) \tag{1}$$

where the voltage over the RC circuit is described as

$$\dot{U}_{\mathrm{P}}\left(t\right) = -\frac{1}{R_p\, C_p}\, U_{\mathrm{P}}\left(t\right) + \frac{1}{C_p}\, I_L\left(t\right), \tag{2}$$

which are couched in terms of the components of the electrical equivalent circuit. As shown in [18], recasting the system in terms of the observed behaviours instead can help to separate the circuit parameters into an immediate part and a lagging part after a current pulse. Therefore, we will start by defining the corresponding parameters:

$$R_{\mathrm{int}} = R_0 + R_p,$$
$$\rho = \frac{R_p}{R_0 + R_p} \Leftrightarrow (1-\rho) = \frac{R_0}{R_0 + R_p},$$
$$\Omega = \frac{1}{R_p\, C_p}.$$

R_{int} is the steady-state (or quasi-static) internal resistance, ρ is the fraction of the response that is not instantaneous, thus representing a dynamic lag and Ω is the natural frequency of the response. With this new set of parameters, equation (1) becomes

$$U_{\text{L}} = U_{\text{OC}} - U_{\text{p}} - \underbrace{(1-\rho)R_{\text{int}}}_{\text{formally } R_0} I_{\text{L}} \tag{3}$$

and equation (2) becomes

$$\dot{U}_p = -\Omega\, U_{\text{p}} + \rho\, R_{\text{int}}\, \Omega\, I_{\text{L}}. \tag{4}$$

Where the model parameters are U_{OC} for the OCV, U_{L} for the terminal battery voltage and U_{p} for the voltage drop over the parallel RC circuit. The main advantage of these transformation is to easily constrain the behavioural parameters to 'sensible' ranges since they are sufficiently decoupled from each other: the dynamic portion of the model can be adjusted without altering the steady-state response.

2.2. *Battery model equations for EKF*

The behavioural model is particularly suitable for the online parameterisation because it can simplify the parametrisation of the covariance matrices of the EKF. Since the model contains more variables than observable states, there is no guarantee for the Kalman filter-based identification to converge towards anything with physical meaning [19]. In [22] the difficult parameterisation of the EKF covariances is solved with an adaptive algorithm for estimating the covariance matrix for the system noise Q and measurement noise R. Here, we assume that the statistics of measurement noise, and battery parameters are constant. In the following, we adapt the assumptions made by Chiang et al. [20] for Li-S batteries and the behavioural model. We start with the standard Thevenin model's state transition equation for the terminal battery voltage U_L, the derivative of equation 1:

$$\dot{U}_{\text{L}} = \dot{U}_{\text{OC}} - \dot{U}_{\text{p}} - \dot{I}_L R_0 - I_L \dot{R}_0. \tag{5}$$

Generally, the OCV of the battery is dependent on the SoC, the operating temperature (T) and usage history (h). Therefore, the corresponding definition of U_{OC} can be described as a function of SoC, T, h, whose derivation leads to

$$\dot{U}_{OC} = \frac{\delta U_{OC}}{\delta SoC}\frac{\delta SoC}{\delta t} + \frac{\delta U_{OC}}{\delta T}\frac{\delta T}{\delta t} + \frac{\delta U_{OC}}{\delta h}\frac{\delta h}{\delta t}. \tag{6}$$

For the representation of the battery in a discrete manner, usually time steps of less than one seconds are used. Due to the naturally slow changing parameters of common Li-ion batteries, the equation can be simplified at each time step by the following assumptions, made by [20]. However, since here we use Li-S batteries, we evaluate the applicability of these assumptions for this battery chemistry as well.

- $\frac{\delta SoC}{\delta t} \approx 0$ holds for a small change in battery charge

Li-S cell are operated under much lower C rates, which makes this assumption more justified than in the case of Li-ion.

- $\frac{\delta U_{OC}}{\delta SoC} \approx 0$ in low plateau

Furthermore, there is no change in OCV over the SoC within the low plateau, which approves the assumption.

- $\frac{\delta T}{\delta t} \approx 0$ when temperature changes slowly

The OCV of Li-S batteries depends more strongly on cell the temperature [18] than the OCV of Li-ion. However, the rate of heat generation is assumed to be lower than that of heat dissipation, which is especially valid at low enough current rates and environmental control.

- $\frac{\delta h}{\delta t} \approx 0$ for long term history

Li-S cells are influenced by the short term discharge history [28, 29], commonly referred as 'history' effect. The precise origins and extent for practical applications are still unexplored. However, it is expected that history effects occur at times longer than a time step. Therefore $\dot{U}_{OC}$ is approximated as 0. Despite the relatively quickly changes of the internal resistance over the SoC between the two plateaus [18], we also assume it to be 0 ($\dot{R}_0 \approx 0$) for small periods. The conversion to the behavioural model can be done from the resulting change of the terminal voltage over time:

$$\dot{U}_{\text{L}} = -\dot{U}_{\text{p}} - R_0 \dot{I}_L. \tag{7}$$

The behavioural interpretation is

$$\dot{U}_{\text{L}} = -\dot{U}_{\text{p}} - (1-\rho)R_{\text{int}}\dot{I}_L, \tag{8}$$

for the terminal voltage and

$$\dot{U}_p = -\Omega\, U_{\text{p}} + \rho\, R_{\text{int}}\, \Omega\, I_{\text{L}} \tag{9}$$

for the voltage drop over the RC circuit. By re-write equation 3 to bring U_p on one side, substituting it into Eq. 9 and including the result for $\dot{U}_p$ in Eq. 8, the behavioural state transition equation can be derived as

$$\begin{aligned}\dot{U}_{\text{L}} = \Omega\big(U_{\text{OC}} - U_{\text{L}} - (1-\rho)R_{\text{int}} I_{\text{L}}\big) - \rho\, R_{\text{int}}\, \Omega\, I_{\text{L}} \\ -(1-\rho)R_{\text{int}}\dot{I}_{\text{L}}.\end{aligned} \tag{10}$$

2.3. *Implementation of the Extended Kalman Filter*

The Kalman filter is an efficient algorithm minimizing the error variance between the true and the estimated state. It is often applied for battery state estimation [30, 31] and for online parameter estimation [32]. The EKF is able to predict battery states using a nonlinear system model f. In the following, the algorithm is summarized for a discrete system [33].

Nonlinear state space model
$x_k = f(x_{k-1}, u_{k-1}, w_{k-1}, k-1) \quad y_k = h(x_k, u_k, v_k, k)$

Definitions
$\hat{A}_k = \left.\frac{\partial f(x_k, u_k, w_k, k)}{\partial x_k}\right|_{x_k=\hat{x}_k^+}, \hat{C}_k = \left.\frac{\partial h(x_k, u_k, w_k, k)}{\partial x_k}\right|_{x_k=\hat{x}_k^-},$

Initialisation for k = 0
$\hat{x}_0^+ = \mathbb{E}[x_0], \;\; P_0^+ = \mathbb{E}[(x_0 - \hat{x}_0^+)(x_0 - \hat{x}_0^+)^T]$

Computation EKF for k = 1, 2, ...
State estimate update: $\hat{x}_k^- = f(\hat{x}_{k-1}^+, u_{k-1}, \bar{w}_{k-1}, k-1)$
Error covariance update: $P_k^- = \hat{A}_{k-1} P_{k-1}^+ \hat{A}_{k-1}^T + Q$
Output estimate: $\hat{y}_k = h(\hat{x}_k^-, \; u_k \;, \; v_k, k)$
Kalman Gain matrix: $L_k = P_k^- \hat{C}_k^T \left[\hat{C}_k P_k^- \hat{C}_k^T + R_k\right]^{-1}$
State estimate measurement update: $\hat{x}_k^+ = \hat{x}_k^- + L_k[y_k - \hat{y}_k]$
Error covariance measurement update: $P_k^+ = (I - L_k \hat{C}_k) P_k^-$

The state vector, describing the transition to the next time step for the parameters of the behavioural model is

$$x = \begin{bmatrix} U_{\mathrm{OC}} & U_{\mathrm{L}} & U_{\mathrm{p}} & \Omega & \rho & R_{\mathrm{int}} \end{bmatrix}^T . \tag{11}$$

With the corresponding state transition functions from equations 9 and 10, the input current $I_{\mathrm{L}} = u$ and the previous considerations ($\dot{U}_{OC} \approx 0, \dot{\Omega} \approx 0, \dot{\rho} \approx 0, \dot{R}_{\mathrm{int}} \approx 0$) the state transition functions can be populated in the following form

$$f(x, u) = \begin{bmatrix} f_1 & f_2 & f_3 & f_4 & f_5 & f_6 \end{bmatrix}^T \tag{12}$$

where f_1 to f_6 are defined as:

$$f_1 = 0, \; f_4 = 0, \; f_5 = 0, \; f_6 = 0 \tag{13}$$

$$\begin{aligned} f_2 = x_1 x_4 - x_2 x_4 - x_4(1 - x_5) x_6 u - x_6 \\ - x_5 x_6 x_4 u - (1 - x_5) x_6 \dot{u} \end{aligned} \tag{14}$$

$$f_3 = -x_4 x_3 + x_5 x_6 x_4 u. \tag{15}$$

Since the measured terminal voltage of the battery is represented by the second state, the measurement equation is

$$h = x_2. \tag{16}$$

The Jacobians of the presented functions f_1 to f_6 , linearising the system around the current mean, are:

$$\hat{A} = \begin{bmatrix} 0 & 0 & 0 & 0 & 0 & 0 \\ x_4 & -x_4 & 0 & x_1 - x_2 - x_6 u & x_6 \dot{u} & a_{2,6} \\ 0 & 0 & -x_4 & -x_3 + x_5 x_6 u & x_6 x_4 u & x_5 x_4 u \\ 0 & 0 & 0 & 0 & 0 & 0 \\ 0 & 0 & 0 & 0 & 0 & 0 \\ 0 & 0 & 0 & 0 & 0 & 0 \end{bmatrix}$$

$$a_{2,6} = -x_4 u - \dot{u} + x_5 \dot{u}. \tag{17}$$

$\hat{C}$ can be obtained as

$$\hat{C} = \begin{bmatrix} 0 & 1 & 0 & 0 & 0 & 0 \end{bmatrix}. \tag{18}$$

While the presented model has a similar complexity to the parameter based method, the tuning of the covariance noise matrices $w \sim (0, Q)$ and $v_k \sim (0, R_k)$ is supposed to be easier. Their parameterisation is explained in section Sec. 2.4.

2.4. Validation

The validation of the proposed method is done by performing two experiments. Firstly, the Li-S battery model presented in [18] generates the voltage input for the EKF parameter estimation and the accuracy of the estimated parameters is evaluated by comparison to the known values from the model (Fig. 2 right). Secondly, the pulse test measurements and identification data from the offline parameterisation (Fig. 2 left) are compared to the online method. In the following the model parameters are shown in the 'conventional' ECN format since as it is customary to map them back with

$$R_{\mathrm{p}} = \rho_{\mathrm{p}} R_{\mathrm{int}}, \quad R_{\mathrm{o}} = R_{\mathrm{int}} - R_{\mathrm{p}}, \quad C_{\mathrm{p}} = \frac{1}{R_{\mathrm{p}} \, \Omega_{\mathrm{p}}}. \tag{19}$$

The online parameterisation uses the measurements error, i.e. the difference between the measured and predicted battery terminal voltage, to correct six parameters or states. While the model determines the separation into the parameters (OCV, R_0, R_{p} C_{p}), the convergence to the right values also depend on the right choices for the system and measurement uncertainties. The values of R and Q determine the relative trust of model prediction and measurement, as these both can generally be ridden with errors. The higher the values in R, the more trusted is the model prediction, such that the predicted states are corrected less, even if a large error between measurement and prediction exists. Large R values thus also mean smaller fluctuations in the system states. Matrix Q determines the trust in each of the states. Here large values, representing more uncertainty, leading to more correction. This rather simple thought mostly determines the parameterisation in this study. The values for Q should be as small as possible, to eliminate fluctuations, but as large enough to follow the unpredicted changes. One example for such is the change of the OCV within the high plateau. Since the model assumes it as constant, only the correction of the Kalman Gain can follow the changes. Therefore the parametrisation of Q is not only assumed based on the relative trusts, but also on the expected violations of the model assumptions. The presented values for Q and P_0

$$Q = \begin{bmatrix} 0.02 & 0 & 0 & 0 & 0 & 0 \\ 0 & 0.01 & 0 & 0 & 0 & 0 \\ 0 & 0 & 0.01 & 0 & 0 & 0 \\ 0 & 0 & 0 & 0.0002 & 0 & 0 \\ 0 & 0 & 0 & 0 & 0.3 & 0 \\ 0 & 0 & 0 & 0 & 0 & 0.005 \end{bmatrix} \times 10^{-4} \tag{20}$$

$$P_0 = \begin{bmatrix} 0.02 & 0 & 0 & 0 & 0 & 0 \\ 0 & 1 & 0 & 0 & 0 & 0 \\ 0 & 0 & 1 & 0 & 0 & 0 \\ 0 & 0 & 0 & 0.00001 & 0 & 0 \\ 0 & 0 & 0 & 0 & 1 & 0 \\ 0 & 0 & 0 & 0 & 0 & 1 \end{bmatrix} \tag{21}$$

were derived iteratively in combination with mentioned thoughts. The initial values for the state vector are chosen to be close but not identical to the known values of a fully charged Li-S battery, to account for a level of uncertainty between different batteries.

$$x_0 = \begin{bmatrix} 2.43\text{ V} & 2.43\text{ V} & 0\text{ V} & 0.025 & 0.1 & 0.172\,\Omega \end{bmatrix}^T \tag{22}$$

2.4.1. *Battery model results*

For the simulation of the terminal voltage with the known data from the battery model, the realistic but simple NEDC current profile [34, 35] is used (Fig. 2 left). As also shown, the identification is able to quickly adjust to the right values, even if the initial conditions for R_0, R_p and C_p are incorrect. Especially the OCV and R_0 can be estimated precisely and without fluctuations, which makes this algorithm suitable for identifying the battery SoC, as illustrated in Sec. 6.

2.4.2. *Offline parameterisation results*

The offline identification data of the cell parameters over SoC was gathered measuring the response of 3.4 Ah OXIS Energy long life chemistry cells to a mixed current pulse profile (300 mA, 1450 mA and 2900 mA) [18]. In order to identify current-related changes, the identification was done at for each pulse individually with a window of 300 s before and after. The method used is the prediction error minimization (PEM) algorithm, which is described in full detail by Ljung [36].

The parametrisation results, presented in Fig. 2 right, illustrate that, despite a significant reduction in running time, the online estimation with the EKF provides a comparable identification quality than the offline method. Especially for the OCV and R_0 the zoomed-in area demonstrate that the parameter variations can be followed precisely. Therefore, the presented parameter estimation method appears valid for the whole discharge range of Li-S batteries.

3. Experimental design

The online parameterisation is applied in two realistic scenarios. Hereby current profiles according to the New European Drive Cycle (NEDC) [34] and the Urban Dynamo-meter Driving Schedule (UDDS) [37] were used in a controlled environment at 20 °C (Thermal Chamber: Memmert ICP260). Two cells were individually tested to reduce the impact of manufacturing variations. The tested cells are pre-cycled (C/10 charge, C/5 discharge, 30 °C) 3.4 Ah Li-S long life chemistry cells, developed by OXIS Energy.

Furthermore the two different current profiles (NEDC and UDDS) are used with three different gains in order to test the batteries reaction as well as the SoC estimation performance to different power demands (Fig. 3). Since both cells follow the same pattern, we only use and present the results of cell 1 in Sec. 4 Sec. 5 and most of Sec. 6. However, to present as many results as possible we also included tests from cell 2 in Sec. 6.4. The details of the six tests and the measured usable capacities of both cells are summarised in Table 1.

Table 1: Discharge experiments

Cycle	Cap. Cell 1	Cap. Cell 2	Av. Current
NEDC 1.2	2.93 Ah	2.98 Ah	0.15 A
NEDC 1.8	2.69 Ah	2.68 Ah	0.22 A
NEDC 2.2	2.52 Ah	2.63 Ah	0.30 A
UDDS 1.2	3.11 Ah	3.13 Ah	0.13 A
UDDS 1.8	2.88 Ah	3.07 Ah	0.19 A
UDDS 2.2	2.58 Ah	2.53 Ah	0.26 A

For all the tests the capacities and reference SoCs are calculated by Coulomb counting for each test separately. This is done by integrating the measured current, following the cell's recommended voltage range between 2.45 V (SoC = 100%) and 1.5 V (SoC = 0%)

$$SoC = SoC_{(0)} - \frac{1}{3600Q_\text{cap}} \int_0^t i(\tau)d\tau. \tag{23}$$

Generally it is difficult to predict the capacity of the cell with Coulomb counting. However, it can be calculated retrospectively for a given voltage window and used as reference SoC in theory. This means that factors like self discharge and precipitation related to capacity changes are included within the reference SoC, which makes it a precise practical value for each scenario respectively.

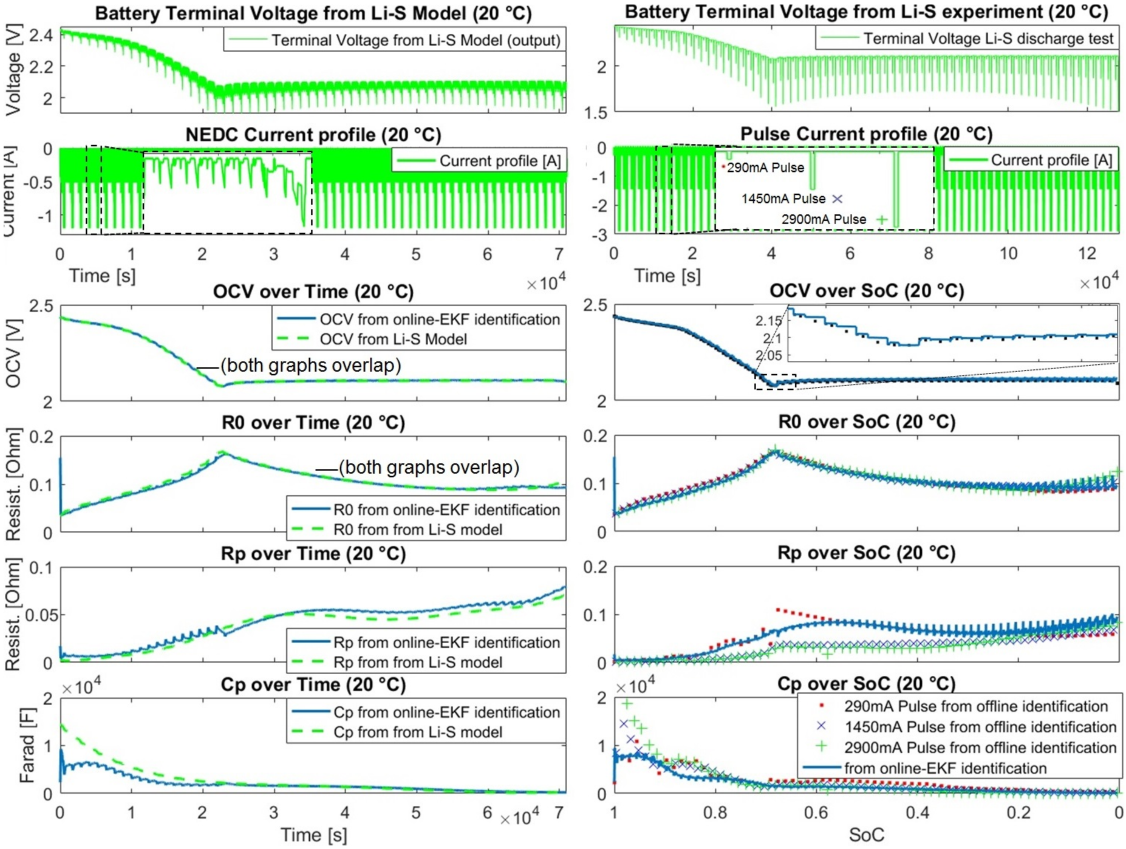

Figure 2: Online parameter identification results

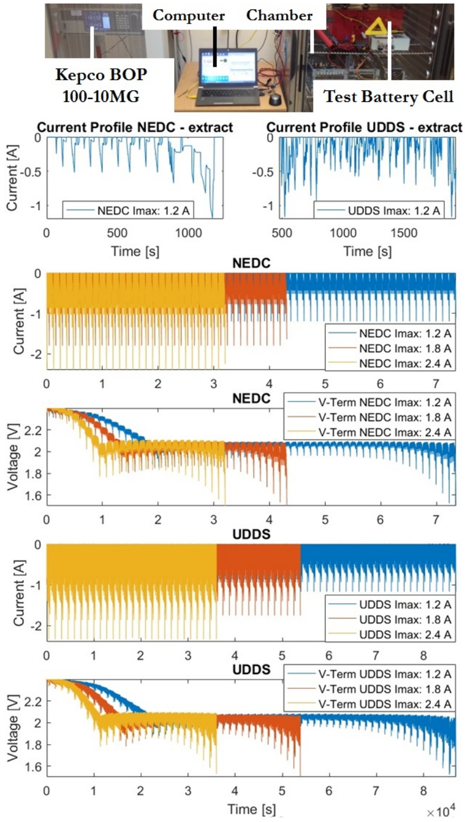

Figure 3: Experimental set-up and applied discharge currents

4. Current - R_0 relationship

The results of the parameter estimation over time for all current profiles are shown in Fig. 4. Generally, the values of the online identification correspond well to the offline obtained values presented in Fig. 2. However, the internal resistance of the cell, R_0, has a different pattern. Towards the end of discharge R_0 rises more quickly than predicted by the pulse discharge tests [18] and shows a relationship with the applied current density. The zoomed in areas in Fig. 4 show the normalised discharge current together with the identified R_0. While a large current increases the internal resistance, lower currents or relaxation periods lead to a decrease in resistance. This is particularly visible in the NEDC cycle test. The more uniform currents in the UDDS cycle, containing less relaxation periods, unveil a more persistent growth of R_0. Furthermore, it is visible that while the internal resistance rises more quickly with higher currents, larger values are reached with smaller rates towards the end of discharge. Here, the high currents cause the battery voltage to drop to the cut of voltage of 1.5 V before the resistance values can grow further.

The current dependencies in the observed R_0 suggest that it contains, next to the resistance of the electrolyte and current collectors [16], a diffusion part, which has been also reported and modelled in [38, 39] to fit the impedance spectroscopy data. Since we use a different current profile and identification method, also intended to be useful for the SoC estimation, we suggest as a simple solution to separate R_0 in into a charge transfer R_{ct} and a diffusion R_{diff} part. While R_{ct} rises generally with lower SoC due to lower availability of cathode active surface area and of reaction species, the dynamic behaviour, R_{diff}, can be explained by the build-up of concentration gradients of species within the cell. High current pulses therefore build up stronger gradients, increasing R_{diff} as well as R_{ct}, due to stronger gradients in the electrolyte and fewer species available at the cathode surface to undergo the reaction.

The building up of internal gradients could also explain why this effect has not been found before. Common techniques, using identification windows [25] with artificial current pulses [17, 18], leave long resting periods in between the pulses. The current pulses, applied after open circuit condition, are therefore not enough to build up the concentration gradients contrary to the way in which a Li-S cell would be used in most applications. Here the continuously running EKF estimation method in combination with realistic current profiles is more suitable to represent real world usage.

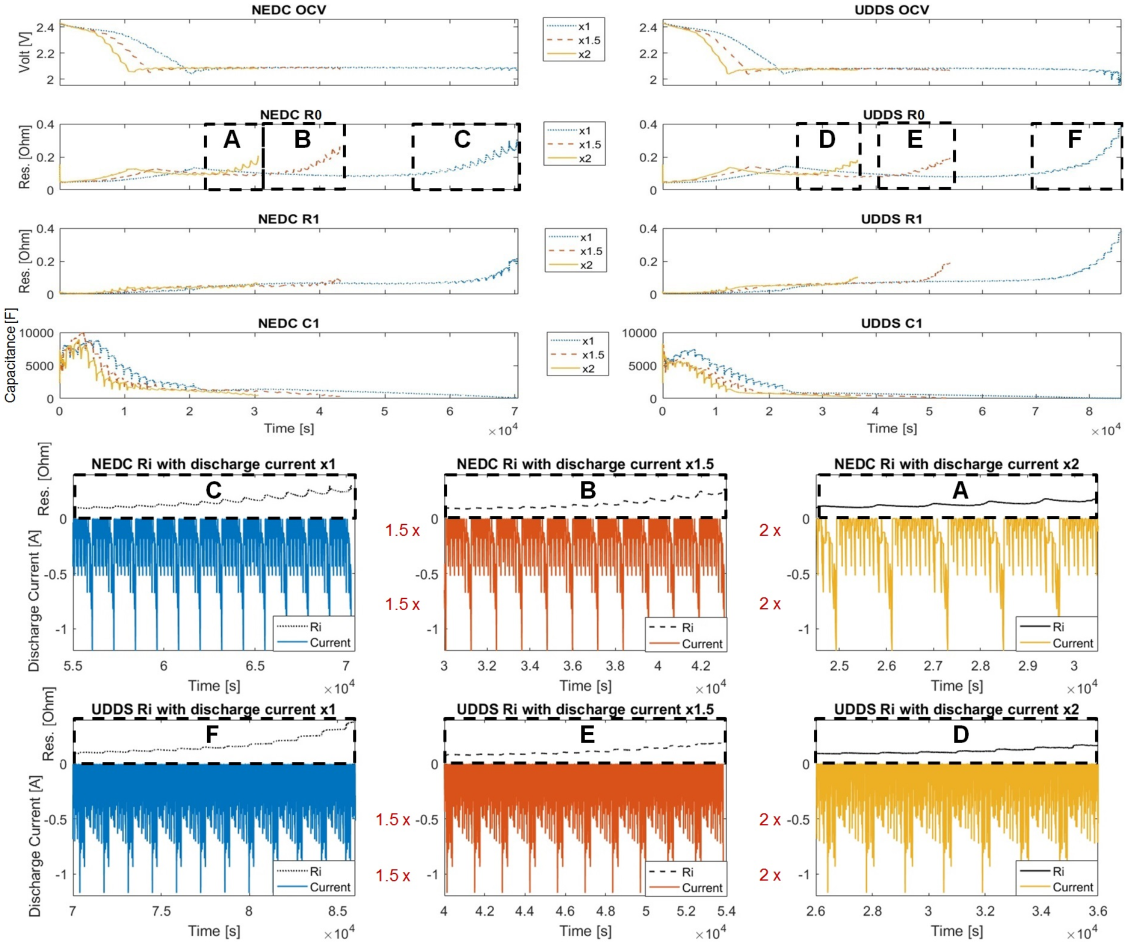

Figure 4: EKF online parametrisation results for different current profiles

5. Modelling of the dynamic internal resistance

The existing methods for parameter based SoC estimation for classic Li-ion batteries use the relationship between (online identified) OCV and SoC. As mentioned before, this would not be sufficient for Li-S batteries due to their constant OCV within the low plateau. Therefore the internal resistance is used as additional information. The results of the EKF method have shown that the interval resistance varies with the discharge current rate. To reduce the fluctuations for the SoC estimation, this relationship should be accounted for by the equivalent circuit model in a preferably simple way. Therefore we divide internal resistance in two parts: one part is associated with the charge transfer resistance, depends only on the SoC and thus denoted R_{ct}. The other part is associated with the build-up of diffusion gradients across the cell, denoted R_{diff}, and has dependencies of SoC and current. The dynamic component is calculated via a first order differential equation allowing the rise of R_{diff} when current is applied and a gradual decrease when the battery is left to rest.

This approach allows us to implement the current dynamics through a simple additional state within the existing battery model [18]. The internal resistance is therefore represented by

$$\underbrace{R_0}_{\text{similar to EKF ident.}} = \underbrace{R_{\text{ct}}}_{\text{from existing model}} + \underbrace{R_{\text{diff.}}}_{\text{introduced dynamics}} \tag{24}$$

Where R_{diff} is represented by

$$\dot{R}_{\text{diff}} = \frac{1}{R_{\text{dyn1}} R_{\text{dyn2}}} R_{\text{diff}} + \frac{1}{R_{\text{dyn2}}} I_{\text{L}}. \tag{25}$$

R_{dyn1} and R_{dyn2} are varying parameters over SoC, with no physical meaning. They are chosen to represent the dynamic changes of the internal resistance over time in a similar manner to the identified values. For their parametrisation we subtract the static R_0 from the model in [18] for 20 °C from the R_0 identified by the EKF.

$$R_{\text{diff}} = R_0 - R_{\text{ct}} \tag{26}$$

The result (Fig. 5 A) shows the differences between the model parametrised by pulse data and the EKF method. The origins of them can either be due to cell variations, but also are likely to have methodical reasons. However, since the main purpose of the identification is to capture the increase in R_{diff} towards the end of discharge, the parametrisation of the dimensionless factors R_{dyn1} and R_{dyn2} is only done for the positive values. The methodology is similar to the parameter identification is Sec. 2, but simplified. Again we chose a behavioural interpretation of Eq. 25 and change the parameters to a steady state value and a time constant

$$\dot{R}_{\text{diff}} = -\Omega_{\text{R}} R_{\text{diff}} + \Omega_{\text{R}} R_{\text{dyn1}} I_{\text{L}}, \tag{27}$$

where Ω_{R} is

$$\Omega_{\text{R}} = \frac{1}{R_{\text{dyn1}} R_{\text{dyn2}}}. \tag{28}$$

The state vector becomes,

$$x = \begin{bmatrix} R_{\text{diff}} & \Omega_{\text{R}} & R_{\text{dyn1}} \end{bmatrix}^T \tag{29}$$

and the state transition functions

$$f(x,u) = \begin{bmatrix} f_1 & f_2 & f_3 \end{bmatrix}^T. \tag{30}$$

Where f_1 to f_3 are

$$f_1 = -x_2 x_1 + x_2 x_3 u, \quad f_2 = 0, \quad f_3 = 0, \tag{31}$$

similar to the R_{p} and C_{p} values defined in section Sec. 2. The measurement equation is

$$h = x_1. \tag{32}$$

The Jacobians are:

$$\hat{A} = \begin{bmatrix} -x_2 & -x_1 + x_3 u & x_2 u \\ 0 & 0 & 0 \\ 0 & 0 & 0 \end{bmatrix} \tag{33}$$

$$\hat{C} = \begin{bmatrix} 1 & 0 & 0 \end{bmatrix}. \tag{34}$$

The identified values of the parameters of the dynamic part of the internal resistance are also shown in Fig. 5 A for the NEDC drive cycle with different gains. To simplify the presented model, all curves are combined to one function (Matlab fitting tool [40]) for R_{dyn1} and R_{dyn2} respectively to

$$f_{R_{\text{dyn1}}}(SoC) = 0.9148\, e^{(-10.79 SoC)} \tag{35}$$

and

$$f_{R_{\text{dyn2}}}(SoC) = 3071\, e^{(5.036 SoC)}. \tag{36}$$

The results of the improved model are presented in Fig. 5 B, together with the EKF identification results. The dynamic part R_{diff} and the static part R_0 are plotted separately to show each part of the resistance working with different current inputs. Generally the model fits well to the EKF identification. However, for the lowest applied current density the model cannot represent the increasing internal resistance. This is presumably due to the made simplifications and to some factors playing a role at relatively long response times, such as precipitation [41]. For the SoC estimation we accept this error in order to maintain the model's simplicity.

6. State of charge estimation

Since the first EKF is only used to get the battery model parameters, a second one is used to relate them to the SoC. The battery model presented in [18] uses two

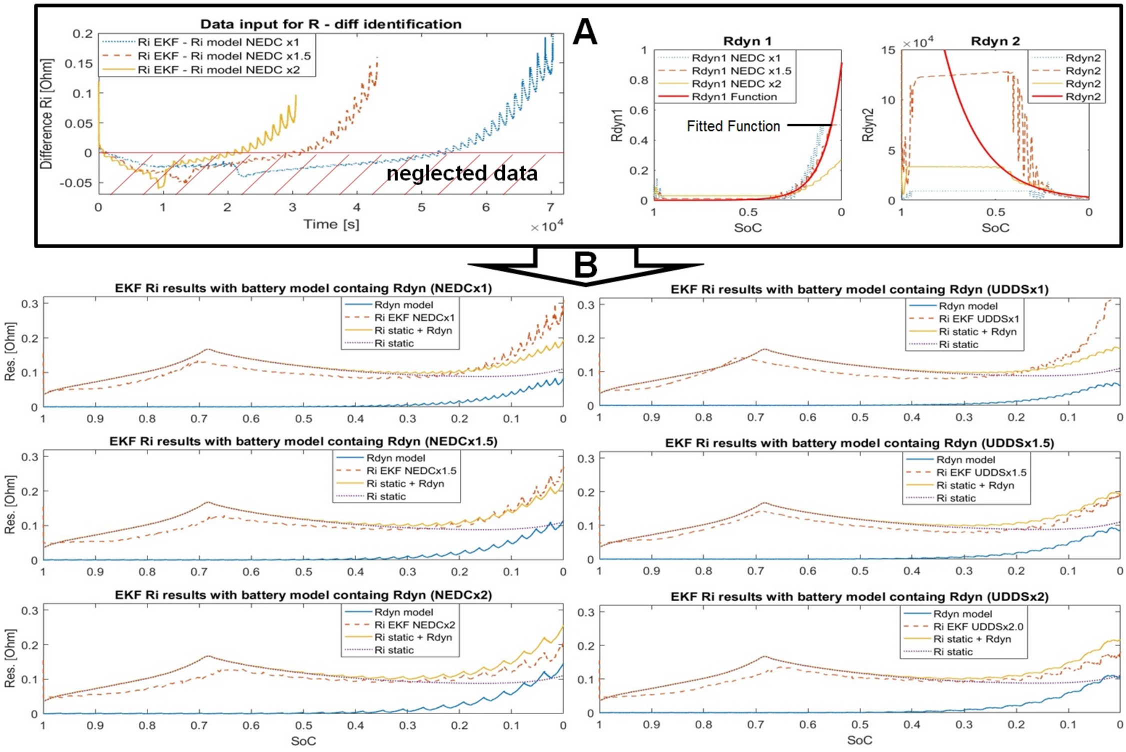

Figure 5: Modelling of R_{diff}: Parametrizing R_{dyn1} and R_{dyn2} (A), Comparison of identification results and dynamic resistance model R_0 + R_{diff} (B)

polynomial functions for the static resistance R_{ct} and OCV respectively to represent the battery behaviour over the discharge range. For the sake of completeness they are presented as follows

$$\begin{aligned} f_{\mathrm{OCV}}(SoC) = (1-\gamma_{\mathrm{m,c}}(SoC))\ & f_{\mathrm{OCV-low}}(SoC) \\ +\gamma_{\mathrm{m,c}}(SoC)\ & f_{\mathrm{OCV-high}}(SoC) \end{aligned} \tag{37}$$

and R_{ct}

$$\begin{aligned} f_{\mathrm{Rct}}(SoC) = (1-\gamma_{\mathrm{m,c}}(SoC))\ & f_{\mathrm{Rct-low}}(SoC) \\ +\gamma_{\mathrm{m,c}}(SoC)\ & f_{\mathrm{Rct-high}}(SoC). \end{aligned} \tag{38}$$

The two polynomial functions are combined smoothly via a partial sinusoidal differentiable function γ:

$$\gamma_{\mathrm{m,c}}(SoC) := \begin{cases} 0, & \text{if a} \\ \frac{1}{2}+\frac{1}{2}\sin(2m(SoC-c)) & \text{if b} \\ 1 & \text{if c,} \end{cases} \tag{39}$$

where the conditions a, b, c stand for the different ranges,

$$\begin{aligned} \text{a}:\ 2m(SoC-c) &< -\frac{1}{2}\pi, \\ \text{b}:\ -\frac{1}{2}\pi \leq 2m(SoC-c) &< \frac{1}{2}\pi, \\ \text{c}:\ 2m(SoC-c) &> \frac{1}{2}\pi. \end{aligned} \tag{40}$$

Here m is a scaling factor for the maximal gradient of the sinusoidal function, determining the transition region between the polynomials and c represents the point where both functions are equally represented. Once the internal resistance and OCV are known over the discharge range, the dynamic internal resistance can be calculated as follows. R_{diff} is included as a state for the SoC estimating EKF, which leads to the following state space model

$$\begin{aligned} \dot{x}(t) &= A(t)x(t) + B(t)u(t) \\ y(t) &= C(t)x(t) + D(t)u(t). \end{aligned} \tag{41}$$

The dynamic states $x = [x_1\ x_2]^T$ of the system are the dynamic internal resistance R_{diff}, as presented in previous section, and the SoC, calculated through Coulomb counting. The corresponding state space representation gives

$$A = \begin{bmatrix} \frac{-1}{f_{R_{\mathrm{dyn1}}}(x_2)\ f_{R_{\mathrm{dyn2}}}(x_2)} & 0 \\ 0 & 0 \end{bmatrix} \quad B = \begin{bmatrix} \frac{1}{f_{R_{\mathrm{dyn2}}}(x_2)} \\ \frac{-1}{3600Q_{\mathrm{cap}}} \end{bmatrix} \\ C = \begin{bmatrix} 1 & f_{R_{\mathrm{ct}}}(x_2) \\ 0 & f_{OCV}(x_2) \end{bmatrix} \tag{42}$$

with the current I_{L} as an input.

6.1. State of charge estimation with dual EKF

For the application of the EKF algorithm with the presented Li-S battery model, the Jacobians of the matrices A and C are needed. With the relating functions over SoC, denoted as x_2, we therefore need the derivatives of $f_{OCV}(x_2)$, $f_{R_{\mathrm{ct}}}(x_2)$, $f_{R_{dyn1}}(x_2)$ and $f_{R_{dyn2}}(x_2)$. Using one exponential function for each R_{dyn1} and R_{dyn2} the Jacobian matrix of A is obtained as follows:

$$\hat{A}(1,1) = \frac{-1}{f_{R_{\mathrm{dyn2}}}(x_2)\ f_{R_{\mathrm{dyn1}}}(x_2)} \quad \hat{A}(2,1) = 0 \quad \hat{A}(2,2) = 0 \tag{43}$$

$$\begin{aligned} \hat{A}(1,2) = \Bigg[& \frac{\dot{f}_{R_{\mathrm{dyn2}}}(x_2)}{f_{R_{\mathrm{dyn2}}}(x_2)^2\ f_{R_{\mathrm{dyn1}}}(x_2)} \\ & + \frac{\dot{f}_{R_{\mathrm{dyn1}}}(x_2)}{f_{R_{\mathrm{dyn2}}}(x_2)\ f_{R_{\mathrm{dyn1}}}(x_2)^2} \Bigg] x_1 \\ & - \left[\frac{\dot{f}_{R_{\mathrm{dyn2}}}(x_2)}{f_{R_{\mathrm{dyn2}}}(x_2)^2} \right] I_{Bat}, \end{aligned} \tag{44}$$

where the derivatives of $f_{R_{\mathrm{dyn1}}}(x_2)$ and $f_{R_{\mathrm{dyn2}}}(x_2)$ are defined as

$$\dot{f}_{R_{\mathrm{dyn1}}}(x_2) = -9.875008\ e^{(-10.79x_2)} \tag{45}$$

$$\dot{f}_{R_{\mathrm{dyn2}}}(x_2) = 15465.556\ e^{(5.036x_2)}. \tag{46}$$

Following the same principle for C it's Jacobian matrix is obtained as

$$\begin{aligned} \hat{C}(1,1) = 1 \quad & \hat{C}(1,2) = \dot{f}_{R_{ct}}(x_2) \\ \hat{C}(2,1) = 0 \quad & \hat{C}(2,2) = \dot{f}_{OCV}(x_2). \end{aligned} \tag{47}$$

The derivatives of the combined functions $\dot{f}_{\mathrm{OCV}}$ and $\dot{f}_{\mathrm{R_{ct}}}$ with respect to x_2 are influenced by the introduced factor γ, here substituted by $f_\gamma(x_2)$.

$$\begin{aligned} f_{\mathrm{OCV}}(x_2) = (1 - f_\gamma(x_2)) & f_{\mathrm{OCV-low}}(x_2) \\ +\ f_\gamma(x_2) & f_{\mathrm{OCV-high}}(x_2) \end{aligned} \tag{48}$$

Derivation with respect to x_2 leads to

$$\begin{aligned} \dot{f}_{\mathrm{OCV}}(x_2) = \dot{f}_{\mathrm{OCV-low}}(x_2) - (\dot{f}_\gamma(x_2) & f_{\mathrm{OCV-low}}(x_2) \\ +f_\gamma(x_2) & \dot{f}_{\mathrm{OCV-low}}(x_2)) \\ +\dot{f}_\gamma(x_2) & f_{\mathrm{OCV-high}}(x_2) \\ +f_\gamma(x_2) & \dot{f}_{\mathrm{OCV-high}}(x_2). \end{aligned} \tag{49}$$

Where $\dot{f}_\gamma$ is defined by

$$\dot{\gamma}_{m,c}(x_2) := \begin{cases} 0, & \text{if a} \\ m\cos(2m(x_2-c)), & \text{if b} \\ 0, & \text{if c} \end{cases} \tag{50}$$

with same conditions for a, b, c as in Eq. 40. The derivation of the static internal resistance R_{ct}, given by the Eq. 38, follows the same pattern and is not presented. Instead, the derivation of the covariance matrices R and Q is examined thoroughly. In the process of finding the covariances, values capable of improving the convergence with wrong initial conditions within the high plateau and values enhancing the correct estimation towards the low plateau were found. As one advantage, the dual filter offers the opportunity to distinguish between the high and low plateau, simply by evaluating the identified OCV. Therefore R and Q are varied between the plateaus, using an 'if' function included in the second EKF. If the identified OCV is larger than 2.15 V, Q and R are emphasised on the OCV identification and if the identified OCV is lower than 2.15 V Q and R rely on the results for Coulomb counting and the internal resistance. The resulting the parameterisation of the covariance matrices for the two main discharge regions of Li-S batteries are

$$R_{\text{high}} = \begin{bmatrix} 0.15 & 0 \\ 0 & 0.00054 \end{bmatrix}, Q_{\text{high}} = \begin{bmatrix} 0.1 & 0 \\ 0 & 0.01 \end{bmatrix} \tag{51}$$

for the high plateau and

$$R_{\text{low}} = \begin{bmatrix} 0.00015 & 0 \\ 0 & 0.549 \end{bmatrix}, Q_{\text{low}} = \begin{bmatrix} 0.1 & 0 \\ 0 & 0.0000001 \end{bmatrix} \tag{52}$$

within the low plateau. In both cases the initial condition for the probabilities P is

$$P_0 = \begin{bmatrix} 10 & 0 \\ 0 & 10 \end{bmatrix}. \tag{53}$$

6.2. SoC estimation with an initially fully charged battery

The results of the proposed SoC estimation algorithms are evaluated qualitatively for their convergence time, with imprecise initial values for the SoC state, and quantitatively by their estimation accuracy. As a measure for the accuracy, the root mean squared error (RMSE) over the whole discharge range is used

$$\text{RMSE} = \frac{1}{\sqrt{n}} \left(\sum_{i=1}^{n} (SoC_{t,i} - \hat{SoC}_{t,i})^2 \right)^{0.5}. \tag{54}$$

Where n is the number of data points, $SoC_{t,i}$ is the reference SoC from the measurement and $\hat{SoC}_{t,i}$ is the estimated SoC by the proposed technique.

Since the model does not include a current rate dependency for the discharge capacity of Li-S cells, the SoC estimator (Fig. 6) uses the identified capacity of 9778 As (2.72 Ah) for all applied currents. This value has been obtained from a pulse current test at 20 °C in [18] and used for SoC estimation in [13], and therefore allows the comparability to other SoC estimation methods. The initial conditions for the parameter identification are the same as in Eq. 22.

The results of the drive cycle tests show measured capacities from 2.52 Ah (for NEDC) to 3.11 Ah (for UDDS), which is a variation of 21% compared to the rated capacity of the cell model. The large difference between measured cell capacity in practical applications indicate again that Coulomb counting on its own is not sufficient for SoC estimation.

Table 2: RSME SoC Estimation with UDDS and NEDC current profile with different gains

Current	SoC_0	UDDS RSME	NEDC RSME
×1	1	0.0346	0.0257
	0.7	0.0346	0.0257
	0.6	0.0455	0.0350
×1.5	1	0.0118	0.0274
	0.7	0.0118	0.0274
	0.6	0.0360	0.0336
×2	1	0.0523	0.0581
	0.7	0.0523	0.0581
	0.6	0.0556	0.0680

However, the estimation results of the dual EKF estimator are promising. As shown in Fig. 6, the over all estimation results vary within 6.8% for all the test cases as illustrated in Table 2. In addition to the accuracy, the convergence time with the wrong initial SoC ($SoC_0 = 1, 0, 7, 0, 6$) could also be improved compared to the estimation results presented in [13]. Here the assignment of different covariance values to the plateaus improved the convergence significantly, which is possible due to the simple distinction of the two voltage plateaus of Li-S cells. The best results are archived for the two middle current densities due to the close match between model and measured capacity. However, the variations of the errors are small for all currents which is a sign for the robustness of the estimation.

Surprisingly the largest estimation error is not reached in lower current density cases where the model is most inaccurate and the usable capacity is about 14% more than the rated one, it is the case of higher rates. Here the SoC estimation slowly drifts to 9.5% percent error towards the end of discharge (NEDC x2). This is presumably caused by the emphasis on the Coulomb counting within the low plateau and could be improved by better use of the behaviour of the internal resistance. However, with an average error of about 6.8% in the worst case of all six SoC estimation evaluation tests, the approach is considered as sufficiently robust (see Table 2).

6.3. SoC estimation with an initially partly discharged battery

Promising results could also reached by testing the filters ability to handle imprecise initial conditions with a partly discharged battery. Here we started the simulation at the SoC of 0.6, which is roughly 10% lower than the transition point in between both voltage plateaus. This scenario is more realistic since the Li-S battery is likely to self discharge when the SoC estimation system is switched off. For the simulation the initial conditions of

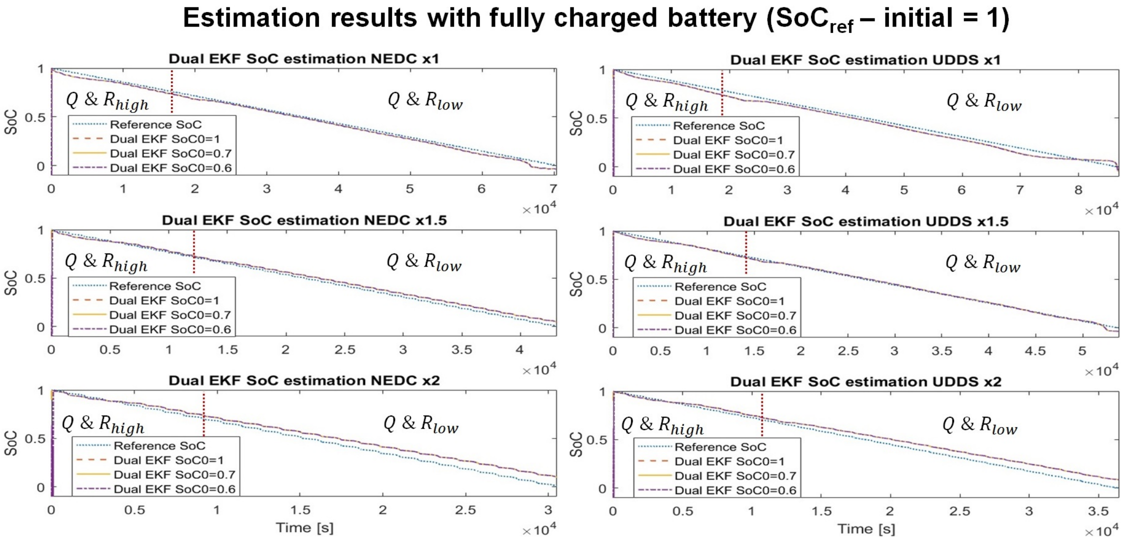

Figure 6: Results of the SoC estimation with different current profiles and rates

the online parametrisation EKF stays the same than before (Eq. 22), but is highly imprecise now, and the initial SoC of the second EKF is set to 1. The first output of the test is that the online parametrisation is robust against imprecise initial conditions. The OCV and internal resistance converge in all six cases to steady values within 50 s to 100 s simulation time, which is particular useful for the SoC estimation since it relies on precise parameters. And indeed, the results presented in Fig. 7 and Table 3 show that the SoC also converges within the same period. However, the convergence towards the reference SoC stops at the transition point of the voltage plateaus.

After the identified OCV falls under 2.15 V the estimation changes it's pattern to place emphasis on Coulomb counting. This means that the correction of the state is slowly and can only be seen for the lower currents (UDDS ×1, NEDC×1). Since the starting point of the simulation was chosen about 10% SoC beneath the transition point, also the estimation errors for this case are in that region. The slow convergence of the SoC estimation within the low plateau is one disadvantage of the presented method and can likely be improved by a better understanding and modelling of the internal resistance towards the end of discharge. Though the properties of Li-S cells help here to keep the estimation error reasonable. The self discharge is expected be present only in the high plateau [42], which founds the assumption that a self discharged Li-S battery is likely to be near the transition point between both plateaus for a long time. Therefore the presented limitation is expected to be small in most of applications.

Table 3: RSME SoC Estimation with UDDS and NEDC current profile with different gains for initially partly discharged battery

Current	SoC_0	UDDS RSME	NEDC RSME
×1	1	0.1061	0.1030
×1.5	1	0.1100	0.1214
×2	1	0.1422	0.1538

6.4. *SoC estimation with multiple cycles*

Although we focused our studies exclusively on the discharge process, we also present one of our experiments with three subsequent NEDC cycles with a constant charge of 0.32 A in between. Here we get good results with small additions to the presented SoC estimation, despite the lack of a charging model or a deep understanding of the charging process.

The additions to the estimator are a linear decay of the internal resistance, a coulombic efficiency of 0.9 and heavily emphasised Coulomb counting during charging

$$\begin{aligned} R_{\text{charge}} &= \begin{bmatrix} 0.00015 & 0 \\ 0 & 55 \end{bmatrix}, \\ Q_{\text{charge}} &= \begin{bmatrix} 0.1 & 0 \\ 0 & 0.0000000001 \end{bmatrix}. \end{aligned} \tag{55}$$

The slow descent of the R_{int} is mostly assumed because the constant charge current does not allow the parameter estimation to adjust automatically. In tests in Fig. 8 revealed a variation in the discharge capacity, variances in

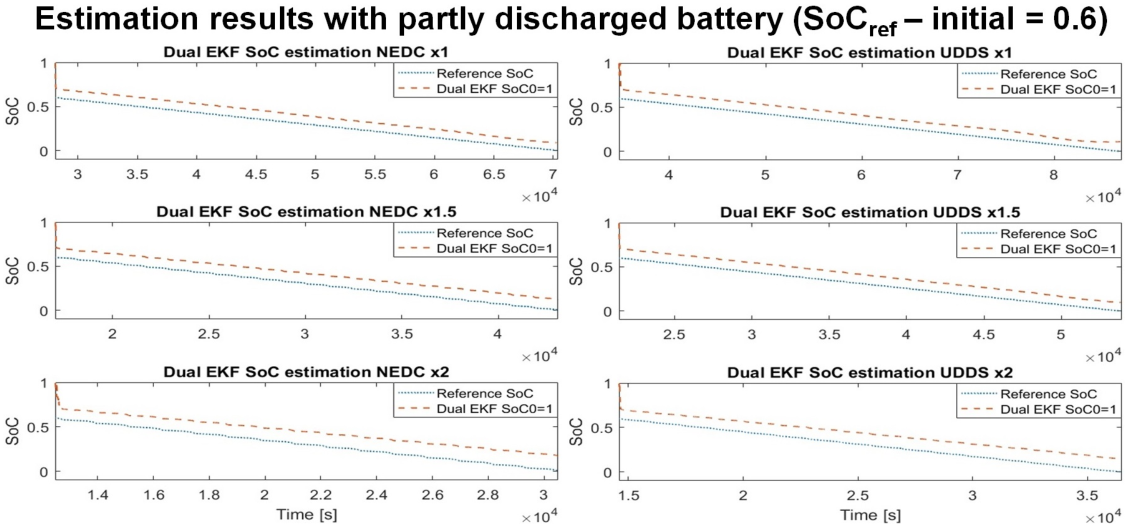

Figure 7: Results of the SoC estimation with different current profiles and rate densities with partly discharged battery

the charging efficiency and an unknown (not modelled) charge curve. Here it is visible how useful the uncertainty is for the state estimation. During charge the SoC estimator can roughly estimate the SoC through Coulomb counting, while the uncertainties adjust for inaccuracies of the model or differences in the battery behaviour. Especially in the high plateau the correction works well and the drift from the crude charging assumptions is corrected within seconds after the discharge starts again. Here is one most significant improvements of the dual EKF method against a single EKF version, presented in [13] (Fig. 8 extracts). After the second charge the single EKF method roughly has the same error than the dual EKF, but needs considerable more time to converge back to the reference SoC in the subsequent discharge. The overall accuracy of the dual EKF for the entire test period is 0.0450 RSME and can be seen as accurate enough for most applications. However, it has to be invested more effort to understand the charging process to ensure the results are robust for more diverse user cases. Furthermore the robustness has to be proven with drive cycles that assume a recuperation of kinetic energy during the drive cycle.

7. Conclusion

This study introduces and discusses three major aspects of the SoC estimation for Li-S batteries. Firstly, it is shown that an online parameter estimation with an extended Kalman filter can identify the parameters of an behavioural interpretation of a Thevenin equivalent circuit reliably. While this method is considerable faster than offline methods, it can identify the model parameters continuously and therefore is able to be used with practical current profiles, as long as they contain some dynamic changes.

In the second main part the proposed online identification method is used with two different drive cycle current profiles, each applied with three varying gains for the power demand. In all of our experiments, a relationship was found between the discharge current rate and the identified internal resistance. Since this behaviour fits the current understanding of the inner cell reactions in the literature, a dynamic internal resistance term is defined and represented in a reduced order model to improve the prediction of the terminal battery voltage with diverse currents.

In the third part, a dual extended Kalman filter is designed for robust SoC estimation. Using the identified values of the OCV and internal resistance, the estimation accuracy can be improved by adjusting the algorithm to the specific properties of Li-S batteries. While in the low plateau, the OCV itself is a poor SoC indicator, it is reliable and precise within the high plateau. Therefore the estimation in the high plateau trusts the identified OCV from the online parameter identification, while in the low plateau the Coulomb counting and internal resistance are the dominant factors.

The accuracy of the estimation results demonstrates the effectiveness of employing multiple sources of information for SoC estimation for Li-S batteries. With the emphasis on the OCV, the convergence from imprecise initial conditions can be improved. However, it also leads to a Coulomb counting emphasised estimation within the low plateau. Here the fact that the majority of the self

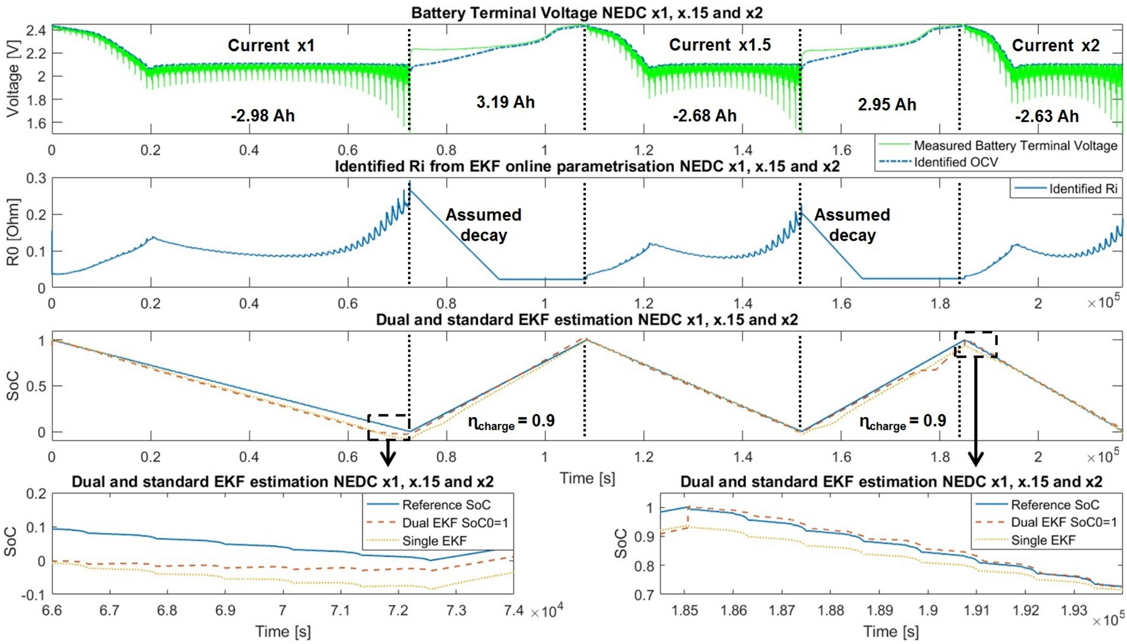

Figure 8: Results of the SoC estimation with three NEDC current profiles with constant charge

discharge happens only in the high plateau of Li-S cells helps. To improve the estimation accuracy in the low plateau, a mechanism should be designed to count for the battery capacity changes with different rates and current profiles, which will be done in our future studies.

Another direction is to employ high fidelity electrochemical cell models for the SoC estimation. Having these, we aim not only to improve the current weaknesses of Li-S battery control models (capacity prediction) but also to enhance the understanding of the discharge reaction path.

8. Acknowledgement

This research was undertaken as part of the project 'Revolutionary Electric Vehicle Battery' (REVB), co-funded by Innovate UK under grant TS/L000903/1; university funding is provided by EPSRC under grant number EP / L505286/1 . Enquiries for access to the data referred to in this article should be directed to researchdata@cranfield.ac.uk. (The data used in this article is described at `10.17862/cranfield.rd.c.3723934`; it is subject to an embargo, and will be available from May 2022.)

References

[1] V. Kolosnitsyn, E. Karaseva, Lithium-sulfur batteries: Problems and solutions, Russian Journal of Electrochemistry 44 (2008) 506–509.

[2] Y. Diao, K. Xie, S. Xiong, X. Hong, Shuttle phenomenon–the irreversible oxidation mechanism of sulfur active material in Li–S battery, Journal of Power Sources 235 (2013) 181–186.

[3] X. Ji, L. F. Nazar, Advances in Li–S batteries, Journal of Materials Chemistry 20 (2010) 9821–9826.

[4] H. Yamin, E. Peled, Electrochemistry of a nonaqueous lithium/sulfur cell, Journal of Power Sources 9 (1983) 281–287.

[5] Y. V. Mikhaylik, J. R. Akridge, Polysulfide shuttle study in the Li/S battery system, Journal of the Electrochemical Society 151 (2004) A1969–A1976.

[6] M. U. Patel, R. Demir-Cakan, M. Morcrette, J.-M. Tarascon, M. Gaberscek, R. Dominko, Li-s battery analyzed by UV/Vis in Operando mode, ChemSusChem 6 (2013) 1177–1181.

[7] Y. V. Mikhaylik, I. Kovalev, R. Schock, K. Kumaresan, J. Xu, J. Affinito, High energy rechargeable Li-S cells for EV application: status, remaining problems and solutions, Ecs Transactions 25 (2010) 23–34.

[8] M. Marinescu, T. Zhang, G. J. Offer, A zero dimensional model of lithium–sulfur batteries during charge and discharge, Physical Chemistry Chemical Physics 18 (2016) 584–593.

[9] H. S. Ryu, Z. Guo, H. J. Ahn, G. B. Cho, H. Liu, Investigation of discharge reaction mechanism of lithium | liquid electrolyte | sulfur battery, Journal of Power Sources 189 (2009) 1179–1183.

[10] M. R. Busche, P. Adelhelm, H. Sommer, H. Schneider, K. Leitner, J. Janek, Systematical electrochemical study on the parasitic shuttle-effect in lithium-sulfur-cells at different temperatures and different rates, Journal of Power Sources 259 (2014) 289–299.

[11] V. Kolosnitsyn, E. Kuzmina, E. Karaseva, On the reasons for low sulphur utilization in the lithium–sulphur batteries, Journal of Power Sources 274 (2015) 203–210.

[12] S. Piller, M. Perrin, A. Jossen, Methods for state-of-charge determination and their applications, Journal of power sources 96 (2001) 113–120.

[13] K. Propp, D. J. Auger, A. Fotouhi, S. Longo, V. Knap, Kalman-variant estimators for state of charge in lithium-sulfur batteries, Journal of Power Sources 343 (2017) 254–267.

[14] A. Fotouhi, D. J. Auger, K. Propp, S. Longo, M. Wild, A review on electric vehicle battery modelling: From lithium-ion toward lithium–sulphur, Renewable and Sustainable Energy Reviews 56

(2016) 1008–1021.
[15] X. Hu, S. Li, H. Peng, A comparative study of equivalent circuit models for Li-ion batteries, Journal of Power Sources 198 (2012) 359–367.
[16] A. Jossen, Fundamentals of battery dynamics, Journal of Power Sources 154 (2006) 530–538.
[17] V. Knap, D.-I. Stroe, R. Teodorescu, M. Swierczynski, T. Stanciu, Electrical circuit models for performance modeling of lithium-sulfur batteries, in: Energy Conversion Congress and Exposition (ECCE), 2015 IEEE, IEEE, 2015, pp. 1375–1381.
[18] K. Propp, M. Marinescu, D. J. Auger, L. O'Neill, A. Fotouhi, K. Somasundaram, G. J. Offer, G. Minton, S. Longo, M. Wild, V. Knap, Multi-temperature state-dependent equivalent circuit discharge model for lithium-sulfur batteries, Journal of Power Sources 328 (2016) 289–299.
[19] G. L. Plett, Extended Kalman filtering for battery management systems of LiPB-based HEV battery packs: Part 1. background, Journal of Power sources 134 (2004) 252–261.
[20] Y.-H. Chiang, W.-Y. Sean, J.-C. Ke, Online estimation of internal resistance and open-circuit voltage of lithium-ion batteries in electric vehicles, Journal of Power Sources 196 (2011) 3921–3932.
[21] L. Thévenin, Extension de la loi d'Ohm aux circuits électromoteurs complexes [extension of Ohm's law to complex electromotive circuits], in: Annales Télégraphiques, volume 10, 1883, pp. 222–224.
[22] H. He, R. Xiong, H. Guo, Online estimation of model parameters and state-of-charge of LiFePO 4 batteries in electric vehicles, Applied Energy 89 (2012) 413–420.
[23] R. Xiong, H. He, F. Sun, K. Zhao, Evaluation on state of charge estimation of batteries with adaptive extended Kalman filter by experiment approach, IEEE Transactions on Vehicular Technology 62 (2013) 108–117.
[24] J. Xu, C. C. Mi, B. Cao, J. Deng, Z. Chen, S. Li, The state of charge estimation of lithium-ion batteries based on a proportional-integral observer, Vehicular Technology, IEEE Transactions on 63 (2014) 1614–1621.
[25] A. Fotouhi, D. J. Auger, K. Propp, S. Longo, Electric vehicle battery parameter identification and soc observability analysis: NiMH and Li-S case studies, in: Proc. 8th IET Int. Conf. on Power Electronics, Machines and Drives, 2016, pp. 1–6.
[26] H. He, R. Xiong, H. Guo, S. Li, Comparison study on the battery models used for the energy management of batteries in electric vehicles, Energy Conversion and Management 64 (2012) 113–121.
[27] A. Fotouhi, D. J. Auger, K. Propp, S. Longo, Accuracy versus simplicity in online battery model identification, IEEE Transactions on Systems, Man, and Cybernetics: Systems (2016).
[28] A. Rosenman, R. Elazari, G. Salitra, E. Markevich, D. Aurbach, A. Garsuch, The effect of interactions and reduction products of lino3, the anti-shuttle agent, in Li-S battery systems, Journal of The Electrochemical Society 162 (2015) A470–A473.
[29] A. Ferrese, J. Newman, Modeling lithium movement over multiple cycles in a lithium-metal battery, Journal of The Electrochemical Society 161 (2014) A948–A954.
[30] D. Simon, Kalman filtering, Embedded systems programming 14 (2001) 72–79.
[31] G. Welch, G. Bishop, An introduction to the Kalman filter. department of computer science, university of north carolina, 2006.
[32] G. L. Plett, Extended Kalman filtering for battery management systems of LiPB-based HEV battery packs, Journal of Power Sources 134 (2004) 252–261.
[33] G. L. Plett, Sigma-point Kalman filtering for battery management systems of LiPB-based HEV battery packs, Journal of Power Sources 161 (2006) 1356–1368.
[34] S. Samuel, L. Austin, D. Morrey, Automotive test drive cycles for emission measurement and real-world emission levels – a review, Proceedings of the Institution of Mechanical Engineers, Part D: Journal of Automobile Engineering 216 (2002) 555–564.
[35] R. Kötz, S. Müller, M. Bärtschi, B. Schnyder, P. Dietrich, F. Büchi, A. Tsukada, G. Scherer, P. Rodatz, O. Garcia, et al., Supercapacitors for peak-power demand in fuel-cell-driven cars, in: ECS Electro-Chemical Society, 52nd Meeting,, San Francisco, 2001, pp. 564–575.
[36] L. Ljung, System identification: Theory for the user, PTR Prentice Hall Information and System Sciences Series 198 (1987).
[37] M. Fellah, G. Singh, A. Rousseau, S. Pagerit, E. Nam, G. Hoffman, Impact of real-world drive cycles on PHEV battery requirements, Technical Report, SAE Technical Paper, 2009.
[38] V. Kolosnitsyn, E. Kuzmina, E. Karaseva, S. Mochalov, A study of the electrochemical processes in lithium–sulphur cells by impedance spectroscopy, Journal of Power Sources 196 (2011) 1478–1482.
[39] Z. Deng, Z. Zhang, Y. Lai, J. Liu, J. Li, Y. Liu, Electrochemical impedance spectroscopy study of a lithium/sulfur battery modeling and analysis of capacity fading, Journal of The Electrochemical Society 160 (2013) A553–A558.
[40] MathWorks, MATLAB version 8.5.0.197613 (R2015a), 2015.
[41] T. Zhang, M. Marinescu, L. O'Neill, M. Wild, G. Offer, Modeling the voltage loss mechanisms in lithium–sulfur cells: the importance of electrolyte resistance and precipitation kinetics, Physical Chemistry Chemical Physics 17 (2015) 22581–22586.
[42] V. Knap, D.-I. Stroe, M. Swierczynski, R. Teodorescu, E. Schaltz, Investigation of the self-discharge behavior of lithium-sulfur batteries, Journal of The Electrochemical Society 163 (2016) A911–A916.

Paper A14

Concurrent Real-Time Estimation of State of Health and Maximum Available Power in Lithium-Sulfur Batteries

Vaclav Knap, Daniel J. Auger, Karsten Propp and Abbas Fotouhi

The paper has been submitted in 2017.

Concurrent Real-Time Estimation of State of Health and Maximum Available Power in Lithium-Sulfur Batteries

Vaclav Knap[a,*], Daniel J. Auger[b,], Karsten Propp[b], Abbas Fotouhi[b]

[a] *Department of Energy Technology, Aalborg University, Aalborg, 9000, Denmark*
[b] *School of Aerospace, Transport and Manufacturing, Cranfield University, College Road, Cranfield, Beds., MK43 0AL, United Kingdom*

Abstract

Lithium-Sulfur (Li-S) batteries are a prospective alternative to today's widely used lithium-ion batteries, especially for their promise of higher capacity and lower weight. However, there are many knowledge gaps which need to be filled before they can be widely used practically. One such gap, targeted in this paper, is combined state-of-charge, state-of-health and maximum available power estimation for Li-S batteries. These devices exhibit a complex behaviour due to their chemistry mechanisms, which requires the tailoring of modelling and estimation specifically for them. Therefore, the approach of dual Kalman filters have been used in this work. The first extended Kalman filter identifies online the parameters of the Li-S equivalent electrical circuit model. The parameters are consequently used for the second extended Kalman filter to estimate the state-of-charge and state-of-health. The estimator has been applied to the measurement of fresh and aged Li-S pouch cells and it has been shown that it can successfully track all states. However, the estimation of the capacity fade is shown to be more complex, because the practical available capacity varies highly with applied current rates and mission profile dynamics. Moreover, the maximum available power is estimated through behaviour model based approach from the online identified parameters.

Keywords: extended Kalman filter, lithium-sulfur battery, maximum available power, state of charge, state of health

---

1. Introduction

An ongoing effort to develop lighter batteries with a higher capacity have resulted into Lithium-Sulfur (Li-S) batteries. They are an alternative to the nowadays broadly used Lithium-ion (Li-ion) battery cells and they have six times higher theoretical specific energy and two times higher theoretical energy density than the Li-ion batteries [1]. Furthermore, they are expected to be cheaper [1] and safer [2]. However, there are still obstacles for their wide and successful commercialization. The first type of the obstacles is related to the actual cell performance and lifetime, which are hindered by e.g. the fast capacity fade during cycling [3] and the high self-discharge at the high state-of-charge (SOC) levels [4]. While the chemical challenges are addressed at cell development or material level [5], the practical ones have to be addressed by system design in order to operate the Li-S cells in the safe and optimal way due to their complex chemistry [6].

The battery management system (BMS) is an inseparable part of the practical use of batteries, which takes care about safe and efficient operating of the battery [7]. Typically, BMS includes state estimation functions, which provide information about state-of-charge (SOC) and state-of-health (SOH), which are crucial as for the proper battery functioning, as for the user. Many different methods for the state estimations were investigated. Frequently mentioned methods for SOC estimation are: ampere-hour counting, open-circuit voltage (OCV) based, model based, impedance based, static battery characteristics based, fuzzy logic and machine learning based estimations. The SOH estimation is usually based on various capacity and/or impedance estimation techniques and also correlations of those quantities to some observable effects [7]. These estimation techniques are usually tailored to specific battery chemistries, as they might have unique attributes and behavior. It is possible to find many works which have been done on widely used Lead-acid [8, 9, 10], Nickel-metal Hydride (NiMH) [11, 12, 13] and Lithium-ion [10, 14, 15] batteries. However, these methods applied to the other battery chemistries are not directly suitable for the Li-S batteries. For example: Coulomb counting method is not suitable due to high self-discharge [4] and variable shape and length of voltage charging curve due to polysulfide shuttle and 'history' effect [16]. Moreover, the Li-S batteries have an unique shape of open-circuit voltage [17], which is flat approximately for the interval from 0 to 70% SOC. This reduces their observability and it prevents a separate use of any open-circuit voltage based technique.

To the present day in the field of Li-S batteries, there has been proposed and demonstrated only a limited amount of functional approaches for SOC estimation. The SOC estimation based on Kalman variant estimators (extended, unscented and particle filter) was presented in [18], where the filter was applied to the battery model developed in [19] in a classical manner that the SOC was estimated according to combination of Coulomb counting and voltage response of the battery. An another approach in state estimation, discussed in [17], is based

---

[*] Corresponding author
E-mail address: vkn@et.aau.dk

on an observability of the SOC from the battery parameters, such as open-circuit voltage and internal resistance, which can provide advantages as these identified parameters might be easier to track and express during the laboratory degradation tests. The first step, following this approach, is to implement an online battery parameter identification. Three identification algorithms: gradient descent, genetic algorithm and prediction error minimization were investigated and compared in [20], where also the SOC estimation of a NiMH battery based on an adaptive neuro-fuzzy inference system was demonstrated, which can be in a similar way applied to the Li-S battery. Furthermore, the parameter identification can be also based on the extended Kalman filter, which was presented for Li-S batteries in [21], and it was directly used in a dual Kalman filter manner for the SOC estimation of Li-S batteries. Accordingly, we can summarize that there exists already some base ground for the SOC estimation at Li-S batteries. However, the area of SOH estimation at Li-S batteries has not been covered at all.

Therefore, in this paper we introduce the SOC and SOH estimation, utilizing the parameter identification introduced in [21]. The presented SOH estimation allows to estimate capacity fade and resistance change caused by the battery ageing without an the use of any degradation model, which is especially beneficial at the current stage of lesser knowledge and practical experience of the Li-S batteries.

The structure of the paper is as follows: The methodology is described in Section II, where the battery states for state of charge and health estimation are defined. Moreover, the Li-S battery model, its offline parametrization, standard implementation of Extended Kalman filter, its used for online parameter identification, metric for estimation evaluation and the structure of the model and test procedure are introduced. The specific implementation of SOC and SOH estimation, together with its results is presented in Section III. The maximum available power estimation is described and shown in Section IV. The paper is concluded in Section V.

2. Methodology

2.1. State definitions

States of the battery receive a great amount of an interest. However, they are not always perceived in the same and unique way. The more consensus is about the state-of-charge definition, which is usually understood as an amount of charge, which is available to be extracted from the actual battery capacity [7, 22]. Sometimes, the nominal capacity term is used instead of the actual capacity [23]. However, that might mislead to an assumption of neglecting the capacity change during the battery life. Moreover, the amount of the extractable charge in the battery varies with the temperature or the applied current. The capacity dependence of the current is typically described by the Peukert's law [24]. The extending the Peukert equation by a temperature dependency was described in [25].

As an indicator for the state-of-health of the battery is the most commonly used a change in the actual capacity, a capacity fade [9, 12]. Some methods estimates the capacity fade according to its relationship to the change of impedance, which is usually growing during the battery ageing [26]. Furthermore, the impedance was accommodated as an another indicator for the SOH [14, 22] and it is also related to the maximum available power of the battery, as the impedance growth highly contributes to the power fade. However, other factors might also be considered for the SOH estimation [23], as for example the porosity of the electrodes [27] or the terminal voltage [28].

To summarize, it is important to clearly state, which definition is followed in the work. Definitions in this work are based on [7, 22], where the initial capacity $\bar{Q}_{\text{cap}}$ is the maximum extractable charge from the fully charged battery at the beginning of life under the specific conditions (i.e. temperature, C-rate, cut-off limits). The actual capacity Q_{cap} represents the maximum extractable charge from the fully charged battery at the actual battery age under the specific conditions. The definitions for the initial internal resistance $\bar{R}_0$ and the actual internal resistance R_0 corresponds to the similar definitions as the capacity definitions, but to the internal resistance instead of the capacity.

State-of-charge: SOC represents a present amount of charge Q_{present}, which is possible to extract from the battery, related to the actual capacity. It is noted as χ and expressed as:

$$SOC = \chi = \frac{Q_{\text{present}}}{Q_{\text{cap}}} \tag{1}$$

State-of-health: SOH consists from two quantities representing capacity fade η_{Q} and internal resistance change η_{R}. The SOH can be written as:

$$SOH = [\eta_{\text{Q}}\ \eta_{\text{R}}]^T \tag{2}$$

The capacity fade (η_{Q}) is computed as the actual capacity divided by the nominal capacity at the beginning of life:

$$\eta_{\text{Q}} = \frac{Q_{\text{cap}}}{\bar{Q}_{\text{cap}}} \tag{3}$$

The internal resistance change (η_{R}) is computed as the internal resistance at the beginning of life divided by the actual internal resistance:

$$\eta_{\text{R}} = \frac{\bar{R}_0}{R_0} \tag{4}$$

2.2. Li-S battery model and its parametrization

For the estimation of defined states it is needed to relate the behaviour of the Li-S cells to them. For the relationship of parameters over the SOC, a behavioural version of the Thevenin electrical circuit network, illustrated in Fig. 1 a), was applied. The details of the derivation of this model are presented in our previous work [19]. In this paper, we introduce the model briefly as the algebra of the following sections rely on it. Tests were based on discharging OXIS Energy 3.4 Ah long life Li-S cells in different temperatures with varying current rates shown in Fig. 1 b). The original idea of the application of different current pulses was to capture the open-circuit voltage (V_{OC}), the internal resistance (R_0) and the transient behaviour of the cell over its discharge range; moreover, to explore the effects of the current rate.

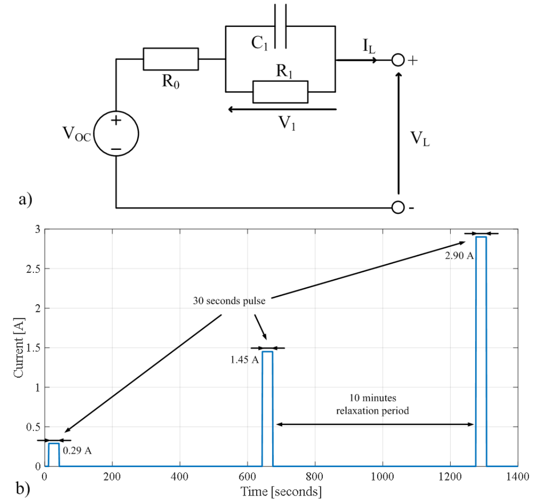

Figure 1: a) Equivalent circuit model used for modelling the Li-S battery. b)Mixed pulse discharge test - the detail on three current pulses.

However, if it was found that the rate dependencies of the model parameters are small and that they could be neglected without decreasing the model accuracy significantly. Since the models intentional usage is also the state estimation, polynomial functions in the form of

$$f_{parameter}(\chi) = p_{10}x_1^9 + p_9x_1^8 + p_8x_1^7 + p_7x_1^6 + p_6x_1^5 \\ +p_5x_1^4 + p_4x_1^3 + p_3x_1^2 + p_2x_1 + p_1 \tag{5}$$

were fitted describing the parameters over the SOC. While fitted polynomial functions are generally a standard method, it is difficult to reproduce the harsh transitions between the high- and low-plateau of the Li-S cells with them. Therefore two polynomial functions were combined for the V_{OC} and R_0 and joined together at the transition point. The model implements combined functions for the V_{OC}

$$f_{\mathrm{V_{OC}}}(\chi) = (1 - \gamma_{\mathrm{m,c}}(\chi))\ f_{\mathrm{V_{OC}-low}}(\chi) \\ +\gamma_{\mathrm{m,c}}(\chi)\ f_{\mathrm{V_{OC}-high}}(\chi) \tag{6}$$

and R_0

$$f_{R0}(\chi) = (1 - \gamma_{\mathrm{m,c}}(\chi))\ f_{\mathrm{R0-low}}(\chi) \\ +\gamma_{\mathrm{m,c}}(\chi)\ f_{\mathrm{R0-high}}(\chi). \tag{7}$$

Since the linearisation of the applied Kalman filter methods need differentiable functions, γ combines both polynomials smoothly

$$\gamma_{\mathrm{m,c}}(\chi) := \begin{cases} 0, & \text{if a} \\ \frac{1}{2} + \frac{1}{2}\sin\left(2m(\chi - c)\right), & \text{if b} \\ 1, & \text{if c} \end{cases} \tag{8}$$

Where the conditions a, b and c stands for the different ranges of the function,

$$\begin{aligned} \mathrm{a}:\ & 2m(\chi - c) < -\frac{1}{2}\pi, \\ \mathrm{b}:\ -\frac{1}{2}\pi \leq\ & 2m(\chi - c) < \frac{1}{2}\pi, \\ \mathrm{c}:\ & 2m(\chi - c) > \frac{1}{2}\pi, \end{aligned} \tag{9}$$

where m is a scaling factor for the maximal gradient of the sinusoidal function, determining the transition range between both polynomials and c represents the point where both functions are equally represented. The resulting state space model has the form

$$\begin{aligned} \dot{x}(t) &= A(t)x(t) + B(t)u(t) \\ y(t) &= C(t)x(t) + D(t)u(t). \end{aligned} \tag{10}$$

relies on the nonlinear functions of V_{OC}, R_0, C_1, R_1 over the SOC. The dynamic states $x = [x_1\ x_2]^T$ of the system are the voltage over the RC circuit V_1 and the SOC χ, calculated through Coulomb counting. The corresponding state space representation gives

$$\begin{aligned} A &= \begin{bmatrix} \frac{-1}{f_{R_1}(\chi)\, f_{C_1}(\chi)} & 0 \\ 0 & 0 \end{bmatrix} \quad B = \begin{bmatrix} \frac{1}{f_{C_1}(\chi)} \\ \frac{-1}{3600 Q_{\mathrm{cap}}} \end{bmatrix} \\ C &= \begin{bmatrix} -1 & f_{\mathrm{V_{OC}}}(\chi) \end{bmatrix} \quad D = \begin{bmatrix} f_{R_0}(\chi) \end{bmatrix}. \end{aligned} \tag{11}$$

2.3. Online parameter identification

In contrast to the standard state estimation, where a model identified offline is used to predict the system's output and the error between the prediction and measurements is used to correct the states of interest, an online parameter identification method can be used to identify the parameters directly. However, that means the identification has to be fast enough to run on common BMS hardware and that the identification results have to be reliable with different current profiles. While the main concept of online identification was proposed in [29] and [30, 31] for common Li-ion batteries, Propp et al. adapted the identification for Li-S batteries. Since the principles of this work are used here as well, they are also introduced here briefly. The online parametrization fits the parameters with the derivative of the terminal battery voltage V_L of the Thevenin model

$$\dot{V}_{\mathrm{L}} = \dot{V}_{\mathrm{OC}} - \dot{V}_{\mathrm{p}} - \dot{I}_L R_0 - I_L \dot{R}_0. \tag{12}$$

Generally, the OCV of the battery is dependent on the SoC, the operating temperature (T) and usage history (h). Therefore, the corresponding definition of V_{OC} can be described as a function of SoC, T, h, whose derivation leads to

$$\dot{V}_{OC} = \frac{\delta V_{OC}}{\delta SoC}\frac{\delta SoC}{\delta t} + \frac{\delta V_{OC}}{\delta T}\frac{\delta T}{\delta t} + \frac{\delta V_{OC}}{\delta h}\frac{\delta h}{\delta t}. \tag{13}$$

For the representation of the battery in a discrete manner, usually time steps of less than one seconds are used. Slow changing parameters therefore can be eliminated from the equation for simplification. So the SOC $\left(\frac{\delta SoC}{\delta t} \approx 0\right)$, the change of the OCV over time $\left(\frac{\delta V_{OC}}{\delta SoC} \approx 0\right)$, the temperature changes $\left(\frac{\delta T}{\delta t} \approx 0\right)$ and the long term history $\left(\frac{\delta h}{\delta t} \approx 0\right)$ can be approximated as 0. It is furthermore assumed that the internal resistance variation are negligible ($\dot{R}_0 \approx 0$) for small periods. The resulting simplified relationship for the terminal voltage over time

$$\dot{V}_\mathrm{L} = -\dot{V}_\mathrm{p} - R_0 \dot{I}_L \tag{14}$$

was then changed to a behavioural interpretation to improve the identification process. For the terminal voltage

$$\dot{V}_\mathrm{L} = -\dot{V}_\mathrm{p} - (1-\rho) R_{int} \dot{I}_L, \tag{15}$$

and for the voltage drop over the RC circuit

$$\dot{V}_p = -\Omega\, V_\mathrm{p} + \rho\, R_{int}\, \Omega\, I_\mathrm{L}. \tag{16}$$

By re-write the behavioural interpretation of the equation for the terminal battery voltage

$$V_\mathrm{L} = V_\mathrm{OC} - V_\mathrm{p} - \underbrace{(1-\rho)R_{int}}_{\text{formally } R_0} I_\mathrm{L} \tag{17}$$

to bring V_p on one side, substituting it into Eq. 16 and including the result for $\dot{V}_p$ in Eq. 15, the behavioural state transition equation can be derived as

$$\begin{aligned}\dot{V}_\mathrm{L} = \Omega(V_\mathrm{OC} - V_\mathrm{L} - (1-\rho)R_{int} I_\mathrm{L}) - \rho\, R_{int}\, \Omega\, I_\mathrm{L} \\ -(1-\rho)R_{int}\dot{I}_\mathrm{L}.\end{aligned} \tag{18}$$

For the online identification with a Kalman Filter based Algorithm the system is now expressed by its parameters as the state vector

$$x = \begin{bmatrix} V_\mathrm{OC} & V_\mathrm{L} & V_\mathrm{p} & \Omega & \rho & R_{int} \end{bmatrix}^T. \tag{19}$$

With the corresponding state transition functions from equations 16 and 18, the input current $I_\mathrm{L} = u$ and the previous considerations the state transition functions can be populated as

$$f(x,u) = \begin{bmatrix} f_1 & f_2 & f_3 & f_4 & f_5 & f_6 \end{bmatrix}^T \tag{20}$$

where f_1 to f_6 are defined as:

$$f_1 = 0,\ f_4 = 0,\ f_5 = 0,\ f_6 = 0 \tag{21}$$

$$\begin{aligned} f_2 = x_1 x_4 - x_2 x_4 - x_4(1-x_5)x_6 u - x_6 \\ -x_5 x_6 x_4 u - (1-x_5)x_6 \dot{u} \end{aligned} \tag{22}$$

$$f_3 = -x_4 x_3 + x_5 x_6 x_4 u. \tag{23}$$

Since the measured terminal voltage of the battery is represented by the second state, the measurement equation is

$$h = x_2. \tag{24}$$

The Jacobians for the presented functions f_1 to f_6, linearising the system around the current mean for the extended Kalman filter, are therefore:

$$\hat{A} = \begin{bmatrix} 0 & 0 & 0 & 0 & 0 & 0 \\ x_4 & -x_4 & 0 & x_1 - x_2 - x_6 u & x_6 \dot{u} & a_{2,6} \\ 0 & 0 & -x_4 & -x_3 + x_5 x_6 u & x_6 x_4 u & x_5 x_4 u \\ 0 & 0 & 0 & 0 & 0 & 0 \\ 0 & 0 & 0 & 0 & 0 & 0 \\ 0 & 0 & 0 & 0 & 0 & 0 \end{bmatrix} \tag{25}$$

$$a_{2,6} = -x_4 u - \dot{u} + x_5 \dot{u}.$$

$\hat{C}$ can be obtained as

$$\hat{C} = \begin{bmatrix} 0 & 1 & 0 & 0 & 0 & 0 \end{bmatrix}. \tag{26}$$

This method has been proven to show robust identification results as long as there are some dynamics in the current profile. to apply the introduced online parametrization, the system has to be implemented in an extended Kalman filter algorithm, which is introduced in the following section.

2.4. Standard Extended Kalman filter implementation

The EKF implementation described in detail can be found for example in [32] and [33]. The EKF consists from two steps: time update and measurement update. During the time update, the state is estimated ahead in time (predicted) and during the measurement update, the state is adjusted (corrected) according an actual measurement at that time. The representation of the EKF update equations with approximation of the state and measurement vector without noise values can be written as:

Time update (prediction):

$$\mathbf{x}_\mathrm{k}^- = f(x_{\mathrm{k}-1}, u_{\mathrm{k}-1}, 0) \tag{27}$$

$$\mathbf{P}_\mathrm{k}^- = A_\mathrm{k} P_{\mathrm{k}-1} A_\mathrm{k}^T + W_\mathrm{k} Q_{\mathrm{k}-1} W_\mathrm{k}^T \tag{28}$$

$$\mathbf{y}_\mathrm{k}^- = h(x_\mathrm{k}^-, 0) \tag{29}$$

Measurement update (correction):

$$\mathbf{K}_\mathrm{k} = P_\mathrm{k}^- C_{\mathrm{k}-1}^T (C_\mathrm{k} P_\mathrm{k}^- C_\mathrm{k}^T + V_\mathrm{k} R_{\mathrm{k}-1} V_\mathrm{k}^T)^{-1} \tag{30}$$

$$\mathbf{x}_\mathrm{k} = x_\mathrm{k}^- + K_\mathrm{k}(y_\mathrm{k} - y_\mathrm{k}^-) \tag{31}$$

$$\mathbf{P}_\mathrm{k} = (I - K_\mathrm{k} C_\mathrm{k}) P_\mathrm{k}^- \tag{32}$$

The process and noise measurement covariance matrices are formed as

$$Q_k = E[w_k w_k^T], R_k = E[v_k v_k^T], \tag{33}$$

which were derived literately in this study.

2.5. Estimation evaluation

The estimation algorithms are evaluated according their absolute maximum error:

$$x_{\_MaxErr} = \begin{bmatrix} \max(\left|\chi_{\_Ref} - \chi_{\_Est}\right|) \\ \max(\left|\eta_{Q\_Ref} - \eta_{Q\_Est}\right|) \\ \max(\left|\eta_{R\_Ref} - \eta_{R\_Est}\right|) \end{bmatrix} \tag{34}$$

and their absolute mean error:

$$x_{\_AvgErr} = \begin{bmatrix} \frac{1}{n}\sum_{t=1}^{n}(\left|\chi_{\_Ref} - \chi_{\_Est}\right|) \\ \frac{1}{n}\sum_{t=1}^{n}(\left|\eta_{Q\_Ref} - \eta_{Q\_Est}\right|) \\ \frac{1}{n}\sum_{t=1}^{n}(\left|\eta_{R\_Ref} - \eta_{R\_Est}\right|) \end{bmatrix} \tag{35}$$

The subscript *Est* stands for estimated states and the subscript *Ref* represents reference values of the states. Coulomb counting provides reference for χ. Moreover, obtained data from the parametrization (Section 2.2) are used as a reference for capacity fade η_Q and the resistance change η_R.

2.6. Test procedure and model structure

The laboratory tests were performed as the base for tunning and evaluation of the estimators. The current profiles (in this work specifically considered mixed pulse discharge, NEDC and UDDS) were applied to the battery, which was placed at the thermal chamber with the controlled temperature environment and it was connected to the battery test station. The tests on the fresh cell were done in MACCOR battery test system and the tests on the aged cell were performed in Digatron battery test system. The measured quantities of the battery, such as current and voltage, were recorded and they were used as an input to the model with the estimators. The temperature for the simulations was considered constant of 20° C. The layout of the test procedure is in Fig. 2.

The model layout with the estimators is shown in Fig. 3. Current, voltage and temperature are the inputs. The first extended Kalman filter estimates online the circuit model parameters in terms of behaviour model, which are also translated to Thevenin model parameters. The estimated parameters V_{OC} and R_0 are fed, together with current and temperature, into the SOC and SOH estimator, which returns the outputs of χ, η_Q and η_R. Furthermore, all the behaviour circuit model parameters are used as the input for the maximum available power estimator, which estimates the maximum available power in the specific time period Δt for charging and discharging, together with maximum available current and voltage.

3. Implementation and results

3.1. Modelling and structure of the filters

The states of the interest are SOC (χ) and SOH (η_{Q}, η_{R}). Therefore, the state vector is constructed as:

$$\mathbf{x} = \begin{bmatrix} \chi \\ \eta_{\mathrm{Q}} \\ \eta_{\mathrm{R}} \end{bmatrix} \tag{36}$$

The SOC change is based on coulomb counting. However, there are not used any process models for SOH, as the change of SOH is assumed to be very slow in comparison to SOC. η_{Q} and η_{R} are assumed to be observed from the increasing mean value of the error. The change of state then takes form with consideration of no noise as:

$$\dot{\mathbf{x}} = \begin{bmatrix} -\frac{I_{\mathrm{L}}}{\bar{Q}_{\mathrm{cap}} * \eta_{\mathrm{Q}}} \\ 0 \\ 0 \end{bmatrix} \tag{37}$$

The considered measurement vector has form:

$$\mathbf{Y} = \begin{bmatrix} V_{\mathrm{oc}} \\ R_0 \end{bmatrix} \tag{38}$$

where, V_{oc} is open-circuit voltage and R_0 is internal resistance. They are obtained through online parameter identification.

The function $h(x_{\mathrm{k}}^{-}, 0)$, relating the estimated measurements (estimated parameters V_{oc} and R_0), to the estimated states is based on the model and the fitted polynomials described in Section 2.2.

The full C matrix for EKF is:

$$\mathbf{C} = \begin{bmatrix} \frac{\partial V_{\mathrm{oc}}}{\partial \chi} & \frac{\partial V_{\mathrm{oc}}}{\partial \eta_{\mathrm{Q}}} & \frac{\partial V_{\mathrm{oc}}}{\partial \eta_{\mathrm{R}}} \\ \frac{\partial R_0}{\partial \chi} & \frac{\partial R_0}{\partial \eta_{\mathrm{Q}}} & \frac{\partial R_0}{\partial \eta_{\mathrm{R}}} \end{bmatrix} \tag{39}$$

With the assumptions that the capacity fade does not have influence on V_{oc} and R_0, together with that resistance change does not influence V_{oc}, the C matrix can be rewritten as:

$$\mathbf{C} = \begin{bmatrix} \frac{\partial V_{\mathrm{oc}}}{\partial \chi} & 0 & 0 \\ \frac{\partial R_0}{\partial \chi} & 0 & \frac{\partial R_0}{\partial \eta_{\mathrm{R}}} \end{bmatrix} = \begin{bmatrix} c_{11} & 0 & 0 \\ c_{21} & 0 & c_{23} \end{bmatrix} \tag{40}$$

c_{11} and c_{21} are obtained by the derivative of $h(x_{\mathrm{k}}^{-}, 0)$ with respect to χ. c_{23} takes form:

$$c_{31} = \frac{\partial R_0}{\partial \eta_{\mathrm{R}}} = \frac{\partial \frac{\bar{R}_0}{\eta_{\mathrm{R}}}}{\partial \eta_{\mathrm{R}}} = -\frac{\bar{R}_0}{{\eta_{\mathrm{R}}}^2} \tag{41}$$

The full A matrix for EKF has the form:

$$\mathbf{A} = \begin{bmatrix} \frac{\partial f_\chi}{\partial \chi} & \frac{\partial f_\chi}{\partial \eta_{\mathrm{Q}}} & \frac{\partial f_\chi}{\partial \eta_{\mathrm{R}}} \\ \frac{\partial f_{\eta_{\mathrm{Q}}}}{\partial \chi} & \frac{\partial f_{\eta_{\mathrm{Q}}}}{\partial \eta_{\mathrm{Q}}} & \frac{\partial f_{\eta_{\mathrm{Q}}}}{\partial \eta_{\mathrm{R}}} \\ \frac{\partial f_{\eta_{\mathrm{R}}}}{\partial \chi} & \frac{\partial f_{\eta_{\mathrm{R}}}}{\partial \eta_{\mathrm{Q}}} & \frac{\partial f_{\eta_{\mathrm{R}}}}{\partial \eta_{\mathrm{R}}} \end{bmatrix} \tag{42}$$

Which without use of any process model for η_{Q} and η_{R} results into:

$$\mathbf{A} = \begin{bmatrix} 0 & \frac{\partial f_\chi}{\partial \eta_{\mathrm{Q}}} & 0 \\ 0 & 0 & 0 \\ 0 & 0 & 0 \end{bmatrix} = \begin{bmatrix} 0 & a_{12} & 0 \\ 0 & 0 & 0 \\ 0 & 0 & 0 \end{bmatrix} \tag{43}$$

$$\mathbf{a_{12}} = \frac{\partial f_\chi}{\partial \eta_{\mathrm{Q}}} = \frac{\partial - \frac{I_{\mathrm{L}}}{\bar{Q}_{\mathrm{cap}} * \eta_{\mathrm{Q}}}}{\partial \eta_{\mathrm{Q}}} = \frac{I_{\mathrm{L}}}{{\eta_{\mathrm{Q}}}^2 * \bar{Q}_{cap}} \tag{44}$$

The observability of such system can be determined from the 'observability grammian' having a full column rank. The grammian takes form as follows in (45), where c_{11} and c_{23} have to be non zero.

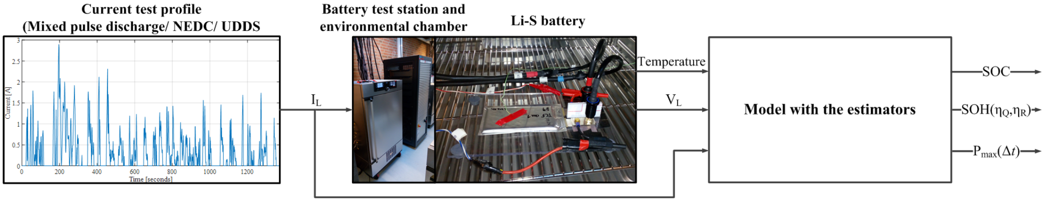

Figure 2: Test procedure layout.

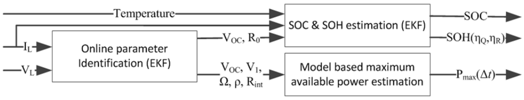

Figure 3: Model layout with the topology of the estimators.

$$\mathbf{W_0} = \begin{bmatrix} C \\ CA \\ CA^2 \end{bmatrix} = \begin{bmatrix} c_{11} & 0 & 0 \\ c_{21} & 0 & c_{23} \\ 0 & a_{12} * c_{11} & 0 \\ 0 & a_{12} * c_{21} & 0 \\ 0 & 0 & 0 \\ 0 & 0 & 0 \end{bmatrix} \qquad (45)$$

The linearization of the state change is considered as:

$$\mathbf{\Delta x}_{\mathrm{k}} = x_{\mathrm{k-1}} + \Delta x * T_s \qquad (46)$$

where T_s is a simulation step size.

3.2. Numerical values

The initial value for *a posteriori* error covariance is set as:

$$P = \begin{bmatrix} 0.1 & 0 & 0 \\ 0 & 0.1 & 0 \\ 0 & 0 & 0.1 \end{bmatrix} \qquad (47)$$

The measurement noise covariance R represents a measurement noise of V_{OC} and R_0 and is set to be

$$R = \begin{bmatrix} 0.2^2 & 0 \\ 0 & 0.6^2 \end{bmatrix}, \qquad (48)$$

emphasising higher trusts in the more consistent open circuit voltage identification than the fluctuating internal resistance (Fig. 5 a)). The process noise covariance Q, related to the uncertainty of the process models, is set as:

$$Q = \begin{bmatrix} 0.0001^2 & 0 & 0 \\ 0 & 0.0001^2 & 0 \\ 0 & 0 & 0.1^2 \end{bmatrix}. \qquad (49)$$

Here the arbitrary parameter tuning is based on slow changes, smaller variance values, for the χ and η_{Q} states and faster parameter changes, or higher variances, for η_{R}, that needs to follow relatively quick changes at high states of charges (Fig. 5 c)). Furthermore the states are assumed to be uncorrelated as the diagonal Q matrix indicates.

3.3. Results

3.3.1. Fresh cell

The mixed pulse discharge profile was applied to the fresh cell and the measurement data was fed to the estimator, as illustrated in Fig. 2. The reference and estimated states are shown in Fig. 4 and their error values are summarized in Table 1. When all the states were initialize with one (= fully charged, fresh cell), the average errors were 0.0080, 0.0125 and 0.0140; and the maximum errors were 0.0306, 0.0559 and 0.7714 for χ, η_{Q} and η_{R}, respectively. However, the maximum error value of η_{R} is caused by the initialization of the parameter estimator and it is reached only at the very beginning. When the current is firstly applied, the resistance quickly converge close to the reference value already after one second. Therefore, the 'real' maximum error of the estimator performance is 0.2606 and the same metric is going to be used further on to evaluate the 'real' performance of the estimator and not the error caused by the parameter estimator initialization. In this ideal case, one can see that the state estimator provides relatively high accurate results with the average error below two percents and the maximum error below six percents. The least reliable state is the η_{Q}. Moreover, the η_{R} does not always match the reference, which is probably due to the settling times to reach convergence and also because the parameter's dependence on the current. In Fig. 5 a), one can see that the parameters of V_{OC} and R_0 used for the state estimation are identified very closely to the reference, while the remaining parameters of R_1 and C_1 varies a bit. The R_1 is identified to be little bit higher at the low voltage plateau and the C_1 is identified little bit lower at the high voltage plateau in comparison to the model.

The next step was to see the convergence capability of the applied Kalman filter when the initial state values are wrongly set. In the first case, all the states are set to be 0.7 in the beginning. From Fig. 4 is apparent that the χ and the η_{R} converged almost instantly. The χ estimation error was reduced already in the first step of the simulation, after 1 second, from 0.3 to 0.1264. The error of η_{R} in the beginning of the simulation was 0.4714, which in 10 seconds of relaxation reduced to 0.4307 and after the first second of the current being applied it dropped to 0.1301. The η_{Q} took longer time and it continuously settled in the middle of the high voltage plateau, after around 0.15 of SOC being discharged.

So far, the initial SOC (SOC_{ini}) was always set to be at the high voltage plateau. When the SOC_{ini} was set to 0.6, which is at the low voltage plateau, the filter was not able to converged

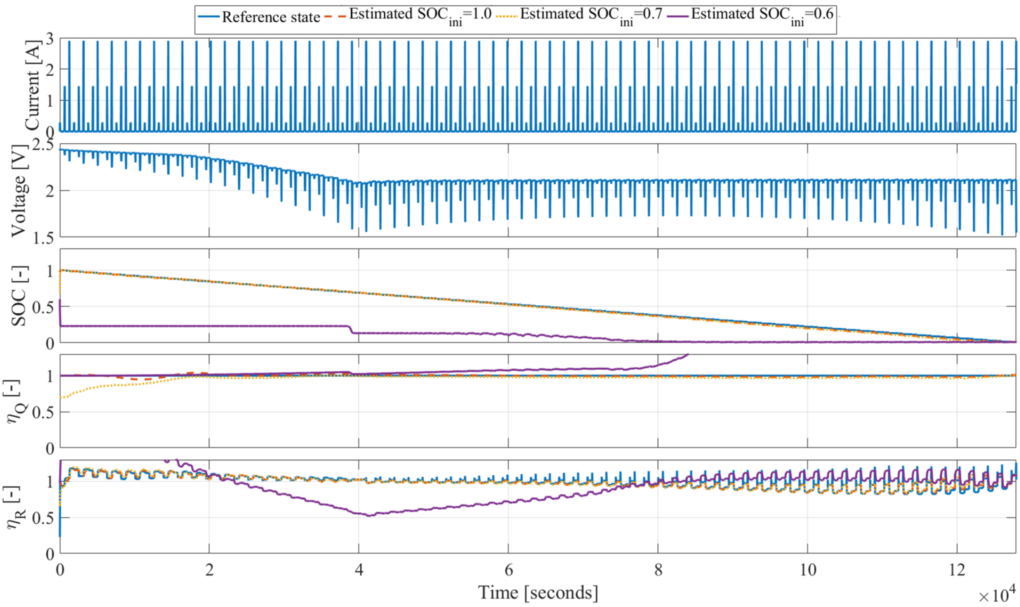

Figure 4: The mixed pulse discharge test profile and the estimated results for the various SOC_{ini} values at the fresh Li-S cell. It shows the capability of the estimator to converge to the states in the cases when the SOC_{ini} is set to match the reference SOC value or to be mismatched, but still at the high voltage plateau as the SOC reference was. If the SOC_{ini} was instead at the low voltage plateau, the estimator was not able to converge.

Table 1: The errors of the state estimation for the fresh cell with various initial conditions.

Initial conditions	Average Errors	Maximum Errors
$[\chi = 1\ \eta_\mathrm{Q} = 1\ \eta_\mathrm{R} = 1]$	[0.0080 0.0125 0.0140]	[0.0306 0.0559 0.2606]
$[\chi = 0.7\ \eta_\mathrm{Q} = 0.7\ \eta_\mathrm{R} = 0.7]$	[0.0112 0.0370 0.0174]	[0.1264 0.3000 0.1301]
$[\chi = 0.6\ \eta_\mathrm{Q} = 1\ \eta_\mathrm{R} = 1]$	[0.3963 0.3796 0.2440]	[0.7688 1.3897 1.2931]

the SOC over the whole discharging period. Moreover, the originally well set η_Q diverged in the second half of the discharge and the η_R was highly off in the first half of the discharge.

To see what happens when the situation is opposite, the reference SOC is at the low voltage plateau, while the SOC_{ini} is at the high voltage plateau, the simulation was run for only a part of the mixed pulse discharge profile with the initial reference SOC to be 0.6764, which means that the discharge starts already at the low voltage plateau. The obtained results are shown in Fig. 5 b). When the SOC_{ini} was one, all the states diverged. However, when the SOC_{ini} was 0.6, the states were again estimated very well. Therefore, it is very important that the SOC_{ini} is present at the same voltage plateau as is the reference or real SOC. In the case, when the SOC_{ini} was wrongly at the high voltage plateau, the η_Q raised rapidly and steadily over the value of 2. Such 'non-sense' value can be used as an indicator for the wrong estimation and re-set the estimated SOC value.

This stability issue of the estimator based on the initial conditions of the SOC, whereas the cell is at high or low voltage plateau can be solved in the following way. The initial conditions for the parameter identification, in meaning of $[V_{OC}\ V_L\ V_1\ \Omega\ \rho\ R_{int}]$ are adjusted to be:

$$x_0 = \begin{bmatrix} V_{meas} & V_{meas} & 0 & 0.025 & 0.1 & 0.172 \end{bmatrix}^T \tag{50}$$

Where V_{meas} is the actually measured voltage at the cell. Subsequently, the initialization of the SOC/SOH Kalman filter contains following condition:

$$SOC_{ini} := \begin{cases} c + 0.01, & \text{if } V_{OC} \geq V_{OC,max\_lp} \\ c - 0.01, & \text{if } V_{OC} < V_{OC,max\_lp} \end{cases} \tag{51}$$

Where the c stands for the SOC transition point between the high and low voltage plateau. Moreover, the V_{OC,max_lp} is the maximum V_{OC} value obtained from the Li-S battery model. In such way, the estimator starts with the SOC_{ini} value which will lead to the convergence. Of course, if the more accurate guess of the initial condition exists, it shall be inputted.

3.3.2. Aged cell

The goal of the SOH estimation is to estimate and track the health of the cell. The cell under the investigation was aged by 40 cycles of continuous charge (0.34 A) and discharge (0.68 A) at the elevated temperature of 50 °C; and stored at the shelf for approximately six months at room temperature. Afterward, the continuous discharge, mixed pulse discharge and driving

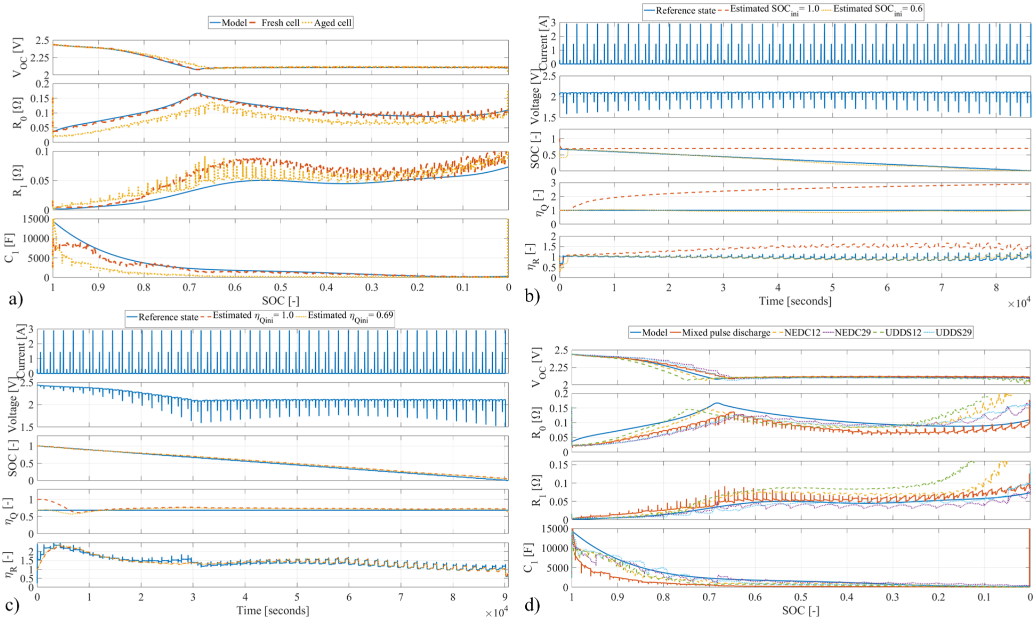

Figure 5: a) Comparison of the battery model and online identified parameters for the fresh and aged cell. It shows that when the cell ages the inflection point between the high and low voltage plateaus is moving to the right (to lower SOC). b) The mixed pulse discharge test profile and the estimated results for the fresh cell, when the discharge starts already at the low voltage plateau. If the SOC_{ini} is also at the low voltage plateau, the state converges, otherwise they do not. c) The mixed pulse discharge test profile and the estimated results for the aged cell. The estimates converge for all states. The accuracy is higher with the initial estimate closer to the reference state. d) Battery model identified parameters for the aged cell at various mission profiles. The absolute available capacity obtained during the discharge causes the shifting of the inflection point at the V_{OC} and R_0 curves due to the SOC relativity to the available capacity. At the end of the discharge, there is a rapid increase of the resistance, dependent on the current rate and the dynamic of the mission profiles.

cycles of NEDC and UDDS were applied to it at °C. The obtained capacity from the mixed pulse discharge test at 20 °C was 1.86 Ah, which results in η_{Q} to be 0.69.

The estimation for the mixed pulse discharge profile, shown in Fig. 5 c), works well, similarly as at the fresh cell, only with the lower accuracy. The error values are summarized in Table 2. The χ got slightly over estimated at the low voltage plateau with the highest misfit being 0.0550 for $\eta_{\mathrm{Q_{ini}}} = 1$ and 0.0461 for $\eta_{\mathrm{Q_{ini}}} = 0.69$. This χ over estimation is probably caused in the 'offset' present in the estimated value of the η_{Q} at the low voltage plateau. At this region the estimated value in an average was 0.74 for $\eta_{\mathrm{Q_{ini}}} = 1$ and 0.71 for $\eta_{\mathrm{Q_{ini}}} = 0.69$, while the reference was 0.69. It is also seen that, when the initial value of the η_{Q} was closer to the reference, the accuracy was again improved.

It is important to remind that only the model of the fresh cell is implemented in the estimator and it has no knowledge, only assumptions, introduced in Section 3.1, how the parameters will change with the change of states. In Fig. 5 a), the actual identified parameters are shown. The low voltage plateau has shrunk more than the high voltage plateau; and therefore the inflection point is moved to the right. Otherwise, the V_{OC} is not changed. However, the R_0 seems to be lower than at the fresh cell, except the very low SOC, where it has increasing tendency.

Besides the mixed pulse discharge profile, also four mission driving profiles were applied to the cell and proceeded to the state estimation. The profiles were: NEDC with the maximum current of 1.2 A (= NEDC12) and of 2.9 A (= NEDC29), and the UDDS also with the maximum currents of 1.2 A (= UDDS12) and of 2.9 A (= UDDS29). The profiles with the estimation results are presented in Fig. 6. The χ more or less follows the reference. However, the confidence is reduced and the error can be again related to the estimated η_{Q}. From the reference η_{Q}, one can see that it varies from 0.8110 to 1.1965, while the value obtained from the mixed pulse discharge profile was 0.69. The different numbers come from the obtained capacity from the specific tests, which was 1.8592, 2.8221, 2.2029, 3.2499 and 2.4172 Ah for the mixed pulse discharge, NEDC12, NEDC29, UDDS12 and UDDS29, consequently. The actual capacity varies due to its high dependence on the applied current and the dynamics of the profile, which was reported for the Li-S batteries in [34] and investigated and modelled in [35, 36]. How it results into the identified parameters is shown in Fig. 5 d), where the inflection point at V_{OC} and R_0 curves is moving according the available capacity over the discharge, because the SOC is relative to the actual capacity according (1). Moreover, the dynamics related to the applied current rates and the relaxation periods are visible at the rapidly increasing resistance at the end of discharge. Therefore, the estimated η_{Q} in our work is related only to the actual profile. If the applied profile remains

Table 2: The errors of the state estimation for the aged cell.

Initial conditions	Average Errors	Maximum Errors
$[\chi = 1\ \eta_{\mathrm{Q}} = 1\ \eta_{\mathrm{R}} = 1]$	[0.0303 0.0633 0.0777]	[0.0550 0.3162 1.4156]
$[\chi = 1\ \eta_{\mathrm{Q}} = 0.69\ \eta_{\mathrm{R}} = 1]$	[0.0274 0.0406 0.0756]	[0.0461 0.1150 1.4155]
NEDC12	[0.0576 0.0974 0.0828]	[0.1123 0.1565 0.5136]
NEDC29	[0.0827 0.1575 0.1796]	[0.1552 0.2412 0.6127]
UDDS12	[0.0797 0.1900 0.1163]	[0.1592 0.3258 0.6686]
UDDS29	[0.0461 0.0696 0.1301]	[0.0890 0.1632 0.6686]

similar, then the η_{Q} will straightforwardly indicate the capacity fade ongoing in the cell. In order to have a referent, or so-called independent, actual capacity, which would be related to the capacity fade independent of the mission profile, the dynamics such as transport limitations have to be included in the model.

The estimated η_{R} seems to have the similar character for all the driving cycles and also the mixed pulse discharge at the aged cell. In the detail, it is shown in Fig. 7. Additionally, the average of the aged cell curves is plotted to highlight the observable trend. At the high voltage plateau, high SOC, the η_{R} is highly increased an creates the peak around the value of 2. During the flat low voltage plateau at the middle SOC region, there is smaller increase to around 1.2 and at the end of discharge (SOC close to 0), there is a decrease down to around 0.6. If this behaviour would be observable over the other cells and mission profiles during the ageing, it could be also used to couple the resistance change to the capacity fade as it is often done at other battery chemistries.

4. Estimation of the maximum available power

An estimation of the available power is the another required functionality of the BMS, besides the SOC and SOH estimation. Especially in EV applications, there are certain situations when the high power is required from the battery, for example during the acceleration. In these situations, the safety operation limits can be reached quickly, which will result into limitation of the provided power and its sudden decrease, causing an unexpected and possibly dangerous situation for a driver. Therefore, the estimation of the available power is applied to predict the maximum power which can be provided, typically in period of 1 to 20 seconds. In this way, the provided power can be limited from the beginning, causing the smooth operation and expected continuous decrease later on [7].

There are usually considered three main methods for the estimation of the available power. The first is based on a characteristic map, which is stored in a memory of the BMS. It is composed of static relationships of power towards the other battery states and quantities and it is obtained offline from the battery tests. During ageing, some of the battery parameter changes, and thus the characteristic map has to be updated. The advantage of this method is its easy implementation and simplicity. However, it does not reflect the dynamic states of the battery accurately and it might be difficult to adjust it during the ageing due to lack of the reference measurements (at maximum power). Moreover, it might required considerable space of the memory to store all the data with the inter-dependencies [7, 37].

The second method is based on a dynamic battery model. The maximum power is then predicted according the accuracy of the battery model, reflecting the dynamic states. The obvious advantage of this method in our context is that the battery parameters can be identified online. Therefore, the battery parameters would be adjusted according to ageing and also specific chemistry effects (a history effect of the Li-S batteries) to provide more precise estimated [7, 38].

The third method, considered for this purpose, uses ANFIS. However, an additional filtering is required for training on power pulses. Moreover, the real-time applicability on a low cost hardware is questionable. [7, 39].

4.1. Implementing of the maximum available power estimation

The implemented maximum available power estimation is based on the dynamic battery model approach, when the battery parameters are identified online. The used battery model is the behavioral battery model for the Li-S batteries described in [19], which uses the parameters representing the dynamic bandwidth (Ω), the total steady-state resistance (R_{int}) and the dynamic fraction of the response (ρ_p), instead of R_0, R_1 and C_1.

The core battery equations are:

$$v_\ell = V_{\mathrm{oc}} - (1-\rho)R_{\mathrm{int}} i_\ell - v_C, \tag{52}$$

$$\frac{dv_C}{dt} = -\Omega v_C + \rho R_{\mathrm{int}} \Omega i_\ell. \tag{53}$$

The Laplace transform of (53) is

$$s\bar{v}_C - V_{C0} = -s\Omega\bar{v}_C + \rho R_{\mathrm{int}}\Omega\bar{\imath}_\ell$$

which can be rearranged as

$$(s+\Omega)\bar{v}_C = \rho R_{\mathrm{int}}\Omega\bar{\imath}_\ell + V_{C0}$$

and again to

$$\bar{v}_C = \underbrace{\rho R_{\mathrm{int}} \cdot \frac{\Omega}{s+\Omega}}_{\text{transfer function}} \cdot \bar{\imath}_\ell + \underbrace{\left(\frac{V_{C0}}{\Omega}\right)\frac{\Omega}{s+\Omega}}_{\text{initial condition}}. \tag{54}$$

Let's assume that the future current has a constant value, I_ℓ. Note that

$$\mathcal{L}\{I_\ell\} = \frac{I_\ell}{s}.$$

Substituting this in (52) and (54) gives

$$v_\ell = V_{\mathrm{oc}} - (1-\rho)R_{\mathrm{int}} I_\ell - v_C \tag{55}$$

$$\bar{v}_C = \rho R_{\mathrm{int}} I_\ell \cdot \frac{\Omega}{s(s+\Omega)} + V_{C0} \cdot \frac{1}{s+\Omega}. \tag{56}$$

Now

$$\frac{\Omega}{s(s+\Omega)} = \frac{1}{s} - \frac{1}{s+\Omega}$$

so

$$\bar{v}_C = \rho R_{\mathrm{int}} I_\ell \cdot \frac{1}{s} + (V_{C0} - \rho R_{\mathrm{int}} I_\ell)\,\frac{1}{s+\Omega}.$$

We can take the inverse Laplace transform:

$$v_C(t) = \rho R_{\mathrm{int}} I_\ell + (V_{C0} - \rho R_{\mathrm{int}} I_\ell)e^{-\Omega t}$$

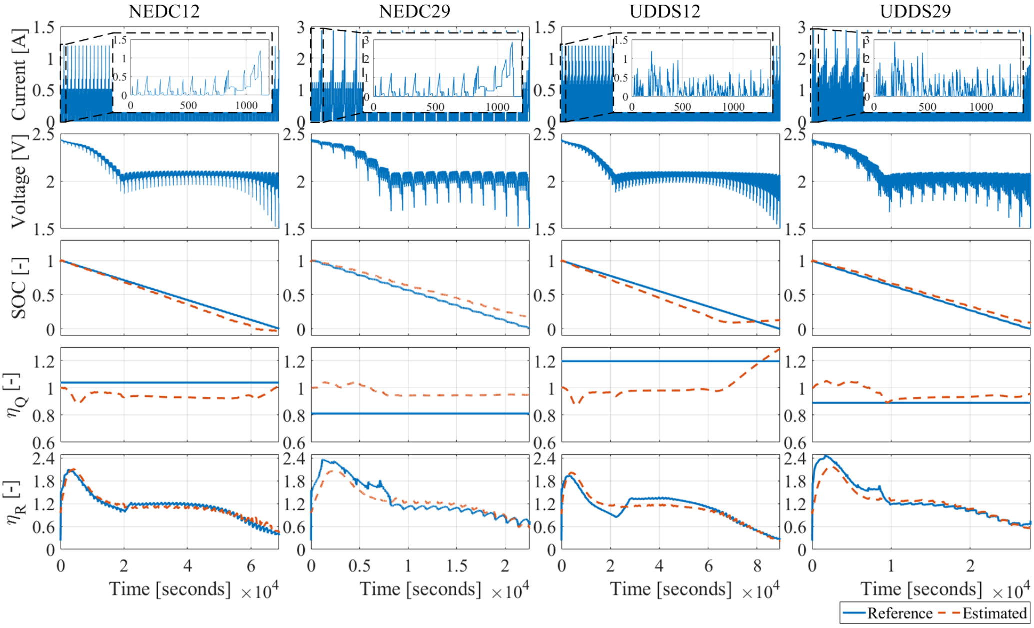

Figure 6: The driving cycle mission profiles and the estimated results for the aged cell. The χ roughly follows the reference. The accuracy of the χ is dependent on the estimated η_Q, which varies with the total discharged capacity of the cell under different mission profiles, due to their different current rates and dynamics. The η_R is in general followed well and similar between the different driving cycles.

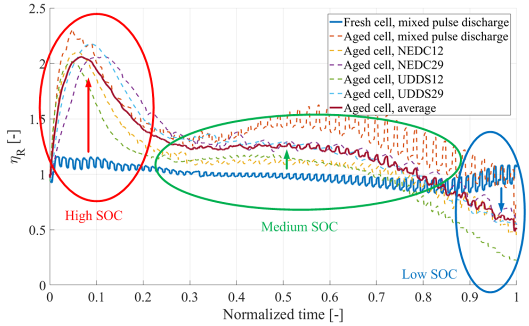

Figure 7: The estimated η_R at the aged cell compared to the fresh cell. The changes in the η_R due to ageing are very similar at any mission profile. At the high SOC region, the η_R is rapidly growing. Over the middle SOC region, the η_R slightly grows. Finally, at the low SOC region, the η_R increases.

so we end up with

$$v_\ell(t) = V_{\text{oc}} - R_{\text{int}} I_\ell + (\rho R_{\text{int}} I_\ell - V_{C0}) e^{-\Omega t}$$

or, equivalently,

$$v_\ell(t) = (V_{\text{oc}} - V_{C0} e^{-\Omega t}) - R_{\text{int}}(1 - \rho \cdot e^{-\Omega t}) I_\ell.$$

Let us assume that at some point $T \geq 0$ seconds in the future, we want to know the minimum and maximum currents such that $v_\ell(T) \in [V_{\min}, V_{\max}]$. For convenience, we can write

$$V' = V_{\text{oc}} - V_{C0} e^{-\Omega T}$$

and

$$R' = R_{\text{int}}(1 - \rho e^{-\Omega T})$$

In practical applications, $V', R' > 0$ since $V_{\text{oc}} > V_{C0}$ and $\rho < 1$. We can then write

$$v_\ell(T) = V' - R' I_\ell.$$

To keep $v_\ell(T) \in [V_{\min}, V_{\max}]$, we need to satisfy

$$V_{\min} \leq V' - R' I_\ell,$$

which becomes

$$I_\ell \leq I_{V_{\min}} \tag{57}$$

where $I_{V_{\min}} = (V' - V_{\min})/R'$; similarly, we need

$$V_{\max} \geq V' - R' I_\ell,$$

which becomes

$$I_\ell \geq I_{V_{\max}} \tag{58}$$

where $I_{V_{\max}} = -(V_{\max} - V')/R'$.

In practice, we are likely to also want to ensure that the current is constrained to a specified window, $I_\ell \in [I_{\min}, I_{\max}]$. The most conservative of these will be the most important. Effectively, the current that gives the maximum discharge power is given by

$$I_{P_{\text{dis.max}}} = \min\left(I_{V_{\min}}, I_{\max}\right)$$

with the corresponding power given by

$$P_{\text{dis.max}} = \left(V' - R' I_{P_{\text{dis.max}}}\right) I_{P_{\text{dis.max}}}.$$

Similarly, the current that gives the maximum charge power is

$$I_{P_{\text{ch.max}}} = \max\left(I_{V_{\max}}, I_{\min}\right)$$

with the corresponding power given by

$$P_{\text{ch.max}} = \left(V' - R' I_{P_{\text{ch.max}}}\right) I_{P_{\text{ch.max}}}.$$

4.2. Power estimation validation

In order to validate the maximum available power estimation, the modified mixed pulse discharge profile was applied to the Li-S cell with considered maximum current pulses and it is shown in Fig. 8. After the first set of the discharging pulses with currents of 0.29, 1.45 and 2.90 A, consequently, the discharging pulse with 6.8 A was applied and after the second set of the discharging pulse, the charging pulse with 1.7 A was applied. When the voltage limits of 1.5 V for discharging and 2.45 V for charging were reach during these maximum current pulses, the operation mode switched from the constant current mode to constant voltage mode in order to obtain the maximum power at those conditions.

We have considered two cases for the power estimation, at first the instantaneous power at $T = 1$ second, shown in Fig. 8 and then for the 'accelerating' pulse for $T = 10$ seconds. The accuracy of the estimation is evaluated from the whole 30 second maximum current pulse for the instantaneous power. For the 'accelerating' pulse, only the last 20 seconds of the pulse are considered, as the estimated power is for 10 seconds applying of the maximum current, so the estimated power can be compared just after the first 10 seconds of the applied pulse.

The absolute maximum and average error are compute similarly to (34) and (35), consequently, and they are presented in Table 3. Under the selected boundaries of maximum allowed voltage and current limits, the cell was able to provide 14.78 W for discharge and 4.14 W for charge during the applied pulses. The absolute maximum errors seem to reach high significant values related to the maximum cell performance. However, the absolute average errors are fairly acceptable. It is also important to keep on mind that the model was derived and account to maximum discharging current 2.9 A and no charging model or parameters are implemented. Therefore, the performance of the maximum available power estimator, while applied current of 6.8 A for discharge, which is more than two times more for what was the model parametrized, and 1.7 A charging current, is considered more than acceptable.

Table 3: The errors of maximum available power estimation.

T	Quantity	Average Errors	Maximum Errors
1 s	$[V_{min}\ V_{max}]$ [V]	[0.0080 0.0460]	[0.1840 0.1556]
	$[I_{P_{dis.max}}\ I_{P_{ch.max}}]$ [A]	[0.3022 0.0249]	[1.7750 0.7759]
	$[P_{dis.max}\ P_{ch.max}]$ [W]	[0.5049 0.1381]	[3.0365 1.9128]
10 s	$[V_{min}\ V_{max}]$ [V]	[0.0110 0.0525]	[0.2148 0.1548]
	$[I_{P_{dis.max}}\ I_{P_{ch.max}}]$ [A]	[0.6119 0.0284]	[3.6860 0.3566]
	$[P_{dis.max}\ P_{ch.max}]$ [W]	[0.9924 0.1586]	[6.1106 0.8736]

5. Conclusion

In this work, the new SOC and SOH estimation method for the Li-S batteries have been introduced, together with specifically tailored model based maximum available power estimation. The estimation is based on two extended Kalman filters, where the first filter is used for online parameter identification of the battery electrical circuit model from the voltage and current measurements. Consequently, the estimated parameters and the current measurement are used to the second extended Kalman filter to estimate the SOC (χ) and SOH, in terms of the capacity fade (η_Q) and the resistance change (η_R) and for the model based maximum available power estimator to provide maximum power, current and voltage for both charging and discharging at the specific time step in future.

At first, the robustness and the accuracy of the SOC and SOH estimator has been presented at the mixed pulse discharge profile at the fresh cell, in order for the estimator be later on applied to the aged cell. The estimator does not include any process model of the Li-S battery degradation and it is solely based on the error correction. The estimator has shown the capability to track the χ, η_Q and η_R at the aged cell. However, the accuracy of the χ is dependent on the estimated (η_Q), which varies over the different mission profiles, together with that how the available capacity varies at them due to their different current rates and dynamics. Therefore, there is a need for the concept clarification of the actual capacity at the Li-S batteries according to their dynamics and history. Moreover, the model for the available capacity change would be helpful in order to provide an information about the absolute capacity fade. In terms of the absolute capacity fade, the η_R could be used as a supportive indicator, as it has shown more consistent trend between the fresh and the aged cell. However, the question of how it evolves under the different degradation causes has to be still answered.

The implemented maximum available power estimator was presented and validated by comparing to the experimental tests. It proofed to be useful also when the current of 6.8 A was applied, which is more than two times for what was the model originally parametrized and it also provides relatively accurate estimates for charging mode, for which the charging model is lacking at all.

Acknowledgment

This research was undertaken as a part of joint initiative of the ACEMU and REVB projects. The authors gratefully acknowledge the Danish Council for Strategic Research (1313-

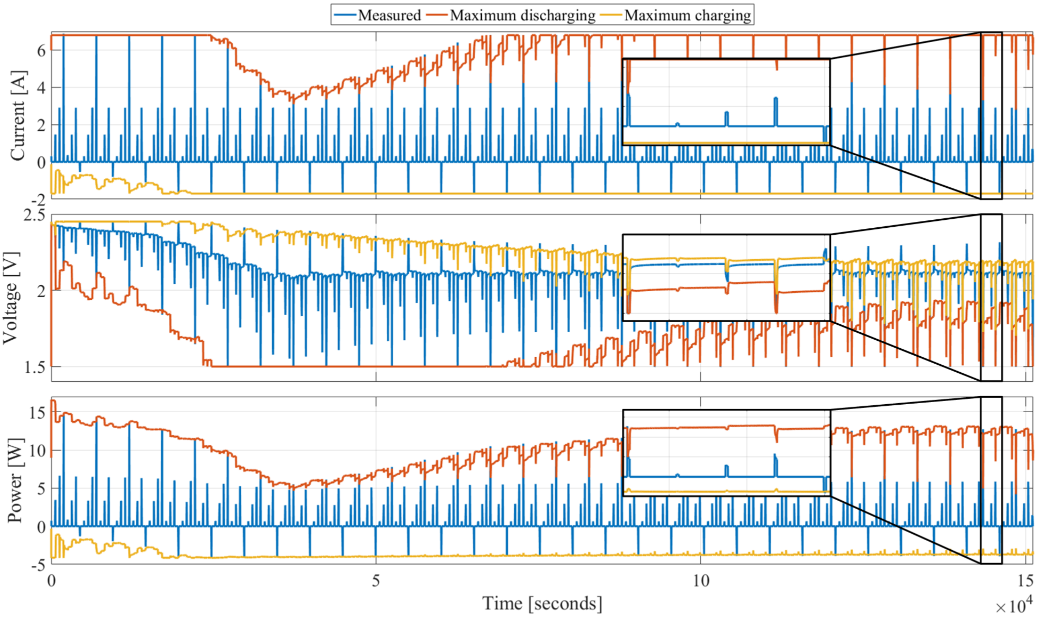

Figure 8: The mixed pulse profile for maximum available power estimation and the instantaneous maximum available power at 1 second.

00004B) and EUDP (1440-0007) for ACEMU part; and Innovate UK (TS/L000903/1) and EPSRC (EP/L505286/1) for REVB part for providing financial support. Moreover, the authors would like to thank OXIS Energy for supplying the Lithium-Sulfur battery cells.

[1] P. G. Bruce, S. A. Freunberger, L. J. Hardwick, J.-M. Tarascon, Li-O2 and Li-S batteries with high energy storage, Nat. Mater. 11 (02) (2012) 19–29. doi:10.1038/nmat3191.

[2] I. a. Hunt, Y. Patel, M. Szczygielski, L. Kabacik, G. J. Offer, Lithium sulfur battery nail penetration test under load, Journal of Energy Storage 2 (2015) 25–29. doi:10.1016/j.est.2015.05.007.

[3] S. Risse, N. A. Cañas, N. Wagner, E. Härk, M. Ballauff, K. A. Friedrich, Correlation of capacity fading processes and electrochemical impedance spectra in lithium/sulfur cells, Journal of Power Sources 323 (2016) 107–114. doi:10.1016/j.jpowsour.2016.05.032.

[4] V. Knap, D.-I. Stroe, M. Swierczynski, R. Teodorescu, E. Schaltz, Investigation of the Self-Discharge Behavior of Lithium-Sulfur Batteries, J. Electrochem. Soc. 163 (6) (2016) A911–A916. doi:10.1149/2.0641606jes.

[5] W. T. Xu, H. J. Peng, J. Q. Huang, C. Z. Zhao, X. B. Cheng, Q. Zhang, Towards Stable Lithium-Sulfur Batteries with a Low Self-Discharge Rate: Ion Diffusion Modulation and Anode Protection, ChemSusChem 8 (17) (2015) 2892–2901. doi:10.1002/cssc.201500428.

[6] M. Wild, L. O'Neill, T. Zhang, R. Purkayastha, G. Minton, M. Marinescu, G. J. Offer, Lithium Sulfur Batteries, A Mechanistic Review, Energy Environ. Sci.doi:10.1039/C5EE01388G.

[7] W. Waag, C. Fleischer, D. U. Sauer, Critical review of the methods for monitoring of lithium-ion batteries in electric and hybrid vehicles, Journal of Power Sources 258 (2014) 321 – 339. doi:10.1016/j.jpowsour.2014.02.064.

[8] M. Shahriari, M. Farrokhi, Online state-of-health estimation of vrla batteries using state of charge, IEEE Transactions on Industrial Electronics 60 (1) (2013) 191–202. doi:10.1109/TIE.2012.2186771.

[9] B. S. Bhangu, P. Bentley, D. A. Stone, C. M. Bingham, Nonlinear observers for predicting state-of-charge and state-of-health of lead-acid batteries for hybrid-electric vehicles, IEEE Transactions on Vehicular Technology 54 (3) (2005) 783–794. doi:10.1109/TVT.2004.842461.

[10] M. Coleman, C. K. Lee, C. Zhu, W. G. Hurley, State-of-charge determination from emf voltage estimation: Using impedance, terminal voltage, and current for lead-acid and lithium-ion batteries, IEEE Transactions on Industrial Electronics 54 (5) (2007) 2550–2557. doi:10.1109/TIE.2007.899926.

[11] M. Galeotti, C. Giammanco, L. Cin, S. Cordiner, A. D. Carlo, Synthetic methods for the evaluation of the state of health (soh) of nickel-metal hydride (nimh) batteries, Energy Conversion and Management 92 (2015) 1 – 9. doi:10.1016/j.enconman.2014.12.040.

[12] P. Singh, C. F. Jr., D. Reisner, Fuzzy logic modelling of state-of-charge and available capacity of nickel/metal hydride batteries, Journal of Power Sources 136 (2) (2004) 322 – 333, selected papers presented at the International Power Sources Symposium. doi:10.1016/j.jpowsour.2004.03.035.

[13] A. Fotouhi, K. Propp, D. J. Auger, Electric vehicle battery model identification and state of charge estimation in real world driving cycles, in: Computer Science and Electronic Engineering Conference (CEEC), 2015 7th, 2015, pp. 243–248. doi:10.1109/CEEC.2015.7332732.

[14] G. L. Plett, Extended Kalman filtering for battery management systems of LiPB-based {HEV} battery packs: Part 3. State and parameter estimation , Journal of Power Sources 134 (2) (2004) 277 – 292. doi:10.1016/j.jpowsour.2004.02.033.

[15] M. Charkhgard, M. Farrokhi, State-of-charge estimation for lithium-ion batteries using neural networks and ekf, IEEE Transactions on Industrial Electronics 57 (12) (2010) 4178–4187. doi:10.1109/TIE.2010.2043035.

[16] Y. V. Mikhaylik, J. R. Akridge, Polysulfide Shuttle Study in the Li/S Battery System, J. Electrochem. Soc. 151 (11) (2004) A1969. doi:10.1149/1.1806394.

[17] A. Fotouhi, D. Auger, K. Propp, S. Longo, Electric Vehicle Battery Parameter Identification and SOC Observability Analysis: NiMH and Li-S Case Studies, in: 8th IET International Conference on Power Electronics, Machines and Drives (PEMD 2016), no. April, Institution of Engineering and Technology, 2016, pp. 1–6. doi:10.1049/cp.2016.0142.

[18] K. Propp, D. J. Auger, A. Fotouhi, S. Longo, V. Knap, Kalman-variant estimators for state of charge in lithium-sulfur batteries, Journal of Power

Sources 343 (2017) 254–267. doi:10.1016/j.jpowsour.2016.12.087.

[19] K. Propp, M. Marinescu, D. J. Auger, L. O'Neill, A. Fotouhi, K. Somasundaram, G. J. Offer, G. Minton, S. Longo, M. Wild, V. Knap, Multi-temperature state-dependent equivalent circuit discharge model for lithium-sulfur batteries, Journal of Power Sources 328 (2016) 289–299. doi:10.1016/j.jpowsour.2016.07.090.

[20] A. Fotouhi, D. J. Auger, K. Propp, S. Longo, Accuracy Versus Simplicity in Online Battery Model Identification, IEEE Transactions on Systems, Man, and Cybernetics: Systems PP (99) (2016) 1–12. doi:10.1109/TSMC.2016.2599281.

[21] K. Propp, D. J. Auger, A. Fotouhi, M. Marinescu, V. Knap, S. Longo, Dual extended Kalman filter for online estimation of model parameters and state of charge in lithium-sulfur batteries, unpublished results (2017).

[22] A. Farmann, W. Waag, A. Marongiu, D. U. Sauer, Critical review of onboard capacity estimation techniques for lithium-ion batteries in electric and hybrid electric vehicles, Journal of Power Sources 281 (2015) 114 – 130. doi:10.1016/j.jpowsour.2015.01.129.

[23] B. Balagopal, M. Y. Chow, The state of the art approaches to estimate the state of health (soh) and state of function (sof) of lithium ion batteries, in: 2015 IEEE 13th International Conference on Industrial Informatics (INDIN), 2015, pp. 1302–1307. doi:10.1109/INDIN.2015.7281923.

[24] W. Peukert, ber die Abhngigkeit der Kapazitt von der Entladestromstrke bei Bleiakkumulatoren, Elektrotechnische Zeitschrift 20.

[25] A. Hausmann, C. Depcik, Expanding the peukert equation for battery capacity modeling through inclusion of a temperature dependency, Journal of Power Sources 235 (2013) 148 – 158. doi:10.1016/j.jpowsour.2013.01.174.

[26] M. Galeotti, L. Cina, C. Giammanco, S. Cordiner, A. D. Carlo, Performance analysis and {SOH} (state of health) evaluation of lithium polymer batteries through electrochemical impedance spectroscopy, Energy 89 (2015) 678 – 686. doi:10.1016/j.energy.2015.05.148.

[27] A. P. Schmidt, M. Bitzer, rpd W. Imre, L. Guzzella, Model-based distinction and quantification of capacity loss and rate capability fade in li-ion batteries, Journal of Power Sources 195 (22) (2010) 7634 – 7638. doi:10.1016/j.jpowsour.2010.06.011.

[28] G. Richter, Method and device for determining the state of function of an energy storage battery, uS Patent 6,885,951 (Apr. 26 2005).
URL `https://www.google.com/patents/US6885951`

[29] Y.-H. Chiang, W.-Y. Sean, J.-C. Ke, Online estimation of internal resistance and open-circuit voltage of lithium-ion batteries in electric vehicles, Journal of Power Sources 196 (8) (2011) 3921–3932.

[30] H. He, R. Xiong, H. Guo, Online estimation of model parameters and state-of-charge of LiFePO 4 batteries in electric vehicles, Applied Energy 89 (1) (2012) 413–420.

[31] R. Xiong, H. He, F. Sun, K. Zhao, Evaluation on state of charge estimation of batteries with adaptive extended Kalman filter by experiment approach, IEEE Transactions on Vehicular Technology 62 (1) (2013) 108–117.

[32] M. Rhudy, Y. Gu, Understanding nonlinear kalman filters, part ii: An implementation guide, Interactive Robotics Letters.

[33] G. Welch, G. Bishop, An Introduction to the Kalman Filter, Department of Computer Science, University of North Carolina at Chapel Hill, UNC-Chapel Hill, TR 95-041 (July 2006).

[34] V. Knap, T. Zhang, D. I. Stroe, E. Schaltz, R. Teodorescu, K. Propp, Significance of the Capacity Recovery Effect in Pouch Lithium-Sulfur Battery Cells, ECS Transactions 74 (1) (2016) 95–100. doi:10.1149/07401.0095ecst.

[35] T. Zhang, M. Marinescu, S. Walus, G. J. Offer, Modelling transport-limited discharge capacity of lithium-sulfur cells, Electrochimica Acta 219 (2016) 502–508. doi:10.1016/j.electacta.2016.10.032.

[36] T. Zhang, M. Marinescu, S. Walus, P. Kovacik, G. J. Offer, What Limits the Rate Capability of Li-S Batteries during Discharge: Charge Transfer or Mass Transfer?, Journal of The Electrochemical Society 165 (1) (2018) A6001–A6004. doi:10.1149/2.0011801jes.

[37] O. Bohlen, J. B. Gerschler, D. U. Sauer, M. Keller, Robust Algorithms for a Reliable Battery Diagnosis - Managing Batteries in Hybrid Electric Vehicles, in: Proceedings of 22nd Electric Vehicle Symposium (EVS22), Japan, 2006.

[38] W. Waag, C. Fleischer, D. U. Sauer, Adaptive on-line prediction of the available power of lithium-ion batteries, Journal of Power Sources 242 (2013) 548 – 559. doi:10.1016/j.jpowsour.2013.05.111.

[39] C. Fleischer, W. Waag, Z. Bai, D. U. Sauer, On-line self-learning time forward voltage prognosis for lithium-ion batteries using adaptive neuro-fuzzy inference system, Journal of Power Sources 243 (2013) 728 – 749. doi:10.1016/j.jpowsour.2013.05.114.

Paper A15

Transferring the Incremental Capacity Analysis to Lithium-Sulfur Batteries

Vaclav Knap, Theodoros Kalogiannis, Rajlakshmi Purkayastha, Szymon Beczkowski, Daniel-Ioan Stroe, Erik Schaltz and Remus Teodorescu

The paper has been published in the *ECS Transactions*, vol. 77, no. 11, pp. 1919–1927, Jul. 2017, doi:10.1149/07711.1919ecst. Republished here with permission of Electrochemical Society, 2017; permission conveyed through Copyright Clearance Center, Inc.

ECS Transactions, 77 (11) 1919-1927 (2017)
10.1149/07711.1919ecst ©The Electrochemical Society

Transferring the Incremental Capacity Analysis to Lithium-Sulfur Batteries

V. Knap[a], T. Kalogiannis[a], R. Purkayastha[b], S. Bęczkowski[a], D.-I. Stroe[a], E. Schaltz[a] and R. Teodorescu[a]

[a] Department of Energy Technology, Aalborg University, Aalborg, 9000, Denmark
[b] Oxis Energy Ltd, Culham Science Centre, Abingdon, Oxfordshire OX14 3DB, United Kingdom

In order to investigate the battery degradation and to estimate their health, various techniques can be applied. One of them, which is widely used for Lithium-ion batteries, is the incremental capacity analysis (ICA). In this work, we apply the ICA to Lithium-Sulfur batteries, which differ in many aspects from Lithium-ion batteries and possess unique behavior. One of the challenges of applying the ICA to Lithium-Sulfur batteries is the representation of the IC curves, as their voltage profiles are often non-monotonic, resulting in more complex IC curves. The ICA is at first applied to charge and discharge processes at various temperature levels and afterward the technique is applied to a cell undergoing cycling degradation. It is shown that the ageing processes are trackable from the IC curves and it opens a possibility for their utilization for state-of-health estimation.

Introduction

With a growing number of battery applications in today's world, there is a lot of interest into methods of detecting, estimating, and analyzing battery degradation. Consequently, many different health detection and estimation methods and techniques have been proposed. Among these is the incremental capacity analysis (ICA) (1) method, which has generated significant interest in the Lithium-ion (Li-ion) batteries research and development. The method offers the possibility to analyze the ageing processes (e.g. loss of lithium inventory, loss of active material and kinetic changes) of Li-ion batteries and also has the potential to be implemented into a battery management system (2).

Dubarry et al. in (1) characterized ICA as a method which can track the electrochemical properties of a cell during a charge or discharge. These properties that are associated with the intercalations and the phase transformations can be seen at the voltage curves as the steep increases or the plateau regimes and they are translated into identifiable dQ/dV peaks when differentiating the capacity over the voltage. Several studies have been made for different Li-ion chemistries, different C-rates and temperatures as well as aging conditions. Specifically, Kassem et al. (3) stored LFP/G cells at different temperatures and SOC levels. The capacity fade under the different calendar conditions was investigated and the corresponding IC peaks for the different cases were compared. A reverse proportional trend of the IC peak to the temperature and SOC storage levels was observed. Dubarry et al. (4) investigated the IC behavior and identified the possible aging mechanisms of two different designed $LiFePO_4$ – based, 10

Ah Li-ion cells, a prismatic and a cylindrical, for cycle aging and at two different temperatures. Also in (5), Dubarry et al. examined the degradation of ten 1.9 Ah commercial 18650 Li-ion cells with a composite positive electrode by means of IC analysis. The degradation of NMC/G based Li-ion cells were studies in (6) under cycle aging for several depth-of-discharges whereas in (7), LTO cells were tested for 55 ^{o}C and the lifetime of three commercial cells was evaluated. In (8), Dubarry et al. investigated the capacity fade and the aging mechanisms of LFP cells for cycle aging and with discharge C-rates between C/25 to C/2.

Furthermore, different implementation techniques of the ICA have been proposed in the literature, starting from the most simple to directly differentiate the raw data of the capacity over the voltage to more advanced, by employing mathematical models and filters capable of providing more accurate and robust IC curves. Feng et al. (9) used a probability density function at the battery's terminals to generate the IC curve. Riviere et al. (10) built a health estimation model for LFP battery cells, using a butterworth filter for smoothing and identify the IC peaks. Weng et al. (11) analyzed the IC curves by comparing results from the simplest approach of direct fitting the charging curves, obtaining their functions and differentiate them, to a more advanced mathematical model with support vector regression to fit those charging curves. Lastly, Han et al. (2) divided the charging curves based on a specific voltage step, usually 5 mV, and by calculate the corresponding voltage samples in each step the IC peaks are plotted. The challenges of the ICA in general, are that it requires a constant current at low rates (C/25), and specifically for the last approach, a constant sample frequency in order to derive accurately the peaks is also required. The major advantage on the other hand, is that information about the degradation of the Li-ion battery cells can be obtained with a non-destructive approach. However, what is the suitability of this method for emerging battery technologies, such as Lithium-Sulfur (Li-S)?

Li-S batteries differ in many aspects from Li-ion batteries, as for example discussed by Propp et al. (12), a fact which in some cases prevents a straightforward transfer of the methods and approaches to be applied on them. Already at the method applicability, the first difference and challenge can be spotted by comparing the charging and discharging voltage profiles of the Li-ion and Li-S batteries, as illustrated in Fig 1. $LiFePO_4$/G (LFP) based cells have a flat voltage profile for a majority range of state-of-charge (SOC), except with end of charge and discharge. In contrary to that, $Li[NiCoMn]O_2$/G (NMC) voltage profile is continuously decreasing with decrease of the SOC. Thus, the strictly monotonous voltage curves are observed at the Li-ion batteries, while the typical Li-S voltage discharging curve has a 'dip' between the high- and low- voltage plateaus. Moreover, the Li-S charging curve can be monotonous or it can have a 'bump' (high internal resistance) at the beginning of the charging phase, according to the charging conditions and the previous cycling history. Furthermore, the two chemistries are driven by different mechanisms. The Li-ion batteries work based upon an intercalation mechanism, where the ions travel directly between the electrodes. On the other hand, the Li-S batteries are "solution chemistries", where reduction and oxidation reactions of several stages of polysulfide species take place during charging and discharging (13). Therefore, analyzing the incremental capacity (IC) curves should be done carefully by considering the aforementioned differences.

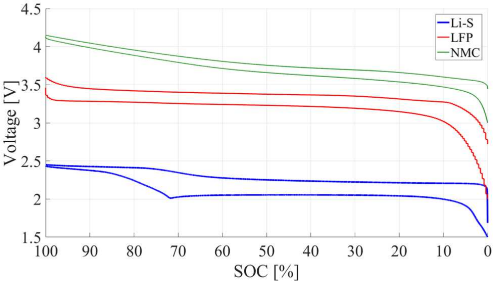

Figure 1. Comparison of charging and discharge voltage profiles of Lithium-Sulfur (Li-S), Lithium-iron-phosphate (LFP) and Lithium-nickel-manganese-cobalt-oxide (NMC) batteries.

Literature Review on ICA Applied to Li-S Batteries

ICA has not been widely applied to Li-S batteries. We have found only few sources which are present and discuss the IC curves. He et al. (14) used ICA for a graphical analysis of the pouch polymer battery with sulfur composite cathode and lithium foil anode in the size of 4×40×26 mm. The peaks in the IC curves are believed to stand for electrochemical reaction equilibriums, where the cathode material is reduced or oxidized. They detected two separate peaks during discharge at 2.10 V and 1.88 V, which implies that the cathode material reduction is happening in two steps in the composite. During the charging, two separate peaks were detected at 2.22 V and 2.36 V, which implies two charging plateaus related to two steps of the cathode material oxidation in the composite. The conclusion drawn is that the composite probably has two “active points” for lithium storage, which are connected to two voltage plateaus during charging and discharging. Ahn et al. (15) investigated coin cells with sulfur-MWCNT composite and precipitated sulfur as cathodes. They detected two peaks close to 2.45 V and 2.1 V during charge and discharge, which corresponds to the potential plateaus obtained from voltage profile during discharge. They are assigned to the formation of high-order (Li_2S_n, $4 \leq n \leq 8$), and low-order (Li_2S_n, $n < 4$) lithium polysulfides, respectively. Kim et al. (16) presented IC curves of a coin cell with HCS-S composite cathode to demonstrate its great electrochemical behavior, because of the full overlap of the peaks during the first and the second cycle. Moreover, this attribute, together with peak sharpness, should point out high reversibility and very fast electrode kinetics. Yersak et al. (17) applied the ICA to the all-solid-state Lithium metal batteries with FeS and S composite cathodes in order to understand and qualitatively determine parallel redox chemistries. A reduction peak at 2.2 V was characterized for S and it remained distinguishable also for the composite cathodes. In these previous works, where the ICA was applied to Li-S batteries, there is missing any note related to the unique character of the Li-S voltage profile and consequently to the specific forms, which are present in the dQ/dV plots.

In our work, we apply ICA to the pre-commercial 3.4 Ah Li-S pouch cells in order to evaluate its transferability to this battery chemistry. At first, the charging and discharging processes at different temperatures are investigated to observe the dQ/dV and also dV/dQ plots and their changes. It is followed by applying the ICA to the degrading cell by cycling to see if the ageing phenomena can be detected.

Experimental

Laboratory Tests

The performed experiments were conducted on a Digatron BTS 600 battery test station on the 3.4 Ah Li-S long-life type cells provided by OXIS Energy. The current of 3.4 A corresponds to 1 C-rate. The considered cut-off limits were 2.45 V or 11 hours for charging and 1.5 V for discharging. During the test, the cells were kept at the temperature controlled environment.

The test procedure for obtaining constant current charging and discharging curves consists of a pre-conditioning cycle (0.1 C-rate charging, 0.2 C-rate discharging) before every charging/discharging cycle at a specific rate. For charging, the currents of 0.1, 0.2 and 0.5 C-rate were used and for discharging, they were 0.1, 0.2, 0.5, 1.0, 1.5, 2.0, 2.5 and 3.0 C-rate. Three temperature levels of 15, 25 and 35 °C were investigated.

Filtering and Processing

The battery voltage was measured during charge/discharge cycle with a 0.2 mV resolution ADC with fixed-time sampling. A first derivative of the voltage is needed for the ICA analysis, however, calculating a derivative of a quantized data is a well-known challenge. The original measured data needs to be smoothed first before the derivative can be found.

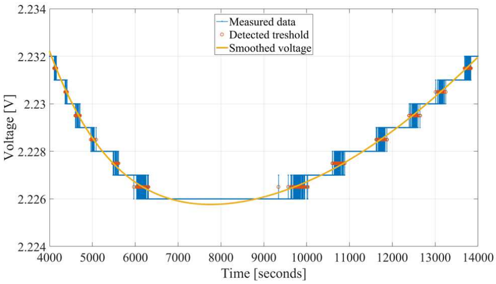

Figure 2. Measured voltage data, points extracted for smoothing and the final smoothed battery voltage.

In these tests, the battery voltage rises rapidly in the beginning of the charge cycle and then varies slowly during the last part of the cycle. Strongly varying signal dynamics poses challenges on finding a robust algorithm to smooth the data.

As can be seen in Fig. 2, the measured voltage data contained long stretches of time where the ADC converter would output a constant value. These portions of time have the highest quantization error. When the battery voltage crossed the threshold voltage of the ADC the quantization error is the smallest. The smoothing procedure creates a derived voltage data set that only included points when the ADC would change its output. These points are marked in Fig. 2 and are used further as a basis of creating a smoothed voltage waveform. A sliding window local fit is then utilized to find the smoothed voltage values.

Using the newly created points a 7-th order polynomial is fitted locally, around x_0, and the value of the polynomial at x_0 is taken as the smoothed value.

Results & Discussion

Charge Curves

For the state-of-health estimation, the charging curves have usually a greater significance than the discharging curves, because of the charging process is more likely to be performed by the constant current than the discharging in various battery applications. In Fig. 3, voltage charging curves for 0.1 C-rate for three temperature levels are shown. The charging curves for 15 and 25 °C have a monotonous trend, while the charging curve at 35 °C shows the kink in the beginning of charging. The monotonous curves can be easily represented in the dQ/dV plot, as it is also presented in Fig. 3, with the characteristic IC peaks. However, the non-monotonic curve shows discontinuity at the voltage level of the kink, which does not form an expected peak.

The obtained peaks at 25 °C are: a high peak at 2.205 V and a low peak at the high voltage spreading between 2.41 and 2.45 V. The low peak is actually composed of two peaks at 2.416 and 2.428 V. The voltage value of the peaks corresponds to the beginning of the low voltage plateau and to the high voltage plateau during charging, respectively. The observed characteristics are in good agreement with the presented IC curves in (15) and (16).

The remaining challenge is about the representing the voltage kink, existent for charging at 35 °C, in the terms of dQ/dV curves. The detail of the kink is shown in Fig. 4c). As the cell is charged, instead of the expected peak, there appears at first the curve with a sharp knee, which is followed by the curve with negative gradient and it ends by the positive decreasing curve followed by a rise to a higher voltage. This presentation prevents an intuitive graphical evaluation, even though it can be observed from Fig. 4a) that the characteristic features of the peak as the very steep rise and slower continuous descent is still present. However, when the data is plotted in an inverse manner as dV/dQ instead of dQ/dV, it provides a better representation of the voltage kink, which takes a form of the loop in the dV/dQ plot, as illustrated in Fig. 4d). No information is lost that way, but the curve features are getting another meaning and allow another intuitive analysis. The peaks in dV/dQ plot represent the voltage regions with higher gradient than previously the plateaus. The typical character of such dV/dQ curve is that it starts at very high values in the beginning of the charging and it decreases until the value close to the zero (for 0.1 C-rate it is approximately at 2.2 V, shown in Fig. 4b)), then either the loop representing the voltage kink starts, or it is followed directly by the slow rise of the peak, which later again decreases. The mathematical meaning stays same as it is demonstrated in Fig. 4e) and Fig. 4f). The dQ/dV peak at 2.427 V reaches the value of 34.22 Ah/V, while one can see in Fig. 4f) the valley at the same voltage with the value of 0.02922 V/Ah (1 / 34.22 = 0.02922).

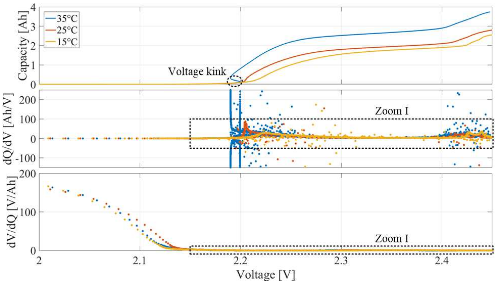

Figure 3. The charging curves for 0.1 C-rate at various temperature levels. The zoomed area is pictured in Fig. 4.

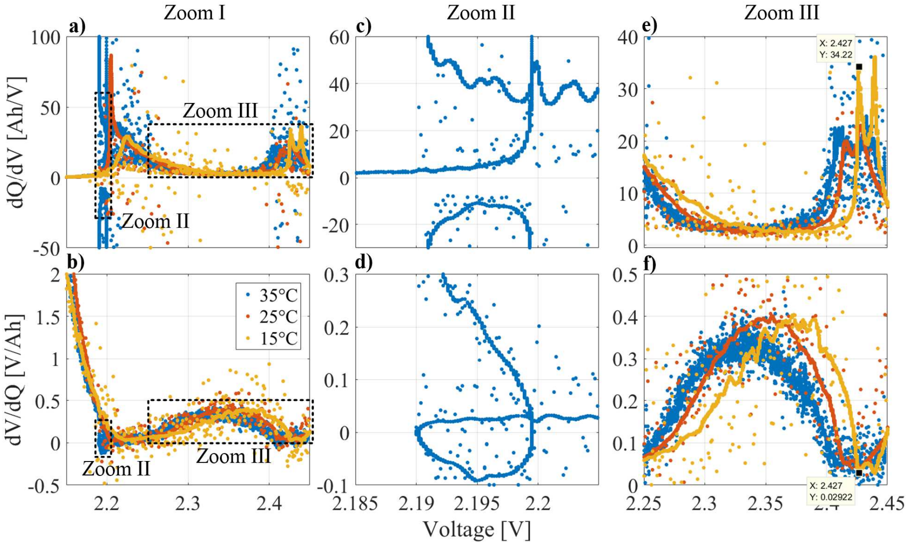

Figure 4. Detail plots for processed 0.1 C-rate charging curves at various temperature levels.

Discharge Curves

The voltage discharge curves have a different character than the charge curves for the Li-S batteries. However, at least for the small currents (0.1 C-rate), they result into fairly similar dQ/dV curves as shown in Fig. 5. There is a smaller peak at the high voltage plateau and there would be a high peak at the low voltage plateau, but due to the non-monotonic curve it results again into the discontinuity artefact. This discontinuity is represented again by a loop in the dV/dQ graph.

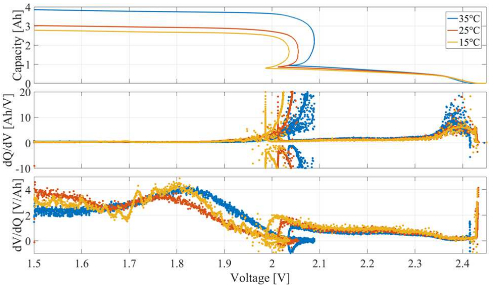

Figure 5. The discharging curves for 0.1 C-rate at various temperature levels.

Degradation Observations

In order to evaluate if ICA is a suitable method for the state-of-health estimation at the Li-S batteries, the Li-S cell was degraded by cycling at 30 °C by 0.1 C-rate charging until 2.45 V or 11 hours and by 0.2 C-rate until 1.5 V. A reference procedure test (RPT) was performed at the beginning of the life and then periodically every 20 cycles to capture the cells changing parameters such as the capacity or the impedance. The evaluation cycle, used for ICA, was performed at the same conditions as the cycling.

The visible sign of the degradation on the dQ/dV curves during discharging, presented in Fig. 6, is only at the peaks at the high voltage region, which are decreasing and moving towards higher voltage with an increasing degradation. The change with the clear trend at the dV/dQ curve is at the peaks appearing immediately after the loop. These peaks are growing and increasing in voltage. It seems that the degradation for these specific conditions is trackable through the dQ/dV and dV/dQ curves. However, the discharge curves do not provide many indicators.

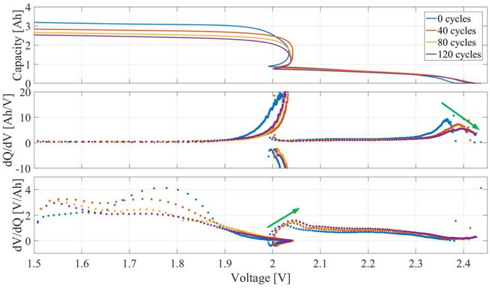

Figure 6. The evolution of the discharge curves for 0.2 C-rate during the aging cycling.

Contrary to the discharge curves, the charge curves provide several indicators of ageing, which makes them very suitable for the SOH estimation, even though the possibility of reversible degradation should be also considered. As it is noticeable from Fig. 7, the dQ/dV peaks at the high voltage plateau have a tendency to move to a higher voltage, which might be caused by the increased resistance, and to grow, which might be a sign of the growing effect of the polysulfide shuttle. At the low voltage plateau, there was clearly one peak at the beginning of life, during ageing the growing kink appears, which results into discontinuity artefact on the dQ/dV curve. However, in this case its character is easier to observe. The curves at the positive plane forms still a sort of quasi-peak, which is decreasing and moving to the right, reflecting a loss of capacity and a resistance growth. As the voltage kink is becoming higher and steeper, the 'knee' at the negative plain is moving to the higher voltage and the top of the knee is getting closer to zero. These changes at the voltage kink area are also clearly visible on the dV/dQ plot, where the loop is increasing its volume and moving towards right. Another noticeable behavior is an increasing gradient in a transition from the low voltage plateau to the high voltage plateau, which is getting steeper during the ageing.

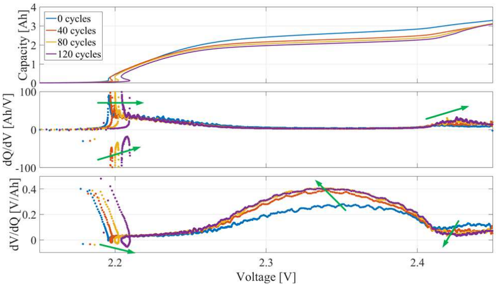

Figure 7. The evolution of the charging curves for 0.1 C-rate during the aging cycling.

Conclusions

The ICA technique was applied to charging and discharging voltage profiles of Li-S cells at various temperatures and unique behavior of the dQ/dV and the dV/dQ plots were detected. The 'classical' two peaks, at high- and low- voltage plateaus, are expected to be related to the formation of long and short polysulfide species, respectively. However, further relation of the curves to the specific mechanisms is missing. When applied to the cell undergoing degradation, the IC curves shown changing character, which reflects ageing phenomena and thus might allow for state-of-health estimation.

Acknowledgments

This work has been part of the ACEMU-project. The authors gratefully acknowledge the Danish Council for Strategic Research (1313-00004B) and EUDP (1440-0007) for providing financial support and would like to thank OXIS Energy for supplying the Lithium-Sulfur battery cells.

References

1. M. Dubarry, V. Svoboda, R. Hwu, and B. Yann Liaw, *Electrochem. Solid-State Lett.*, **9**, A454–A457 (2006).
2. X. Han, M. Ouyang, L. Lu, J. Li, Y. Zheng, and Z. Li, *J. Power Sources*, **251**, 38–54

(2014).
3. M. Kassem, J. Bernard, R. Revel, S. Pélissier, F. Duclaud, and C. Delacourt, *J. Power Sources*, **208**, 296–305 (2012).
4. M. Dubarry, B. Y. Liaw, M. S. Chen, S. S. Chyan, K. C. Han, W. T. Sie, and S. H. Wu, *J. Power Sources*, **196**, 3420–3425 (2011).
5. M. Dubarry, C. Truchot, M. Cugnet, B. Y. Liaw, K. Gering, S. Sazhin, D. Jamison, and C. Michelbacher, *J. Power Sources*, **196**, 10328–10335 (2011).
6. J. V. M. M. Berecibar, M. Dubarry, N. Omar, I. Villarreal, *Evs29*, 1–12 (2016).
7. X. Han, M. Ouyang, L. Lu, and J. Li, *Energies*, **7**, 4895–4909 (2014).
8. M. Dubarry and B. Y. Liaw, *J. Power Sources*, **194**, 541–549 (2009).
9. X. Feng, J. Li, M. Ouyang, L. Lu, J. Li, and X. He, *J. Power Sources*, **232**, 209–218 (2013).
10. E. Riviere, P. Venet, A. Sari, F. Meniere, Y. Bultel, U. Claude, B. Lyon, U. De Lyon, and V. Cedex, *Veh. Power Propuls. Conf. (VPPC), 2015 IEEE*, 1–6 (2015).
11. C. Weng, Y. Cui, J. Sun, and H. Peng, *J. Power Sources*, **235**, 36–44 (2013).
12. K. Propp, M. Marinescu, D. J. Auger, L. O'Neill, A. Fotouhi, K. Somasundaram, G. J. Offer, G. Minton, S. Longo, M. Wild, and V. Knap, *J. Power Sources*, **328**, 289–299 (2016).
13. M. Wild, L. O'Neill, T. Zhang, R. Purkayastha, G. Minton, M. Marinescu, and G. J. Offer, *Energy Environ. Sci.* (2015).
14. X. He, W. Pu, J. Ren, L. Wang, J. Wang, C. Jiang, and C. Wan, *Electrochim. Acta*, **52**, 7372–7376 (2007).
15. W. Ahn, K.-B. Kim, K.-N. Jung, K.-H. Shin, and C.-S. Jin, *J. Power Sources*, **202**, 394–399 (2012).
16. J. Kim, D. J. Lee, H. G. Jung, Y. K. Sun, J. Hassoun, and B. Scrosati, *Adv. Funct. Mater.*, **23**, 1076–1080 (2013).
17. T. a. Yersak, C. Stoldt, and S.-H. Lee, *J. Electrochem. Soc.*, **160**, A1009–A1015 (2013).

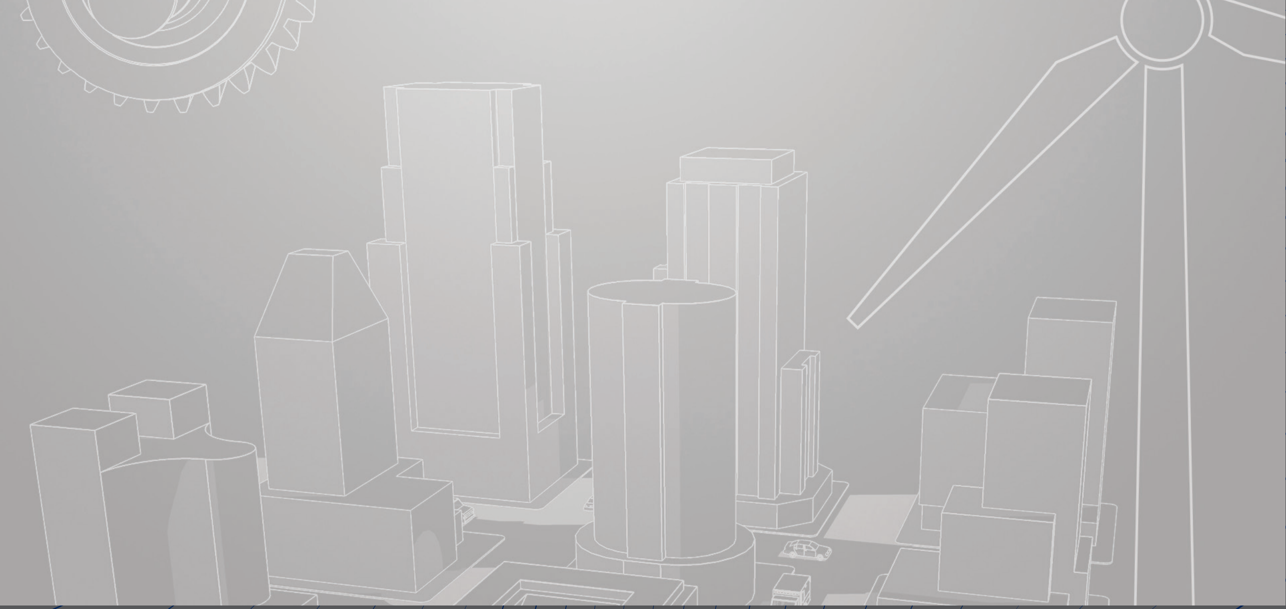

ISSN (online): 2446-1636
ISBN (online): 978-87-7210-070-8

AALBORG **UNIVERSITY PRESS**